

## Methods for Grid-aware Operation and Planning of Active Distribution Networks

Présentée le 27 janvier 2023

Faculté des sciences et techniques de l'ingénieur  
Laboratoire des systèmes électriques distribués  
Programme doctoral en génie électrique

pour l'obtention du grade de Docteur ès Sciences

par

**Rahul Kumar GUPTA**

Acceptée sur proposition du jury

Prof. F. Rachidi-Haeri, président du jury  
Prof. M. Paolone, Dr F. Sossan, directeurs de thèse  
Prof. D. K. Molzahn, rapporteur  
Prof. L. Wehenkel, rapporteur  
Dr S.-R. Cherkaoui, rapporteur



All models are wrong  
but some are useful.

— George Edward Pelham Box

To my parents and teachers...

# Acknowledgements

I would like to express my sincere thanks to both of my thesis directors. I have been very fortunate to have Prof. Mario Paolone as my thesis director. I am very grateful for his careful and unconditional guidance throughout the past four years of my Ph.D. studies. His dedication and energy toward research and teaching have been a great source of inspiration for me. His supervision has continuously improved me as a researcher, enhanced my problem-solving ability, and gained me immensely in analytical and critical thinking. He has been my reference for any questions, whether it is about a piece of theoretical or practical knowledge. I am equally thankful to my thesis co-director Prof. Fabrizio Sossan for his immense support during my Ph.D. and M.Sc. years. Thanks for always being available for any discussion, whether reviewing my first draft of the manuscript, discussing initial results, or brainstorming new ideas. I am very grateful for everything. You two are my role models.

Also, I would like to thank Dr. Rachid Charkaoui and Prof. Jean-Yves Le Boudec for their valuable inputs during my Ph.D. years. I want to thank Ms. Sophie Flynn for taking care of administrative and off-technical things. And much thanks to Sylvain for his support in handling microgrid installations.

Then, I would like to thank my colleagues cum friends. You have enriched my Ph.D. life in multifaceted ways. Mainly, I want to thank Sherif; I got to explore the microgrid setup with him. You have been my savior many times; thanks for all your support. Then, I would like to thank Enrica, Andreas, Lorenzo R., Antonio Z., Marco, Zhaoyang, and Asja for their mentor-like guidance during my Ph.D. years. I want to thank Yihui, Francesco, Vladimir, and Matthieu, with whom I had the opportunity to collaborate. I want to thank Johanna, Willem, Alex, Simone, Lu, and many others, with whom I enjoyed spending time together in the lab. A special thanks to a kind and loving soul, Jihyun. Thanks for always being there with me. Thanks for keeping my days fun and adventurous.

Finally, the greatest thanks go to my *Ma, Papa, Bhaiya-* and *Bhabhi-ji*. Thanks to my *Dada-ji* and late *Dadi-ji*. You always have been by my side in happy and challenging times. Thanks to all my teachers, in particular, Ganesh Rai and Chittibabu B., for their early guidance in pursuing a career in science. Thanks to my Alma mater, Sita High School Hariharganj, St. Xavier's College Ranchi, and NIT Rourkela.

*Lausanne, 3 Oct 2022*

Rahul K. Gupta





# Abstract

Modern power systems face significant operational challenges due to the accelerated and much needed deployment of decentralized renewable generation. As a matter of fact, such deployment has increased power imbalances leading to increased reserve requirements in power transmission grids and is causing operational issues in power distribution grids associated with the delivered quality-of-service (especially concerning voltage quality) as well as lines and transformers congestions. A potential solution to tackle these challenges is to define efficient and scalable control frameworks in active distribution networks (ADNs) capable of: (i) satisfying the local ADNs' constraints and (ii) aggregating heterogeneous resources at different timescales to provide ancillary services to the transmission network. In this context, this thesis proposes methods for controlling and planning distributed energy resources (DERs) in ADNs. In particular, the thesis deals with three main challenges: (i) developing and experimentally validating grid-aware real-time control frameworks, (ii) estimating power grid's models from distributed measurements to be used for grid-aware control schemes, and (iii) wide-scale planning of DERs in ADNs.

The first part of the thesis proposes real-time grid-aware control frameworks for ADNs hosting heterogeneous, controllable, and stochastic DERs. In particular, it proposes a control and scheduling framework that tracks a pre-defined power profile (*dispatch plan*) at the grid connection point (GCP) of an ADN while ensuring that the grid states (i.e., the nodal voltages and lines/transformer power/current flows) remain within the prescribed limits. However, accounting for the exact grid constraints makes the control problem non-convex and computationally expensive to solve (this category of problems is known as *optimal power flows* – OPF). Due to this, OPF problems are often used for offline optimization schemes such as planning problems. In this context, this part of the thesis proposes, and experimentally validates, computationally tractable OPF-based real-time control schemes. In particular, an accurate and linear OPF (LOPF)-based real-time control scheme relying on power-flow sensitivity coefficients is proposed to obtain a tractable and computationally efficient formulation. In this respect, the work presents and compares different linearization policies for the LOPE. The proposed schemes are applied to formulate suitable model predictive control (MPC) schemes of DERs for tracking day-ahead dispatch plan at the GCP of an ADN. We use the Alternating Direction Method of Multipliers (ADMM)-based distributed optimization scheme, enabling the scalability of an original real-time MPC. Also for this case, the performance of different linearization policies is assessed with particular reference to accuracy and computational speed.

Then, the dominant approach is identified and experimentally validated on a real-scale low voltage microgrid hosted at the EPFL Distributed Electrical Systems Laboratory, representing a replica of the 200kVA/0.4kV CIGRE microgrid benchmark system defined by the CIGRE Task Force C6.04.02.

The above control scheme works well when the ADN is interfaced with sufficient flexible resources. However, it might fail (i.e., resulting in poor control performance - high dispatch tracking error) when the network is interfaced with a high number of stochastic non-controllable DERs. In such a case, the energy rating of flexible resources, for example battery energy storage systems (BESSs), might not be sufficient and may suffer from early saturation of their State-of-Charge (SOC), leading to unreliable dispatch tracking. This part of the thesis tackles this problem with a two-layer MPC. The upper layer MPC, running at a slower timescale, optimizes battery SOC trajectories while minimizing the tracking error considering the forecast of the stochastic demand and generation for the whole day. Then, the lower layer MPC, running at a faster timescale, takes battery SOC (from upper layer) trajectories as constraints while achieving a high-resolution tracking of the dispatch plan. The control scheme is experimentally validated using a 1.5 MVA/2.5 MWh BESS connected to an actual 24-node medium voltage (MV) ADN in Switzerland hosting uncontrollable 3.2 MWp distributed photovoltaic generation, 3.4 MVA hydro generations, and 2.8 MW of base demand.

The above control schemes assume that the grid models (topology and electrical line parameters) are known and, therefore, referred to as *model-based control schemes*. However, distribution networks models might be unavailable, partially missing, or often incorrect. In this context, the second part of the thesis develops the concept of *model-less or measurement-based control schemes* where the network models are inferred from online measurements and then used in the control frameworks. We investigate two approaches. First, the compound admittance matrix ( $\mathbf{Y}$ ) of an ADN is estimated, which is then used to compute relevant sensitivity coefficients. It is referred to as the *indirect estimation* approach. The developed estimation algorithm uses PMU synchrophasors measurements of voltage and current for the  $\mathbf{Y}$  estimation. The algorithm uses a linear estimation model that processes phasor measurements of nodal voltages, injection currents, and branch currents. The estimation scheme is generic and applicable to any unbalanced three-phase distribution network with shunt components and generic topology (i.e., radial or meshed). The work proposes and analyses the performance of a pre-processing strategy on the PMU's raw measurements, which consists of grouping the raw measurements in clusters and then using the averaged measurements from each cluster. The proposed pre-processing step reduces the noise level, ultimately improving the estimation quality of regression-based estimation methods such as least squares (LS) and total least squares (TLS). The proposed approach is validated by numerical experiments for different CIGRE and IEEE benchmark grids. Second, a *direct measurement-based estimation* of the sensitivity coefficients is proposed using the nodal voltage and power measurements. The direct and indirect approaches are then used to formulate a model-less/measurement-based voltage control of the DERs in distribution networks. Finally, we compare them concerning the uncertainty of the sensitivity coefficients estimates.

Since all the above control schemes rely on the flexibility offered by DERs and the *amount* of

decentralized renewable energy resources (RERs) connected to the ADNs, the last part of the thesis focuses on *assessing and planning those DERs and RERs in the distribution networks of a whole country*. In particular, it focuses on (i) assessing the hosting capacity of ADNs concerning Photovoltaic (PV) plants and (ii) planning controllable assets (e.g., BESS) as an alternative to grid reinforcement. However, as the countrywide models of the distribution grids are generally unavailable, this part first tackles the challenge of estimating realistic *synthetic models* of power distribution networks using public data sets. It is done by developing an unsupervised approach to infer the grid's topology and characteristics starting from the publicly available locations of the Extra High Voltage (EHV) substations and geo-referenced socio-economic data such as population density and heat demand map. Then, it determines the PV hosting capacity of distribution networks by formulating a grid-aware planning problem. The LOPF models developed previously are used to account for the grid constraints. Then, an optimal planning problem of BESSs in ADNs is proposed to increase the hosting capacity of the distribution networks. Finally, we derive cost-optimal plans for the countrywide deployment of PV generation and BESS considering the MV power distribution infrastructure's technical limitations. The method is applied to Switzerland as a case study.

**Key words:** Active distribution networks (ADNs), AC optimal power flow (AC-OPF), admittance matrix estimation, alternating direction method of multipliers (ADMM), battery energy storage system (BESS), congestion management, data-driven control, data-driven estimation, dispatching, distributed control, grid-aware control, hosting capacity, inference, least-squares, linear optimal power flow, measurement-based control, microgrids, model-less control, model predictive control, optimal planning, optimal power flow, photovoltaic, recursive least squares, robust voltage control, sensitivity coefficients, stochastic optimization, synthetic power networks.



# Résumé

Les réseaux électriques modernes sont confrontés à des défis opérationnels importants en raison du déploiement accéléré et indispensable de la production renouvelable décentralisée. En fait, ce déploiement augmente les déséquilibres de puissance, ce qui entraîne une augmentation des besoins de réserve dans les réseaux de transport d'électricité et cause des problèmes opérationnels dans les réseaux de distribution d'électricité associés à la qualité du service fourni (en particulier concernant la qualité de la tension) ainsi qu'à la congestion des lignes et des transformateurs. Une solution potentielle pour relever ces défis est de définir des environnements de contrôle efficaces et évolutifs dans les réseaux de distribution actifs (ADNs) capables de : (i) satisfaire les contraintes locales des ADNs et (ii) agréger des ressources hétérogènes à différentes échelles de temps pour fournir des services auxiliaires au réseau de transmission. Dans ce contexte, cette thèse propose des méthodes de contrôle et de planification des ressources énergétiques distribuées (DERs) dans les ADNs. En particulier, la thèse aborde trois défis principaux : (i) le développement et la validation expérimentale de environnements de contrôle en temps réel adaptés au réseau, (ii) l'estimation des modèles du réseau électrique à partir de mesures distribuées à utiliser pour les schémas de contrôle adaptés au réseau, et (iii) la planification à grande échelle des DERs dans les ADNs.

La première partie de la thèse propose des environnements de contrôle en temps réel pour les ADNs hébergeant des DERs hétérogènes, contrôlables et stochastiques. En particulier, elle propose un environnements de contrôle et de programmation qui suit un profil de puissance prédéfini (plan de répartition) au point de connexion au réseau (GCP) d'un ADN tout en garantissant que les états du réseau (c'est-à-dire les tensions nodales et les flux de puissance/courant des lignes/transformateurs) restent dans les limites prescrites. Cependant, la prise en compte des contraintes exactes du réseau rend le problème de contrôle non convexe et coûteux à résoudre (cette catégorie de problèmes est connue sous le nom de *répartition optimale des puissances* – OPF). Pour cette raison, les problèmes OPF sont souvent utilisés pour des schémas d'optimisation hors ligne tels que les problèmes de planification. Dans ce contexte, cette partie de la thèse propose, et valide expérimentalement, des schémas de contrôle en temps réel basés sur les OPE. En particulier, un schéma de contrôle en temps réel basé sur l'OPF linéaire et précis (LOPF) qui s'appuie sur les coefficients de sensibilité du flux de puissance est proposé pour obtenir une formulation traçable et efficace en termes de calcul. À cet égard, le travail présente et compare différentes politiques de linéarisation pour le LOPE. Les schémas proposés sont appliqués pour formuler des schémas de contrôle prédictif de

modèle (MPC) appropriés pour les DERs afin de suivre le plan de répartition du jour précédent au GCP d'un ADN. Nous utilisons un schéma d'optimisation distribué basé sur la méthode des multiplicateurs à direction alternée (ADMM), ce qui permet l'extensibilité d'un MPC original en temps réel. Toujours pour ce cas, les performances de différentes politiques de linéarisation sont évaluées, notamment en regard de précision et de vitesse de calcul. Ensuite, l'approche dominante est identifiée et validée expérimentalement sur un micro-réseau basse tension à échelle réelle hébergé au Laboratoire des systèmes électriques distribués de l'EPFL, représentant une réplique du système de référence de micro-réseau CIGRE de 200kVA/0.4kV défini par la Task Force C6.04.02 du CIGRE.

Le schéma de contrôle ci-dessus fonctionne bien lorsque l'ADN est interfacé avec des ressources flexibles suffisantes. Cependant, il peut échouer (c'est-à-dire entraîner une mauvaise performance de contrôle - erreur de suivi de la répartition) lorsque le réseau est interfacé avec un nombre élevé de DER stochastiques non contrôlables. Dans un tel cas, l'énergie nominale des ressources flexibles, par exemple les systèmes de stockage d'énergie par batterie (BESSs), peut ne pas être suffisante et peut souffrir d'une saturation précoce de leur état de charge (SOC), conduisant à un suivi peu fiable du dispatching. Cette partie de la thèse aborde ce problème avec un MPC à deux couches. Le MPC de la couche supérieure, fonctionnant à une échelle de temps plus lente, optimise les trajectoires de l'état de charge des batteries tout en minimisant l'erreur significative du suivi en considérant la prévision de la demande et de la production stochastiques pour la journée entière. Ensuite, le MPC de la couche inférieure, fonctionnant à une échelle de temps plus rapide, prend les trajectoires du SOC de la batterie (de la couche supérieure) comme contraintes tout en réalisant un suivi à haute résolution du plan de répartition. Le schéma de contrôle est validé expérimentalement en utilisant une BESS de 1.5 MVA/2.5 MWh connectée à un ADN de moyenne tension (MV) de 24 nœuds en Suisse, hébergeant une production photovoltaïque distribuée incontrôlable de 3.2 MWp, une production hydroélectrique de 3.4 MVA, et une demande de base de 2.8 MW.

Les schémas de commande ci-dessus supposent que les modèles du réseau (topologie et paramètres des lignes électriques) sont connus et sont donc appelés "schémas de commande basés sur les modèles". Cependant, les modèles des réseaux de distribution peuvent être indisponibles, partiellement manquants, ou souvent incorrects. Dans ce contexte, la deuxième partie de la thèse développe le concept de *systèmes de contrôle sans modèle ou basés sur la mesure* où les modèles de réseau sont déduits des mesures en ligne et ensuite utilisés dans les environnements de contrôle. Nous étudions deux approches. La première consiste à estimer la matrice d'admittance composée ( $\mathbf{Y}$ ) d'un ADN, qui est ensuite utilisée pour calculer les coefficients de sensibilité pertinents. C'est ce que l'on appelle l'approche *estimation indirecte*. L'algorithme d'estimation développé utilise les mesures de tension et de courant des synchrophaseurs des PMU pour l'estimation de  $\mathbf{Y}$ . L'algorithme utilise un modèle d'estimation linéaire qui traite les mesures des phasors des tensions nodales, des courants d'injection et des courants de branche. Le schéma d'estimation est générique et applicable à tout réseau de distribution triphasé déséquilibré avec des composants shuntés et une topologie générique (c'est-à-dire radiale ou maillée). Le travail propose et analyse la performance d'une stratégie de prétraitement des mesures brutes du PMU, qui consiste à regrouper les mesures brutes en

clusters et ensuite à utiliser les mesures moyennes de chaque cluster. L'étape de prétraitement proposée réduit le niveau de bruit, améliorant finalement la qualité d'estimation des méthodes d'estimation basées sur la régression telles que les moindres carrés (LS) et les moindres carrés totaux (TLS). L'approche proposée est validée par des expériences numériques pour différents réseaux de référence CIGRE et IEEE. Deuxièmement, une estimation *basée sur une estimation direct* des coefficients de sensibilité est proposée en utilisant les mesures de tension et de puissance nodales. Les approches directe et indirecte sont ensuite utilisées pour formuler un contrôle de la tension des DER dans les réseaux de distribution basé sur un modèle sans mesure. Enfin, nous les comparons en ce qui concerne l'incertitude des estimations des coefficients de sensibilité.

Puisque tous les schémas de contrôle ci-dessus reposent sur la flexibilité offerte par les DERs et la quantité de ressources d'énergie renouvelable décentralisées (RERs) connectées aux ADNs, la dernière partie de la thèse se concentre sur l'évaluation et la planification de ces DERs et RERs dans les réseaux de distribution d'un pays entier. En particulier, elle se concentre sur (i) l'évaluation de la capacité d'accueil des ADN concernant les centrales photovoltaïques (PV) et (ii) la planification des source actifs contrôlables (par exemple, BESS) comme une alternative au renforcement du réseau. Cependant, comme les modèles nationaux des réseaux de distribution ne sont généralement pas disponibles, cette partie s'attaque d'abord au défi d'estimer des modèles synthétiques réalistes des réseaux de distribution d'électricité en utilisant des ensembles de données publiques. Pour ce faire, une approche non supervisée est développée pour déduire la topologie et les caractéristiques du réseau à partir des emplacements des sous-stations à très haute tension (THT) accessibles au public et des données socio-économiques géoréférencées telles que la densité de population et la carte de demande de chaleur. Ensuite, il détermine la capacité d'accueil PV des réseaux de distribution en formulant un problème de planification sensible au réseau. Les modèles LOPF développés précédemment sont utilisés pour prendre en compte les contraintes du réseau. Ensuite, un problème de planification optimale des BESSs dans les ADNs est proposé pour augmenter la capacité d'accueil des réseaux de distribution. Enfin, nous dérivons des plans optimaux en termes de coûts pour le déploiement à l'échelle nationale de la production PV et des BESS en tenant compte des limitations techniques de l'infrastructure de distribution électrique MT. La méthode est appliquée à la Suisse comme étude de cas.

**Mots clés :** Réseaux de distribution actifs (ADN), flux de puissance optimal (OPF) en courant alternatif, estimation de la matrice d'admittance, méthode des multiplicateurs dans le sens alternatif (ADMM), système de stockage d'énergie par batterie (BESS), gestion de la congestion, commande pilotée par les données, estimation pilotée par les données, répartition de l'énergie, commande distribuée, commande en fonction du réseau, capacité d'accueil photovoltaïque, moindres carrés, flux de puissance optimal linéaire, basé sur la mesure, micro-réseaux, contrôle sans modèle, contrôle prédictif de modèle, planification optimale, flux de puissance optimal, photovoltaïque, moindres carrés récursifs, contrôle de tension robuste, coefficients de sensibilité, optimisation stochastique, réseaux synthétiques.





# Contents

<b>Acknowledgements</b>	<b>i</b>
<b>Abstract</b>	<b>iii</b>
<b>List of figures</b>	<b>xv</b>
<b>List of tables</b>	<b>xxi</b>
<b>Nomenclature</b>	<b>xxv</b>
<b>1 Introduction</b>	<b>1</b>
<b>I Model-based Control of Active Distribution Networks</b>	<b>7</b>
<b>Prelude</b>	<b>9</b>
<b>2 Model-based Grid-aware Dispatching of Active Distribution Networks</b>	<b>11</b>
2.1 State-of-the-Art . . . . .	11
2.2 Problem Statement . . . . .	13
2.3 Linearized Power Flow Model . . . . .	14
2.3.1 Policies for Sensitivity Coefficients Computation . . . . .	15
2.4 Day-Ahead Dispatch Computation . . . . .	17
2.4.1 Forecasts of Stochastic Resources . . . . .	17
2.4.2 Computation of the Dispatch Plan . . . . .	19
2.5 Real-time Model Predictive Control (RT-MPC) for Dispatch tracking . . . . .	21
2.5.1 Centralized Formulation . . . . .	21
2.5.2 Distributed Formulation using ADMM . . . . .	23
2.5.3 Short-term Forecasts . . . . .	25
2.6 Distributed Energy Resource Models . . . . .	25
2.6.1 BESS . . . . .	25
2.6.2 PV Power Plants . . . . .	26
2.7 Performance Comparison of Different Linearized OPF Policies for RT-MPC . . .	27
2.7.1 Simulation Setup . . . . .	27
2.7.2 Comparison of MPC with Different Linear Grid Models . . . . .	29
2.7.3 Control Performance . . . . .	32

## Contents

---

2.8	Experimental Validation and Results . . . . .	32
2.8.1	Microgrid Setup . . . . .	34
2.8.2	Controllable Distributed Energy Resources . . . . .	34
2.8.3	Monitoring and Actuation Layers . . . . .	35
2.8.4	Implementation of the Algorithms . . . . .	36
2.8.5	Experimental Results . . . . .	37
2.8.6	Further Analysis . . . . .	41
2.9	Discussion . . . . .	44
<b>3</b>	<b>Reliable Dispatch Tracking of Active Distribution Network using Batteries</b>	<b>47</b>
3.1	State-of-the-Art . . . . .	47
3.2	Problem Statement . . . . .	50
3.3	Day-Ahead Dispatch Computation . . . . .	51
3.3.1	Day-Ahead Load and Renewable Power Generation Forecast . . . . .	52
3.3.2	Day-Ahead Problem Formulation . . . . .	52
3.4	Real-time Operation via Two-layer Model Predictive Control . . . . .	53
3.4.1	Intra-day and Short-time Forecasting . . . . .	53
3.4.2	Grid Model using the AR-OPF . . . . .	53
3.4.3	Real-time Model Predictive Control (RT-MPC) of BESS . . . . .	56
3.5	Experimental Validation . . . . .	59
3.5.1	Experimental Setup . . . . .	59
3.5.2	Experimental Results . . . . .	64
3.5.3	Further Analysis . . . . .	71
3.6	Discussion . . . . .	74
<b>II</b>	<b>Model-less and Measurement-based Control of Active Distribution Networks</b>	<b>75</b>
	<b>Prelude</b>	<b>77</b>
<b>4</b>	<b>Data-driven Estimation of Compound Admittance Matrix and Power-Flow Sensitivity Coefficients</b>	<b>79</b>
4.1	Problem Statement . . . . .	79
4.2	State-of-the-Art . . . . .	81
4.3	Indirect Estimation of Sensitivity Coefficients via Estimation of Compound Admittance Matrix . . . . .	84
4.3.1	Polyphase Grid Model . . . . .	85
4.3.2	Estimation Model . . . . .	89
4.3.3	Estimation Techniques . . . . .	90
4.3.4	Measurement Pre-processing by Cluster Averaging . . . . .	91
4.3.5	Computation of Sensitivity Coefficients using Estimated Admittance Matrix and Error Propagation . . . . .	93
4.3.6	Simulation Setup for the Admittance Matrix Estimation . . . . .	98

4.3.7	Results and Discussion . . . . .	100
4.4	Direct Estimation of Sensitivity Coefficients . . . . .	110
4.4.1	Estimation Model . . . . .	110
4.4.2	Estimation Technique . . . . .	111
4.4.3	Simulation and Results . . . . .	115
4.4.4	Performance Metrics for Sensitivity Coefficient Estimation . . . . .	115
4.4.5	Estimation Results . . . . .	118
4.5	Performance Comparison of Direct and Indirect Methods for the Estimation of Sensitivity Coefficients . . . . .	121
4.5.1	Simulation Setup . . . . .	121
4.5.2	Performance Comparison . . . . .	122
4.6	Discussion . . . . .	124
<b>5</b>	<b>Model-less Robust Control of ADNs using Measurements-based Estimated Sensitivity Coefficients</b>	<b>127</b>
5.1	State-of-the-Art . . . . .	127
5.2	Problem Statement . . . . .	129
5.3	Problem Formulation . . . . .	130
5.3.1	Voltage Control Problem without Considering Uncertainty on the Estimates (Non-robust) . . . . .	130
5.3.2	Robust Voltage Control Problem . . . . .	131
5.4	Simulation and Results . . . . .	132
5.4.1	Test-case and Input Data . . . . .	132
5.4.2	Estimation Results . . . . .	133
5.4.3	Control Results . . . . .	135
5.5	Experimental Validation . . . . .	137
5.5.1	Experimental Setup . . . . .	137
5.5.2	Experimental Results . . . . .	139
5.6	Discussion . . . . .	144
<b>III</b>	<b>Countrywide Impact of Large Renewable Deployment on the Planning of Active Distribution Networks</b>	<b>145</b>
	<b>Prelude</b>	<b>147</b>
<b>6</b>	<b>Countrywide Synthetic Network Estimation, Computation of PV Hosting Capacity and Battery Energy Storage Requirements for Power Distribution Networks</b>	<b>149</b>
6.1	Problem Statement . . . . .	150
6.2	State-of-the-Art . . . . .	150
6.3	Estimation of Countrywide Models of Medium Voltage Power Distribution Networks: the Case of Switzerland . . . . .	153
6.3.1	Identification of EHV Areas . . . . .	153

## Contents

---

6.3.2	Identification of HV/MV Primary Substation: Locations and Characteristics . . . . .	154
6.3.3	Identification of MV/LV Secondary Substation: Location and Characteristics . . . . .	158
6.3.4	Power Networks Routing . . . . .	160
6.4	PV hosting Capacity and Energy Storage Requirements for Power Distribution Networks . . . . .	164
6.4.1	Input Data . . . . .	165
6.4.2	The PV Hosting Capacity Problem . . . . .	167
6.4.3	Increasing the PV Hosting Capacity with BESSs . . . . .	170
6.4.4	Optimal Allocation of PV and BESSs . . . . .	173
6.5	Results and Discussion . . . . .	174
6.5.1	Case Study . . . . .	174
6.5.2	Deployment of PV Plants . . . . .	175
6.5.3	Deployment of PV Plants and BESSs for Case 0 and Case 1 . . . . .	175
6.5.4	Cost Comparison . . . . .	177
6.6	Further Analysis . . . . .	178
6.6.1	Verification of Optimal Power Flow Results . . . . .	178
6.6.2	Validation of Synthetically Generated MV Networks . . . . .	180
6.7	Discussion . . . . .	181
<b>7</b>	<b>Conclusion</b>	<b>183</b>
	<b>Appendix</b>	<b>187</b>
<b>A</b>	<b>Performance Comparison of RT-MPC using Linearized vs. AR-OPF</b>	<b>189</b>
A.1	Accuracy of the Grid Model: . . . . .	189
A.2	Computational Performance: . . . . .	190
A.3	Control Performance: . . . . .	191
<b>B</b>	<b>Validation of Error Propagation using Monte-Carlo Simulations</b>	<b>193</b>
	<b>Bibliography</b>	<b>212</b>
	<b>Curriculum Vitae</b>	<b>213</b>

# List of Figures

2.1	Distributed computation of the control set-points using the ADMM technique: the resources solve their local problems in parallel and communicates the intermediate set-points to an aggregator that solves the OPF problem associated to the microgrid dispatch. This iterative procedure is followed until convergence.	25
2.2	Equivalent circuit diagram of a BESS.	26
2.3	CIGRE low voltage benchmark network.	28
2.4	(a-c) refers to active power profiles of three days	28
2.5	MPC operation using M3* on day 1.	33
2.6	The microgrid setup used for the experimental validation. We consider three controllable resources (a battery B at bus 5, and two curtailable PV plants PV1 and PV2 at bus 11 and 9) and a load emulator (L1 at bus 3).	34
2.7	Experimental setup: (a) Rooftop PV plants PV1 and PV2 (b) Load emulator and (c) Lechlance battery energy storage system. The ratings are reported in Table 2.8.	35
2.8	Feasible PQ set for the available DERs: a) battery can be controlled to provide both +/- active (P) and reactive powers (Q), b) PV1 can only provide + P (PV1 converter is not designed to receive external reactive set-points), and c) PV2 can be controlled to provide + P and +/- Q.	36
2.9	Data flow: Dispatch plan computation starts at 23:00 UTC day-before operation, using the PV and load forecasts, and is stored on the central data-server. Real-time operations start at 00:00 UTC. SCADA and short-term forecasters store their outputs to the data server each second, and ADMM computes power set-points and implements each 30 sec.	37
2.10	(a-c) Dispatch plan computation for day 1: 4th September 2019.	38
2.11	(a-c) The experimental results for real-time control using the distributed MPC on day 1: 4th September 2019.	39
2.12	(a-c) Dispatch plan computation for day 2: 10th September 2019.	41
2.13	(a-c) The experimental results for real-time control using the distributed MPC on day 2: 10th September 2019.	42
2.14	Computation time with number of BESS units for Day 2 (Simulation).	43
3.1	Schematic representation of the SOC evolution of the BESS with myopic single-layer MPC and farsighted two-layer MPC.	51
3.2	Schematic dataflow of the proposed scheduling and control framework.	52

## List of Figures

3.3	Illustration of the adopted nomenclature with respect to the generic two-port $\Pi$ model of a transmission line. . . . .	54
3.4	(a) BESS converter capability function $\phi$ in eq.3.2a with AC and DC voltage. (b) Equivalent circuit diagram of BESS. . . . .	57
3.5	Sequence of decisions computed during real-time operations. . . . .	58
3.6	(a) Topology with locations of the PMUs, PV plants, hydro-power plants, (b) Location of the substations and lines on the map, and (c) BESS and PV infrastructure: (1) Satellite view of the centralized PV plant of capacity 1.8 MWp, (2) battery container and (3) interior of the battery. . . . .	60
3.7	(a) PMU installation at a monitored substation, 1) Zaphiro PMU box 2) GPS antenna, (3) current sensor (4) cables and (b) GHI and temperature measurement box (metebox) at a PV plant: 1) pyranometer, (2) temperature sensor (3) antenna (4) power supply (5) NI Compact RIO. . . . .	61
3.8	IT communication infrastructure for the experimental setup (vSwitch refer to virtual switches). . . . .	63
3.9	Flow-chart showing real-time operation during 24 hours. . . . .	64
3.10	Predicted day-ahead scenario set for day 1 (01-Mar-2022). . . . .	65
3.11	(a-c) Dispatch plan computation for day 1 (01-Mar.-2022). Each line-plot in different color represents a different day-ahead scenario. . . . .	66
3.12	(a-c) Real-time operation for day 1 (01-Mar.-2022). . . . .	67
3.13	Predicted day-ahead scenario set for day 2 (22-Mar-2022). . . . .	68
3.14	(a-c) Dispatch plan computation for day 2 (22-Mar.-2022). Each line-plot in different color represents a different day-ahead scenario. . . . .	69
3.15	(a-c) Real-time operation for day 2 (22-Mar.-2022). . . . .	70
3.16	Dispatch tracking over a week (25-Feb.-2022, Friday to 03-Mar.-2022, Thursday): (a) Power at the GCP and dispatch plan, (b) SOC evolution. . . . .	71
3.17	Validation of OPF model for real-time operation with PMU measurements: (a-c) shows CDF of the incurred error on the modeling of voltage (in pu), current (in pu) and total grid losses (in kW). . . . .	72
3.18	PDC reporting latency comprising of PMU latency, network latency and PDC latency. . . . .	73
4.1	Schematic flow diagram for indirect and direct estimation of the sensitivity coefficients. . . . .	80
4.2	Compound electrical parameters of the overall electrical circuit of the grid: compound branch impedance matrices $\mathbf{Z}_l(l \in \mathcal{L})$ and shunt admittance matrices $\mathbf{Y}_t(t \in \mathcal{T})$ . The polyphase terminals and wires are bundled into single line for the sake of clarity. . . . .	85
4.3	Flow diagram for the admittance matrix estimation using cluster-averaged data. . . . .	101
4.4	Topology of the adopted IEEE 4-bus network. . . . .	101

4.5	Estimation performance of the parameters (a) conductances (b) susceptance and (c) shunts of the IEEE 4-bus untransposed and unbalanced test network with raw measurements, block-averaged and with cluster-averaged data with LS. Error bars on top of each estimated value shows the uncertainty of the estimates (99 % confidence interval) using (4.50). L1, L2, L3 refer to different branches and a, b, c refer to different phases of the IEEE 4-bus system in Fig. 4.4. . . . . .	103
4.6	Element-wise relative error computed via (4.49) on real (left) and imaginary (right) part of the estimated compound admittance matrix for the IEEE 4-bus test network using the raw data in (a-b), using the block-averaging in (c-d) and using the cluster-averaged in (e-f) with LS. . . . .	104
4.7	NMSE ( $\mathcal{E}_Y$ ) as a function of the cluster size for IEEE 4-bus network. . . . .	106
4.8	Distribution of the 86400 time steps during the day into 24 clusters as a result of cluster averaging: (a) measurements assigned to different clusters with number of elements (right) per cluster, (b) nodal voltage magnitudes (in pu) and (c) nodal current magnitudes (in pu) for all the nodes and phases (except slack node) for 24 hrs. . . . .	108
4.9	Distribution of negative and zero sequence components normalised by the positive sequence component after block-averaging and cluster averaging on raw-data. . . . .	110
4.10	Flow diagram for two-stage estimation of sensitivity coefficients. . . . .	112
4.11	IEEE4 balanced system . . . . .	115
4.12	(a) Nodal active (in kW), (b) reactive (in kVar) power injections and (c) nodal voltage magnitudes for non-zero injection nodes. . . . .	116
4.13	Coefficients estimates and their uncertainty using the LS. . . . .	118
4.14	Coefficients estimates and their uncertainty using the RLS-F . . . . .	119
4.15	Coefficients estimates and their uncertainty using the RLS-CT. . . . .	119
4.16	Coefficients estimates and their uncertainty using the RLS-SF . . . . .	120
4.17	Coefficients estimates and their uncertainty using the RLS-DE . . . . .	120
4.18	Coefficients estimates and their uncertainty using the <i>indirect method with raw-data for IT 0.5</i> . . . . .	123
4.19	Coefficients estimates and their uncertainty using the <i>indirect method with cluster-averaging for IT 0.5</i> . . . . .	123
5.1	Flow-chart of the model-less/measurement-based robust voltage control framework. . . . .	129
5.2	Topology of the CIGRE low-voltage system with distributed PV units. . . . .	132
5.3	(a) Nodal active (in kW) and (b) reactive (in kVar) power injections for non-zero injection nodes. . . . .	133
5.4	Coefficients estimates and their uncertainty using the RLS-SF . . . . .	134
5.5	Coefficients estimates and their uncertainty using the RLS-DE . . . . .	134
5.6	Distribution of daily nodal voltage magnitudes using (a) non-robust and (b) robust voltage control. . . . .	135



## List of Figures

---

5.7	Control results using RLS-DF for robust, non-robust and model-based controls: (a) voltage magnitude, (b) active power and (c) reactive power for node 15. . . .	136
5.8	Flow-chart showing real-time operation during 24 hours. . . . .	138
5.9	Coefficients estimates and their uncertainty for day 1. . . . .	139
5.10	Experimental validation results for day 1: (a) voltage magnitude, (b) PV at node 11 (c) PV at node 9 and uncontrollable (d) active power (e) reactive powers at other nodes. . . . .	141
5.11	Coefficients estimates and their uncertainty for day 2. . . . .	142
5.12	Experimental validation results for day 2: (a) voltage magnitude, (b) PV at node 11 (c) PV at node 9 and uncontrollable (d) active power (e) reactive powers at other nodes. . . . .	143
6.1	Flow chart for the estimation of countrywide models of medium voltage power distribution networks. . . . .	153
6.2	Identification of EHV areas: (a) locations of the considered 148 EHV substations in Switzerland and (b) approximated regions served by each substation after Voronoi partitioning. . . . .	154
6.3	Estimated electricity demand map of: (a) Switzerland and (b) a single EHV area. The blue polygon refers to an EHV area obtained using Voronoi partition. . . .	156
6.4	Identification of the substations locations: (a) the EHV area is divided into clusters, (b) large clusters are divided into smaller ones, (c) convex hull of the aggregated clusters (in red) and final locations of the HV substations (in blue). .	157
6.5	Probability density function (PDF) plots of estimated electricity demands for (a) HV and (b) MV substations. . . . .	158
6.6	Identified HV/MV and MV/LV substations for (a) the example EHV area (5 and 142, respectively) and (b) Switzerland (776 and 17'844) . . . . .	159
6.7	Routing procedure:(a) example EHV area with HV and MV substations, (b) highly-connected base topology, (c) meshed grid topology at an intermediate stage of the procedure, (d) final topology highlighting the current levels in the cables, and (e) total capital cost (expressed in km for length of cables used) as a function of the iteration. . . . .	162
6.8	Re-routing: (a) routed network using algorithm 6.2 resulting in a meshed network, (b) routed network using algorithm 6.3 which divides it into two radial networks. . . . .	163
6.9	Routed MV networks for the example EHV area. . . . .	164
6.10	CDF plots (a) nodal voltages and (b) lines currents of estimated networks shown in different colors. . . . .	164
6.11	Distribution of (a) capacity factor and (b) maximum PV capacity per MV node due to land constraint. . . . .	166
6.12	Simplified land-use map of Switzerland. . . . .	166
6.13	Demand and PV scenarios: (a) standard load profiles for different sector, (b) scenario considered for the PV and battery sizing problem. . . . .	167

6.14 Investments to achieve a target level of installed PV generation capacity: (a, c) total cost, and (b, d) marginal cost. Top: for randomly chosen 10 MV networks, bottom: for all estimated MV networks in Switzerland (distribution with symmetric quantiles). . . . .	173
6.15 Installed PV generation capacity (in MW) across Switzerland for scenario A in (a) and (b), scenario B in (c) and (d), and scenario C in (e) and (f), for Case 0 and Case 1, respectively. Scenarios refer to the installed capacity of PV generation and are defined in Table 6.9. . . . .	176
6.16 Cost per TWh of PV energy production for the two cases. . . . .	177
6.17 (a) BESS cost and size: (a) BESSs power rating and energy capacity and (b) system cost breakdown for Case 1 for different levels of installed PV generation capacity. . . . .	178
6.18 One of synthetically generated network as test case for the verification of linear grid model. . . . .	179
6.19 Plots showing convergence of the BESS sizes and the objective by correcting the linear power flow coefficients with newest battery injections from previous iteration: (a) BESS power and energy size and (b) Cost of the PV-BESS system. . . . .	180
6.20 CDF plots (a) nodal voltages error and (b) branch current error. . . . .	180
6.21 CDF plots: (a) nodal voltages and (b) lines currents of original network and the estimated networks shown in different colors. . . . .	181
A.1 Performance comparison of MPC using L-OPF and AR-OPF as grid models. . . . .	190
A.2 (a-c) Dispatch plan computation for day 1 (22-Mar.-2022). . . . .	192



## List of Tables

2.1	Nominal demands and controllable units . . . . .	27
2.2	Performance comparison of distributed MPC <i>control performance</i> using different linear grid models . . . . .	30
2.3	Performance comparison of distributed MPC <i>computational performance</i> using different linear grid models . . . . .	30
2.4	Sensitivity on <i>control performance</i> w.r.t. horizon length for the dominant model.	31
2.5	Sensitivity on <i>computational performance</i> w.r.t. horizon length for the dominant model. . . . .	31
2.6	Sensitivity on <i>control performance</i> w.r.t. the number of controllable units for the dominant model. . . . .	32
2.7	Sensitivity on <i>computational performance</i> w.r.t. the number of controllable units for the dominant model. . . . .	32
2.8	Nominal demands and controllable units . . . . .	35
2.9	Tracking error statistics with and without dispatch control (in (%) normalized by mean of the dispatch plan). . . . .	40
2.10	Computation performance for real-time experiments . . . . .	43
2.11	ADMM computation time with respect to increasing number of controllable units. . . . .	43
2.12	Performance comparison of the centralized vs distributed algorithms. . . . .	44
2.13	Sensitivity of dispatch plan reliability . . . . .	44
3.1	Technical specifications of the 1.5 MW/2.5 MWh BESS for the experimental setup.	61
3.2	Tracking error statistics with different control schemes. . . . .	68
3.3	Computation time. . . . .	71
3.4	MPC Computation time with increasing number of Controllable BESS. . . . .	73
3.5	Data packet-losses. . . . .	73
4.1	Errors specifications for different class of Instrument Transformers. . . . .	99
4.2	Estimation performance for the IEEE 4-bus network. . . . .	102
4.3	NMSE on admittance estimation for different networks. . . . .	105
4.4	NMSE on admittance estimation ( $\mathcal{E}_Y$ ) with different noise levels for IEEE 4-bus network. . . . .	105
4.5	NMSE on admittance estimation ( $\mathcal{E}_Y$ ) with clustering features. . . . .	106

## List of Tables

---

4.6	Estimation performance for the IEEE 4-bus network with availability of measurements on injection current and branch currents. . . . .	107
4.7	Percentage of negative and zero sequence components with respect to positive sequence components. . . . .	109
4.8	Line data and nodal injections for IEEE4 system in Fig. 4.11. . . . .	115
4.9	Performance comparison of different estimation techniques for $K_{2,2}^P$ with different IT classes. . . . .	119
4.10	Performance comparison of different estimation techniques for $K_{2,3}^P$ with different IT classes. . . . .	120
4.11	Performance comparison of different estimation techniques for $K_{2,2}^Q$ with different IT classes. . . . .	121
4.12	Performance comparison of different estimation techniques for $K_{2,3}^Q$ with different IT classes. . . . .	121
4.13	Performance comparison of indirect and direct method for IEEE4 system (the coefficient $K_{2,3}^P$ ). . . . .	123
4.14	Performance comparison of indirect and direct method for <i>modified</i> IEEE4 system (the coefficient $K_{2,3}^P$ ). . . . .	124
5.1	Performance comparison of different voltage control methods: maximum nodal voltage magnitude. . . . .	137
5.2	Estimation performance on day 1. . . . .	140
5.3	Estimation performance on day 2. . . . .	142
5.4	Computation time . . . . .	144
6.1	Composition of electricity demand in different sectors for Switzerland for 2014. . . . .	155
6.2	Statistics on HV and MV substations . . . . .	158
6.3	Cable ratings from a commercial source. . . . .	161
6.4	Transformer rating. . . . .	161
6.5	Replacement scheme for lines. . . . .	161
6.6	Number of identified grid components. . . . .	164
6.7	A comparison of the PV generation potential. . . . .	166
6.8	Costs of PV and BESSs. . . . .	171
6.9	Deployment of PV and BESS in the two cases. . . . .	177
6.10	Nominal Load and PV per node . . . . .	179
6.11	Accuracy of the linear power flow. . . . .	179
6.12	Comparison of actual and estimated networks. . . . .	181
A.1	Error on the modeled voltage, currents and grid losses. . . . .	191
A.2	Computation time . . . . .	191
A.3	Dispatch tracking error . . . . .	191
B.1	Performance comparison with number of samples in Monte-Carlo simulations. . . . .	194
B.2	Performance comparison with respect to uncertainty on the admittance matrix. . . . .	194

# Nomenclature

## Abbreviation

ADMM	Alternating Direction Method of Multipliers.
ADN	Active Distribution Network.
AR-OPF	Augement Relaxed Optimal Power Flow.
BESS	Battery Energy Storage System.
CDF	Cumulative Distribution Function.
CI	Confidence Interval.
CWC	Coverage Width-based Criterion.
DER	Distributed Energy Resources.
DSO	Distribution System Operator.
EHV	Extra High Voltage.
EV	Electric Vehicle.
GCP	Grid Connection Point.
GHI	Global Horizontal Irradiance.
GIS	Geographic Information Systems.
GMM	Gaussian Mixture Model.
GPS	Global Positioning System.
HV	High Voltage.
ICT	Information and Communication Technologies.
IT	Instrument Transformer.
LS	Least Squares.
LTPs	Linear Transformation Parameters.
LV	Low Voltage.
MAE	Maximum Absolute Error.
MC	Monte-Carlo
MPC	Model Predictive Control.
MPP	Maximum Power Potential.
MV	Medium Voltage.
NMSE	Normalized Mean Square Error.
OPF	Optimal Power Flow.
PDC	Phasor Data Concentrator.
PICP	Prediction Interval Coverage Probability
PINAW	Prediction Interval Normalized Average Width.

## Nomenclature

---

PMU	Phasor Measurement Unit.
PV	Photovoltaic.
QoS	Quality of Service.
RER	Renewable Energy Resources.
RLS	Recursive Least Squares.
RLS-CT	RLS with Constant Trace.
RLS-DF	RLS with Directional Forgetting.
RLS-F	RLS with Forgetting.
RLS-SF	RLS with Selective Forgetting.
RMSE	Root Mean Square Error.
RT	Real-time.
RT-MPC	Real-time Model Predictive Control.
RTSE	Real Time State Estimator.
SCADA	Supervisory Control and Data Acquisition.
SD	Standard Deviation.
SOC	Second Order Cone Program.
SOE/SOC	State-of-Energy/State-of-Charge.
SVD	Singular Value Decomposition.
TLS	Total Least Squares.
TSO	Transmission System Operator.
UDP	User Datagram Protocol.
UTC	Universal Time Coordinated.
WLS	Weighted Least Squares.
<b>Variables</b>	
$\hat{e}_k$	Uncovered dispatch error at time index $k$ .
$\mathbf{i},  \mathbf{i} $	Vector containing branch/line current complex-phasors, magnitudes.
$\mathbf{p}, \mathbf{q}$	Controllable nodal active and reactive power injections
$\mathbf{p}^{\text{unc}}, \mathbf{q}^{\text{unc}}$	Uncontrollable active and reactive power injections.
$\mathbf{v},  \mathbf{v} $	Vector containing nodal voltage complex-phasors, magnitudes.
$f_{l,k}, \bar{f}_{l,k}$	Square of current magnitude of line $l$ at time index $k$ and its auxiliary upper bound.
$p^l, q^l$	Active and reactive grid losses in the linear grid model.
$p^r, q^r$	Active and reactive power injection from $r$ -th controllable resources.
$p^{\text{bess}}, p^{\text{pv}}, p^{\text{load}}, p^{\text{hydro}}$	Active power injections from BESS, PV, Load and Hydro plant.
$q^{\text{bess}}, q^{\text{pv}}, q^{\text{load}}, q^{\text{hydro}}$	Reactive power injections from BESS, PV, Load and Hydro plant.
$s_0 = p_0 + j q_0$	Apparent ( $s_0$ ), active ( $p_0$ ), reactive ( $q_0$ ) power at the grid connection point (node index 0).
SOC	State-of-Charge of an energy storage system.
$v,  v , v^\diamond$	Nodal voltage phasor, its magnitude and square of the magnitude.
$v_{l,k}^\diamond, \bar{v}_{l,k}^\diamond$	Square of voltage magnitude at bus $l$ at time index $k$ and its auxiliary upper bound.

### Parameters

$2b_l$	Shunt susceptance of line $l$ .
$\mathbb{H}$	Adjacency matrix of the graph of a power grid.
$\mathbf{A}^v, \mathbf{A}^i, \mathbf{A}^l, \mathbf{b}^v, \mathbf{b}^i, \mathbf{b}^l$	Parameters for a linearized grid model.
$\mathbf{i}^{\max}$	Vector of lines ampacity limits.
$\mathbf{Y}, Y_{ij}$	Compound admittance matrix of a power grid and its generic element.
$\mathcal{A}, \mathcal{A}^{\mathcal{P}}$	Incidence matrix of the graphs associated to single and multi-phase networks, respectively.
$\rho$	Penalty parameter in the ADMM algorithm.
$\bar{\mathbf{p}}, \hat{\mathbf{p}}$	Realized power injection measurements, forecasts/estimation of power injections.
$E^{\text{bess}}, P^{\text{bess}}$	BESS energy and power capacities.
$I_l^{\max}$	Square of maximum current limit of the $l$ -th line.
$K^p, K^q$	Voltage sensitivity coefficients with respect to nodal active and reactive power injections.
$N_b$	Number of nodes in a network.
$N_e$	BESS allowed number of cycles per day chosen as a function of a targeted lifetime.
$N_l$	Number of lines in a power network.
$P^{\text{pv}}$	PV active power rating.
$R^{\text{bess}}$	BESS series equivalent resistance.
$S_{\max}^{\text{pv}}, S_{\max}^{\text{bess}}$	Apparent power converter capability for PV and BESS.
$T_s$	Time resolution of real-time control.
$v^{\diamond, \max}, v^{\diamond, \min}$	Upper and lower bounds on the square of nodal voltage magnitudes.
$v^{\max}, v^{\min}$	Upper and lower bounds on the nodal voltage magnitudes.
$w_l, w_e, w_r$	Weighting coefficient associated to the grid losses, dispatch energy errors and $r$ -th DER resource objective function.
$z_l = r_l + jx_l$	Longitudinal impedance of line $l$ .

### Functions

$\Re(x), \Im(x)$	Real and Imaginary parts of a complex number $x$ .
$f_r, f_{\text{bess}}, f_{\text{pv}}$	Cost function of a controllable resources indexed $r$ , BESS and PV.
$\Phi_r, \Phi_{\text{bess}}, \Phi_{\text{pv}}$	Constraint function of a controllable resources indexed $r$ , BESS and PV.

### Sets and Indices

$\mathbb{C}$	Complex number set.
$\mathbb{R}$	Real number set.
$\mathcal{L}$	Set of line indices in a grid.
$\mathcal{N}$	Set of node indices in a grid.
$\Omega$	Uncertainty set.





# 1 Introduction

## Context and Motivations

Power distribution networks are undergoing substantial changes due to the accelerated deployment of distributed energy resources (DERs) in the form of local generation plants such as stochastic renewable energy resources (RERs), stochastic demands such as electric vehicle (EV)-charging stations, and distributed battery energy storage systems (BESS). In contrast to the conventional power system, where the power flows mainly in one direction from centralized generation units via transmission to distribution networks, modern power systems are characterized by way more complex energy flows involving the whole infrastructure. This is due to increased DERs integration, especially RERs, and their stochastic nature. On the one hand this phenomenon has resulted in power imbalances leading to increased reserve requirements in power transmission grids as reported by several transmission system operators (TSOs) (e.g., Californian [1] and Australian system operators [2]), on the other hand it is at the origin of operational issues in power distribution grids concerning the delivered quality-of-service (mainly associated to voltage quality), as well as lines and transformers congestions [3, 4]). As a matter of fact, the distribution system operators (DSOs) face significant challenges associated with grid reinforcements and the capability of being dispatched, while TSOs are experiencing increasing needs for the allocation and deployment of adequate regulating power reserves. These aspects pose severe challenges to the DSOs' and TSOs' conventional planning and operational practices to accommodate the stochastic, partially controllable, and semi-bidirectional nature of the DERs, defining the notion of Active Distribution Networks (ADNs) [5, 6].

Within the context of ADNs, they are defined by CIGRE and IEEE Working Groups [7, 8] as follows.

*“ADNs have systems in place to control a combination of distributed energy resources, defined as generators, loads and storage. DSOs have the possibility of managing the electricity flows using a flexible network topology. DERs take some degree of responsibility for system support, which will depend on a suitable regulatory environment and connection agreement.”*

These systems adopt advanced information and communication technologies (ICT) and distributed metering units [9]. ADNs are likely to install a high number of low-cost distribution-grade phasor measurement units (PMUs), and smart meters [10, 11, 12] and deploy real-time state estimation (RTSE) algorithms. Such a situational aware infrastructure may serve as a backbone for deploying advanced control schemes to optimally operate ADNs at different time horizons with different objectives while maintaining nodal voltages, lines, and transformer power-flows within safe operational bounds and utilizing the flexibility offered by the DERs [13, 14].

As acknowledged by the technical literature, a major challenge in exploiting the flexibility of DERs is to keep the local grid constraints (nodal voltages, lines, and transformers' physical limits) within safe operation limits. However, as widely known, any ADN optimal control problem accounting for the exact grid constraints makes it non-convex (i.e., the so-called optimal power flow – OPF problem), hence difficult to solve within a strict time deadline as OPF problems are usually computationally expensive. Therefore, they are often used for offline optimization schemes such as for ADNs' planning purposes. In this respect, several efficient techniques have been proposed in the literature. However, either they cannot meet the strict time deadlines of real-time controls, or the assumptions do not hold for real-life power networks. Another challenge to implement OPF-driven control of ADNs is that the necessary parameters to model the grid constraints are not always available and/or may be incorrect if available. Inaccurate information on the grid's parameters leads to erroneous models, causing inaccuracy in the estimates of grid analysis tools such as power flow, state estimation, etc. To address this issue, the accurate and time-synchronised measurements from PMUs could be used for the on-line estimation of grid models. In this respect, existing methods in the literature either ignored the presence of shunt elements in the distribution networks or made unrealistic assumptions about the measurements' noise. Therefore, they may not be applicable to real-life networks.

The above two challenges are addressed in this Thesis. The first is tackled by developing control schemes using convex OPF models such as linearized power flow and relaxed OPF. The derived control schemes have been used to showcase how to leverage heterogeneous DERs flexibility to dispatch ADNs while satisfying the local operational constraints. The second challenge related to the non-availability of grid models is addressed by developing measurement-based/data-driven/model-less control schemes. In this respect, the Thesis presents original techniques to estimate the compound admittance matrix and power-flow sensitivity coefficients of a generic untransposed and unbalanced power network with a generic topology (i.e., either radial or meshed). The estimated models are then used to formulate control schemes for ADNs. The above control schemes are validated on real-life ADNs hosted at the EPFL Distributed Electrical Systems Laboratory or operated by Swiss DSO.

Finally, to scale the results of the DER controls and study the impact of large-scale deployment of RERs, such as in a country, the Thesis proposes a process for the countrywide estimation of the ADNs' hosting capacity of stochastic RERs (such as photovoltaic plants). The proposed

---

process also computes the amount of BESSs necessary to increase RERs installation beyond the ADNs' hosting capacity.

## Thesis Outline

The Thesis is organised as follows.

Chapter 2 presents a grid-aware control and scheduling algorithms for DERs in ADNs. The developed scheduling scheme, a stochastic-based optimization accounting for the uncertainty of the generation and demand, is designed to compute day-ahead dispatch plans. The associated real-time controller, based on model predictive control (MPC), tracks the day-ahead dispatch plan during the day. Both the control and scheduling stages account for the grid operational constraints (i.e., nodal voltages, lines, and transformer capacity) via the power-flow sensitivity coefficient-based linearized OPF model. The Chapter also presents the experimental validation of the proposed framework on a real-scale microgrid hosted at the EPFL Distributed Electrical Systems Laboratory, Switzerland.

In Chapter 3, we go a step further from the work in Chapter 2 by proposing a reliable dispatching framework in case the available BESS energy capacity is insufficient to cover the dispatch error. This specific problem is addressed by developing a two-layer MPC scheme where the first layer (acting at a slower pace) computes short-term schedule for the BESS utilization and the second layer (acting at a faster pace) tracks the dispatch plan in real-time considering constraint on BESS utilization imposed by the first layer. In this scheme, the control accounts for the grid constraints via the augmented relaxed (AR)-OPF model [15], which provides the exact solution of the OPF. The proposed framework is validated on a real-life medium voltage network hosting 1.5 MW/2.5 MWh BESS, 3.2 MW PV, 3.4 MVA hydro generation and 2.8 MW of base demand.

In Chapter 4, we present an estimation scheme for the measurement-based estimation of the compound admittance matrix of an untransposed and unbalanced power network with a generic topology. The estimated admittance matrix is used to compute the power-flow sensitivity coefficients. A tool to quantify the uncertainty on the estimated sensitivity coefficient is also presented. Furthermore, the Chapter presents another scheme for the estimation of the sensitivity coefficient where only localized power and nodal voltage magnitude measurements are required. The two methods are numerically validated and compared in terms of estimation accuracy and variance of the estimates.

In Chapter 5, we present a data-driven/model-less control scheme where, first, the measurements are used to estimate the power-flow sensitivity coefficients (using the method developed in Chapter 4); then, they are used in a real-time control. Furthermore, the chapter presents a robust voltage control scheme where the uncertainty of the estimated power-flow sensitivity coefficients is accounted for. The proposed control scheme is experimentally validated on a real-scale microgrid hosted at the EPFL Distributed Electrical Systems Laboratory.

## Chapter 1. Introduction

---

In Chapter 6, we study the impact of a large amount of RERs deployment on the planning of countrywide distribution networks. To do that, the Chapter presents a scheme to generate synthetic distribution network models on a country scale. Then, the Chapter presents an optimal planning process to compute the PV hosting capacity of the distribution networks. It also presents a planning scheme for optimal sizing and siting of the BESS when the ADNs exceed their PV hosting capacity. Furthermore, the Chapter presents an optimization scheme for cost-optimal countrywide allocation of the PV-BESS units for a given PV installation target.

Finally, Chapter 7 summarizes the main findings of the Thesis and future perspectives.

It is worth noting that, in view of the large amount of subjects treated by the Thesis, the literature survey is integrated at the beginning of each Chapter.

## Contributions

The original contributions of each Chapter of this Thesis are listed below.

### Chapter 2

- Formulation of a generic and computationally-efficient scheduling and control framework to dispatch heterogeneous resources hosted in ADNs while accounting for grid constraints via linearized power-flow grid models.
- Formulation of a distributed optimization-based real-time MPC scheme for DERs.
- First experimental validation of a rigorous distributed MPC-based framework on a real-scale microgrid accounting for the grid constraints.

### Chapter 3

- Formulation of a two-layer MPC scheme consisting of a farsighted MPC (acting on a longer horizon till the end of the day) and a myopic MPC (acting on a shorter horizon of 5 minutes), to avoid BESS SOC saturation in dispatching ADNs.
- Formulation of a real-time control where the power grid is modeled by an exact convex model of the AC-OPF, i.e., the AR-OPF. Thanks to its exactness, the AR-OPF guarantees the feasible operation of the grid with respect to any possible grid state. Compared to the SOCP-based AC-OPF models, it uses a network model that take into account shunt elements resulting in a correct binding of the grid's branch currents.
- We report the first real-scale experimental validation of a grid-aware AC-OPF-based real-time MPC deployed on a real MV distribution network hosting uncontrollable 3.2 MWp of distributed photovoltaic generation, 3.4 MVA of hydro generations, and a 2.8

---

MW base demand. A grid-connected 1.5 MVA/2.5 MWh BESS was the sole controllable resource in this setup.

## **Chapter 4**

- Formulation of a linear model for the estimation of the compound admittance matrix of generic untransposed three-phase distribution networks with generic meshed/radial topologies taking into account both branch and shunt admittance matrices of the grid branches (i.e. with no approximation on the grid model).
- Development of a pre-processing strategy on the raw PMU measurements for improving the performance of least squares (LS) and total least squares (TLS)-based admittance estimation schemes. The pre-processing reduces the impact of measurements noise, ultimately improving the estimation performance of both LS and TLS.
- Development of an error propagation tool to quantify the uncertainty on the estimated sensitivity coefficients derived from the estimated compound admittance matrix.
- Recursive least square (RLS)-based estimation of power-flow sensitivity coefficients and performance evaluation with different variants of RLS.
- Performance comparison of the above two estimation schemes of the power-flow sensitivity coefficients with respect to estimation accuracy and variance.

## **Chapter 5**

- Formulation of a robust voltage control problem using the measurement-based estimated sensitivity coefficients and their uncertainties. Performance comparison of different estimation techniques of measurement-based estimations of sensitivity coefficients.
- Experimental validation of the proposed robust-voltage control scheme on a real-scale microgrid.

## **Chapter 6**

- Development of an unsupervised method to estimate synthetic models of medium voltage distribution grids of a country using publicly available data.
- Development of a tractable convex OPF model to compute the PV hosting capacity of ADNs, including cost-optimal BESSs siting and sizing. Use of the proposed convex optimization problem to determine countrywide cost-efficient PV and BESS deployments plans to accommodate a target PV generation level accounting for the capacity factor of PV generation.

## **Chapter 1. Introduction**

---

- Assessment of the optimal deployment plan for PV systems and BESSs in Switzerland to accommodate the PV generation target envisaged by the national energy strategy accounting for the constraints of the distribution grids.

# **Model-based Control of Active Distribution Networks**

## **Part I**





# Prelude

Controlling heterogeneous and stochastic energy resources connected to medium and low voltage power distribution grids is crucial to displace centralized electricity generation in favor of distributed renewable generation. This change of paradigm impacts the planning and operational practices of both distribution system operators (DSOs) and transmission system operators (TSOs). Indeed, DSOs may face significant issues associated with grid reinforcements and the capability of being dispatched, while TSOs will experience increasing needs for allocating and deploying regulating power.

Day-ahead and intra-day scheduling of distributed energy resources (DERs) and, in general, heterogeneous DERs have been advocated in the literature to minimize the effect of uncertainties. Such a scheduling determines before operations an expected power trajectory (*dispatch plan*) at a particular time resolution that are followed during the real-time operation.

In this context, this part of the thesis presents *two* different real-time control schemes. The *first*, in (Chapter 2), presents a model predictive control (MPC) scheme for tracking the dispatch plan. MPC allows to optimize storage elements, such as battery energy storage systems (BESSs), especially when the power injections are changing rapidly due to their stochastic nature. In this work, a linearized grid model is used to obtain a tractable and linear formulation. The linearized grid model uses power-flow sensitivity coefficients. The chapter also demonstrates a distributed control using the alternating direction method of multiplier (ADMM). The framework is validated on a real-life low-voltage microgrid hosted at the EPFL Distributed Electrical Systems Laboratory. The *second*, in (Chapter 3), builds and improve upon the work of Chapter 2. It is done by (i) developing a scheme to avoid early saturation of the controllable resource during dispatching (for the cases when the grid is interfaced with high amount of stochastic resources but not enough flexibility from the controllable resources) and (ii) using a better optimal power flow (OPF) model by a relaxed AC-OPF formulation. This control scheme is also experimentally validated using a 1.5 MVA/2.5 MWh BESS connected to an actual Swiss DSO's 24-node medium-voltage (MV) ADN hosting uncontrollable 3.2 MWp distributed photovoltaic generation, 3.4 MVA hydro generations, and 2.8 MW base demand.



## 2 Model-based Grid-aware Dispatching of Active Distribution Networks

*Accelerated displacement of conventional generation by renewable energy resources (REs) has increased the the stochasticity of electricity generation in the power transmission and distribution grids. On the one hand, transmission grids are facing the challenge of sufficient provision of ancillary services such as the scheduling and deployment of reserves. On the other hand, power distribution grids are experiencing poor quality of service (QoS) and increased events of congestion in existing lines and transformers. This Chapter tackles these challenges by developing a scheduling and control framework for distributed energy resources (DERs) in active distribution networks (ADNs). The framework consists of two algorithmic stages. The first one (day-ahead scheduling) determines an aggregated dispatch plan based on the forecasts of the stochastic demand and generations and controllable DERs' flexibility. In the second layer (real-time control), a model predictive control (MPC) is developed to optimize the DERs' active and reactive power set-points so that their aggregated contribution tracks the dispatch plan while obeying DERs' operational constraints as well as the grid's ones. In both the layers, the grid constraints are taken into account by a linearized optimal power flow (OPF) model, to retain convexity and tractability, based on grids' sensitivity coefficients. In view of such a simplification applied to the grid constraints, the work investigates different linearized OPF models and compares them with respect to grid modeling accuracy and computational performance. The real-time MPC is formulated as a distributed optimization scheme using the alternating direction method of multipliers (ADMM), enabling the scalability of the real-time MPC. Finally, the proposed framework is experimentally validated on a real-scale microgrid that reproduces the network specifications of the CIGRE microgrid benchmark system.*

*The Chapter includes results of publication [16, 17].*

### 2.1 State-of-the-Art

Day-ahead and intra-day scheduling of DERs and, in general, heterogeneous DERs has been advocated in the literature as a way to minimize the effect of uncertainties (e.g., [18, 19]) on the bulk transmission system imbalances and, at the same time, solve local (regional) distribution

grid operational issues. It consists in determining an average power trajectory (*dispatch plan*) at a certain time resolution before operations that is then followed during real-time (RT) operation. Different scheduling problems have been solved by existing works. For example, works in [20, 21, 22, 23] aim at minimizing power imbalances and in [24] at maximizing economic benefit. The work in [25] achieve load levelling and dispatch by controlling BESS. During RT operation, the realized power profile deviates from the dispatch plan because of forecast errors causing issues such as: power imbalances, lines/transformers congestions, voltage outside bounds etc. To tackle these issues, several works proposed real-time controls and energy management schemes [26, 27, 28, 29] with different objectives. The work in [26] proposed a real-time control for voltage regulation, in [27] for congestion management, in [28] for energy management and dispatch tracking, and in [29] for frequency regulation. An extensive literature review on micro-grids controls and energy management schemes is presented in [30]. However, the above works did not account for the grid constraints.

As known, accounting for the exact grid constraints makes the control problem non-convex and computationally expensive to solve. In [31, 32], interior-point optimization schemes are used to solve the non-convex OPF problem. However, they exhibit several drawback, for example, they may converge to local solutions, are sensitive to initialization, and are generally characterized by higher computational burden. To solve these issues, the convexification of power flow equations are typically proposed by relaxing non-convex constraints or by linearizing them (this last is usually adopted to increase the OPF tractability). [33] surveys different relaxation schemes applied to the OPF problem. The works in [34] and [35] proposed the use of semi-definite relaxation by using bus-injection model (BIM) and branch-flow model (BFM). The works that proposed Second-Order-Cone-Program (SOCP) relaxation are applied to the radial distribution network and may results in exact models when specific assumptions are met. However, the solutions are not exact for networks characterized by branches with shunt elements. The work in [15] proposed the so-called Augmented-Relaxed-OPF, which provides exact solutions even for networks with a radial technology where branches' shunt elements are not neglected. It is achieved by adding extra constraints on the upper and lower bounds of the nodal voltage magnitudes and currents. However, these schemes do not apply to meshed networks. Another approach is based on the linearization of power flow equations, for example, in [36, 37]. These schemes rely on the first (e.g.[36]) or multiple (e.g.[37]) order Taylors series expansion of the power flow equations to express the nodal voltages, lines current, and losses as a function of the power injections. A linearization method based on an iterative approach is described in [38], and in [39] applied to distribution networks. However, it can only be applied to networks without shunt elements. An alternative linearization method that can be applied to both radial and meshed networks and accounts for shunt elements too is using grids' sensitivity coefficients [40] where these sensitivity coefficients (of nodal voltages, lines currents and grid losses) are used to formulate an OPF problem.

In this work we use linearized OPF to achieve a computationally tractable real-time formulation. Also, the linearized OPF using the sensitivity coefficients is applicable to a generic network (i.e., meshed and radial with no approximations on branches models), in this work

we use this model to account for the grid constraints. In particular, we investigate different approaches to compute the most accurate sensitivity coefficients for model predictive control (MPC) of DERs in ADNs. The accuracy is defined by modeling accuracy of the grid states (i.e., nodal voltages) and line current flows against the true values, the latter obtained by solving non-linear power flow, a posteriori. In this Chapter, first we describe different policies for linearized OPF models. Then, we present the derived scheduling and control framework. The real-time controls using different linearized OPF models are assessed with respect to modeling accuracy and computational speed. Finally, the dominant scheme is used to carry out an experimental validation of the proposed framework.

The main contributions of this work compared to the existing literature are the formulation of a generic and computationally-efficient scheduling and control framework to dispatch heterogeneous resources while accounting for grid constraints and its experimental validation in a real-life setup. With respect to previous efforts of experimental validation in [20, 23, 28, 29] and MPC-based control in [41, 42, 43, 44, 45, 46, 47], we report the first experimental validation of a rigorous distributed MPC-based framework on a real-scale microgrid accounting for the grid constraints.

## 2.2 Problem Statement

We consider a distribution grid with a generic topology (meshed or radial) interfacing heterogeneous controllable and uncontrollable DERs. The grid is dispatched at its grid connection point (GCP) according to a pre-determined dispatch plan (to be determined the day before operation). The dispatch action is achieved by coordinating the DERs operations while respecting their own constraints along with those of the grid. Inspired by the conventional power system scheduling and operational approaches along with existing electricity market design [48], the framework consists of two stages described below.

- **Day-ahead scheduling:** the grid operator computes a dispatch plan for the next day based on the forecast of the stochastic generation and demand, the status of controllable resources, and local grid constraints. The dispatch plan not only reflects the predictions of the stochastic quantities but also ensures that DERs have a suitable level of flexibility to track the dispatch plan in real-time. We assume that the dispatch plan has a 5-minutes time resolution and is computed at 23:00 UTC the day before operations. This phase is detailed in Sec. 2.4.
- **Real-time operations:** DERs are controlled in real-time, so to compensate for power mismatches at the ADN's GCP between the realization and dispatch plan. The control problem is formulated as a distributed MPC. It accounts for future uncertainties along the optimization horizon as well as DERs' and grid's constraints. The distributed formulation decouples the DERs' and the grid's problems, which can be solved iteratively until convergence. Real-time operations start at 00:00 UTC and end at 23:59:59 UTC.

The formulation is detailed in Sec. 2.5.

In both stages, the grid constraints are represented by the so-called optimal power flow (OPF) model, which is generally non-convex. Thus, one of the objective of this Chapter is to find a suitable OPF model that is computationally tractable and meets the accuracy requirements of real-time controls of ADNs. Then, the dominant grid model is used to formulate the scheduling and control framework.

### 2.3 Linearized Power Flow Model

We consider a generic distribution network (meshed or radial) consisting of  $N_b$  nodes and  $N_l$  branches. Let vectors  $\mathbf{v} \in \mathbb{C}^{(N_b-1)}$  and  $\mathbf{i} \in \mathbb{C}^{N_l}$  represent nodal voltages and branch currents phasors respectively. Their magnitudes are denoted by  $|\mathbf{v}| \in \mathbb{R}^{(N_b-1)}$  and  $|\mathbf{i}| \in \mathbb{R}^{N_l}$  respectively. The symbols  $\mathbf{p} \in \mathbb{R}^{(N_b-1)}$  and  $\mathbf{q} \in \mathbb{R}^{(N_b-1)}$  are the nodal active and reactive controllable injections for all nodes except the slack node. Scalars  $p^l, q^l \in \mathbb{R}$  are the total active and reactive transmission losses seen at the GCP. Let the index  $t$  denote the current time index, previous and next time indices are denoted by  $t-1$  and  $t+1$  respectively. All the symbols for the time  $t$  are denoted with subscript  $t$ . The symbol  $\Delta t$  be the time interval between the subsequent time indices. Let  $\hat{\mathbf{p}}_t^{\text{unc}} \in \mathbb{R}^{(N_b-1)}$ , and  $\hat{\mathbf{q}}_t^{\text{unc}} \in \mathbb{R}^{(N_b-1)}$  be the forecasts of the uncontrollable active and reactive power nodal injections (for subsequent intervals  $t\Delta t$ ). The net active/reactive power injection is the sum of controllable and uncontrollable active/reactive powers, i.e.,  $\mathbf{p}_t^{\text{unc}} + \mathbf{p}_t$  and  $\mathbf{q}_t^{\text{unc}} + \mathbf{q}_t$ . Let the realized values in the previous time-steps be denoted by  $\tilde{\square}$  (for example,  $\tilde{\mathbf{p}}_{t-1}$  and  $\tilde{\mathbf{p}}_{t-1}^{\text{unc}}$  for controllable and uncontrollable active power injections at timestep  $t-1$ ). We assume following hypothesis.

**Hypothesis 2.1** *The system is in steady-state and can be modeled by phasors, which is able to track small power-dynamics and system state changes.*

**Hypothesis 2.2** *The nodes are modelled as voltage-independent PQ injections.*

**Hypothesis 2.3** *The grid's compound admittance matrix is known with a high accuracy.*

**Hypothesis 2.4** *The grid states are made available by a state estimation process.*

Using the First Order Taylor's approximation, the linearized equation for nodal voltages can be expressed as

$$|\mathbf{v}_t| = |\tilde{\mathbf{v}}_{t-1}| + \frac{\partial |\mathbf{v}|}{\partial \mathbf{p}} \bigg|_{\substack{\tilde{\mathbf{v}}_{t-1}, \\ \tilde{\mathbf{p}}_{t-1} + \tilde{\mathbf{p}}_{t-1}^{\text{unc}}, \\ \tilde{\mathbf{q}}_{t-1} + \tilde{\mathbf{q}}_{t-1}^{\text{unc}}}} (\mathbf{p}_t + \hat{\mathbf{p}}_t^{\text{unc}} - \tilde{\mathbf{p}}_{t-1} - \tilde{\mathbf{p}}_{t-1}^{\text{unc}}) + \frac{\partial |\mathbf{v}|}{\partial \mathbf{q}} \bigg|_{\substack{\tilde{\mathbf{v}}_{t-1}, \\ \tilde{\mathbf{p}}_{t-1} + \tilde{\mathbf{p}}_{t-1}^{\text{unc}}, \\ \tilde{\mathbf{q}}_{t-1} + \tilde{\mathbf{q}}_{t-1}^{\text{unc}}}} (\mathbf{q}_t + \hat{\mathbf{q}}_t^{\text{unc}} - \tilde{\mathbf{q}}_{t-1} - \tilde{\mathbf{q}}_{t-1}^{\text{unc}}) \quad (2.1)$$

where,  $\left. \frac{\partial |\mathbf{v}|}{\partial \mathbf{p}} \right|_{\substack{\tilde{\mathbf{v}}_{t-1}, \\ \tilde{\mathbf{p}}_{t-1} + \tilde{\mathbf{p}}_{t-1}^{\text{unc}}, \\ \tilde{\mathbf{q}}_{t-1} + \tilde{\mathbf{q}}_{t-1}^{\text{unc}}}} \in \mathbb{R}^{(N_b-1) \times (N_b-1)}$  and  $\left. \frac{\partial |\mathbf{v}|}{\partial \mathbf{q}} \right|_{\substack{\tilde{\mathbf{v}}_{t-1}, \\ \tilde{\mathbf{p}}_{t-1} + \tilde{\mathbf{p}}_{t-1}^{\text{unc}}, \\ \tilde{\mathbf{q}}_{t-1} + \tilde{\mathbf{q}}_{t-1}^{\text{unc}}}} \in \mathbb{R}^{(N_b-1) \times (N_b-1)}$  are the partial derivatives of the nodal voltage magnitudes (evaluated at operating point  $\tilde{\mathbf{v}}_{t-1}, \tilde{\mathbf{p}}_{t-1} + \tilde{\mathbf{p}}_{t-1}^{\text{unc}}, \tilde{\mathbf{q}}_{t-1} + \tilde{\mathbf{q}}_{t-1}^{\text{unc}}$ ) with respect to the nodal power injections, also referred to as voltage sensitivity coefficients.

Rearranging the terms in (2.1), the linearized model for nodal voltages can be expressed as:

$$|\mathbf{v}_t| = \mathbf{A}_t^v \begin{bmatrix} \mathbf{p}_t \\ \mathbf{q}_t \end{bmatrix} + \mathbf{b}_t^v \quad (2.2a)$$

where,

$$\mathbf{A}_t^v = \begin{bmatrix} \left. \frac{\partial |\mathbf{v}|}{\partial \mathbf{p}} \right|_{\substack{\tilde{\mathbf{v}}_{t-1}, \\ \tilde{\mathbf{p}}_{t-1} + \tilde{\mathbf{p}}_{t-1}^{\text{unc}}, \\ \tilde{\mathbf{q}}_{t-1} + \tilde{\mathbf{q}}_{t-1}^{\text{unc}}}} & \left. \frac{\partial |\mathbf{v}|}{\partial \mathbf{q}} \right|_{\substack{\tilde{\mathbf{v}}_{t-1}, \\ \tilde{\mathbf{p}}_{t-1} + \tilde{\mathbf{p}}_{t-1}^{\text{unc}}, \\ \tilde{\mathbf{q}}_{t-1} + \tilde{\mathbf{q}}_{t-1}^{\text{unc}}}} \end{bmatrix} \in \mathbb{R}^{(N_b-1) \times 2(N_b-1)} \quad (2.2b)$$

and

$$\mathbf{b}_t^v = |\tilde{\mathbf{v}}_{t-1}| + \mathbf{A}_t^v \begin{bmatrix} \hat{\mathbf{p}}_t^{\text{unc}} - \tilde{\mathbf{p}}_{t-1} - \tilde{\mathbf{p}}_{t-1}^{\text{unc}} \\ \hat{\mathbf{q}}_t^{\text{unc}} - \tilde{\mathbf{q}}_{t-1} - \tilde{\mathbf{q}}_{t-1}^{\text{unc}} \end{bmatrix} \in \mathbb{R}^{(N_b-1)} \quad (2.2c)$$

A similar expression can be written for branches current magnitudes and grid losses as

$$|\mathbf{i}_t| = \mathbf{A}_t^i \begin{bmatrix} \mathbf{p}_t \\ \mathbf{q}_t \end{bmatrix} + \mathbf{b}_t^i \quad (2.2d)$$

$$\begin{bmatrix} p_t^l \\ q_t^l \end{bmatrix} = \mathbf{A}_t^l \begin{bmatrix} \mathbf{p}_t \\ \mathbf{q}_t \end{bmatrix} + \mathbf{b}_t^l, \quad (2.2e)$$

where  $\mathbf{A}^i \in \mathbb{R}^{N_l \times 2(N_b-1)}$ ,  $\mathbf{A}^l \in \mathbb{R}^{2 \times 2(N_b-1)}$ ,  $\mathbf{b}^i \in \mathbb{R}^{N_l}$  and  $\mathbf{b}^l \in \mathbb{R}^2$  are linear transformation matrices, and vectors respectively. Similar to the voltage sensitivity coefficient matrix,  $\mathbf{A}^v$ , the  $\mathbf{A}^i$  and  $\mathbf{A}^l$  are composed by sensitivity coefficients of lines currents and grid losses, respectively. Hereafter, these parameters are called Linear Transformation Parameters (LTP). They are computed using the grid states and the compound admittance matrix (assumed to be known by Hypothesis 4.3-4.4). Several methods exist in the literature for the computation of the sensitivity coefficients such as [40, 49, 50, 51, 52, 53, 54, 55]. In this work, we use the method developed in [40, 55]. The method allows to uniquely compute the sensitivity coefficients as a function of the grid topology and grid state. It has a unique solution for every operating point when the load-flow Jacobian is locally invertible (refer to Theorem 8.1 in [56]).

### 2.3.1 Policies for Sensitivity Coefficients Computation

The linear model (2.2) is defined for a single time step, in the sense that the values of the matrices at time  $t$  are computed based on the former knowledge of all the nodal injections



at time  $t$ . However, in practical applications, like real-time control and scheduling of ADNs, which typically require to compute the control actions for future time intervals, determining the LTPs entails the use of point predictions of the nodal injections with a look-ahead time that depends on the length of the control horizon. From this standpoint, we can envisage three policies to compute and update the LTPs.

1. The LTPs are computed using a single operating point and kept fixed throughout the time-ahead control horizon. This corresponds to a case when the operator does not have forecasts of the uncontrollable injections.  $\mathbf{A}_{t+1}^v$  and  $\mathbf{b}_{t+1}^v$  are computed based on the last known operating point, i.e., the measurements at  $t-1$ , they are:

$$\mathbf{A}_{t+1}^v = \begin{bmatrix} \frac{\partial |\mathbf{v}|}{\partial \mathbf{p}} \bigg|_{\substack{\tilde{\mathbf{v}}_{t-1}, \\ \tilde{\mathbf{p}}_{t-1} + \tilde{\mathbf{p}}_{t-1}^{\text{unc}}, \\ \tilde{\mathbf{q}}_{t-1} + \tilde{\mathbf{q}}_{t-1}^{\text{unc}}}} & \frac{\partial |\mathbf{v}|}{\partial \mathbf{q}} \bigg|_{\substack{\tilde{\mathbf{v}}_{t-1}, \\ \tilde{\mathbf{p}}_{t-1} + \tilde{\mathbf{p}}_{t-1}^{\text{unc}}, \\ \tilde{\mathbf{q}}_{t-1} + \tilde{\mathbf{q}}_{t-1}^{\text{unc}}}} \end{bmatrix} \quad (2.3)$$

$$\mathbf{b}_{t+1}^v = |\tilde{\mathbf{v}}_{t-1}| + \mathbf{A}_{t+1}^v \begin{bmatrix} \hat{\mathbf{p}}_t^{\text{unc}} - \tilde{\mathbf{p}}_{t-1} - \tilde{\mathbf{p}}_{t-1}^{\text{unc}} \\ \hat{\mathbf{q}}_t^{\text{unc}} - \tilde{\mathbf{q}}_{t-1} - \tilde{\mathbf{q}}_{t-1}^{\text{unc}} \end{bmatrix} \quad (2.4)$$

2. The LTPs are estimated using the point forecasts of the uncontrollable load/generation for each time interval. Based on the point forecasts,  $|\hat{\mathbf{v}}_t|$  is obtained. The LTPs are

$$\mathbf{A}_{t+1}^v = \begin{bmatrix} \frac{\partial |\mathbf{v}|}{\partial \mathbf{p}} \bigg|_{\substack{\hat{\mathbf{v}}_t, \\ \hat{\mathbf{p}}_t^{\text{unc}}, \\ \hat{\mathbf{q}}_t^{\text{unc}}}} & \frac{\partial |\mathbf{v}|}{\partial \mathbf{q}} \bigg|_{\substack{\hat{\mathbf{v}}_t, \\ \hat{\mathbf{p}}_t^{\text{unc}}, \\ \hat{\mathbf{q}}_t^{\text{unc}}}} \end{bmatrix} \quad (2.5)$$

$$\mathbf{b}_{t+1}^v = |\hat{\mathbf{v}}_t| + \mathbf{A}_{t+1}^v \begin{bmatrix} \hat{\mathbf{p}}_{t+1}^{\text{unc}} - \hat{\mathbf{p}}_t^{\text{unc}} \\ \hat{\mathbf{q}}_{t+1}^{\text{unc}} - \hat{\mathbf{q}}_t^{\text{unc}} \end{bmatrix} \quad (2.6)$$

3. The LTPs are computed based on optimized trajectory of the control action during previous time interval. It applies to the case when the grid model is used to formulate a MPC problem. The optimized voltages are denoted by  $|\hat{\mathbf{v}}_{t+1}|$ , the optimized injections from controllable resources are denoted by  $\hat{\mathbf{p}}_{t+1}$  and  $\hat{\mathbf{q}}_{t+1}$ ; the LTPs are

$$\mathbf{A}_{t+1}^v = \begin{bmatrix} \frac{\partial |\mathbf{v}|}{\partial \mathbf{p}} \bigg|_{\substack{\hat{\mathbf{v}}_t, \\ \hat{\mathbf{p}}_t + \hat{\mathbf{p}}_t^{\text{unc}}, \\ \hat{\mathbf{q}}_t + \hat{\mathbf{q}}_t^{\text{unc}}}} & \frac{\partial |\mathbf{v}|}{\partial \mathbf{q}} \bigg|_{\substack{\hat{\mathbf{v}}_t, \\ \hat{\mathbf{p}}_t + \hat{\mathbf{p}}_t^{\text{unc}}, \\ \hat{\mathbf{q}}_t + \hat{\mathbf{q}}_t^{\text{unc}}}} \end{bmatrix} \quad (2.7)$$

$$\mathbf{b}_{t+1}^v = |\hat{\mathbf{v}}_t| + \mathbf{A}_{t+1}^v \begin{bmatrix} \hat{\mathbf{p}}_{t+1}^{\text{unc}} - \hat{\mathbf{p}}_t - \hat{\mathbf{p}}_t^{\text{unc}} \\ \hat{\mathbf{q}}_t^{\text{unc}} - \hat{\mathbf{q}}_t - \hat{\mathbf{q}}_t^{\text{unc}} \end{bmatrix} \quad (2.8)$$

Later in this Chapter, we compare the above approaches for a real-time MPC problem in Sec. 2.5, and we perform a detailed assessment of the corresponding performance in Sec. 2.7.

## 2.4 Day-Ahead Dispatch Computation

The objective of the day-ahead scheduling is to compute the dispatch plan that is the active power trajectory that the targeted ADN should follow at its GCP<sup>1</sup> during operations. The design requirements of the dispatch plan are:

- stochastic variations from the dispatch plan due to distributed generation and demand should be compensated by the controllable resources while respecting their operational constraints;
- the power regulation made by the controllable resources does not violate grid constraints;
- the power factor at the GCP is bounded by the values imposed by the grid operator.

The dispatch plan is computed with a stochastic optimization framework, where the stochastic injections of distributed generation and demand are modelled through forecast scenarios as described in the next section. Grid constraints are modelled with the linearized grid model discussed in the previous section. Operational constraints of the controllable resources are modelled accounting for the active-reactive power (PQ) capability of their power converters and SOC constraints.

### 2.4.1 Forecasts of Stochastic Resources

The dispatch computation relies on power-injection forecasts (for each node of the network) modeled by scenarios. Although beyond the scope of this work, a data-driven scheme is developed for generating day-ahead scenarios of demand and PV and hydropower generation,<sup>2</sup> the two sources of renewable generation of the experimental test site. We assume that the PV generation is aggregated behind-the-meter (BTM) with the local loads, whereas the hydropower generation is from stand-alone distributed power plants. Most nodes in this network hosts uncontrollable distributed renewable generation (e.g., PV) and demands (e.g., electrical appliances in residential and commercial buildings). Generally, they are characterized by a high degree of volatility due to the reduced smoothing effect given by the small number of single load units. A survey of forecasting methods accounting for local effects is presented in [58]. Based on these relatively standard approaches, we develop data-driven schemes for stochastic demand and renewable generation forecasts. These schemes are described below.

---

<sup>1</sup>In this work, we only consider a single GCP, although the same approach can be adopted for the formulation of dispatch plans for multiple GCPs e.g., [57].

<sup>2</sup>These two types of RERs are specifically considered as they are part of the experimental setup described in Sec. 2.8 and 3.5.1.

### Demand Forecast

The developed demand forecast algorithm uses nodal historical data-sets updated on a rolling horizon whenever new data is available. **Algorithm 2.1** shows the key steps: the first one refers to the disaggregation of the true demand from the aggregated nodal injections (denoted by  $\mathcal{P}_l$ ), followed by the clustering and multivariate Gaussian fitting of the true demand. These steps are described below.

---

#### Algorithm 2.1 Dayahead demand forecasting <sup>(3)</sup>

---

**Require:** Historical nodal power injections ( $\mathcal{P}_l$ ), GHI ( $\mathcal{G}$ ), air temperature ( $T^{\text{air}}$ ), node index  $l \in \mathcal{N} = \{1, \dots, N\}$

```

1: for  $l = 1 : |\mathcal{N}|$  do
2:   if node  $l$  contains a PV plant then
3:      $[\mathcal{P}_l^{\text{load}}, \text{PV-config}] = \text{Disaggregation}(\mathcal{P}_l, \mathcal{G}, T^{\text{air}})$ 
4:   else
5:      $\mathcal{P}_l^{\text{load}} = \mathcal{P}_l$ 
6:   end if
7:    $[\mathcal{P}_l^{C_1}, \dots, \mathcal{P}_l^{C_{N_c}}] = \text{Clustering}(\mathcal{P}_l^{\text{load}}, \text{features})$ 
8: end for
9: for  $c = 1 : N_c$  do
10:   $\Delta \mathcal{P}_l^{C_i} = \mathcal{P}_l^{C_i} - \text{mean}(\mathcal{P}_l^{C_i})$ 
11:   $\Omega_l^{C_i} = \text{cov}(\Delta \mathcal{P}_l^{C_i})$  (multivariate Gaussian fitting)
12:   $\Delta \tilde{\mathcal{P}}_l^{C_i} = \text{mvnrnd}(\Omega_l^{C_i}, N_{sc})$ 
13:   $\tilde{\mathcal{P}}_l^{C_i} = \Delta \tilde{\mathcal{P}}_l^{C_i} + \text{mean}(\mathcal{P}_l^{C_i})$ 
14: end for
```

---

- **Disaggregation:** scheme separates the true demand from the behind-the-meter (BTM) PV generation. We use the unsupervised disaggregation (step 4 in **Algorithm 2.1**) process proposed in [59]. In brief, the method relies on the net nodal power injections ( $\mathcal{P}_l$ ), global horizontal irradiance (GHI)  $\mathcal{G}$ , and air temperature  $T^{\text{air}}$  from the same area. It models the PV generation as a function of GHI, considering several tilt and azimuth of PV panels, enabling the identification of the patterns of the PV generation in the measured data set. As side result, it provides the disaggregated (or actual) demand that is used to develop the corresponding day-ahead forecast model.
- **Clustering:** is applied on the estimated demand profiles ( $\mathcal{P}_l^{\text{load}}$ ) to group them into  $N_c$  clusters based on features (such as day-types in step 8, **Algorithm 2.1**). We use four clusters ( $N_c = 4$ ): Mondays to Thursdays ( $C_1$ ) are into one day type, Fridays ( $C_2$ ), Saturdays ( $C_3$ ) and Sundays ( $C_4$ ) into other three separate day type clusters.
- **Multivariate-Gaussian-based scenario generation:** each day type cluster is fitted to a Multivariate-Gaussian model via the following steps: (i) computation of the zero mean scenarios for the historical data set (step 10, **Algorithm 2.1**), (ii) computation of the time

---

<sup>3</sup>The functions `mean`, `cov` and `mvnrnd` are MATLAB functions to compute mean, correlations and generate random scenarios (using the mean, covariance and the number of samples), respectively.

cross-correlation matrix (step 11), (iii) sampling of  $N_{sc}$  number of scenarios<sup>4</sup> using the time-correlated multivariate Gaussian distribution model (step 12) and, finally, generate the demand scenarios by adding the cluster mean (step 13).

### PV Generation

It is modeled<sup>5</sup> starting from the day-ahead GHI forecasts provided by a commercial forecasting service, SoDA [60]. In the rest of the manuscript, we used this service for day-ahead GHI forecasts. The SoDa service provides the forecasts for the present and the next day with a time resolution of 15-minutes and updated every 6 hours. The method uses gradient boosting as part of machine learning scheme and uses inputs such as historical data-sets of HelioClim-3 [61], McClell clear sky irradiance model [62], and Global Forecast Service (GFS) Numerical Weather Prediction (NWP).<sup>6</sup> It provides point predictions and 5% and 95% confidence intervals that are fundamental to generate scenarios when computing the dispatch plan. The 15-minutes forecasts are linearly interpolated to obtain estimates with 5-minutes time sampling. To convert the GHI forecasts to power generation, we use a physics-based model tool-chain [63] that takes air temperature ( $T^{\text{air}}$ ), tilt, and azimuth angles and nominal capacity of the PV plant. These parameters are obtained from the PV-config output from step 4, **Algorithm 2.1** as the true configurations of the PV plants are not known a-priori.

#### 2.4.2 Computation of the Dispatch Plan

Let  $r = 1, \dots, R$  be the index of the controllable resources that can participate to the dispatch,  $\mathcal{T} = [t_0, t_0 + 1, \dots, t_N]$  the set of time indices of the scheduling horizon delimited by  $t_0$  and  $t_N$ . The set  $\Omega$  collects the scenarios indexed by  $\omega$  for stochastic uncontrollable generation and demand. The active and reactive nodal power injections of controllable and uncontrollable resources for scenario  $\omega$  are denoted by  $\mathbf{p}_t^\omega, \mathbf{q}_t^\omega$  and  $\mathbf{p}_t^{\text{unc},\omega}, \mathbf{q}_t^{\text{unc},\omega}$  respectively, where those last are from scenario forecasts. The nodal injections of the controllable resources are the decision variables of the problem and are collected in the vector  $\mathbf{x}_t^{r,\omega} = [p_t^{r,\omega}, q_t^{r,\omega}]$ . Let  $s_{0,t}^\omega = p_{0,t}^\omega + j q_{0,t}^\omega$  be the complex power at the slack bus for time  $t$  and scenario  $\omega$ . Let the complex number  $s_t^{\text{disp}} = p_t^{\text{disp}} + j q_t^{\text{disp}}$  be the decision variable for the dispatch plan for time  $t$ , where  $p_t^{\text{disp}}$  and  $q_t^{\text{disp}}$  refer to the active and reactive power respectively.

The main idea behind the proposed formulation is to determine a dispatch plan that can be tracked for any of the forecast scenarios. The problem consists in determining the injections of the controllable resources so as to minimize the deviation between the dispatch plan  $s_t^{\text{disp}}$  and slack power for all the scenarios  $s_{0,t}^\omega, \omega \in \Omega$ . Moreover, the cost function includes a

<sup>4</sup>The number of scenarios is chosen such that it covers the variability of power injections with a confidence interval of 5-95 %. In other words, the realization should fall within the extremes of the predicted scenarios with a probability of 90 %.

<sup>5</sup>PV generation is modeled independently of the demand forecast as they are generated by independent forecast processes.

<sup>6</sup>[www.ncei.noaa.gov/products/weather-climate-models/global-forecast](http://www.ncei.noaa.gov/products/weather-climate-models/global-forecast).

## Chapter 2. Model-based Grid-aware Dispatching of Active Distribution Networks

resource-specific term  $f_r^D(p_t^{r,\omega}, q_t^{r,\omega})$  that reflects the willingness of each controllable resource to provide regulating power (specific cost functions are described in Sec 2.6) and a coefficient  $w_r$  to weight them. Both the cost function and the coefficient can be designed by the modeller, for instance, based on a combination of resource's operating conditions (such as minimizing wear and tear, power ramping, power variations etc.) or the monetary cost associated to its operation. The cost function should be convex in order to keep the convexity of the overall problem formulation. The impact of the term  $w_r$  is investigated in Sec. 2.8.5. The problem that we solve is:

$$\hat{s}^{\text{disp}} = \arg \min_{s^{\text{disp}}} \sum_{\omega \in \Omega} \sum_{t \in \mathcal{T}} \left\{ (s_{0,t}^{\omega} - s_t^{\text{disp}})^2 + \sum_{r=1}^R w_r f_r^D(p_t^{r,\omega}, q_t^{r,\omega}) \right\} \quad (2.9a)$$

subject to the power flow at the GCP as a function of the nodal injections and losses

$$p_{0,t}^{\omega} = \sum_{r=1}^R p_t^{r,\omega} + \mathbf{1}^\top \mathbf{p}_t^{\text{unc},\omega} + p_t^{l,\omega} \quad \forall t \in \mathcal{T}, \omega \in \Omega, \quad (2.9b)$$

$$q_{0,t}^{\omega} = \sum_{r=1}^R q_t^{r,\omega} + \mathbf{1}^\top \mathbf{q}_t^{\text{unc},\omega} + q_t^{l,\omega} \quad \forall t \in \mathcal{T}, \omega \in \Omega, \quad (2.9c)$$

$$\begin{bmatrix} p_t^{l,\omega} & q_t^{l,\omega} \end{bmatrix}^\top = \mathbf{A}_t^{l,\omega} \begin{bmatrix} \mathbf{p}_t^\omega & \mathbf{q}_t^\omega \end{bmatrix}^\top + \mathbf{b}_t^{l,\omega} \quad \forall t \in \mathcal{T}, \omega \in \Omega, \quad (2.9d)$$

power factor constraint at the GCP imposed by  $\cos(\theta)_{\min}$

$$|p_{0,t}^{\omega}| / |s_{0,t}^{\omega}| \geq \cos(\theta)_{\min} \quad \forall t \in \mathcal{T}, \omega \in \Omega, \quad (2.9e)$$

linear voltage and current constraints ( $v^{\min}$ ,  $v^{\max}$  are voltage limits, and  $\mathbf{i}^{\max}$  lines' ampacities)

$$v^{\min} \leq \mathbf{A}_t^{v,\omega} \begin{bmatrix} \mathbf{p}_t^\omega & \mathbf{q}_t^\omega \end{bmatrix}^\top + \mathbf{b}_t^{v,\omega} \leq v^{\max} \quad \forall t \in \mathcal{T}, \omega \in \Omega, \quad (2.9f)$$

$$0 \leq \mathbf{A}_t^{i,\omega} \begin{bmatrix} \mathbf{p}_t^\omega & \mathbf{q}_t^\omega \end{bmatrix}^\top + \mathbf{b}_t^{i,\omega} \leq \mathbf{i}^{\max} \quad \forall t \in \mathcal{T}, \omega \in \Omega, \quad (2.9g)$$

and constraints for all controllable resources

$$\Phi_r^D(x_t^{r,\omega}) \leq 0 \quad \forall t \in \mathcal{T}, \omega \in \Omega, r = 1, \dots, R. \quad (2.9h)$$

Once the problem in (2.9) is solved, the dispatch plan is the real part of its solution  $\hat{s}^{\text{disp}}$ :

$$\hat{p}^{\text{disp}} = \Re \left\{ \hat{s}^{\text{disp}} \right\}. \quad (2.10)$$

Here, the coefficients  $\mathbf{A}_t^{v,\omega}$ ,  $\mathbf{A}_t^{i,\omega}$ ,  $\mathbf{A}_t^{l,\omega}$ ,  $\mathbf{b}_t^{v,\omega}$ ,  $\mathbf{b}_t^{i,\omega}$ ,  $\mathbf{b}_t^{l,\omega}$  represent LTPs for time index  $t$  and scenario  $\omega$ , and they are computed by the second policy in Sec. 2.3.1 (as it is based on scenario forecasts) using the day-ahead forecasts.

### Relaxation of the Non-Convex Power Factor Constraint

Eq. (2.9e) is non-convex and infeasible when the real power at the GCP is zero. As proposed in [64], we express the active power at the GCP as

$$p_{0,t}^\omega = p_{0,t}^{+, \omega} - p_{0,t}^{-, \omega} \quad (2.11)$$

and replace Eq. (2.9e) with the following set of linear constraints:

$$p_{0,t}^{+, \omega} + p_{0,t}^{-, \omega} \geq q_{0,t}^\omega \tan(\pi/2 - \theta_m) \quad (2.12)$$

$$p_{0,t}^{+, \omega} + p_{0,t}^{-, \omega} \leq -q_{0,t}^\omega \tan(\pi/2 - \theta_m) \quad (2.13)$$

$$p_{0,t}^{+, \omega} \geq 0, p_{0,t}^{-, \omega} \leq 0, \quad (2.14)$$

for all  $t \in \mathcal{T}, \omega \in \Omega$ , where  $\theta_m$  refers to the angle corresponding to  $\cos(\theta)_{\min}$ . The two terms of (2.11)  $(p_{0,t}^{+, \omega}, p_{0,t}^{-, \omega})$  should be mutually exclusive (i.e.,  $p_{0,t}^{+, \omega}$  and  $p_{0,t}^{-, \omega}$  can not be non-zero at the same time). To this end, we augment the cost function (2.9a) with the following new term

$$\sum_{\omega \in \Omega} \sum_{t \in \mathcal{T}} \nu ((p_{0,t}^{+, \omega})^2 + (p_{0,t}^{-, \omega})^2) \quad (2.15)$$

that promotes  $p_{0,t}^{+, \omega}, p_{0,t}^{-, \omega}$  being mutually exclusive, where  $\nu \geq 0$  weighs the significance of obeying power factor constraints.

The above dispatch computation problem is convex thanks to linear constraints and quadratic objective function, and hence it can be solved efficiently by any off-the-shelf solver.

## 2.5 Real-time Model Predictive Control (RT-MPC) for Dispatch tracking

In the following, we describe the real-time control problem for tracking the day-ahead dispatch plan. Its objective is to determine the set-point for the controllable resources to track the dispatch plan while respecting the grid and resources constraints. Since the problem requires the knowledge of the state of the grid (i.e., nodal voltages and line currents), models of the DERs, and power flow at the GCP, the problem is initially formulated as a centralized MPC. We then acknowledge that the problem can be formulated as consensus among multiple sub-problems as in [65, 66], and we derive a distributed formulation solved by means of the ADMM technique.

### 2.5.1 Centralized Formulation

During real-time operations, the controllable resources are controlled so to track the dispatch plan at the GCP. The decision variable for the active and reactive nodal injection for resources  $r$  at time  $t$  is denoted by  $x_t^r = [p_t^r, q_t^r]$  and collected in  $\mathbf{x}^r = [x_{\underline{t}}^r, \dots, x_{t_H}^r]$  for the length of

the optimization horizon delimited by current time interval  $\underline{t}$  and the control horizon  $t_H$ . Let  $f_r(x_t^r)$  denote the actuation cost of a generic resource  $r$  (the specific cost functions are described in Sec 2.6) and  $\hat{p}_t^{\text{disp}}$  the dispatch plan set-point at time  $t$  from (2.10). The real-time control problem is formulated as MPC. The problem consists in minimizing the actuation costs of the resources subject to their operational constraints, dispatch plan objective, local grid constraints, and power factor limitations over the length of the optimization horizon. The problem is:

$$\min_{\mathbf{x}^1, \dots, \mathbf{x}^R} \sum_{r=1}^R \sum_{t=\underline{t}+1}^{t_H} f_r(x_t^r) \quad (2.16a)$$

subject to the dispatch constraint

$$\hat{p}_t^{\text{disp}} = \sum_{r=1}^R p_t^r + \mathbf{1}^\top \mathbf{p}_t^{\text{unc}} + p_t^l \quad t = \underline{t} + 1, \dots, t_H \quad (2.16b)$$

where  $\mathbf{p}_t^{\text{unc}}$  is modeled by real-time forecasts  $\hat{\mathbf{p}}_t^{\text{unc}}$ . Then, the power factor constraint at the GCP, imposed by  $\cos(\theta)_{\min}$

$$q_t^{\text{gcp}} = \sum_{r=1}^R q_t^r + \mathbf{1}^\top \mathbf{q}_t^{\text{unc}} + q_t^l \quad t = \underline{t} + 1, \dots, t_H \quad (2.16c)$$

$$|q_t^{\text{gcp}}| \leq \frac{|\hat{p}_t^{\text{disp}}|}{\tan(\pi/2 - \theta_m)} \quad t = \underline{t} + 1, \dots, t_H \quad (2.16d)$$

the constraints for all controllable resources

$$\Phi_r(x_t^r) \leq 0 \quad r = 1, \dots, R, \quad t = \underline{t} + 1, \dots, t_H \quad (2.16e)$$

and the constraints of the grid

$$(2.9f), (2.9g) \quad t = \underline{t} + 1, \dots, t_H \quad (2.16f)$$

$$(2.2e) \quad t = \underline{t} + 1, \dots, t_H. \quad (2.16g)$$

The formulation in (2.16) is convex thanks to the quadratic objective of the resources (as described later in Sec. 2.6) and linear constraints. For convenience in the following formulation, we denote the inequality (2.16d), (2.16f) and equality (2.16c), (2.16g) constraints with  $\Psi_{\text{ineq}}(\mathbf{x}^1, \dots, \mathbf{x}^R) \leq 0$  and  $\Psi_{\text{eq}}(\mathbf{x}^1, \dots, \mathbf{x}^R) = 0$ , respectively. The power balance equality constraint in (2.16b) and (2.16c) can be relaxed by adding auxiliary variables associated to the dispatch tracking error and minimize them in the objective (2.16a).

Solving the problem in (2.16) requires knowing the individual resource models and accessing their state during real-time operations. It is, therefore, referred to as centralized. Due to the privacy and security concerns for the resources' owners, the centralized approach may be impractical. For this reason, we resort to a distributed formulation that also assures better scalability with respect to the number of controllable resources. The distributed formulation

has the inherent potential to preserve privacy concerning models of the resources.

### 2.5.2 Distributed Formulation using ADMM

Following the method described in [28], we introduce a barrier function  $g$  with zero cost when the tracking error (2.16b) is respected and infinity otherwise:

$$g(x_t^1, \dots, x_t^R) = \begin{cases} 0 & \text{(2.16b) is respected} \\ \infty & \text{otherwise.} \end{cases} \quad (2.17)$$

Let  $\mathbf{z}^r$  be the auxiliary variables to copy the behaviour of original variables  $\mathbf{x}^r$ , the so-called copied variables. We can reformulate the optimization problem (2.16) as:

$$\underset{\substack{\mathbf{x}^1, \dots, \mathbf{x}^R \\ \mathbf{z}^1, \dots, \mathbf{z}^R}}{\text{minimize}} \quad \sum_{t=\underline{t}+1}^T \left\{ \sum_{r=1}^R f_r(x_t^r) + g(z_t^1, \dots, z_t^R) \right\} \quad (2.18a)$$

subject to:

$$\mathbf{x}^r = \mathbf{z}^r \quad r = 1, \dots, R \quad (2.18b)$$

$$\Psi_{\text{eq}}(\mathbf{z}^1, \dots, \mathbf{z}^R) = 0 \quad (2.18c)$$

$$\Psi_{\text{ineq}}(\mathbf{z}^1, \dots, \mathbf{z}^R) \leq 0. \quad (2.18d)$$

The problem in (2.18) is a standard sharing problem and separable in  $\mathbf{x}^r$ . It can be solved in a distributed manner by each resources; then, the solutions from each resource can be sent to the aggregator that accounts for the global constraints and objectives. The set of constraints (2.18b) can be moved into the cost function by using a sequence of Lagrangian multipliers, denoted by  $\mathbf{y}^r$ . The augmented Lagrangian can be written as:

$$L_\rho = \sum_{t=\underline{t}+1}^T \left\{ \sum_{r=1}^R f_r(x_t^r) + g(z_t^1, \dots, z_t^R) \right\} + \frac{\rho}{2} \sum_{r=1}^R \left( \|\mathbf{x}^r - \mathbf{z}^r\|_2^2 \right) + \sum_{r=1}^R \mathbf{y}^{r\top} (\mathbf{x}^r - \mathbf{z}^r). \quad (2.19)$$

Let  $\mathbf{u}^r = \mathbf{y}^r / \rho$  be the scaled dual variable,  $\rho$  being the penalty parameter, the above problem can be solved in following three iterative steps using the scaled-ADMM sharing problem [66]:

- **Original variables update**  $\mathbf{x}_{k+1}^r :=$

$$\arg \min_{\mathbf{x}^r} \left\{ \sum_{t=\underline{t}+1}^{t_H} f_r(x_t^r) + \frac{\rho}{2} \|\mathbf{x}^r - \mathbf{z}_k^r + \mathbf{u}_k^r\|_2^2 \right\} \quad (2.20a)$$

subject to

$$\Phi_r(x_t^r) \leq 0 \quad t = \underline{t} + 1, \dots, t_H. \quad (2.20b)$$



- **Copied variables update**  $[\mathbf{z}_{k+1}^1, \dots, \mathbf{z}_{k+1}^R] :=$

$$\arg \min_{\mathbf{z}^1 \dots \mathbf{z}^R} \left\{ \sum_{t=\underline{t}+1}^{t_H} \{g(\mathbf{z}_t^1, \dots, \mathbf{z}_t^R)\} + \frac{\rho}{2} \sum_{r=1}^R \|\mathbf{x}_{k+1}^r - \mathbf{z}^r + \mathbf{u}_k^r\|_2^2 \right\} \quad (2.21a)$$

subject to

$$\Psi_{\text{eq}}(\mathbf{z}^1, \dots, \mathbf{z}^R) = 0 \quad (2.21b)$$

$$\Psi_{\text{ineq}}(\mathbf{z}^1, \dots, \mathbf{z}^R) \leq 0. \quad (2.21c)$$

- **Dual variable updates**

$$\mathbf{u}_{k+1}^r = \mathbf{u}_k^r + \mathbf{x}_{k+1}^r - \mathbf{z}_{k+1}^r \quad r = 1, \dots, R. \quad (2.22)$$

Here,  $\|\cdot\|_2$  refers to the euclidean-norm,  $k$  is the ADMM iteration index, and  $\rho$  being the standard ADMM penalty parameter. The original variable updates (also referred to as resource problems) (2.20) are computed in parallel for each resource,  $r = 1, \dots, R$ , then the copied variable update (grid aggregator problem) (2.21) solves an OPF accounting for the local solutions from each resource, and finally dual variables are updated in (2.22). Then, the updated solutions of the grid aggregator (copied and dual variables) are sent to the resources for next iteration. Eq. (2.20), (2.21) and (2.22) are solved till convergence. The problem in (2.20)-(2.22) is distributed because the resource problems (2.20) can be solved in parallel and independently without requiring the knowledge of the model of other resources as well as those of the grid. The resource problem requires just the updated solution from the grid (referred to as copied variable) through a communication channel. The flow diagram of the distributed computation is shown in Fig. 2.1.

The distributed algorithm converges when the primal residual norm  $r^k = \|\mathbf{X}^k - \mathbf{Z}^k\|_2$  and the dual residual norm  $s^k = \rho \|\mathbf{Z}^{k+1} - \mathbf{Z}^k\|_2$  are both smaller than a feasibility tolerance as in [66], where  $\mathbf{X} = [\mathbf{x}^1; \dots; \mathbf{x}^R]$ ,  $\mathbf{Z} = [\mathbf{z}^1; \dots; \mathbf{z}^R]$ . For the penalty parameter  $\rho$ , we follow a self-adaptive scheme [66, 67]:

$$\rho^{k+1} := \begin{cases} \tau_{\text{incr}} \rho^k & r^k > \mu s^k \\ \rho^k / \tau_{\text{decr}} & s^k > \mu r^k \\ \rho^k & \text{otherwise,} \end{cases} \quad (2.23)$$

where  $\tau_{\text{incr}}$  and  $\tau_{\text{decr}}$  apply an adjustment scheme to guide the primal and dual residual norms to converge to zero. We fix  $\mu = 10$  and  $\tau_{\text{incr}} = 2$  and  $\tau_{\text{decr}} = 2$  as reported in [67]. The ADMM algorithm is initialized with  $\mathbf{u}^r = 0$ ,  $\mathbf{z}^r = 0$  and  $\rho = 10$ . In the first step, the resources problems (2.20) are solved providing  $\mathbf{x}^r$ . Then, the grid problem (2.21) is solved to update  $\mathbf{z}^r$  and  $\mathbf{u}^r$ . The penalty parameter is updated via (2.23). A sensitivity analysis on the algorithm convergence with different initializations will be investigated in future works.

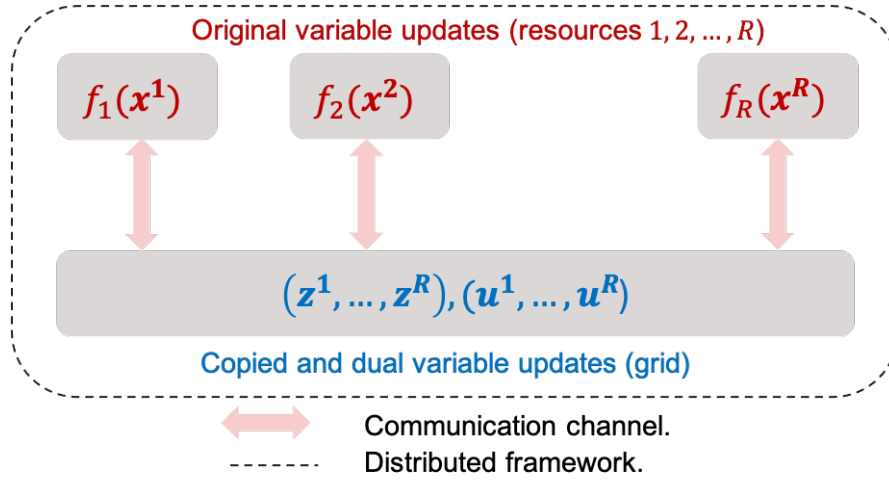


Figure 2.1: Distributed computation of the control set-points using the ADMM technique: the resources solve their local problems in parallel and communicates the intermediate set-points to an aggregator that solves the OPF problem associated to the microgrid dispatch. This iterative procedure is followed until convergence.

### 2.5.3 Short-term Forecasts

The RT-MPC requires short-term forecasts of the uncontrollable demand and generation. In view of the very short-horizon of the RT-MPC, we use the persistent predictor<sup>7</sup> to obtain the forecasts of current time-step using the last observations (i.e.,  $\hat{\mathbf{p}}_t^{\text{unc}} = \tilde{\mathbf{p}}_{t-1}^{\text{unc}}$ ). The short term forecasts are updated each 30 seconds.

## 2.6 Distributed Energy Resource Models

In this section, we describe the DERs optimization models which are used in the formulation of the dispatch and real-time control problem. Since, the experimental setup include battery storages and controllable PV plants, we report their models below.

### 2.6.1 BESS

The objective is to compute power set-points while obeying physical limits on the power rating and reservoir size. We account for BESS losses by integrating its equivalent series resistance into the network admittance matrix using the method described in [64]. The approach integrates the equivalent resistance into the grid's admittance matrix by adding a extra line for a battery as shown in Fig. 2.2. It allows retaining the convexity of the control problem without the need of any auxiliary variables. An alternative approach for modeling battery losses is adopting two different charging and discharging efficiencies (this approach

<sup>7</sup>More advanced forecaster will be investigated in future works.

is referred to as the efficiency model). However, this model requires introducing auxiliary variables: one for discharging and the other for charging, along with an indicator function. In this work, we opted to use an equivalent resistance model instead because it allows modeling the total battery losses by a single lumped resistance integrating the converter, battery, and switchgear losses, also embedding the quadratic dependency of the BESS losses with respect to its power flows. This approach is extensively described in [64].

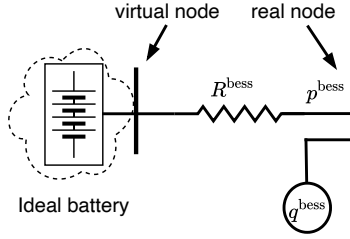


Figure 2.2: Equivalent circuit diagram of a BESS.

Let the series  $x_t^{\text{bess}} = [p_t^{\text{bess}}, q_t^{\text{bess}}]$  be the decision variables for active and reactive power, the BESS decision problem is the following feasibility problem:

$$f_{\text{bess}}(x_t^{\text{bess}}) = 1 \quad (2.24a)$$

and the constraint set  $\Phi_{\text{bess}}(x_t^{\text{bess}})$  is

$$\text{SOE}_t = \text{SOE}_{t-1} - p_t^{\text{bess}} T_s \quad (2.24b)$$

$$(p_t^{\text{bess}})^2 + (q_t^{\text{bess}})^2 \leq (S_{\text{max}}^{\text{bess}})^2 \quad (2.24c)$$

$$aE_{\text{max}}^{\text{bess}} \leq \text{SOE}_t \leq (1-a)E_{\text{max}}^{\text{bess}} \quad (2.24d)$$

where,  $\text{SOE}_t$  is the BESS state-of-energy,  $T_s$  is the sampling time,  $S_{\text{max}}^{\text{bess}}$ , and  $E_{\text{max}}^{\text{bess}}$  are the power and reservoir capacities respectively, and  $0 \leq a < 0.5$  is a fixed parameter to specify a margin on SOE limits. The constraint (2.24c) is to restrict the battery's apparent power within its four-quadrant converter capability. They are approximated by a set of piece-wise linear equations to make the control problem linear.

### 2.6.2 PV Power Plants

PV power plants can accept a control signal to curtail generation and implement a reactive power set-point. However, the curtailment action should be kept at a minimum to avoid an excessive impact on the PV capacity factor. The objective of this problem is determining active and reactive power set-points  $x_t^{\text{pv}} = [p_t^{\text{pv}}, q_t^{\text{pv}}]$  so as to minimize the curtailment and operate at near-unity power factor while subject to the apparent power limit  $S_{\text{max}}^{\text{pv}}$  of the converter. As PV generation is stochastic, the active power injection  $p_t^{\text{pv}}$  is upper-bounded by the theoretical maximum generation potential, that depends primarily on local irradiance conditions. We denote the upper bound of  $p_t^{\text{pv}}$  by  $\hat{p}_t^{\text{pv}}$ . It is derived from short-term point predictions of the

## 2.7 Performance Comparison of Different Linearized OPF Policies for RT-MPC

irradiance for the horizon 30 sec-30 min by applying the same physical modelling tool-chain described for the day-ahead stage. Short-term point predictions for the whole horizon are from averaging measurements over the last 2 minutes interval. While doing this, we assume irradiance persistence, that is often regarded to as the reference forecasting model for very-short term look-ahead times [68]. In this work, we rely on short-term point predictions that are continuously updated by leveraging real-time measurements. In the case of slower refresh times of the control, one could implement prediction intervals to derive robust decisions as in [69, 70, 71] to hedge against longer-term uncertainties. With reference to the resource problem in (2.20), the PV cost function is

$$f_{\text{pv}}(x_t^{\text{pv}}) = (p_t^{\text{pv}} - \hat{p}_t^{\text{pv}})^2 + (q_t^{\text{pv}})^2 \quad (2.25a)$$

subject to the constraint set  $\Phi_{\text{pv}}(x_t^{\text{pv}})$

$$(p_t^{\text{pv}})^2 + (q_t^{\text{pv}})^2 \leq (S_{\text{max}}^{\text{pv}})^2 \quad (2.25b)$$

$$0 \leq p_t^{\text{pv}} \leq \hat{p}_t^{\text{pv}} \quad (2.25c)$$

Equations (2.25b) and (2.25c) are the constraints on active and reactive power injections that account for power converter's capability and PV generation potential. The capability constraint in (2.25b) are approximated by a set of piece-wise linear equations to make the control problem linear.

## 2.7 Performance Comparison of Different Linearized OPF Policies for RT-MPC

In this section, we present a performance comparison of linearized OPF models presented in Sec. 2.3.1 for the application of RT-MPC in a distribution test network. The dominant scheme from this comparative analysis will be used for the experimental validation in the next section (Sec. 2.8).

### 2.7.1 Simulation Setup

Table 2.1: Nominal demands and controllable units

node Id	Demand (kVA)	pf	Resource (rating)
1, 11, 16, 18	200, 15, 55, 47	0.95	–
15	52	0.95	PV (60 kWp)
17	35	0.95	BESS (500 kWh/300 kW)

The MPC scheme is simulated for the CIGRE low voltage benchmark network [5], i.e., a three-phase balanced 0.4 kV/400 kVA, an 18-node system shown in Fig. 2.3. The nominal values of

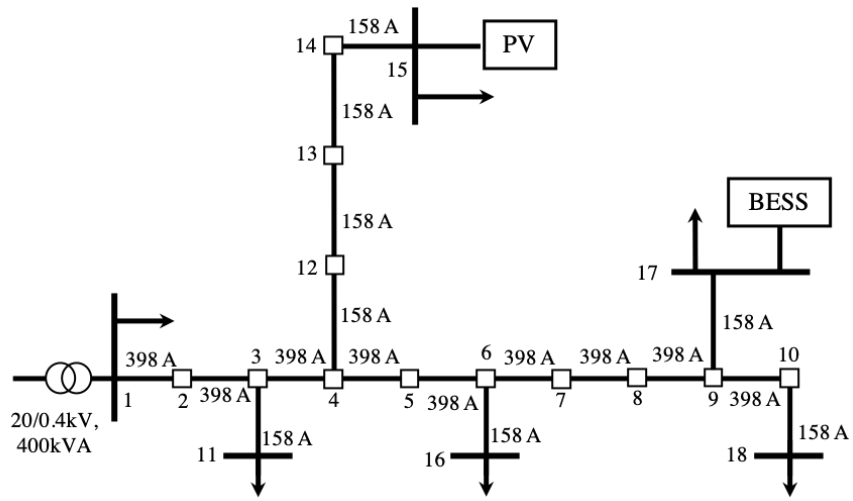
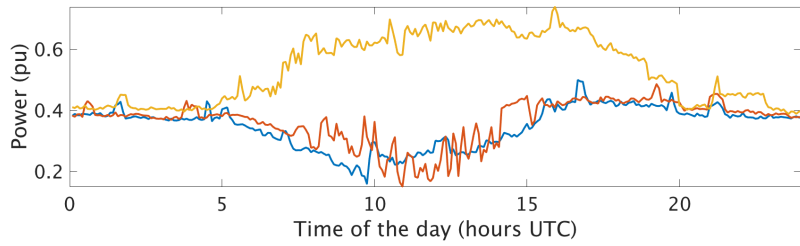
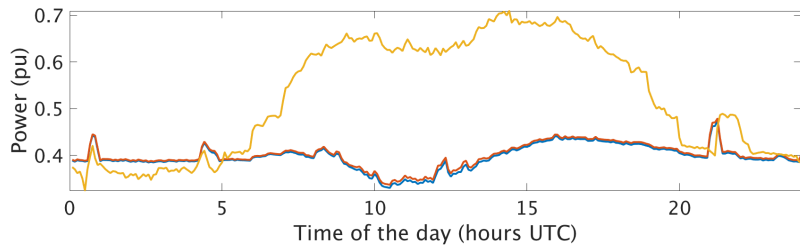


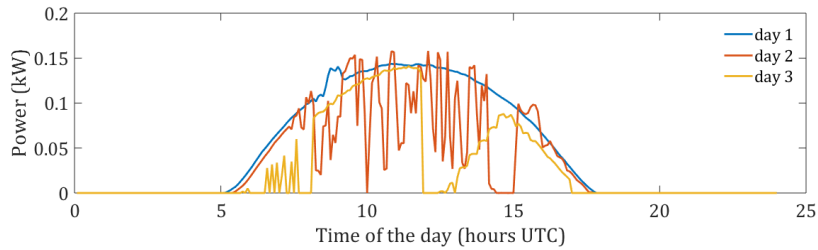
Figure 2.3: CIGRE low voltage benchmark network.



(a) Prosumption at the GCP for three days.



(b) Dispatch plan at the GCP for three days.



(c) MPP PV forecast for three days.

Figure 2.4: (a-c) refers to active power profiles of three days

the uncontrollable nodal demands are shown in Table 2.1. We simulate for a weekend (day 1, and day 2), and a working day (day 3). The demand and PV data is from the experimental measurements described in [72]. They refer to 4 buildings of EPFL. Fig. 2.4a shows the prosumption at the GCP for the 3 days. The dispatch plan<sup>8</sup> is computed using the procedure described in Sec. 2.4, and it is shown in Fig. 2.4b. The PV forecast for three days is shown in Fig. 2.4c.

### 2.7.2 Comparison of MPC with Different Linear Grid Models

**Metrics:** to measure the control performance of the linear grid models (defined in Sec. 2.3.1) applied to the distributed MPC scheme are listed below.

- *ADMM convergence speed:* it is measured in time and number of iterations, both expressed in terms of their mean, max and min values;
- *Tracking error of the dispatch signal:* it is the error between the pre-defined dispatch plan and the net prosumption after MPC. We show the RMSE (root mean square error), mean and maximum tracking error;
- *Error of the linear grid model:* nodal voltages and branch currents are compared against a *posteriori* AC power flow. We report the RMSE, mean and maximum error of voltage and currents.

Table 2.2 and 2.3 report the results of the dispatching simulation for 3 days, where the MPC operates at 5-minute resolution over a shrinking horizon of 24 hours. If ADMM does not converge by the 5-minute deadline, a fallback control strategy is used. In such a case, we re-implement the previous control setpoint. An alternative fall-back strategy would be to project the solution obtained by the final ADMM iteration onto a pre-computed feasible set using the procedure proposed in [73]. Such a strategy will be investigated and compared in future works. The MPC scheme presented above is simulated using the linearized grid model with three linearization policies (denoted by M1, M2, and M3) defined in Sec. 2.3.1, and the fourth model denoted by M3\*, uses M3, but with averaged sensitivity coefficients (averaged with respect to next time interval). The max ADMM iterations was limited to 100 for above simulations.

As it can be observed in Table 2.3, M3\* is the fastest concerning the mean convergence speed. If we compare the maximum simulation time, M3\* is 1.1 – 2.8 times faster than others. All the models perform equally on the tracking error performance. Regarding the voltage error, M2 exhibits the highest error in all the days with a maximum error up to 4%. Also, the mean voltage error is highest with M2. Concerning the current error, the M1, M2, and M3 have the highest errors compared to the ground truth values; it has a maximum current error up to

<sup>8</sup>As this section focuses on finding the best linearized OPF policy for RT-MPC, we do not discuss the performance of the proposed day-ahead dispatch computation scheme of Sec. 2.4. It will be discussed in detail in Sec. 2.8.5.

## Chapter 2. Model-based Grid-aware Dispatching of Active Distribution Networks

Table 2.2: Performance comparison of distributed MPC *control performance* using different linear grid models

Day	Model	Tracking error (kW)			Voltage error (pu)			Current error (pu)		
		RMSE	Mean	Max	RMSE	Mean	Max	RMSE	Mean	Max
1	M1	3.6	-0.33	21.4	6.1e-5	4.4e-9	7.4e-4	5.5e-3	-1.3e-3	6.0e-2
2	M1	1.68	-0.28	13.2	1.5e-4	-1.6e-7	1.8e-3	1.6e-2	-1e-2	0.24
3	M1	1.2	0.1	14.7	5e-5	-5e-8	5.9e-4	5.4e-3	-3.0e-2	0.1
1	M2	0.42	-0.21	2.4	6.3e-3	2.7e-4	4e-2	4e-2	-3e-2	0.18
2	M2	0.85	-6e-2	12.71	6e-3	-1.8e-4	5e-2	4e-2	-2.4e-2	0.18
3	M2	1.04	0.12	12.4	7.7e-3	-4.1e-3	5.4e-2	4.0e-2	-2.0e-2	0.23
1	M3	0.37	-6e-3	2	1.4e-5	-4.1e-6	3.2e-4	7.1e-4	-7.2e-3	3e-2
2	M3	1.2	-1.6e-3	13	9.8e-5	-3.3e-5	1.6e-3	8.2e-3	-1.3e-2	0.12
3	M3	2	0.14	14.4	1.9e-4	-4.2e-5	4.2e-3	1.4e-2	-2.6e-2	0.33
1	M3*	0.5	-0.3	2.4	4.8e-6	-3.3e-7	1.3e-4	5.2e-4	-8e-3	2.3e-2
2	M3*	0.72	-4.3e-2	2.37	3.1e-6	-1.8e-7	5.5e-5	3.7e-3	-1.4e-2	6.0e-2
3	M3*	0.43	-5.3e-2	1.77	1.7e-5	-6.0e-7	4.3e-4	3.1e-3	-3.0e-2	6.0e-2

Table 2.3: Performance comparison of distributed MPC *computational performance* using different linear grid models

Day	Model	Time (sec)			Iterations (#)		
		Min	Mean	Max	Min	Mean	Max
1	M1	2	60	187	3	36.2	100
2	M1	3.9	118	265	7	79	100
3	M1	2.9	121	352	6	77	100
1	M2	1.7	54	242	3	34	100
2	M2	3.7	52	285	6	33	100
3	M2	4.6	80	292	8	53	100
1	M3	27	48	172	17	33	80
2	M3	1.7	123	289	2	81	100
3	M3	4.3	128	273	8	85	100
1	M3*	18.4	41.2	150	13	30.3	78
2	M3*	1.8	35	133	2	17	49
3	M3*	2.1	25.2	126.2	2	13	34

33%, which is putting the grid at the risk of physical damages. M3\* is the best performing in terms of the voltage, and current errors with maximum error percentage of 0.043%, and 6%, respectively, and we select it for the next analysis. M3\* accounts for probable variations in the future sensitivity coefficients by averaging the current and next interval coefficients, and thus models the grid constraints more accurately. This also avoids the re-iteration(s) for correcting the sensitivity coefficients.

### Sensitivity Analysis

To analyse the performance of the distributed MPC scheme with larger number of decision variables, we perform a sensitivity analyses with respect to (1) increase of the MPC prediction horizon length  $T\Delta t$ , and (2) number of controllable units in the MPC scheme.

## 2.7 Performance Comparison of Different Linearized OPF Policies for RT-MPC

1. *Sensitivity with respect to predictive horizon length:* We simulated for shrinking horizon lengths: 3, 6, and 12 hours. We used the same controllable units with equal ratings as before. Table 2.4 and 2.5 compare the results with respect to MPC horizon lengths. Results show that the mean convergence time is smaller for shorter horizon length due to fewer decision variables. Also, the model is consistently accurate in terms of modeling errors of the nodal voltages and lines currents. The tracking error performance with horizon length will be investigated in future work with particular reference to the possibility of bounding the error of the linearized load flow equalities.
2. *Sensitivity with respect to the number of controllable units:* Table 2.7 reports the computational performance (for day 3) when increasing the number of controllable units. We simulate distributed BESSs with equal size among them and total energy capacity as the case before, and placed at nodes 11, 13, 14, 16, and 17. From the table, we observe that even if the number of BESS units is increased up to 5, the increase in convergence time and the number of iterations is not significant, thus denoting good scalability property. The voltage and current errors are consistently small as shown in Table 2.6.

Table 2.4: Sensitivity on *control performance* w.r.t. horizon length for the dominant model.

	Horizon	Tracking error (kW)			Voltage error (pu)			Current error (pu)		
Day	hours	RMSE	Mean	Max	RMSE	Mean	Max	RMSE	Mean	Max
1	12	0.55	-0.23	4	2.7e-6	-2.1e-7	9.9e-5	4.2e-4	-8.1e-3	2.2e-2
1	6	1.28	-0.16	4	8.2e-6	-1.1e-6	1.9e-4	1.1e-3	-5.6e-3	4e-2
1	3	0.81	-0.11	6.4	1.0e-5	-1.3e-6	2.6e-4	1.1e-3	-4.4e-3	3.5e-2
2	12	0.77	-0.11	4.8	4e-6	-4.4e-7	6.2e-5	4e-3	-1.4e-2	6e-2
2	6	0.62	-1e-3	4	3.4e-6	-4.2e-7	5.1e-5	4e-3	-1.2e-2	5.7e-2
2	3	1.82	2.5e-2	6	6e-6	-9.8e-7	1.2e-4	3e-3	-1e-2	3e-2
3	12	0.98	-0.27	14	1.7e-5	-5.5e-7	4.3e-4	3.2e-3	-3e-2	6e-2
3	6	0.6	9.5e-2	7	1.64e-5	-5.5e-7	4.3e-4	3.1e-3	-3e-2	6e-2
3	3	0.98	-0.27	14.2	1.7e-5	-5.5e-7	4.3e-4	3.2e-3	-3e-2	6e-2

Table 2.5: Sensitivity on *computational performance* w.r.t. horizon length for the dominant model.

	Horizon	Time (sec)			Iterations (#)		
Day	hours	Min	Mean	Max	Min	Mean	Max
1	12	21.4	41	165	12	33	78
1	6	9.2	29	127	5	26	71
1	3	3.6	29	114	2	33	68
2	12	1.6	31	224	2	17	51
2	6	1.9	24.5	230	2	17.6	48
2	3	2	22	124	2	24	70
3	12	2	23	176	3	13.3	46
3	6	1.9	29	230	2	18	47
3	3	2	23	175	3	13.3	40



Table 2.6: Sensitivity on *control performance* w.r.t. the number of controllable units for the dominant model.

BESS		Tracking error (kW)			Voltage error (pu)			Current error (pu)		
# units	kWh	RMSE	Mean	Max	RMSE	Mean	Max	RMSE	Mean	Max
2	250	0.42	0.11	1.5	2.8e-5	-1.5e-6	7.4e-4	2.3e-3	-3.3e-2	4e-2
3	168	0.5	0.11	1.7	2.2e-6	-4.6e-8	6.4e-5	1e-3	-3e-2	3e-2
4	125	0.7	0.3	2.3	2.2e-6	-3.2e-8	6.6e-5	8.8e-4	-3.2e-2	3e-2
5	100	0.62	0.25	2.4	2.5e-6	-5e-8	7.9e-5	9e-4	-3e-2	3e-2

Table 2.7: Sensitivity on *computational performance* w.r.t. the number of controllable units for the dominant model.

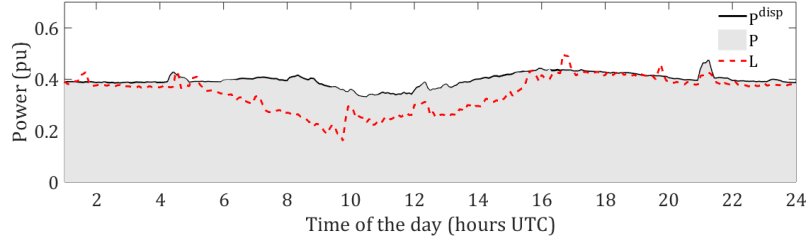
BESS		Time (sec)			Iterations (#)		
# units	kWh	Min	Mean	Max	Min	Mean	Max
2	250	3.6	25	254	7	11	72
3	168	7.3	32	121	6	7.3	25
4	125	6	43	132	4	8.4	23
5	100	5.2	51	149	4	9	22

### 2.7.3 Control Performance

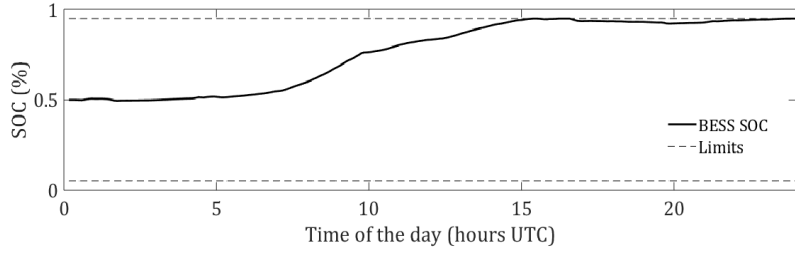
Fig. 2.5 shows the simulation results of the MPC algorithm with the grid model M3\* for day 1. In particular, Fig. 2.5a refers to the performance of the dispatch plan tracking: it can be observed that the prosumption at the GCP highly differs from the dispatch plan due to the incorrect forecast of the prosumption. The MPC is able to control the BESS and PV to achieve a successful dispatch. Fig. 2.5b shows the BESS SOC evolution. Fig. 2.5c shows the active power set-points of the PV resource: the curtailed PV is shown in shaded grey, and maximum possible PV generation in dashed red. From Fig. 2.5c, it can be seen that the control scheme starts curtailing PV generation from the beginning of the day till hour 16. This helps to (i) keep BESS SOC within its operational limits as enforced by the constraints in Sec. 2.6.1, eq. (2.24c)-(2.24d), and (ii) accurately track the dispatch plan. Finally, Figures 2.5d and 2.5e report the cumulative distribution functions of the nodal voltage and branch current modelling errors w.r.t. the AC power flow computations. They show that the voltage and current errors, for the 99% of the estimations, are in the range  $[-7.2e-6 \text{ pu}, 3.8e-7 \text{ pu}]$  and  $[-3.9e-4 \text{ pu}, 1e-3 \text{ pu}]$  respectively.

## 2.8 Experimental Validation and Results

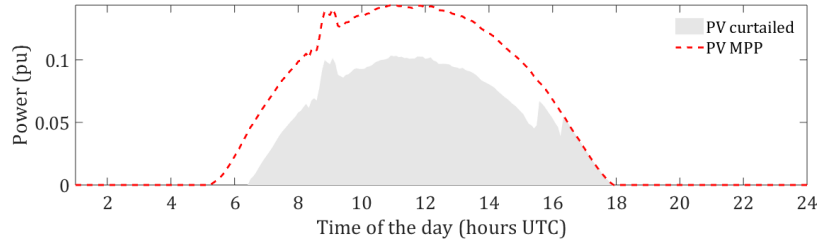
In this section, we present the experimental validation of the proposed control and scheduling framework on a real-scale microgrid at EPFL Distributed Electrical Systems Laboratory. We use the best performing grid model (M3\*) from the previous analysis for the experimental validation. The setup and the obtained experimental results are described below.



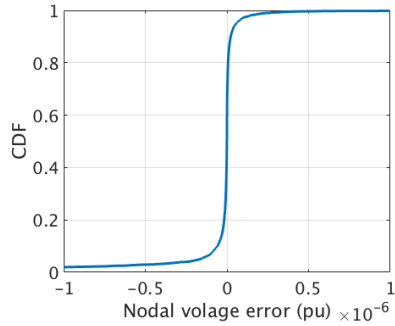
(a) Dispatch plan (black), prosumption realization (shaded area), uncontrolled active power flow at the GCP (dashed red).



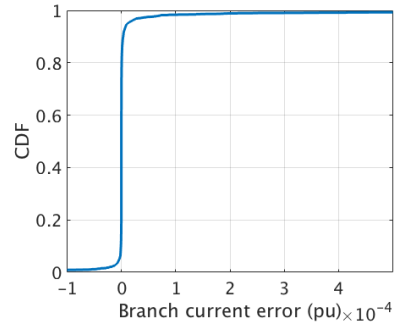
(b) Battery power injection (upper panel), and battery SOC evolution and respective limits (bottom panel).



(c) Curtailed PV (shaded area), and theoretical MPP PV (in dashed red)



(d) CDF plot of the voltage error



(e) CDF plot of the current error

Figure 2.5: MPC operation using M3\* on day 1.



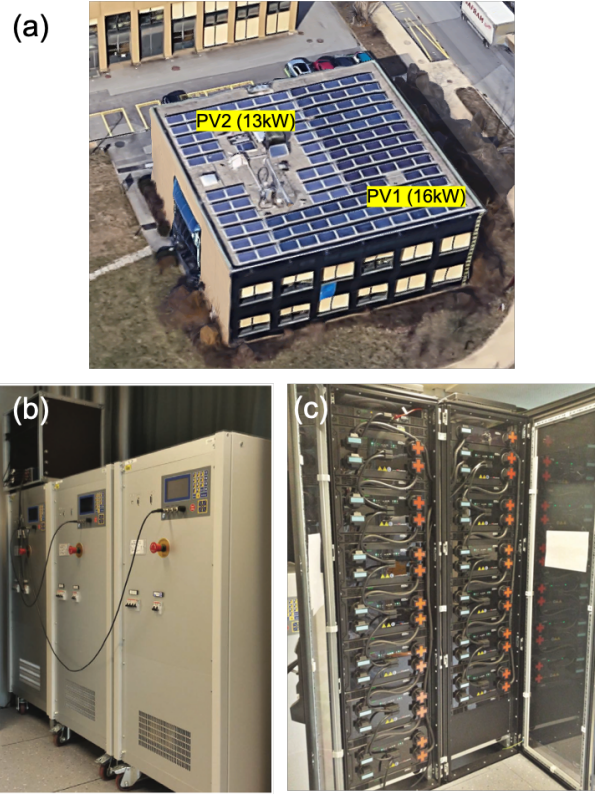


Figure 2.7: Experimental setup: (a) Rooftop PV plants PV1 and PV2 (b) Load emulator and (c) Lechlance battery energy storage system. The ratings are reported in Table 2.8.

Table 2.8: Nominal demands and controllable units

node Id	Demand (kVA)	pf	Resource (rating)
B03	28	0.95	Load emulator (Zenone)
B05	–	–	BESS (25 kWh/25 kW)
B09	–	–	PV2 (13 kWp)
B11	–	–	PV1 (16 kWp)

constraint (2.25b) and (2.25c).

### 2.8.3 Monitoring and Actuation Layers

#### Time-deterministic Metering Infrastructure

As stated in the Hypothesis 2.4, the real-time control problem requires the knowledge of the grid state at a fast pace (e.g. few seconds) to update the linear grid model in (2.2). Time-synchronised and time-tagged phasor measurements are from PMUs, collected with the setup described in [75, 76] that is capable to deliver the measurements at 50 frames per second. A

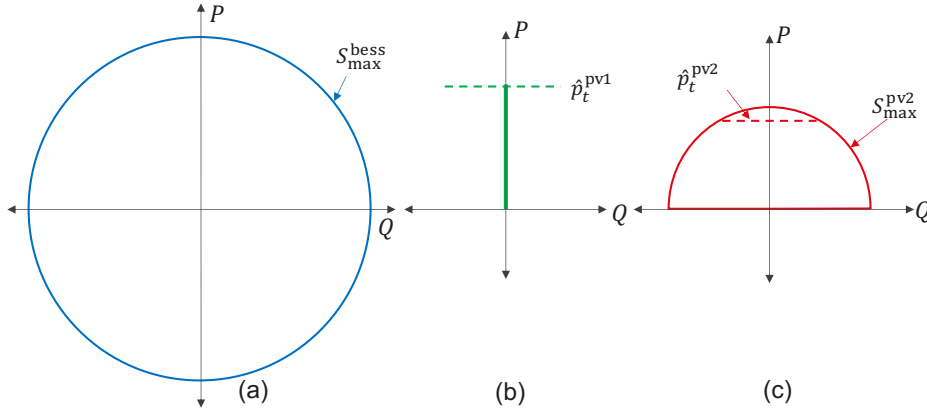


Figure 2.8: Feasible PQ set for the available DERs: a) battery can be controlled to provide both  $\pm$  active (P) and reactive powers (Q), b) PV1 can only provide + P (PV1 converter is not designed to receive external reactive set-points), and c) PV2 can be controlled to provide + P and  $\pm$  Q.

discrete sequential Kalman filter-based state estimator processes the measurements [77] and provides the estimates of the voltage and current phasors of all the nodes and lines with a total latency of less than 80 ms w.r.t. the UTC-GPS time tag of the PMU measurements.

### Data Acquisition and Control System

Each controllable resource is equipped with a micro-controller (National Instruments CRIO 9068) as described in [75]. It is responsible for handling low-level communication tasks such as collecting resource-specific measurements, implementing feasible set-points, and receive set-points from an upper-level controller (i.e., our real-time controller). These functionalities are implemented in National Instruments LabView.

### Communication Infrastructure

The microgrid and its resources communicate over a dedicated IPv4 communication network [75]. A centralized time series database based on InfluxDB<sup>9</sup> facilitates the exchange of information among the resources and the real-time distributed controllers.

#### 2.8.4 Implementation of the Algorithms

Fig. 2.9 shows the sequence of operations and communication flow among of the day-ahead scheduler and real-time controller. In the former phase (upper dashed rectangle), the dispatch plan is computed and stored in the time series database. In the latter (lower dashed rectangle),

<sup>9</sup><https://www.influxdata.com>

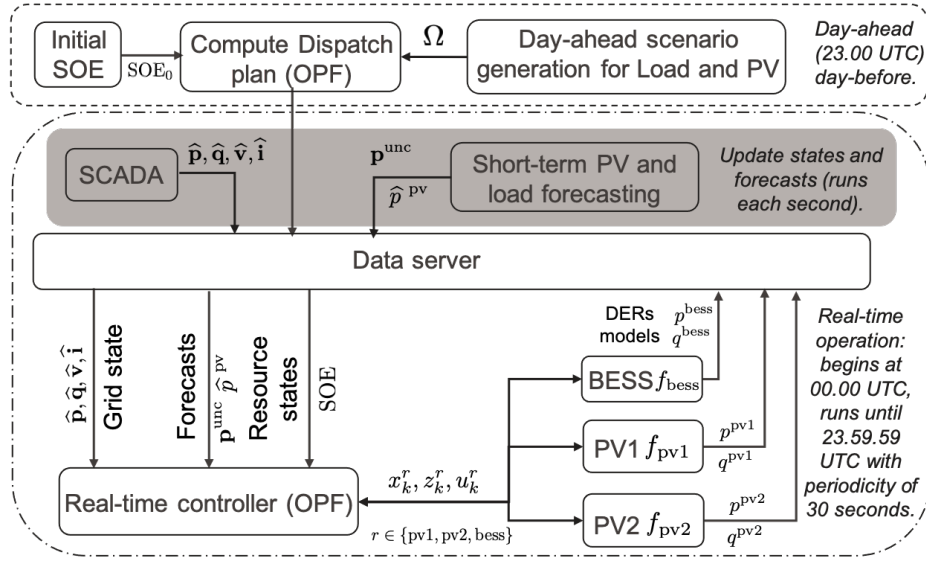


Figure 2.9: Data flow: Dispatch plan computation starts at 23:00 UTC day-before operation, using the PV and load forecasts, and is stored on the central data-server. Real-time operations start at 00:00 UTC. SCADA and short-term forecasters store their outputs to the data server each second, and ADMM computes power set-points and implements each 30 sec.

a real-time local Supervisory Control and Data Acquisition (SCADA), the short-term forecasters, and controllable resources save their outputs in the same database (at 1 sec resolution). The real-time controllers access this information to compute the control actions, which are then sent to the controllable resources for actuation through User Datagram Protocol (UDP). The set-points are sent continuously to minimize packet losses. The ADMM resource problems are solved in parallel; the intermediate variables are also exchanged through UDP.

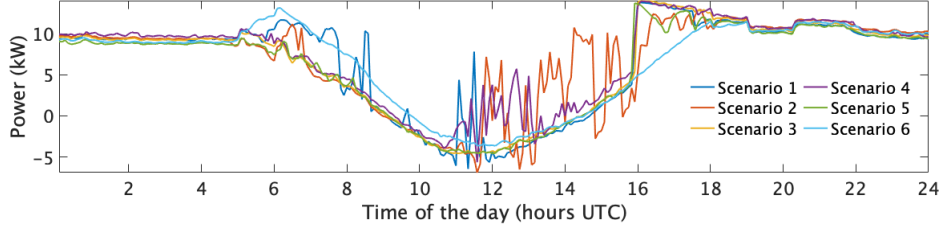
### 2.8.5 Experimental Results

We present the experimental results for two days of operations, Day 1 and Day 2, chosen as they feature different PV generation patterns, being characterized by clear-sky and cloudy conditions, respectively. We focus our analysis on the dispatch plan-tracking performance and the operations of the controllable resources. Grid constraints on nodal voltages and line ampacities are always respected during the experiments and, therefore, not shown. However, they are compared in terms of accuracy with a posteriori AC power flow.

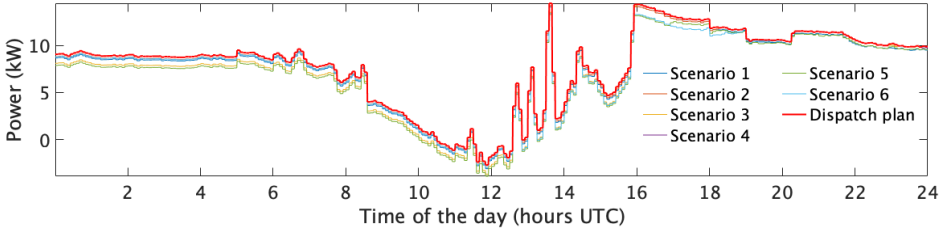
#### Day 1 (4th September 2019)

**Day-ahead Operations:** Fig. 2.10 shows the input and output information of the day-ahead dispatch process. The scenarios of the net demand (i.e., aggregated stochastic demand minus generation plus grid losses) at the GCP are shown in Fig. 2.10a which are inputs to the dispatch plan. The dispatch plan determined by the algorithm is shown in Fig. 2.10b (in red) along with

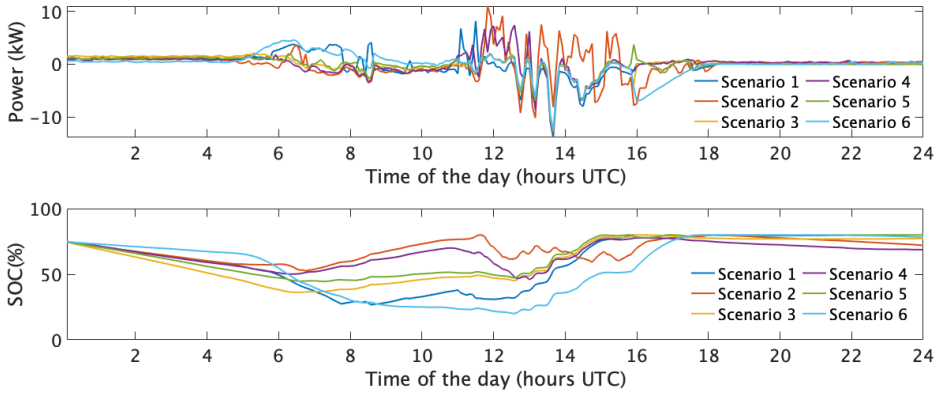
the active power profile scenarios at the GCP (in different colors). The dispatch plan is at a 30 sec resolution. The corresponding battery's power and SOC are shown in Fig. 2.10c. As we can see from Fig. 2.10b, the dispatch plan appears to be tracked in all the scenarios thanks to the compensation action of the battery. Also, to avoid curtailing PV generation and saturating the battery flexibility, the dispatch plan is negative in the central part of the day, denoting that the microgrid exports active power to the upper-level grid. The initial SOC is 0.75, which is the SOC of the battery before the start of the real-time operation.



(a) Day-ahead net demand scenarios (aggregated demand minus generation).



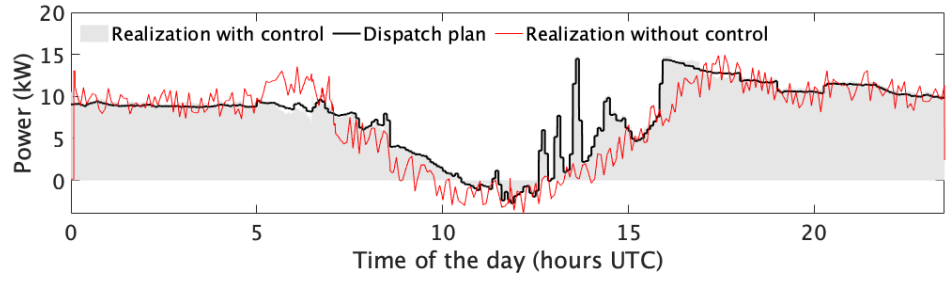
(b) Computed dispatch plan (in red) and scenarios at GCP.



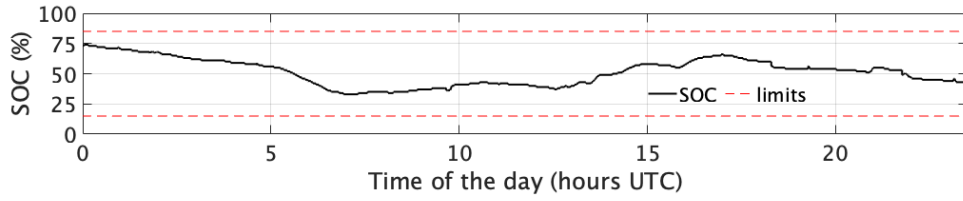
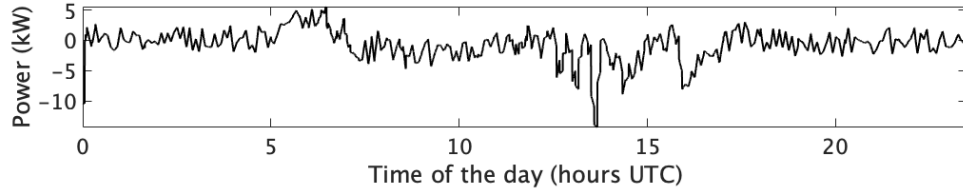
(c) Battery active power injection and SOC for different day-ahead scenarios.

Figure 2.10: (a-c) Dispatch plan computation for day 1: 4th September 2019.

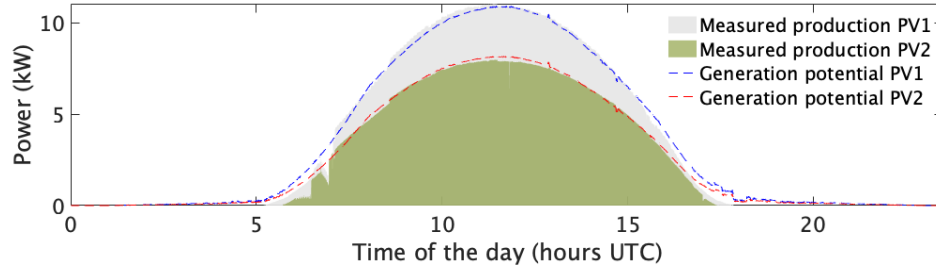
**Real-time Operations:** the real-time stage starts at 00:00 UTC. The active and reactive power set-points of the controllable resources are computed with the distributed MPC algorithm illustrated in Section 2.5. The dispatch plan is tracked at a 30 sec resolution. The control actions are computed one interval in advance with respect to the actuation time (i.e., 30



(a) Dispatch plan (in black), measured power at the GCP (in shaded gray) and power at the GCP without distributed MPC (in red).



(b) Top: realised battery power injection, bottom: SOC and its limits.



(c) Realised generation for PV1 (shaded gray), realised generation for PV2 (shaded green), maximum power for PV1 and PV2 (dashed blue and red).

Figure 2.11: (a-c) The experimental results for real-time control using the distributed MPC on day 1: 4th September 2019.

sec earlier) and then sent to the resources for being actuated at the designed time interval. Fig. 2.11a shows the power at the GCP with and without the dispatch control action<sup>10</sup> (in shaded gray and solid red), and the dispatch plan (in black). As it can be seen, the dispatch plan is tracked with very high fidelity. Fig. 2.11b shows in the upper panel the battery's active power injection, and SOC evolution in the lower panel. Fig. 2.11c shows the measured PV production (in shaded gray and green) and their generation potentials (in dotted blue and red). In this case, there is no curtailment as the battery action alone is sufficient to track the

<sup>10</sup>It is obtained by solving the power-flow equations without considering the actions of the controllable resources, i.e., BESS does not provide any power regulation, and PV plants are operated at MPP.



Table 2.9: Tracking error statistics with and without dispatch control (in (%) normalized by mean of the dispatch plan).

Scenario	Day 1			Day 2		
	RMSE	Mean	MAE	RMSE	Mean	MAE
No dispatch	35.7	12.0	182.2	37.8	25.1	123.5
Dispatch	4.2	-1.77	23.8	4.3	-0.30	21.3

dispatch plan.

To evaluate the dispatch plan-tracking performance, we compute the root mean square error (RMSE), mean, and maximum absolute error (MAE) of the difference between the achieved power at the GCP and the dispatch plan, normalized by the mean of the dispatch plan, with and without control. Results for day 1 are summarised in Table 2.9 and show that the control action achieves way better scores than a simple dispatch plan purely based on forecasts. The mean, max and standard deviations (SD) of the time and number of iterations to solve the distributed MPC problem are shown in Table 2.10. As we can see, the mean and maximum time are well within the 30 sec deadline for the control action actuation.

### Day 2 (10th September 2019)

**Day-ahead Operations:** the scenario forecasts of the net demand at the GCP are shown in Fig. 2.12a. Compared to day 1 that featured clear-sky conditions, day 2 is partly cloudy and exhibits lower PV generation levels. As a consequence, the dispatch plan, shown in Fig. 2.12b, is positive during all day. The corresponding battery's power and SOC are shown in Fig. 2.12c. Again, we can see that the dispatch plan is being tracked with high fidelity in all the scenarios thanks to the compensation action of the battery.

**Real-time Operations:** Fig. 2.13a shows the power at the GCP with and without the dispatch control action, and the dispatch plan. As visible, the dispatch plan overestimates the net demand in the central part of the day and early afternoon.

To track the dispatch plan, the controller charges the battery, which approaches a situation of depleted flexibility as it is near the upper SOC limit. As a consequence, the controller curtails both PV power plants starting from 14h, as shown in Fig. 2.13c. The curtailment action is paramount to follow the dispatch plan at the GCP, which is accurately tracked as visible in Fig. 2.13a.

The tracking performance reported in Table 2.9 scores slightly worse RMSE than day 1 because of the partly cloudy sky conditions which determine higher PV generation variability. Computation performance in Table 2.10 denotes that the control actions are successfully computed within the 30 sec deadline.

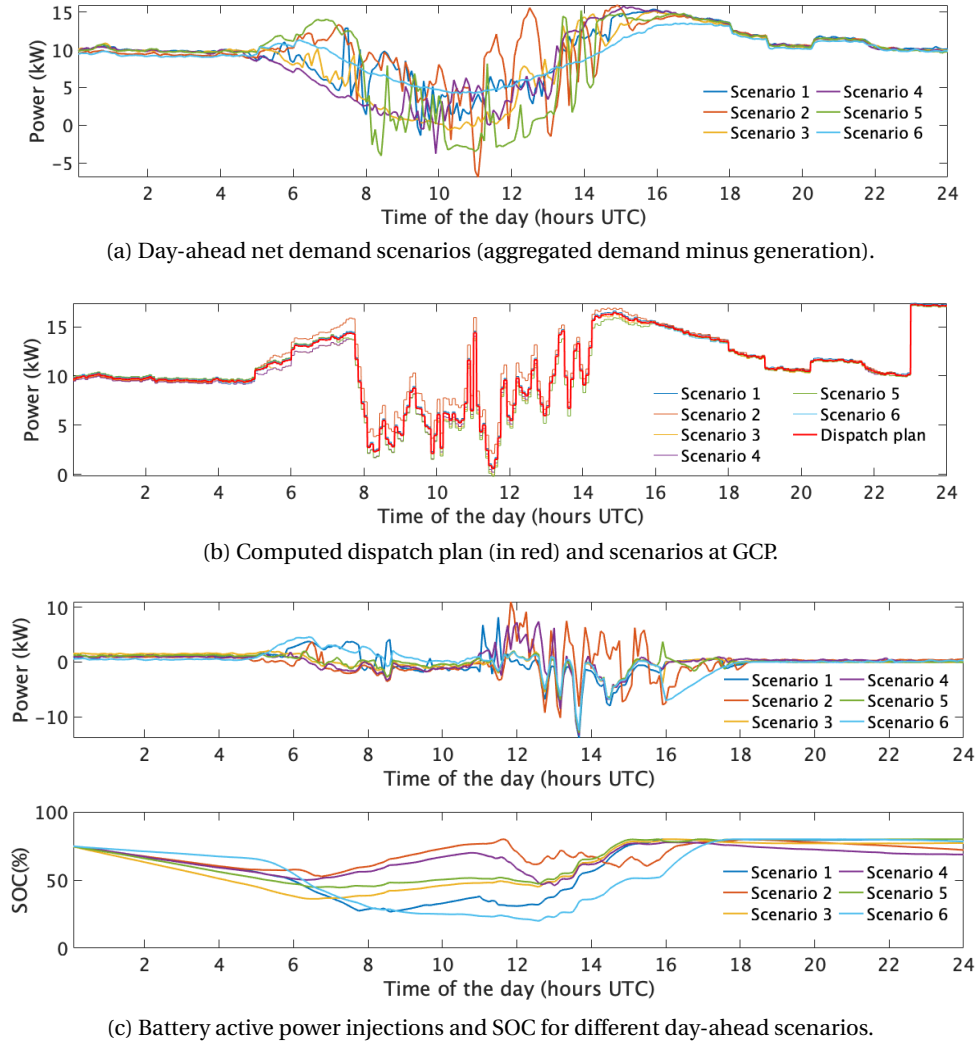


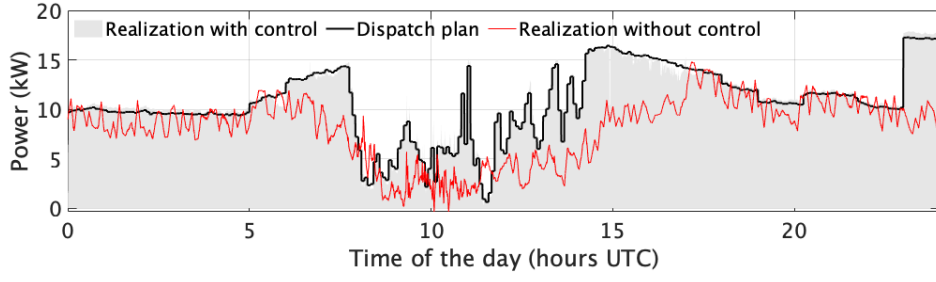
Figure 2.12: (a-c) Dispatch plan computation for day 2: 10th September 2019.

### 2.8.6 Further Analysis

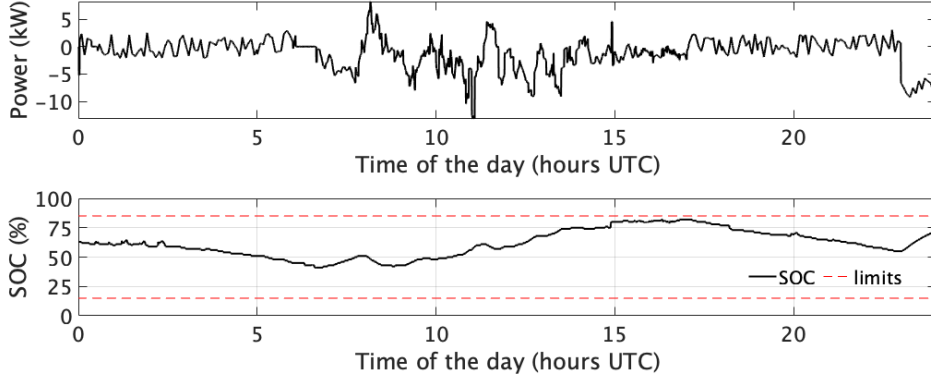
This section is devoted to the following analyses: i) we perform a sensitivity analysis on the performance of the distributed approach by increasing the number of controllable elements and ii) we compare the performance (i.e., optimality and computation time) of the centralized vs the distributed formulations. The analysis is performed by considering the same conditions as day 1.

#### Analysis of the Algorithms Performance with respect to the Number of Controllable Units

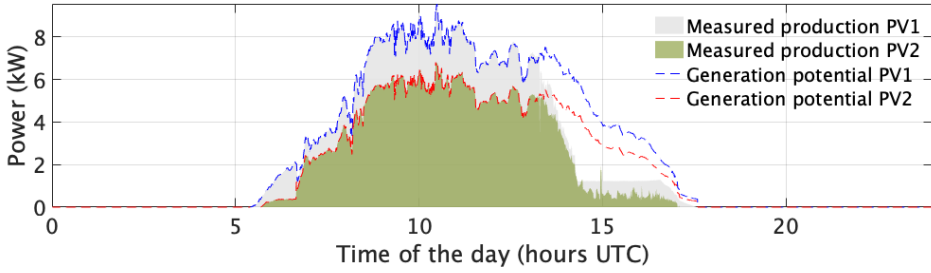
This analysis is carried out by dedicated simulations with different number of distributed BESSs. These resources are considered to have identical power rating and total energy capacity equal to the one of the BESS in the experimental validation. The largest number of



(a) Dispatch plan (in black), measured power at the GCP (shaded gray) and power at the GCP without control (red).



(b) Top: realised battery power injection, bottom: SOC and its limits.



(c) Realised generation for PV1 (shaded gray), realised generation for PV2 (shaded green), maximum power for PV1 and PV2 (dashed blue and red).

Figure 2.13: (a-c) The experimental results for real-time control using the distributed MPC on day 2: 10th September 2019.

controllable BESS is 4 units. This is deemed to be a reasonable estimate as a larger number of BESSs that could be installed in a low-voltage distribution network as the one that we have considered. Indeed, a larger number of BESSs would result in excessively small BESS power ratings (compared to the nominal power of the nodes) and would multiply grid connection costs. The additional BESSs are placed at nodes 5, 6, 7, 8 respectively. Table 2.11 reports the corresponding computational performance. Fig. 2.14 shows the boxplots of the computation time taken by each resource and the grid for the distributed scheme (the figure refers to a daily time horizon). The total computation time is given by the maximum among the resources plus the grid time. As it can be seen, the average computation time for the BESS increases

Table 2.10: Computation performance for real-time experiments

Day	Time (sec)			ADMM iterations		
	Mean	SD	Max	Mean	SD	Max
1	8.10	5.34	18.56	9.34	6.60	19
2	5.90	4.13	13.70	7.03	5.29	17

with the number of units. However, it does not impact the total computation time significantly as the units solve their own problem in parallel. Therefore, increasing the number of controllable BESSs does not influence the solvability of the problem given the real-life solution time constraints.

Table 2.11: ADMM computation time with respect to increasing number of controllable units.

# BESS units	Total time (sec)	
	Mean	Max
1	5.6	11.8
2	5.6	21.3
4	4.7	12.6

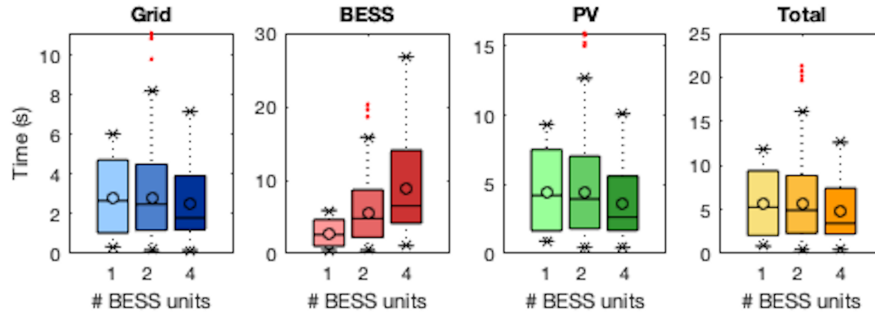


Figure 2.14: Computation time with number of BESS units for Day 2 (Simulation).

### Performance Comparison of the Centralised vs. the Decentralised Algorithms

Table 2.12 shows the results of the comparison in terms of dispatch tracking (measured by RMSE, mean and MAE in % of the mean of the dispatch plan) and computation time performance of the two proposed algorithms i.e., the centralized (Sec. 2.5.1) and distributed (Sec. 2.5.2) RT-MPC. As visible from Table 2.12, the dispatching performance in both cases is very similar. The computation time of the centralized algorithm is shorter than the distributed one. This is to be expected because the distributed optimization formulation requires multiple iterations of the optimization problems to converge to a solution, whereas the centralized algorithm solves a single optimization problem. However, the latter needs to know the complete models of PV and BESS resources, which might not be available in real-life especially

Table 2.12: Performance comparison of the centralized vs distributed algorithms.

Method	Dispatch error			Time (sec)	
	RMSE	Mean	Max	Mean	Max
Centralized	1.6	-0.5	8.9	2.0	3.6
Distributed	3.18	-2.1	10.75	5.6	11.8

when resources belong to different owners. Another advantage of the distributed algorithm is that it is solved by several computers usually characterised by low computing power, whereas the centralized algorithm does require a single computer with larger computing power. Other variants of the ADMM algorithm for improving convergence speed can be deployed in future works as in [78].

### Sensitivity of Dispatch Plan Quality with Weighing Coefficient

We vary the weighing coefficient  $w_r$  over a range of values and recompute the dispatch plan. To quantify the reliability of dispatch plan, we use the mean of RMSE (mRMSE) between each prosumption scenario and the obtained dispatch plan. mRMSE is normalized and expressed in % of the mean of the dispatch plan. As an example, Table 2.13 lists the mRMSE for different  $w_r$  for the dispatch computation on Day 2. It can be seen that the variation in the mRMSE for different values of  $w_r$ , expressed as percentage of the average dispatch plan, is small (less than 4 % for  $w_r$  variation from 0.5e-5 to 0.5) and thus the performance of the proposed problem formulation appears invariant with respect to the value of  $w_r$ .

Table 2.13: Sensitivity of dispatch plan reliability

$w_r$	0.5e-5	0.5-4	0.5e-2	0.5e-1	0.5
mRMSE	2.7	0.7	2.0	2.9	3.8

## 2.9 Discussion

This Chapter proposed and experimentally validated a scheduling and control framework for DERs to track a dispatch plan at the GCP of a distribution network that interconnects heterogeneous resources while respecting constraints on nodal voltages and lines ampacities of the local grid. In the scheduling phase, we determine an aggregated dispatch plan at the GCP by accounting for forecasts of stochastic generation and demand, the state of the controllable resources, and constraints of the grid. During real-time operations, a distributed MPC adjusts the power injections of the controllable DERs to track the dispatch plan subject to the grid's and DERs' operational constraints. We leverage a distributed formulation for improved scalability and privacy-preserving properties (concerning sharing of DER and grid models). To achieve a tractable formulation of the control problem, we used a linearized grid model

based on sensitivity coefficients, computed considering point predictions in the scheduling phase, and updated by using the most recent grid state during real-time operations. The grid model (based on sensitivity coefficients) was updated according to different policies: once per day considering static injections, once per day considering dynamic point predictions of the injections, and dynamically updated during the day. The best performing linearization policy is determined by comparing convergence speed, tracking error, and modeling errors. The analysis showed that the model, where the linear transformation parameters are updated dynamically using the averaged sensitivity coefficients, outperforms others in terms of convergence speed and accuracy in modeling grid constraints. They show that the voltage and current errors, for the 99% of the estimations, are in the range  $[-7.2\text{e-}6 \text{ pu}, 3.8\text{e-}7 \text{ pu}]$  and  $[-3.9\text{e-}4 \text{ pu}, 1\text{e-}3 \text{ pu}]$ , respectively.

The dominant framework is experimentally validated in a real-scale microgrid hosting heterogeneous controllable resources and monitored with PMUs. The dispatch plan, which is at a 30 sec resolution, is computed the day before operations for the next calendar day. The real-time control set-points are implemented every 30 sec for all day. Experimental results, carried out on two distinct days characterized by different irradiance and PV generation patterns, showed that the proposed framework achieves a reliable and accurate dispatch on a 30 sec basis, with RMS and mean tracking errors smaller than 5% and 2%, respectively while respecting all grid constraints.

The methods proposed in this Chapter may not work well when the flexibility offered by DERs is not enough to track the dispatch plan reliably. Also, the linearized grid model deployed for accounting for the grid constraints might not rigorously guarantee the feasible operation of a grid in any possible state. These issues are tackled in the next Chapter.



## 3 Reliable Dispatch Tracking of Active Distribution Network using Batteries

*Dispatching ADNs is an energy-intensive application that, if implemented via BESSs, can require a large capacity and number of these assets in order to fully balance the uncertainties caused by the stochastic demand and generation. The insufficient capacity of the BESSs often leads to their SOC saturation resulting in unreliable dispatch tracking. This Chapter proposes, and experimentally validates, a real-time control scheme that achieves a highly-reliable dispatching of ADNs and ensures that the BESSs' SOC is not saturated during the daily operation. Our proposed scheme uses a two-layer MPC. The upper-layer MPC, running every 5 minutes, optimizes the BESSs' SOC trajectories while minimizing the tracking error, considering the presumption forecast of the whole day. Then, the lower layer MPC, running every 30 seconds, takes the BESSs' SOC trajectories from the upper-layer as constraints while achieving a high-resolution tracking of the dispatch plan over the current 5-minute time horizon. Both layers account for the grid constraints by using the AR-OPF model; an exact convex relaxation of the original AC-OPF (for the first time in the literature for real-time control), in an exact model, to solve a real-time constrained control problem for ADNs. Our proposed framework is experimentally validated using a 1.5 MVA/2.5 MWh BESS connected to an actual 24-node medium-voltage (MV) ADN in Aigle, Switzerland, hosting an uncontrollable 3.2 MWp distributed photovoltaic generation, 3.4 MVA hydro generations, and 2.8 MW base demand.*

*The Chapter includes results of publication [79].*

### 3.1 State-of-the-Art

As discussed in the previous chapter, *dispatching* power-distribution networks is proposed in the existing literature as a way to tackle the problem of bulk transmission system imbalances at the local scale and to solve local distribution grid operational issues (e.g., [18, 19]). This process is achieved by controlling suitable DERs in order to indirectly regulate the power injections of heterogeneous and stochastic resources, according to a pre-defined power trajectory called *dispatch plan* established the day before operation [23, 80]. In these schemes, distribution system operators (DSOs) can determine the day before operation their *dispatch plan* by taking



into account uncertainties of stochastic power injections and can follow it during the day of operation by controlling flexible resources such as BESSs. Different dispatching frameworks have been proposed in the existing literature. For example, the work in [23] proposes and validates a dispatching framework on a medium voltage (MV) feeder by using a utility-scale BESS. The method proposed in the *Chapter 2* validated a dispatching framework on a micro-grid by using multiple controllable DERs. Both controls were formulated to track the dispatch plan, over a short horizon (i.e., 5 minutes). This makes the control myopic, with respect to prosumers' uncertainties in the forthcoming timesteps. The consequence of such schemes is that the early saturation of the flexibility offered by controllable resources (e.g., BESSs' state-of-charge - SOC) can occur hence can interrupt the reliable tracking of the dispatch plan. A way to solve the problem is proposed in *Chapter 2* by optimally curtailing the excess of power from renewable stochastic generation. However, curtailment is often not considered an economical option. Another solution is to increase the time-ahead horizon period (e.g., [81]) in the real-time (RT) model predictive control (MPC) of the schemes proposed in [17, 23]. However, this approach increases the computation time (due to large number of variables) and can exceed the RT actuation-time deadline of the MPC controller. Furthermore, most of the RT controls proposed in the literature assume BESSs to have sufficient capacities. However, this is not always true in real-life setups as different applications have different energy and power requirements. For example, using a BESS for providing primary frequency regulation [82] is a power-intensive application and does not necessarily require a large energy capacity. Two other examples of power-intensive applications are voltage regulation [83], and congestion management [84]. However, dispatching by a BESS (the main focus of this Chapter) is an energy-intensive application, as it needs to compensate for the dispatch energy-errors that occur during the day (or until a sufficient SOC is restored). The previous works in Chapter 2 and [17, 23] were validated with sufficiently sized BESSs. An insufficiently sized BESS, however, results in an early saturation of its capacity and will discontinue the dispatching activity for the rest of the day. Additionally, when the above schemes are implemented on a grid with rich stochastic injections, a successful dispatch requires a large BESS capacity. This large capacity might be challenging to procure by the DSOs, due to regulatory constraints and (sufficiently low) payback times.

Furthermore, previous works did not account for the grid constraints (e.g., [23, 81]). The work in *Chapter 2* did consider the grid constraints via a linearized power flow model. Although the linear power flow model in *Chapter 2* stands correct for most of the cases, it cannot rigorously guarantee the feasible operation of a generic power distribution grid in correspondence to any possible state.<sup>11</sup> In this respect, the full AC power-flow equations could be considered to properly model the grid constraints. However, this leads to the well-known non-convex optimal power-flow (OPF) problem [85, 86]. OPF problems are usually computationally expensive. Hence, they are often used for offline optimizations schemes such as for the planning of grid reinforcements (e.g., [87]). Several OPF-based optimization schemes are presented

---

<sup>11</sup>A performance comparison between the linearized power flow and a convex AC power flow (AR-OPF) is presented in Appendix A.

in [88, 89, 90, 91]; however, either they are quite computationally expensive hence cannot be used for real-time controls, or they are not exact (i.e., the OPF solution is not a solution of the AC power-flow equations). To solve this issue, several convexification approaches (for example [15, 17, 34, 35, 36, 37, 92]) are proposed in the literature. These approaches improve the OPF computational performance for real-time controls. They can be broadly categorized into two types. The *first* one is based on the OPF linearization, for example, in [17, 36, 37, 92]. These schemes rely on the first (e.g., [17, 36, 92]) or multiple (e.g., [37]) order of Taylor's series expansion of the power-flow equations that are used to express, as a function of the power injections, the nodal voltages, line currents, and the losses. In the works [17] and [92], Authors implemented linearized OPFs-based real-time controllers for real-scale ADNs (as also used in *Chapter 2*). The *second* approach relies on the adoption of a suitable relaxation of the power-flow equations to obtain a convex formulation of the OPF [15, 34, 35]. Semi-definite relaxations as second-order-cone-program (SOCP) in a bus injection model [34] and in a branch flow model [35] are the most adopted models. These relaxations are referred to as relaxed-OPF (R-OPF) models. However, as shown in [15], R-OPF applies to a subset of distribution networks. Furthermore, these methods ignore the presence of shunt elements, which is not a realistic assumption for MV distribution networks with branches composed by long coaxial cables. Due to inexactness of these methods, they have not been used in actual networks in real-time controllers. To overcome these shortcomings, in [15], the so-called augmented relaxed (AR)-OPF is proposed; this would account for the shunt elements and provide an exact solution of the OPF if specific conditions are met. AR-OPF is based on a SOCP relaxation of the original power-flow equations. Compared to the other SOCP-based relaxations, the AR-OPF guarantees the exactness of the power-flow solutions, given that some conditions (verifiable *ex-ante*) are met [15]. As it will be described later, the exactness is achieved by including some additional constraints on the SOCP-based relaxation of [35].

Given the above-listed issues, in this Chapter, we propose a real-time grid-aware MPC scheme that: (i) achieves an accurate dispatch tracking of distribution grid while avoiding BESSs' SOC saturation and (ii) integrates an AC-OPF-based grid-aware real-time control by using the AR-OPF. The proposed scheme inherently restores adequate SOC levels for the subsequent day. This is achieved by a proposed two-layer real-time MPC where the upper layer refines the SOC trajectory of the BESS every 5 minutes, based on updated forecasts of prosumers uncertainties for longer-time horizons. Then, the lower-layer MPC computes the BESS's active and reactive power setpoints by considering the SOC trajectory computed by the upper layer as a constraint. The upper-layer MPC is periodically fed with the updated 5-minute forecasts of the stochastic injections for a longer-time horizon (up to the end of the day of operation). Regarding the forecasts, we adopted an integrated data-driven prediction of the prosumption by relying on the day-ahead predicted scenarios, updated global horizontal-irradiance (GHI) forecasts from a commercial service, and the latest power measurements. Our proposed framework was experimentally validated on an actual 24-node medium voltage (MV) grid (in Aigle, Switzerland), hosting an uncontrollable 3.2 MWp distributed photovoltaic generation,

3.4 MVA hydro generations, and a 2.8 MW base demand. A grid-connected 1.5 MVA/2.5 MWh BESS was the sole controllable resource in this setup. The grid was equipped with a state-of-the-art metering and communication infrastructure to determine the grid state at a high refresh rate (i.e., 50 estimations a second) by using 17 commercial distribution-level phasor-measurement units (PMUs). In summary, our main contributions with respect to the existing literature are the following.

- The formulation of a two-layer MPC scheme. Compared to the works in [23, 81], the proposed two-layer MPC avoids BESS SOC saturation by solving a farsighted MPC (considering a longer horizon till the end of the day), along with a myopic MPC (by a shorter horizon of 5 minutes).
- The formulation accounts for the grid constraints by using an exact convex model of AC-OPF, i.e., the AR-OPF. Compared to the linearized OPF model used in Chapter 2,<sup>11</sup> the work presented in this Chapter goes a step further by using a SOCP-based convex relaxation of the original AC OPF, the AR-OPF [15]. Due to its exactness, the AR-OPF guarantees the feasible operation of the grid, with respect to any possible grid state. Compared to the SOCP-based AC-OPF models of [35], it applies to network models that take into account the shunt parameters.
- The experimental validation. To the best of our knowledge, this is the first real-scale experimental validation of a grid-aware AC-OPF-based real-time MPC on a real MV distribution network. The control is assisted by a dedicated metering and communication infrastructure.

## 3.2 Problem Statement

Let us consider a power distribution grid that hosts heterogeneous controllable and uncontrollable DERs. The uncontrollable resources comprise of stochastic renewable power generators and demand, whereas the controllable resource is a grid-connected BESS. The grid is dispatched at its grid-connection point (GCP) by controlling the BESS via a *real-time (RT) controller*, to follow a pre-determined *dispatch plan*. The dispatch plan is computed based on the forecasts of stochastic generation and demand, on the status of the controllable resource (i.e., the BESS), and by taking into account the local grid constraints. The dispatch plan has a 5-minute time resolution and is computed at 23:30 local time the day before operation.

The RT operation begins at 00:00 local time. The purpose of the RT controller is to achieve a fine tracking of the day-ahead dispatch plan and, during the rest of the daily operation, to avoid the saturation of the BESS SOC. At the end of the day, the framework has to restore a sufficient BESS SOC for dispatching the next day. Existing schemes in [17, 23] and Chapter 2 used a RT controller with an MPC look-ahead horizon of 5 minutes. However, this MPC is myopic to the uncertainties of the injections, which eventually leads to BESS SOC saturation,

as schematically shown in Fig. 3.1. In this work, we avoid the BESS SOC saturation by adding a farsighted MPC layer that enforces a SOC budget. This feature is enabled by the proposed two-layered MPC framework, where the upper layer (farsighted) avoids the SOC saturation of the BESS; whereas, the lower layer (myopic) fine tracks the dispatch plan. To summarize,

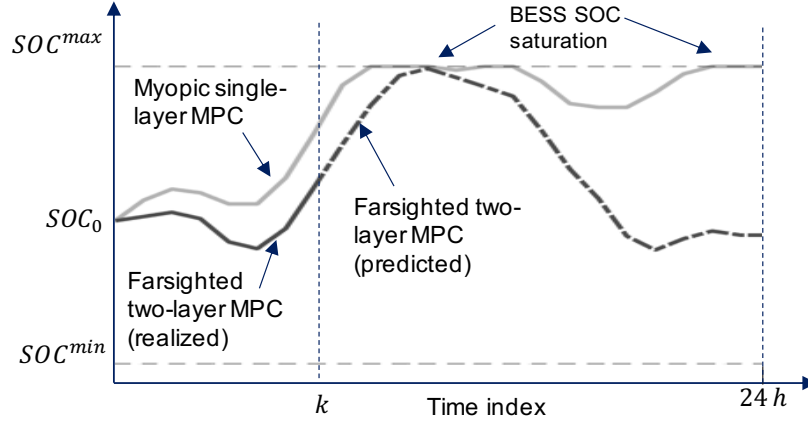


Figure 3.1: Schematic representation of the SOC evolution of the BESS with myopic single-layer MPC and farsighted two-layer MPC.

- The *upper-layer MPC* computes the BESS energy-budget based on latest intra-day forecasts and the current states of both the grid and the BESS. It runs every 5 minutes and considers an MPC horizon till end of the day in a shrinking manner, i.e, horizon length reduces as the day advances. At the beginning of each day, a new 24 hour horizon starts.
- The *lower-layer MPC* optimizes the active and reactive power setpoints of the BESS and considers the energy budget restrictions from the upper-layer MPC and grid constraints. It runs every 30 seconds and considers an MPC horizon of 5 minutes, in a shrinking manner.

The day-ahead and real-time dataflow is shown in Fig. 3.2.

Both the day-ahead and real-stage should account for the grid constraints. In this Chapter, we use AR-OPF, a relaxation of non-linear AC-OPF that guarantees exact solution under certain conditions which are verifiable post optimization.

### 3.3 Day-Ahead Dispatch Computation

The objective of the day-ahead scheduling is to compute the dispatch plan, specifically, the active power-profile that the targeted distribution network should follow at its GCP at a 5-minute resolution, during the next day operation. The dispatch plan is denoted by the

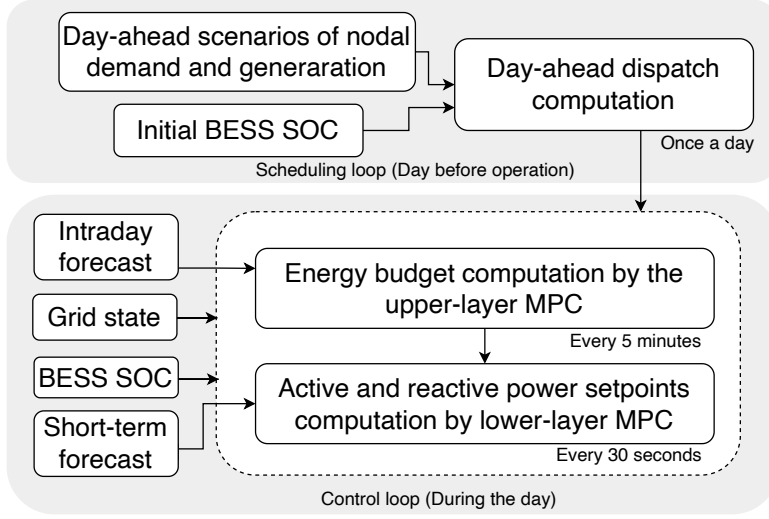


Figure 3.2: Schematic dataflow of the proposed scheduling and control framework.

sequence  $P_y^{\text{disp}}$ ,  $y = 0, 1, \dots, N - 1$ , where index  $y$  is associated with 5-minute discrete intervals of the day of operation, and where  $N = 288$  is the number of time intervals in 24 hours. The dispatch plan accounts for the stochastic variations of the distributed renewable generations and for the demand by day-ahead scenarios produced according to forecasts.

### 3.3.1 Day-Ahead Load and Renewable Power Generation Forecast

We refer to Chapter 2, Section 2.4.1 for day-ahead forecasting of demand and PV generation. Additionally, in our forecast model, the hydropower plants are operated at a given power setpoint and do not have significant intra-day variation, so we model them as constant power injection sources. A validation of the predicted scenarios using above forecasting methods are presented in Sec 3.5.2.

### 3.3.2 Day-Ahead Problem Formulation

We use the dispatch computation algorithm<sup>12</sup> from [64], a stochastic-based optimization problem accounting for the uncertainty of the nodal powers (modeled by day-ahead scenarios) and the grid constraints by co-dist-flow<sup>13</sup> [64]. The problem minimizes the dispatch error considering all the day-ahead scenarios and flexibility offered by the controllable resource. The dispatch plan is computed such that the power regulation made by the controllable resources (BESS in this case) does not violate the grid's and its constraints, and the power

<sup>12</sup>Although, in this Chapter, day-ahead dispatch formulation is based on the work in [64], the linearized-OPF based dispatch formulation of Chapter 2, Sec. 2.4 produces the same results.

<sup>13</sup>The co-dist-flow is an iterative scheme where the dispatch plan is first optimized by neglecting the losses, then they are corrected by solving non-linear AC power flow which is accounted in the next iteration of the optimization. The reader can refer to [64] for more information.

factor at the GCP remains within a pre-defined range. Since the main contribution of this Chapter is on a real-time control scheme, we omit presenting the dispatch formulation.

### 3.4 Real-time Operation via Two-layer Model Predictive Control

The purpose of real-time control is to track the day-ahead dispatch plan, during the day of operation by using a BESS. As stated earlier, the real-time control scheme comprises two layers operating at 5-minute and 30-second time resolutions. The control problems of both layers are formulated as MPC and require forecasts of the nodal power injections. The upper layer MPC uses forecasts of the nodal power-injections at 5-minute time resolutions, whereas the lower layer MPC uses forecasts at 30-second time resolutions. We use data-driven schemes for *intra-day* and *short-term* forecasting for upper and lower MPCs respectively. They are described below.

#### 3.4.1 Intra-day and Short-time Forecasting

A data-driven *intra-day forecasting* scheme has been developed to forecast nodal power injections during the day using the latest measurements of power ( $\mathbf{p}_l^{\text{meas}}$ ) during the day of operation (provided by PMUs), updated GHI forecasts from SoDa [60] and day-ahead scenarios. The scheme is described in **Algorithm 3.1**. Intra-day forecasts  $\hat{\mathbf{p}}_l^{\text{load}}$  is obtained as the weighted sum of the day-ahead scenarios of nodal injections ( $\tilde{\mathcal{P}}_l$  from **Algorithm 2.1**). The weights are derived and updated every 5-minutes based on recent realization from the measurements. The weights are computed by finding the similarity (by norm-2) between the realization ( $\mathbf{p}_l^{\text{meas}}$ ) and day-ahead scenarios ( $\tilde{\mathcal{P}}_l$ ) as in step 5, **Algorithm 3.1**. In step 7-12, updated GHI and air temperature forecasts are obtained from SoDA service, then used to compute PV generation ( $\hat{\mathbf{p}}_l^{\text{pv}}$ ) using a PV model that consists in transposing the GHI data and applying a physical model of PV generation accounting for the air temperature as in [68]. Intra-day forecasts are updated every 5 minutes.

*Short-term forecasts* are obtained by linearly interpolating the latest intra-day forecasts with the time-resolution of 30 seconds and, then we use persistent predictor to correct the forecasts of current timestep using the last observations. The short term forecasts are updated each 30 seconds. The scheme is described in Sec. 2.5.3.

#### 3.4.2 Grid Model using the AR-OPF

Both the MPC layers account for the grid constraints using a convex OPF model. Compared to the linearized OPF in Chapter 2, this work uses a SOCP-relaxation of the original AC OPF model. It uses the AR-OPF model [15] that guarantees exact solution when specific conditions<sup>14</sup> are met (verifiable ex-ante) and can be applied to a network with shunt elements. A

<sup>14</sup>The conditions for exactness, feasibility and optimality of the AR-OPF formulation are described in [15].

#### Algorithm 3.1 Intra-day forecasting

**Require:** Day-ahead load scenarios ( $\tilde{\mathcal{P}}_l = [\mathbf{p}_{l,1}^{\text{load}}, \dots, \mathbf{p}_{l,N_{sc}}^{\text{load}}]$ ), PV-config (from Algorithm 2.1)

```

1: procedure INTRADAYFORECAST
2:   for  $l = 1:|\mathcal{N}|$  do
3:     Retrieve realizations ( $\mathbf{p}_l^{\text{meas}}$ ) till the last 5-minutes slot.
4:      $\mathbf{d} = [d_1, \dots, d_i, \dots, d_{N_{sc}}] = \|\tilde{\mathcal{P}}_l - \mathbf{p}_l^{\text{meas}}\|_2$ 
5:     Weights  $w_i = 1/d_i / \sum_i^{N_{sc}} (1/d_i)$ 
6:     Intra-day load forecast  $\hat{\mathbf{p}}_l^{\text{load}} = \sum w_i \mathbf{p}_{l,i}^{\text{load}}$ 
7:     if node  $l$  contains a PV plant then
8:       Get GHI, temperature ( $\mathcal{G}, T^{\text{air}}$ ) forecasts from SoDa
9:        $\hat{\mathbf{p}}_l^{\text{pv}} = \text{PVmodel}(\mathcal{G}, T^{\text{air}}, \text{PV-config})$ 
10:    else
11:       $\hat{\mathbf{p}}_l^{\text{pv}} = 0$ 
12:    end if
13:  end for
14: end procedure

```

performance comparison between two OPFs (Linear OPF from chapter 2 and AR-OPF) presented in Appendix A confirms the superiority of the AR-OPF model for this specific control application. Therefore, we use AR-OPF [15] in this work for the reliable modeling of the grid constraints. The AR-OPF was originally developed in [15], it is presented below for the sake of completeness of the real-time MPC scheme.

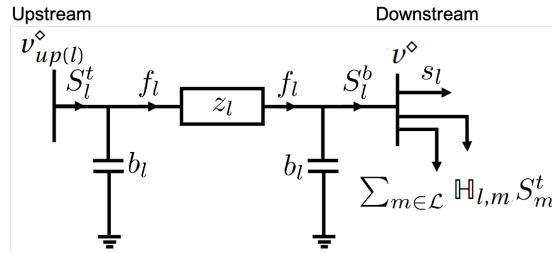


Figure 3.3: Illustration of the adopted nomenclature with respect to the generic two-port  $\Pi$  model of a transmission line.

To introduce the AR-OPF nomenclature, we refer to generic two-port equivalent  $\Pi$ -model of the network branches shown Fig. 3.3. As anticipated before, we consider a radial grid configuration. Let index 0 refer to the slack bus. Buses other than the slack are denoted by  $1, \dots, N_l$  and are in the set  $\mathcal{L}$ . The upstream and downstream buses to bus  $l$  are denoted by symbol  $up(l)$  and  $l$  respectively. The symbol  $\mathbb{H}$  refers to adjacency matrix as defined in [15]. Let  $k$  be the time index in the set  $\mathcal{K} = [1, \dots, K]$ . Let  $S_{l,k}^t = P_{l,k}^t + iQ_{l,k}^t$  and  $S_{l,k}^b = P_{l,k}^b + iQ_{l,k}^b$  be the complex power that is entering the line  $l$  from top and bottom respectively; and  $f_l$  be the square of the current in line  $l$  flowing through  $z_l$  (see Fig. 3.3).  $z_l = r_l + ix_l$  and  $2b_l$  be the longitudinal impedance and shunt capacitance of line  $l$ .  $z_l^*$  refer to complex conjugate of  $z_l$ . Let  $v_{l,k}$  be the voltage phasor,  $v_{l,k}^\diamond$  the square of the voltage magnitude at bus  $l$  and  $v^{\diamond, \min}$  and  $v^{\diamond, \max}$  the squares of the minimum and maximum of nodal voltages operational bounds.

$I_l^{\max}$  is the square of maximum current limits of the line  $l$ . Let  $s_{l,k} = p_{l,k} + i q_{l,k}$  be the power absorbed at bus  $l$ . Let  $s_{l,k}^{\text{bess}} = p_{l,k}^{\text{bess}} + i q_{l,k}^{\text{bess}}$  be the injections from BESS. The uncontrollable injections from demand, PV and hydro generation are modeled by their forecasts denoted as  $\hat{p}_{l,k}^{\text{load}}$ ,  $\hat{p}_{l,k}^{\text{pv}}$  and  $\hat{p}_{l,k}^{\text{hydro}}$  respectively. The nodal active and reactive injections are  $p_{l,k} = p_{l,k}^{\text{bess}} + \hat{p}_{l,k}^{\text{pv}} + \hat{p}_{l,k}^{\text{hydro}} - \hat{p}_{l,k}^{\text{load}}$  and  $q_{l,k} = -q_{l,k}^{\text{bess}} - \hat{q}_{l,k}^{\text{load}} - \hat{q}_{l,k}^{\text{hydro}}$ , respectively.

According to [15], the AR-OPF constraints are composed of the SOCP relaxation of power flow equation (referred as relaxed (R)-OPF). The R-OPF equations are

$$S_{l,k}^t = s_{l,k} + \sum_{m \in \mathcal{L}} \mathbb{H}_{l,m} S_{m,k}^t + z_l f_{l,k} - j(v_{up(l),k}^\diamond + v_{l,k}^\diamond) b_l, \quad \forall l \in \mathcal{L}, \forall k \in \mathcal{K}, \quad (3.1a)$$

$$S_{l,k}^b = s_{l,k} + \sum_{m \in \mathcal{L}} \mathbb{H}_{l,m} S_{m,k}^t, \quad \forall l \in \mathcal{L}, \forall k \in \mathcal{K}, \quad (3.1b)$$

$$v_{l,k}^\diamond = v_{up(l),k}^\diamond - 2\Re\left(z_l^* \left(S_{l,k}^t + j v_{up(l),k}^\diamond b_l\right)\right) + |z_l|^2 f_{l,k}, \quad \forall l \in \mathcal{L}, \forall k \in \mathcal{K}, \quad (3.1c)$$

$$f_{l,k} \geq \frac{|S_{l,k}^t + j v_{up(l),k}^\diamond b_l|^2}{v_{up(l),k}^\diamond}, \quad \forall l \in \mathcal{L}, \quad \forall k \in \mathcal{K}, \quad (3.1d)$$

For the exactness, the AR-OPF [15] introduces auxiliary variables to add security constraints on upper bounds of the nodal voltage and current magnitudes. It is done such that this upper bounds do not depend on original variable  $f$  rather an upper bound  $\bar{f}$ . Let symbols  $\bar{f}$ ,  $\hat{S}$ ,  $\bar{S}$  are auxiliary variables for lines of the grid and  $\bar{v}^\diamond$  for the buses. The AR-OPF equations are defined as follows.

$$\hat{S}_{l,k}^t = s_{l,k} + \sum_{m \in \mathcal{L}} \mathbb{H}_{l,m} \hat{S}_{m,k}^t - j(\bar{v}_{up(l),k}^\diamond + \bar{v}_{l,k}^\diamond) b_l, \quad \forall l \in \mathcal{L}, \forall k \in \mathcal{K}, \quad (3.1e)$$

$$\hat{S}_{l,k}^b = s_{l,k} + \sum_{m \in \mathcal{L}} \mathbb{H}_{l,m} \hat{S}_{m,k}^t, \quad \forall l \in \mathcal{L}, \forall k \in \mathcal{K}, \quad (3.1f)$$

$$\bar{S}_{l,k}^t = s_{l,k} + \sum_{m \in \mathcal{L}} \mathbb{H}_{l,m} \bar{S}_{m,k}^t + z_l f_{l,k} - j(v_{up(l),k}^\diamond + v_{l,k}^\diamond) b_l, \quad \forall l \in \mathcal{L}, \forall k \in \mathcal{K}, \quad (3.1g)$$

$$\bar{S}_{l,k}^b = s_{l,k} + \sum_{m \in \mathcal{L}} \mathbb{H}_{l,m} \bar{S}_{m,k}^t, \quad \forall l \in \mathcal{L}, \forall k \in \mathcal{K}, \quad (3.1h)$$

$$\bar{v}_{l,k}^\diamond = \bar{v}_{up(l),k}^\diamond - 2\Re\left(z_l^* (\hat{S}_{l,k}^t + j \bar{v}_{up(l),k}^\diamond b_l)\right), \quad \forall l \in \mathcal{L}, \forall k \in \mathcal{K}, \quad (3.1i)$$

$$\bar{f}_{l,k} v_{l,k}^\diamond \geq |\max\{|\hat{Q}_{l,k}^b - j \bar{v}_{l,k}^\diamond b_l|, |\bar{Q}_{l,k}^b - j v_{l,k}^\diamond b_l|\}|^2 + |\max\{|\hat{P}_{l,k}^b|, |\bar{P}_{l,k}^b|\}|^2, \quad \forall l \in \mathcal{L}, \forall k \in \mathcal{K}, \quad (3.1j)$$

$$\bar{f}_{l,k} v_{up(l),k}^\diamond \geq |\max\{|\hat{Q}_{l,k}^t + j \bar{v}_{up(l),k}^\diamond b_l|, |\bar{Q}_{l,k}^t + j v_{up(l),k}^\diamond b_l|\}|^2 + |\max\{|\hat{P}_{l,k}^t|, |\bar{P}_{l,k}^t|\}|^2, \quad \forall l \in \mathcal{L}, \forall k \in \mathcal{K}, \quad (3.1k)$$

$$I_l^{\max} v_{up(l),k}^\diamond \geq |\max\{|\hat{P}_{l,k}^t|, |\bar{P}_{l,k}^t|\}|^2 + |\max\{|\hat{Q}_{l,k}^t|, |\bar{Q}_{l,k}^t|\}|^2, \quad \forall l \in \mathcal{L}, \forall k \in \mathcal{K}, \quad (3.1l)$$

$$I_l^{\max} v_{l,k}^\diamond \geq |\max\{|\hat{P}_{l,k}^b|, |\bar{P}_{l,k}^b|\}|^2 + |\max\{|\hat{Q}_{l,k}^b|, |\bar{Q}_{l,k}^b|\}|^2, \quad \forall l \in \mathcal{L}, \forall k \in \mathcal{K}, \quad (3.1m)$$

$$v_{l,k}^{\diamond, \min} \leq v_{l,k}^\diamond, \quad \bar{v}_{l,k}^\diamond \leq v_{l,k}^{\diamond, \max}, \quad \forall l \in \mathcal{L}, \forall k \in \mathcal{K}, \quad (3.1n)$$

$$\bar{P}_{l,k}^t \leq P_l^{\max}, \quad \bar{Q}_{l,k}^t \leq Q_l^{\max}, \quad \forall l \in \mathcal{L}, \forall k \in \mathcal{K}, \quad (3.1o)$$



Eq. (3.1e)-(3.1f) express the lower bound on branch power flows at the sending and receiving ends of the line  $l$ , whereas the eq. (3.1g) and (3.1h) express the upper bound for power flows. Eq (3.1i) expresses the upper bound on the nodal voltages. These variables are then used in upper and lower bounds on the square of longitudinal current in eq. (3.1j) and (3.1k). Eq. (3.1l)-(3.1m) and eq. (3.1n) impose limits on the ampacity and nodal voltage respectively. Eq. (3.1o) expresses upper bound on the active and reactive power flows in line  $l$  where  $P_l^{\max}/Q_l^{\max}$  are bounds on active/reactive power flows in line  $l$ .

#### 3.4.3 Real-time Model Predictive Control (RT-MPC) of BESS

##### BESS Model

The BESS is controlled by an MPC to provide active and reactive power regulations to the grid while respecting the capability of the BESS power converter. Let  $P_l^{\text{bess}}$  and  $E_l^{\text{bess}}$  be the power and energy capacities of BESS connected at bus  $l$ . Typically, the converter capability is represented by a circle  $((p_{l,k}^{\text{bess}})^2 + (q_{l,k}^{\text{bess}})^2 \leq P_l^{\text{bess}2})$ , but it is not true in practice as the power capability of the converter depends on both the AC and DC voltages of the converter. An example of capability curves with different combination of the AC and DC voltage are shown in Fig. 3.4a, and they can be represented by piece-wise-linear functions as follows.

$$\phi(v_t^{dc}, v_t^{ac}, p_l^{\text{bess}}, q_l^{\text{bess}}, P_l^{\text{bess}}) \leq 0. \quad (3.2a)$$

Here,  $v^{dc}$  is the DC bus voltage and  $v_t^{ac}$  is the magnitude of the direct sequence voltage on the AC side of the converter. They can be obtained from measurements.

We model the BESS losses by adding an equivalent resistance in the power flow equations as proposed in [64]. The approach integrates the equivalent resistance into the grid's admittance matrix by adding a extra line ( $l'$ ) for each BESS. It allows retaining the convexity of the AR-OPF problem without the need of any auxiliary variables. Fig. 3.4b shows the equivalent resistance with an ideal voltage source and series resistance ( $R_l^{\text{bess}}$ ). Thanks to this simplification (i.e., adding equivalent resistance into the grid's admittance matrix) the BESS state-of-energy (SOE) ( $SOE_l = SOC_l E_l^{\text{bess}}$ ) evolution with sampling time  $T_s$  is now expressed simply by

$$SOE_{l,k+1} = SOE_{l,k} + T_s p_{l,k}^{\text{bess}}, \quad \forall l \in \mathcal{L}, \forall k \in \mathcal{K}. \quad (3.2b)$$

We constrain the SOE by safety margin of 0.1 per unit of the extremes saturation/depletion of the battery. It is

$$0.1E_l^{\text{bess}} \leq SOE_{l,k} \leq 0.9E_l^{\text{bess}}, \quad \forall l \in \mathcal{L}, \forall k \in \mathcal{K}, \quad (3.2c)$$

Also, to account for the degradation of the BESS caused by its operation, we include the

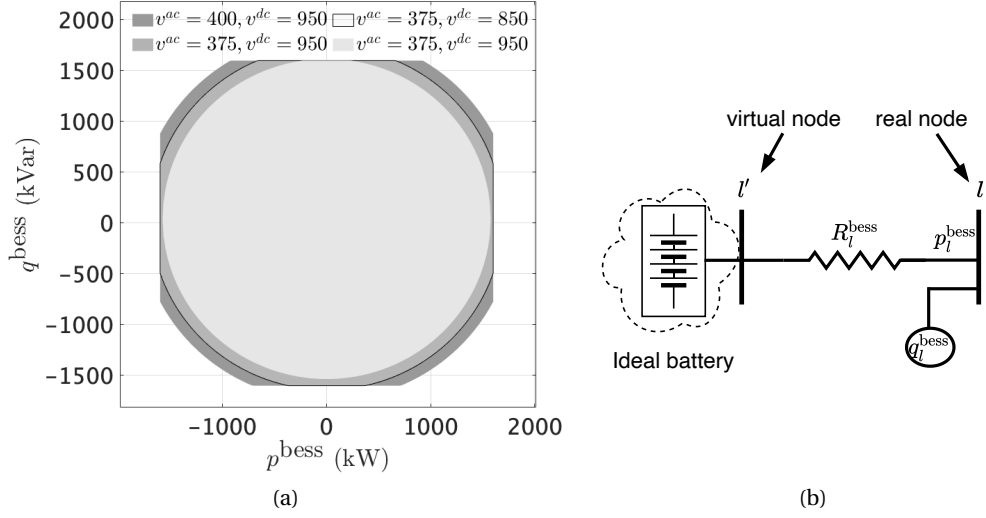


Figure 3.4: (a) BESS converter capability function  $\phi$  in eq.3.2a with AC and DC voltage. (b) Equivalent circuit diagram of BESS.

following constraint that limits the active power by a pre-defined threshold:

$$\frac{T_s}{2 \times 3600} \left| p_{l,k}^{\text{bess}} \right| \leq N_e E_l^{\text{bess}}, \quad \forall l \in \mathcal{L}, \forall k \in \mathcal{K} \quad (3.2d)$$

where  $N_e$  is rated number of cycles for the battery.

#### Model Predictive Control (MPC) Problem

As stated earlier, the real-time control scheme comprises two layers, both formulated as MPC but with different horizon lengths. The upper layer considers intra-day presumption forecast along the whole day via subsequent shrinking horizon and computes successive BESS SOC trajectories. The lower layer considers forecast of 5-minutes interval with a shrinking horizon and computes power setpoints for the BESS while accounting for the SOC trajectory (provided by the upper layer) as hard constraint. This two-layered structure enables full visibility of the uncertainties during the real-time operation, therefore ensuring the BESS SOC to not saturate. Fig. 3.5 explains the sequence of operations during real-time operation per time step. The time intervals are divided into 5-minutes and 30-seconds slots corresponding to the sampling of upper and lower level MPCs.

- The dispatch setpoint to track  $P_y^{\text{disp}}$  is retrieved from the dispatch plan profile with indices  $y = 0, 1, \dots, N-1$  where  $N = 288$  for 24 hours in a day. Intra-day forecasts  $\hat{p}_{l,y}^{\text{load}}, \hat{q}_{l,y}^{\text{load}}, \hat{p}_{l,y}^{\text{pv}}, \hat{p}_{l,y}^{\text{hydro}}$ , are updated.
- The upper layer MPC computes BESS energy budget  $\Delta \text{SOE}_k$ ,  $k = 0, 1, \dots, N-1$  every 5-minutes based on updated intra-day forecasts and current BESS  $\text{SOE}$ .

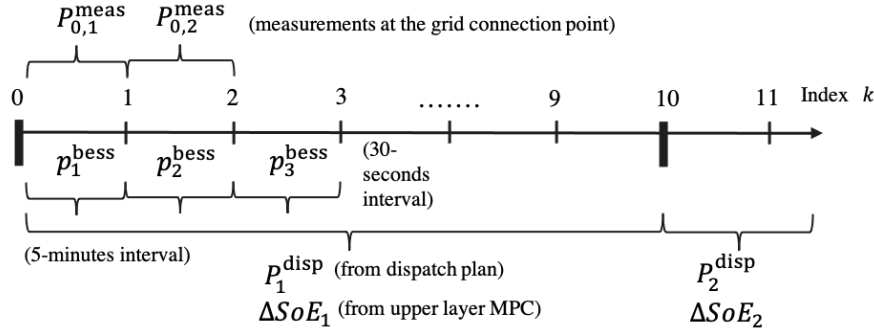


Figure 3.5: Sequence of decisions computed during real-time operations.

- The dispatch setpoint to track by the lower MPC is denoted by  $\bar{P}_k^{\text{disp}} = P_{\lfloor \frac{k}{10} \rfloor}^{\text{disp}}$ , where  $\lfloor \cdot \rfloor$  refers to the floor function. The first and the last 30-seconds index in current 5-minutes interval are denoted by  $\underline{k}$  and  $\bar{k}$  respectively, i.e.,  $\underline{k} = \lfloor \frac{k}{10} \rfloor \times 10$  and  $\bar{k} = \underline{k} + 10 - 1$ . The power measurements at the GCP denoted by  $P_{0,k}^{\text{meas}}$  is obtained. Using  $\bar{P}_k^{\text{disp}}$ ,  $P_{0,k}^{\text{meas}}$  and  $\Delta SOE_k$ , it computes BESS setpoints  $p_k^{\text{bess}}$  at time resolution of 30 seconds with indices  $k = 0, 1, \dots, K-1 \in \mathcal{K}$  with  $K = 2880$  for a 24 hours operation day.

**Upper Layer MPC:** the objective is to minimize the tracking error between the dispatch plan  $P^{\text{disp}}$  and power at the GCP  $P_0^t$ . Note that  $P_0^t$  is a dependent variable related to the uncontrollable power injections, the controllable BESS injections and the grid losses derived from AR-OPF (Eq.(3.1)). The decisions variables are the BESS active and reactive powers to compensate for the uncertainties in the nodal injections, the latter modeled by intraday point forecasts. The objective function to minimize is the weighted<sup>15</sup> sum of the tracking error for the whole day and grid losses<sup>16</sup>:

$$\hat{p}_l^{\text{bess}} = \arg \min_{\forall S, v, s^B} w_p \sum_{j=y}^N \|P_j^{\text{disp}} - P_{0,j}^t\|_2 + w_l \sum_{j=y}^N \sum_{l \in \mathcal{L}} r_l f_{lj} \quad (3.3a)$$

$$\text{subject to} \quad (3.1), (3.2) \quad (3.3b)$$

A bound on the final SOE such that it is restored to a comfortable level by the day's operation is also added.

$$0.45E_l^{\text{bess}} \leq SOE_{l,N} \leq 0.55E_l^{\text{bess}} \quad \forall l \in \mathcal{L}. \quad (3.3c)$$

The budget  $\Delta SOE_l$  is computed using the first element of the BESS setpoint vector from upper-layer MPC:

$$\Delta \widehat{SOE}_l = \hat{p}_{l,1}^{\text{bess}} \times \frac{300}{3600}. \quad (3.3d)$$

<sup>15</sup>The weights  $w_p$ ,  $w_l$  and  $w_e$  may be derived from energy imbalance price in day-ahead electricity market.

<sup>16</sup>Grid losses are included to satisfy exactness conditions of the AR-OPF formulation as in [15]

**Lower Layer MPC:** the problem is formulated as an MPC and its objective is to minimize the energy error incurred over a 5 minutes horizon length with power set-points actuated each 30 sec. The dispatch energy error at time  $k$  comprises of (i) uncovered energy error from time index  $\underline{k}$  to  $k-1$ ,  $\hat{\epsilon}_k = \sum_{j=\underline{k}}^{k-1} (\bar{P}_j^{\text{disp}} - P_{0,j}^{\text{meas}})$  and (ii) the predicted error from  $k$  to  $\bar{k}$  given as  $\epsilon_k = \sum_{j=k}^{\bar{k}} (\bar{P}_j^{\text{disp}} - P_{0,j}^t)$ . The MPC objective is a multi-objective function comprised of the dispatch energy error incurred at the GCP (from current timestep to end of the 5-minute period) and the grid losses:

$$\underset{\forall S, v, s^B}{\text{minimize}} \quad w_e(\epsilon_k + \hat{\epsilon}_k) + w_l \sum_{j=k}^{\bar{k}} \sum_{l \in \mathcal{L}} r_l f_{l,k} \quad (3.4a)$$

$$\text{subject to} \quad (3.1), (3.2). \quad (3.4b)$$

Additionally, the energy budget from the upper layer MPC are added as constraint imposed on the BESS SOE as:

$$SOE_{l,\bar{k}} \geq SOE_{l,\underline{k}} + \Delta \widehat{SOE}_l \quad \text{if} \quad \Delta \widehat{SOE}_l \geq 0, \quad (3.4c)$$

$$SOE_{l,\bar{k}} \leq SOE_{l,\underline{k}} + \Delta \widehat{SOE}_l \quad \text{if} \quad \Delta \widehat{SOE}_l \leq 0. \quad (3.4d)$$

The constraints in (3.4c) sets a threshold SOE to be attained by the end of current 5-minutes duration. It ensures that the BESS is used judiciously by the lower MPC to avoid its saturation and therefore restoring to comfortable SOE value by the end of the daily operation. Thanks to the convex reformulation of the AC power flow equations using AR-OPF, the control problems in (3.3) and (3.4) are convex and can be solved by standard solvers.

## 3.5 Experimental Validation

### 3.5.1 Experimental Setup

#### Medium Voltage Distribution Grid in Aigle, Switzerland

We validate the proposed control scheme on a real MV grid situated in Aigle, Switzerland, a mixed rural/urban system operated by Romande Energie,<sup>17</sup> one of the main Swiss DSOs. It is a radial feeder composed by 24 nodes. The topology and locations of various connected resources are shown in Fig. 3.6a-3.6b. It is a three-phase 21 kV/20 MVA balanced (seen in the observations) system. The grid accommodates a peak power consumption (at the feeder) of 4.2 MWp and 2.8 MWp during the winter and summer, respectively. It hosts aggregated PV generation capacity of 3.2 MWp including a single plant of 1.8 MWp. The grid also hosts distributed hydropower generation of 3.4 MVA allocated in 4 plants. The placement of these generations are shown in Fig. 3.6a. The grid is connected with a 1.5 MW/2.5 MWh BESS at node 11. Figure 3.6c shows exterior and interior of the BESS. The cells are Lithium-Nickel-Manganese-Cobalt-Oxide (Li-NMCo) based and are rated for 4000 equivalent full cycles. It

<sup>17</sup><https://www.romande-energie.ch/>.

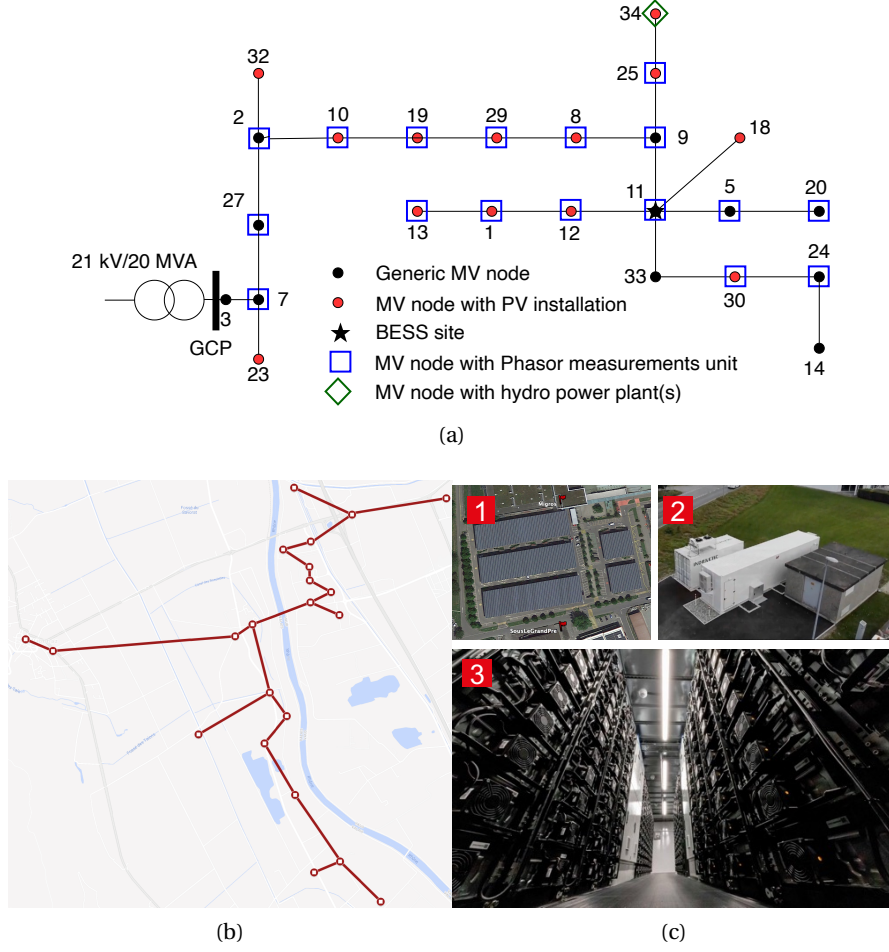


Figure 3.6: (a) Topology with locations of the PMUs, PV plants, hydro-power plants, (b) Location of the substations and lines on the map, and (c) BESS and PV infrastructure: (1) Satellite view of the centralized PV plant of capacity 1.8 MWp, (2) battery container and (3) interior of the battery.

consists in 30 racks in parallel with 11 modules per rack in series (each module composed by 1p22s cell pack) connected to a four-quadrant power converter. The whole setup is installed in a temperature controlled container as shown in Fig. 3.6c. The technical specifications of the BESS and the converter are listed in the Table 3.1.

#### Metering and IT Infrastructure

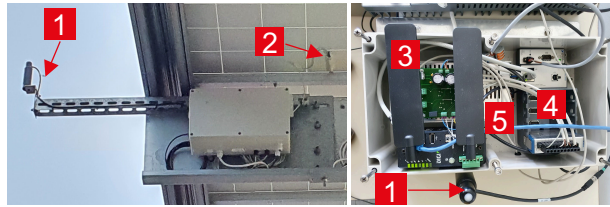
**Phasor Measurement Units (PMUs):** The RT-MPC algorithm relies on the grid awareness provided by a cluster of distributed metering units that provide up-to-date relevant measurements such that they can be accounted as initial conditions, (in the OPF problem in (3.3) and (3.4)) ensuring a safe and secure operation of the grid. In this respect, the MV-distribution

Table 3.1: Technical specifications of the 1.5 MW/2.5 MWh BESS for the experimental setup.

Parameter	Value
Nominal capacity	1.5 MVA/2.5 MWh
GCP Voltage	21 kV
DC bus voltage range	770-1000 V
PCS PQ controllability	4-quadrant operation
PCS efficiency	93 % for all the operating conditions
Total harmonic distortion	< 3 %
CSC operation mode	Compliant
VSC operation mode	Compliant
Cell technology	Lithium Nickel Manganese Cobalt Oxide (NMC)
Number of racks	30 in parallel
Number of modules per rack	11 in series
Cells configuration per module	1p22s
Total number of cells	7260
Cell nominal voltage	3.68 (limits 2.7 - 4.15 V)
Cell nominal capacity	94 Ah (343 Wh)
Battery cycle life	4000 equivalent cycle at 1C rate at 100 % DoD with 80 % of the initial storage capacity available at the end of life



(a)



(b)

Figure 3.7: (a) PMU installation at a monitored substation, 1) Zaphiro PMU box 2) GPS antenna, (3) current sensor (4) cables and (b) GHI and temperature measurement box (metebox) at a PV plant: 1) pyranometer, (2) temperature sensor (3) antenna (4) power supply (5) NI Compact RIO.

grid is equipped with the state-of-the-art monitoring solution SynchroGuard<sup>18</sup> that provides real-time situational awareness of the grid. The setup contains 17 PMUs distributed across the grid, the locations are shown in Fig. 3.6a. Fig 3.7a shows an example of an installed PMU and

<sup>18</sup><https://zaphiro.ch/technology/>.

its components at a substation. The PMUs provide synchronised and time-tagged phasors that are sent to a central server through a phasor data concentrator (PDC). As described later, the PDC is hosted in a local server and is compliant with the IEEE Guide C37.244-2013 [93]. The PDC is responsible for the *data aggregation* and *data pushing* of the PMU measurements. The measured characteristics of this setup, especially the network latency and packet losses, are given in the Sec. 3.5.3. As shown in Fig. 3.18, the average and maximum latencies of most PMUs are below 60 and 180 milliseconds, respectively; this is much lower than the control actuation time of 30 seconds. We also show the packet losses in Table 3.5. As observed, the mean packet losses are below 0.02%. Therefore, the installed measuring and communication infrastructure can be considered reliable for the experimental validation of the RT-MPC [76].

It is worth noting that the metering system is also a source of historical data that is used to obtain day-ahead scenarios, intra and short-term forecasts of the uncontrollable injections.

**GHI and Temperature Measurement box:** For the modelling of the PV generation, we use the historical data of GHI and air temperature from the same region where the PV plants are located. We installed GHI and temperature sensing boxes (Meteobox) to measure the GHI, air- and PV-panel- temperatures. These meteoboxes are installed at three locations<sup>19</sup> in the grid. They provide in real-time measurements with sampling of 500 ms (including communication latency). Fig 3.7b shows the installed meteobox at the site; each one consists of a pyranometer to sense the GHI, two temperature sensors, and a power supply. They each also contain a modem to stream the measured data, by using the public 4G network, to the local data server. The meteobox code is implemented in National Instruments-Comapct-RIO.

**Communication Infrastructure, Centralized Server and Data-logging:** Fig. 3.8 shows the schematic of the communication and server infrastructure that enables the day-ahead and real-time control operations. A centralised local server hosts five virtual machines (VM1, ... VM5) to implement a PDC, RTSE, data-logging, day-ahead dispatch, real-time MPC, a BESS setpoint actuator, and a router. PMU measurements are streamed to the VM1 through the public network. In the VM1, a dedicated PDC is implemented. It is responsible for PMU data aggregation and alignment. Once data aggregation is finished, it is sent to the real-time state estimation (RTSE) (running on the same VM1). After the estimation is done, the measurements and the estimated states are sent, and stored, in the local server database (hosted in VM2). The real-time controls, day-ahead dispatcher and forecasting algorithms are implemented in VM3. VM4 hosts the BESS actuator responsible to measure the BESS state and send actuation messages (e.g., BESS setpoints). To facilitate communication among the VMs, BESS's BMS and its converter, PMUs and meteoboxes, we equip them with a dedicated IPv4 communication network by using Ethernet cables, as shown in Fig. 3.8. The communication network links all the monitoring units (PMUs and meteoboxes), the controllable resources (BESS' BMS and its

---

<sup>19</sup>As distribution networks generally have limited geographical expansion and the substations are close to each other, a few GHI sensors are sufficient to represent GHI variation over the whole distribution network.

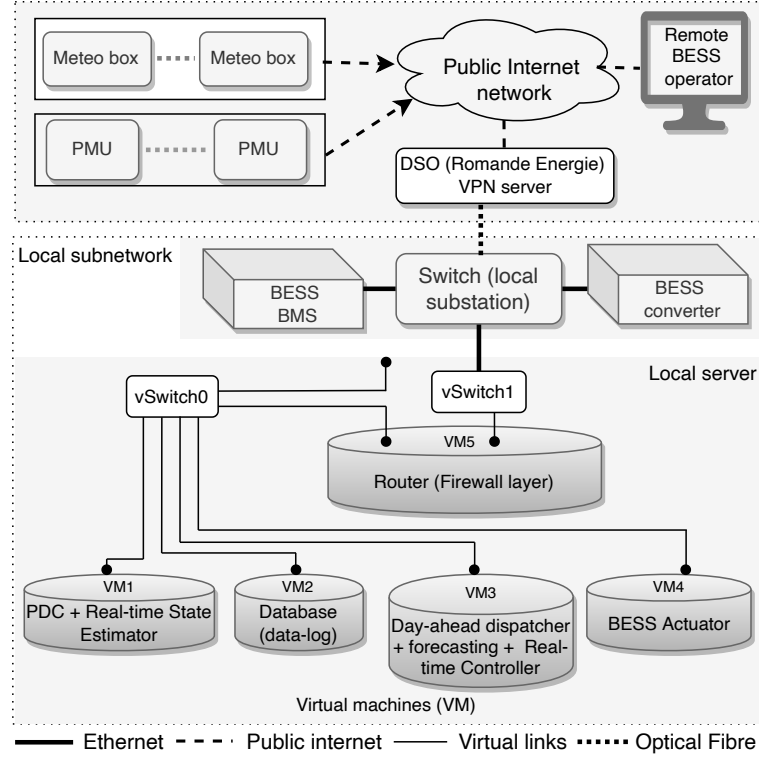


Figure 3.8: IT communication infrastructure for the experimental setup (vSwitch refer to virtual switches).

converter), and the local server. The PMUs and the meteoboxes use public telecom networks (4G), whereas the the BESS BMSs and converters use Ethernet cables. As shown in Fig. 3.8, all the elements are connected to the local substation switch that is physically connected to a DSO control centre by the DSO-owned optical-fibre network. The BESS operator connects to the server, remotely through a secure VPN client provided by the DSO control centre.

**Dataflow:** Fig. 3.9 shows the sequence of the operations and communication flow of the day-ahead and real-time stages. In the day-ahead scheduler (first step), the dispatch plan is computed and stored in the database. The input to the day-ahead stage are the forecast scenarios of the load and generation of different nodes (Sec. 3.3.1) and the estimated state of the BESS. The day-ahead stage is run once a day at 23:30 local time. The real-time stage (second step onwards in Fig. 3.9) shows the steps during real-time operations. In the beginning of 5-minutes time interval, the energy budget is computed by the upper layer MPC based on latest intraday forecasts and current SOC. Then, the lower layer MPC loops every 30 seconds to compute BESS active and reactive setpoints based on short-term forecasts and BESS SOC. This cycle is repeated till 23:59:30 local time.



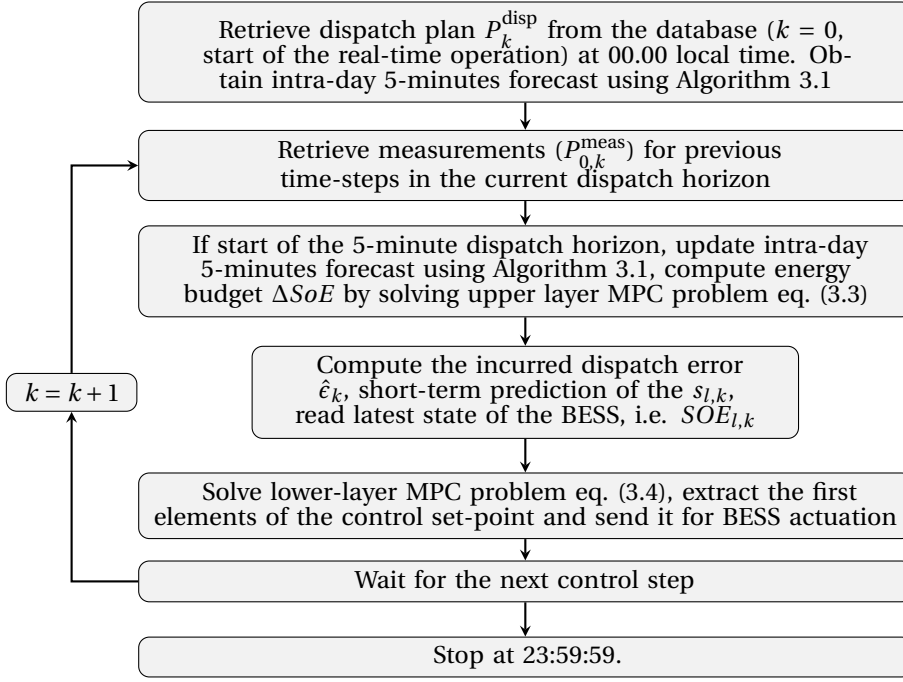


Figure 3.9: Flow-chart showing real-time operation during 24 hours.

### 3.5.2 Experimental Results

This section presents the experimental results obtained by dispatching the MV grid described in Sec. 3.5.1. First, we show results for two typical days representing different characteristics in terms of power injection patterns. The first day is characterized by net imports into the grid, whereas on the second day, the grid exports net power during the middle of the day, thanks to generations from hydro and PV plants. Then, we show control performance for a week-long experiment. The control performance of the proposed two-layer MPC scheme is compared against other two cases: (i) **Without control**, where no compensation from BESS is performed, and (ii) a **Single-layer MPC**, solving lower-layer MPC problem (eq. 3.4) but without SOE budget from upper layer MPC. Since the experiments were performed with the two-layer MPC, and the same experimental conditions can not be reproduced, we perform numerical simulations with single-layer MPC with same conditions as the day of operation for this comparison.

#### Day 1

It corresponds to a clear-sky and weekday, where the demand is relatively higher than the net generations. The main source of uncertainty is the demand. The experimental results are described below.

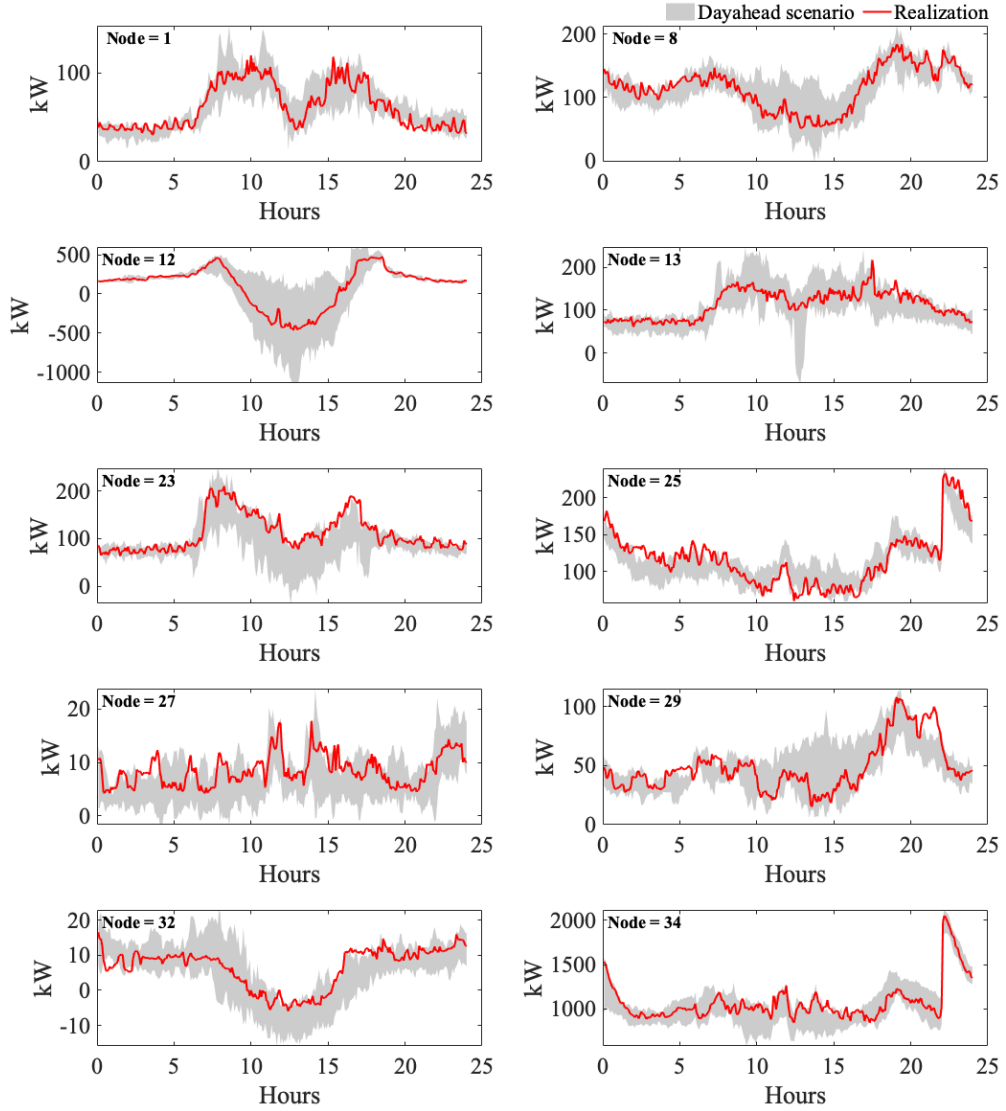


Figure 3.10: Predicted day-ahead scenario set for day 1 (01-Mar-2022).

**Day-ahead Operation:** starts at 23:30 local time the day before. It computes the dispatch plan based on predicted day-ahead scenarios; the number of scenarios,  $N_{sc} = 20$  is used in the following analysis. We show the predicted day-ahead scenarios<sup>20</sup> (in gray area) and the corresponding realization (in red lineplot) in Fig. 3.10. The scenarios are obtained using the forecasting algorithm in Algorithm 2.1; we show the 5-95 % confidence intervals plots for the day-ahead scenarios. As it can be observed, the realization shown in red color plot lies within the day-ahead scenario set for most of the day. The resulting day-ahead scenarios (lineplots in different colors) at the GCP<sup>21</sup> is shown in Fig. 3.11a. The computed dispatch plan is shown

<sup>20</sup>For the sake of brevity, the day-ahead scenarios for all the nodes of the Aigle grid are not shown. We show the ones with dominant power injections.

<sup>21</sup>The day ahead scenarios at the GCP is a by-product of the day-ahead scenarios at all the nodes accounting for the grid losses.

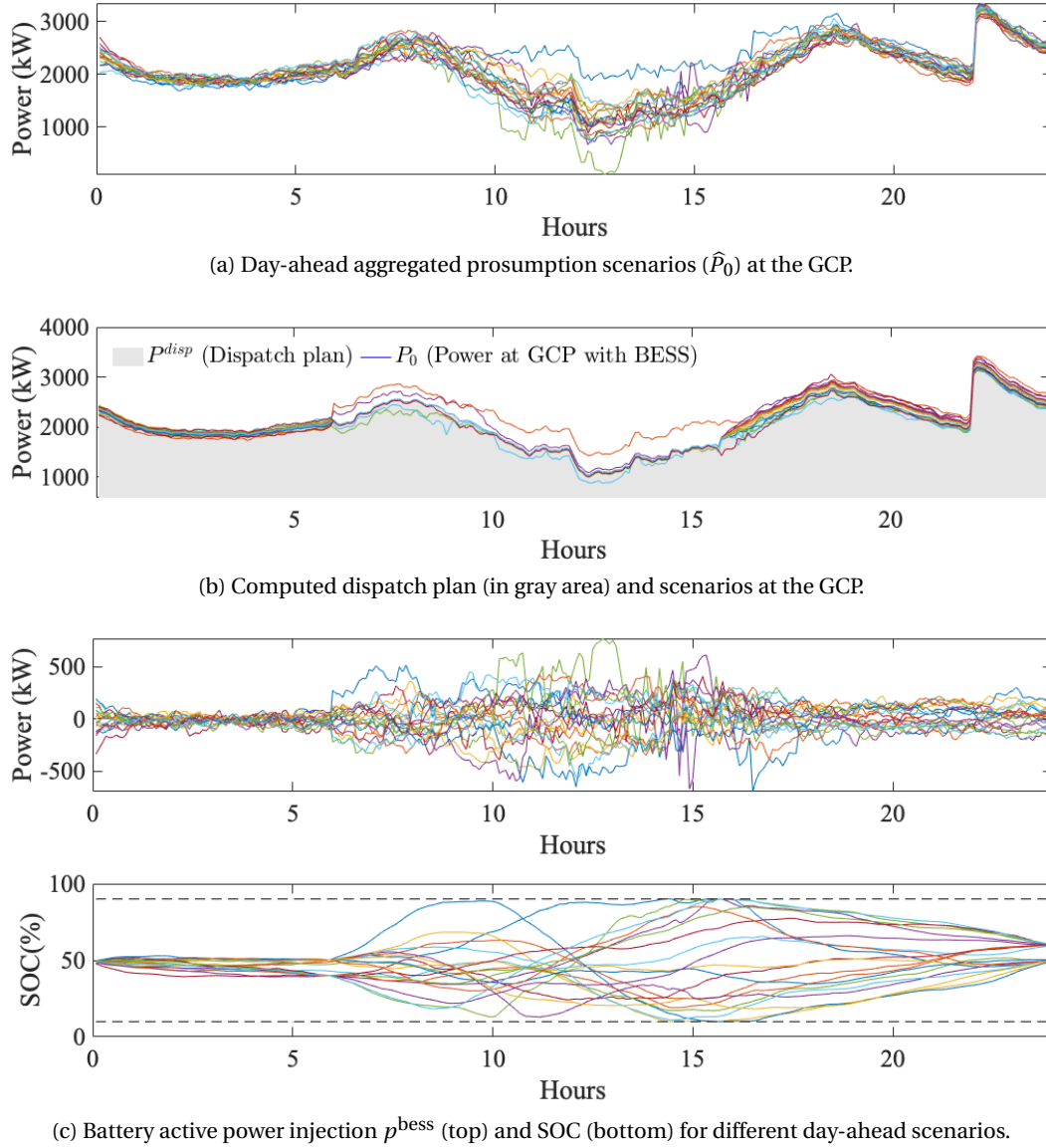
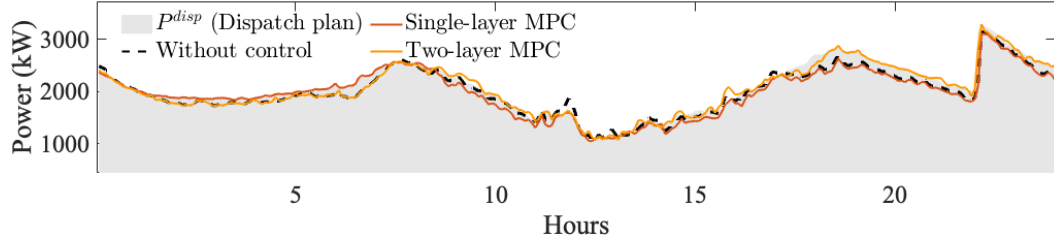


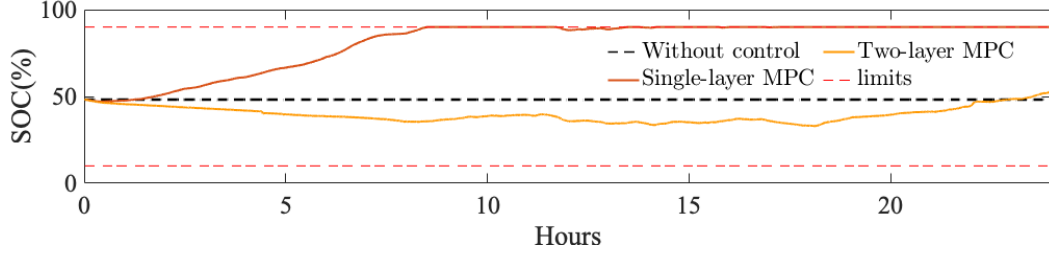
Figure 3.11: (a-c) Dispatch plan computation for day 1 (01-Mar.-2022). Each line-plot in different color represents a different day-ahead scenario.

in Fig. 3.11b along with the power at the GCP with contribution from the BESS. As it can be observed, the dispatch plan still have some uncovered error because of the insufficient size of the BESS. The SOC plot shown in the Fig. 3.11c shows that BESS is reaching its saturation limits with many scenarios. The initial SOC is 50 % which is also the SOC of the battery before the start of the real-time operation.

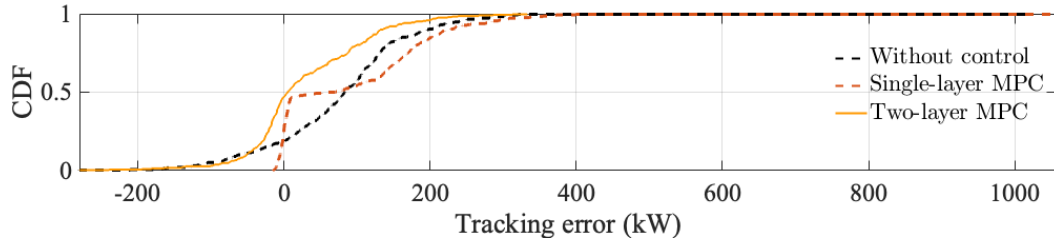
**Real-time Operation:** starts at 00:00 hrs. Fig 3.12a shows the dispatch plan (in gray area), power at the GCP for different control schemes. Fig. 3.12b shows the SOC evolution with different control schemes. Fig 3.12c shows the plot of tracking error cumulative distribution



(a) GCP power tracking the dispatch plan with different control schemes.



(b) SOC of the BESS with different control schemes.



(c) CDF plot of the dispatch tracking error with different control schemes.

Figure 3.12: (a-c) Real-time operation for day 1 (01-Mar.-2022).

function (CDF) as result of different real-time controls. As it can be observed, the single-layer MPC lets the BESS saturate at around 8:00 hrs and it could not be used for the whole day; hence failing the dispatch. In contrast, the two-layer MPC ensures the BESS to never saturate, thanks to the energy budget constraints computed by the upper layer MPC. Also, by looking at the CDF plot of the tracking error in Fig. 3.12c, it is clear that two-layer MPC, on the one hand, achieves better tracking of the dispatch plan with a lower probability of high tracking error. On the other hand, it keeps the BESS SOC within a flexible range. Table 3.2 reports the maximum-absolute-error (MAE), net absolute-energy-error (AEE), root-mean-square-error (RMSE) of the dispatch error using different controls concluding that the control based on two-layer MPC performs the best. The two-layer MPC outperforms the single-layer MPC in RMSE by 40%, MAE by 67% and AEE by 35% respectively.

## Day 2

It corresponds to a day with higher variation in the power injection due to higher uncertainty with next export due to high PV and hydro generations. The results are below.

Table 3.2: Tracking error statistics with different control schemes.

MPC	Day 1			Day 2		
	RMSE (kW)	AEE (kWh)	MAE (kW)	RMSE (kW)	AEE (kWh)	MAE (kW)
None	137	2.5e3	1e3	176	3.2e3	896
Single-layer	148	2.3e3	1e3	124	1.5e3	932
Two-layer	89	1.5e3	332	85	1.5e3	322

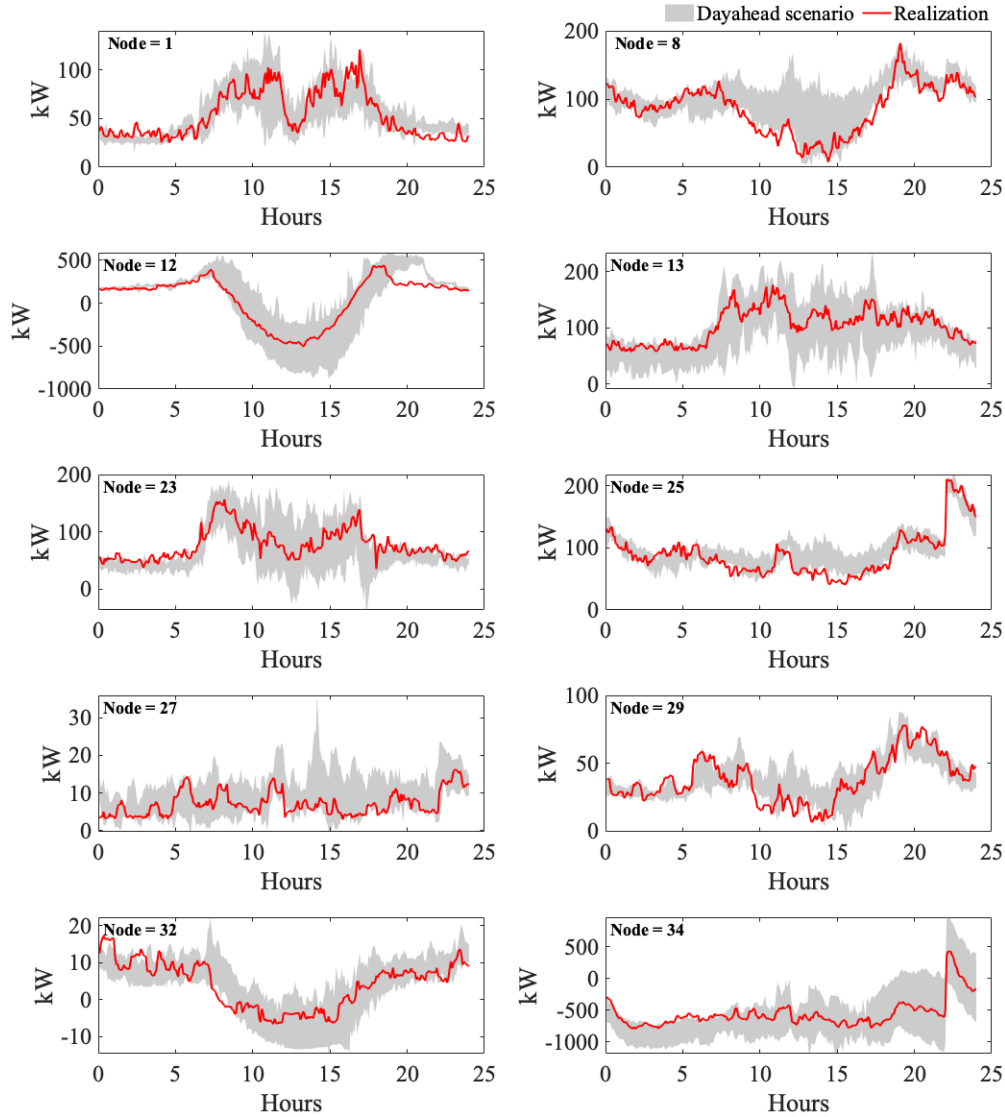


Figure 3.13: Predicted day-ahead scenario set for day 2 (22-Mar-2022).

**Day-ahead Operation:** Fig. 3.13 shows day-ahead forecast for day 2. Compared to day 1, node 34 is producing due to generation from hydropower plants at node 34 and exhibit higher uncertainty. Fig 3.14a shows the day ahead scenarios for day 2. As it can be seen,

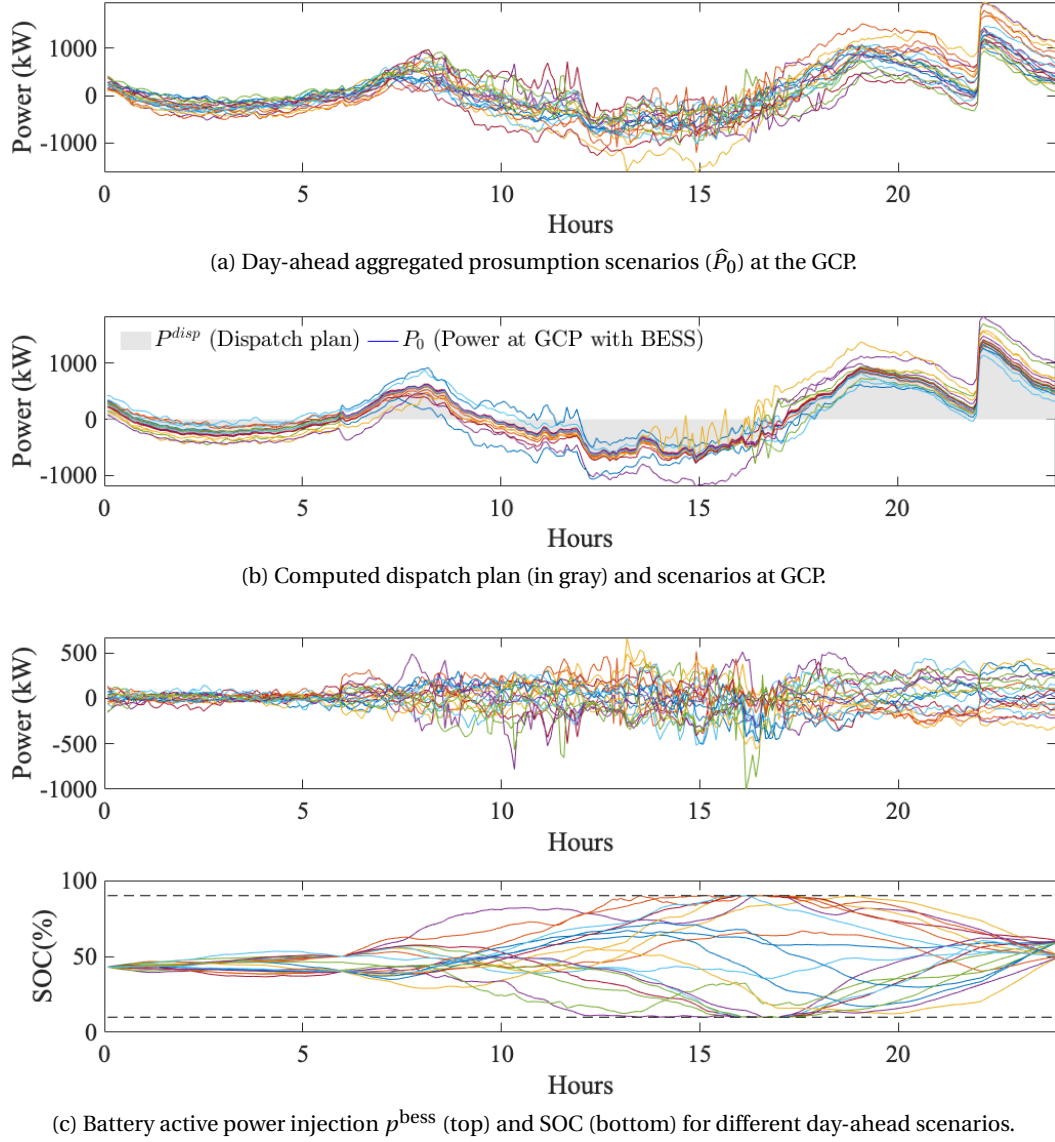


Figure 3.14: (a-c) Dispatch plan computation for day 2 (22-Mar.-2022). Each line-plot in different color represents a different day-ahead scenario.

this day exhibit more variations in power injections resulting in higher uncertainty in the day-ahead scenarios of the GCP. Also, during the middle of the day, the net power at the GCP is negative (producing) as hydro power plants at node 34 are generating. Fig 3.14b shows the computed dispatch plan and compressed scenarios of active powers at the GCP, thanks to the compensations from the BESS. However, the BESS capacity is not enough to cover the uncertainty of all the day-ahead scenarios resulting in spread of the optimized power at the GCP even with contribution of the BESS. It is also evident from the BESS SOC plot in Fig. 3.14c that the it saturates for several day-ahead scenarios. Comparing the dispatch plans for the day 1 and day 2, the tracking is better during the day 1 (spread of the power at the GCP in

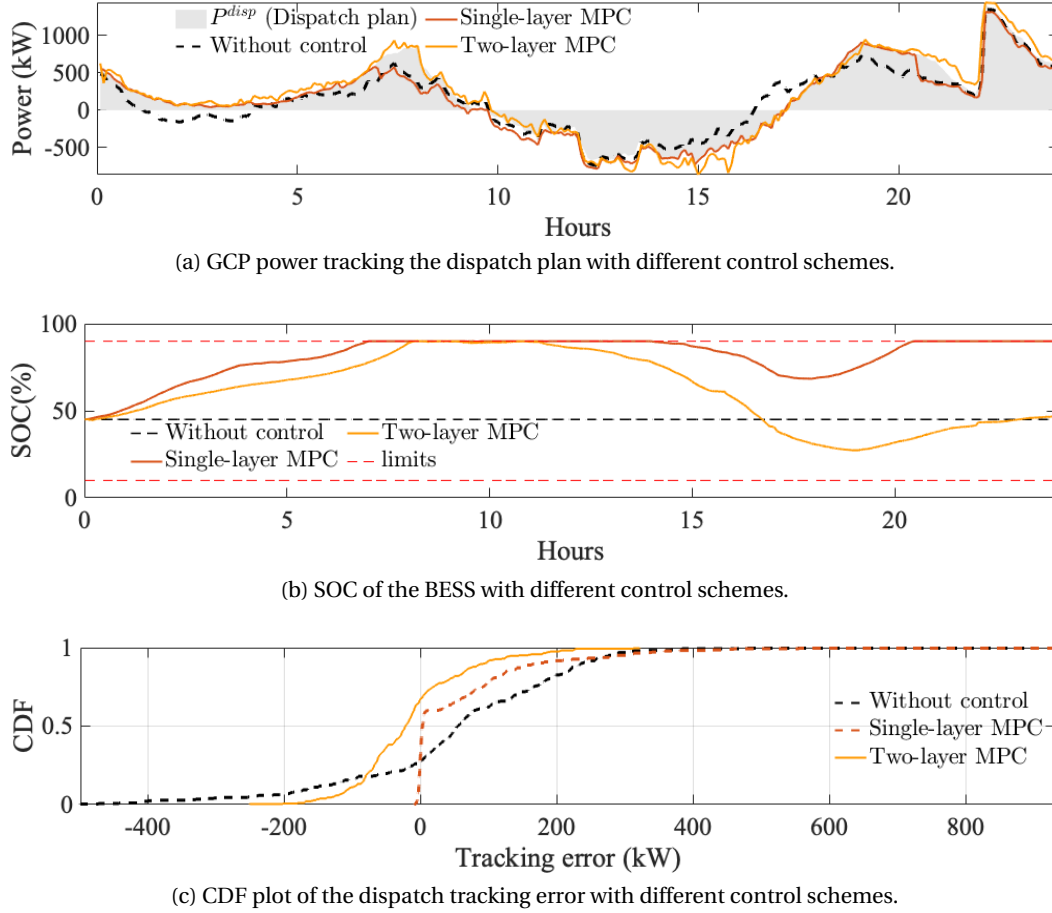


Figure 3.15: (a-c) Real-time operation for day 2 (22-Mar.-2022).

Fig. 3.14b is much larger than Fig. 3.11b). This is due to larger uncertainty in the predicted day ahead forecasts for the injection at the node 34 in Fig. 3.13.

**Real-time Operation:** Fig 3.15a shows the tracked dispatch plan using different control schemes. Again, we show the BESS SOC, and the CDF of the dispatch tracking errors in Fig. 3.15b and 3.15c respectively. As observed, the two-layer MPC achieves fine-tracking of the dispatch plan compared to the other two cases. Moreover, the two-layer MPC restores the BESS SOC to 47% at the end of the day's operation, whereas the single-layer MPC lets the BESS to saturate to the upper limit (90%) from 7.00 hrs to 14.00 hrs and again from 20.00 hrs to 24.00 hrs; hence failing the dispatch during this period. The CDF plot in Fig. 3.15c shows that two-layer MPC achieves lower tracking error with high probability. The metrics reported in Table 3.2 show that the two-layer MPC scores better on RMSE and MAE by 31% and 65% respectively than the single-layer MPC, however similar AEE.

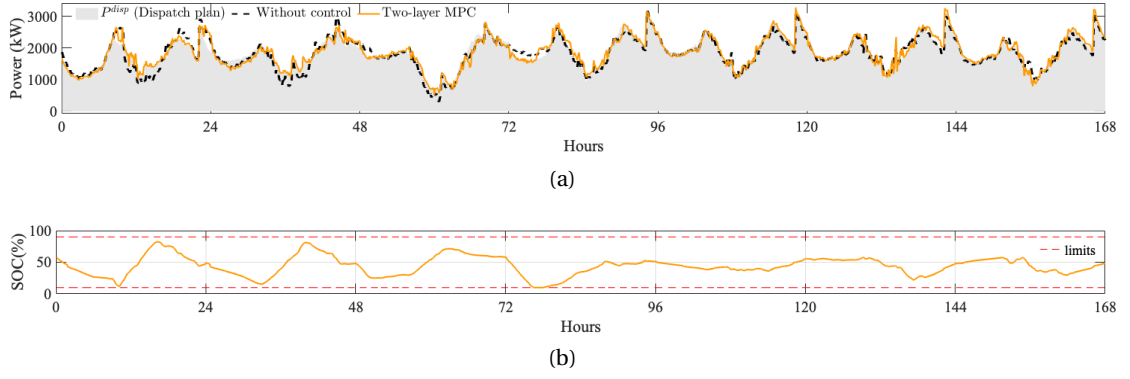


Figure 3.16: Dispatch tracking over a week (25-Feb.-2022, Friday to 03-Mar.-2022, Thursday): (a) Power at the GCP and dispatch plan, (b) SOC evolution.

#### Week-long Experiment

To demonstrate the effectiveness of the dispatching scheme, we run uninterrupted control of the BESS for a whole week. Fig 3.16a shows the dispatch plan, measured GCP power with and without two-layer MPC scheme. In Fig. 3.16b, we show the SOC evolution during the week. It can be observed that the power at the GCP follows the dispatch plan and keeps the BESS SOC within comfortable SOC so that dispatching is continued the next day.

#### 3.5.3 Further Analysis

##### Validation of the Grid Model

We compare the modelled grid quantities by AR-OPF with the measurements to validate that the grid constraints are accounted correctly with small error. Fig. 3.17 shows comparison in form of CDFs for the difference between (modelled vs state estimated) the voltage, current and losses. The CDF plots on voltages and currents correspond to a particular bus/line. It can be seen that the modeled voltages and currents achieve high accuracy. The error on the voltage and current modelling are less than 0.01 pu and on the losses less than 0.2 kW for 99 % of the time. This comparison validates that the OPF model used to model the grid constraints in real-time MPC are realistic.

Table 3.3: Computation time.

Control layers	Min (sec.)	Mean (sec.)	Max(sec.)
Upper-layer MPC	4	9.9	19
Lower-layer MPC	0.15	0.2	0.4



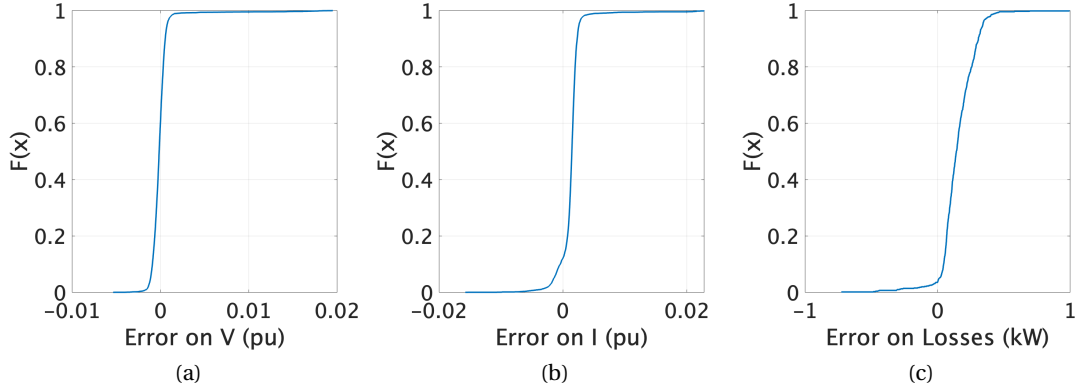


Figure 3.17: Validation of OPF model for real-time operation with PMU measurements: (a-c) shows CDF of the incurred error on the modeling of voltage (in pu), current (in pu) and total grid losses (in kW).

#### Computational Performance

As stated earlier, the RT-MPC stage is solved on VM3 (Fig. 3.8). VM3 is configured with the Windows 10 operating system with specification 64-bit, 8 GB memory and 3.3 GHz CPU. It uses the Mosek [94] solver to solve the real-time optimization problem. Using this setup, in Table 3.3, we list the minimum, mean, and maximum computation times for solving upper- and lower-layer MPCs. As it can be seen, the computation time is within 30 seconds, the time deadline of real-time actuation.

We also perform a sensitivity analysis of the RT-MPC computation time with multiple distributed BESS units. It provides insight into how the computational performance scales with an increasing number of controllable variables. For this analysis, the BESS energy capacities are split equally at different locations, and power capacity remains the same (as in the experimental setup). The additional BESS units are placed at nodes 1, 2, 5, 7, 9, 10, and 20, respectively. The MPC was simulated for real-time operation of day 2. Table 3.4 reports the corresponding computation times for both the upper and lower-layer MPCs. It shows the minimum, average, and maximum time. As it can be observed, the computation time of the upper- and lower-layer MPC scales linearly with an increase in the number of BESS. When the computation time exceeds the actuation time-deadline of 30 seconds, the latter can be increased to accommodate more controllable units (or adopt a more computational-performing hardware).

#### Statistics on PDC Reporting Latency and Packet Losses

To verify the reliability of the communication infrastructure (mainly related to public internet networks), we look at the time latency and packet losses by each PMU. We present statistics on the delays and packet losses per PMUs. Boxplots show the latency of each PMU in Fig. 3.18,

Table 3.4: MPC Computation time with increasing number of Controllable BESS.

BESS units		Control layers	Min	Mean	Max
#	MWh per unit	MPC	Seconds		
2	1.25	Upper	4.3	11.74	22
		Lower	0.16	0.24	0.50
4	0.625	Upper	4.7	13.91	25.6
		Lower	0.18	0.29	0.63
8	0.3125	Upper	5	16.5	29.7
		Lower	0.20	0.34	0.77

and the packet-data loss is shown in Table 3.5. The statistics are shown for the experiments conducted on day 2 (22-Mar-2022). As observed, the delays are in tens of milliseconds which is significantly below the control actuation time deadline. Also, the packet losses are below 0.02 % (on average) and 1.67 % (with 99 % probability). The reported statistics coincide with those reported in [76]. Therefore, we can rely on the developed communication infrastructure for the experimental validation of the proposed RT-MPC.

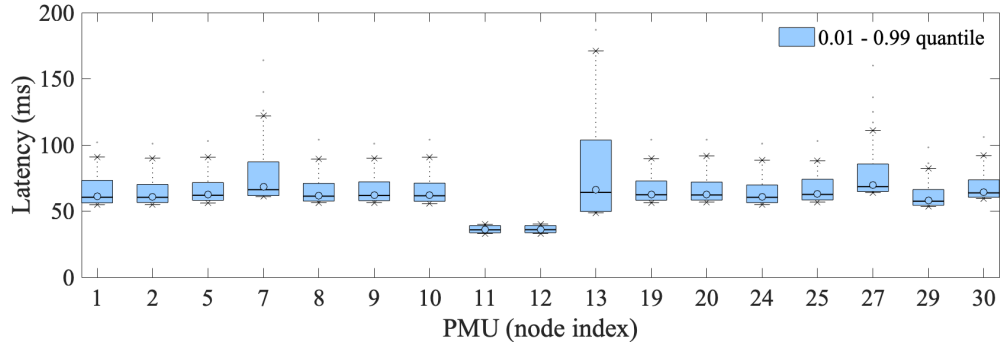


Figure 3.18: PDC reporting latency comprising of PMU latency, network latency and PDC latency.

Table 3.5: Data packet-losses.

PMU ID	1	2	5	7	8	9
Mean (%)	0.038	0.009	0.007	0	0.006	0.007
99 %	1.67	0	0	0	0	0
PMU ID	10	11	12	13	19	20
Mean (%)	0	0	0	0.001	0.021	0.003
99.99 %	0	0	0	0	1.67	0
PMU ID	24	25	27	29	30	—
Mean (%)	0.006	0.019	0.001	0.007	0.001	—
99.99 %	0	1.67	0	0	0	—

### 3.6 Discussion

This Chapter provided a solution to tackle the issue of BESS SOC saturation in dispatching ADNs, where a day-ahead dispatch plan is tracked with the help of a controllable BESS during the day's operation. The solution relies on a two-layer real-time MPC scheme, where a slow and farsighted MPC imposed an energy budget, every 5-minutes based on latest whole day forecasts, on the real-time fast MPC running every 30-seconds. The two-layer scheme ensures that the BESS SOC is not saturated during the day and restored to a comfortable SOC for the next day's dispatch operation. This is useful for reliable and continuous dispatching of ADNs by BESS. The MPCs are fed by data-driven forecasts of the demand and generations. The real-time control scheme accounted for the grid constraints using a convex AC-OPF model. The optimization problem is formulated as convex, achieving optimality and enhanced level tractability and efficient to solve.

The control framework is validated on a real MV grid located in Aigle Switzerland hosting 3.2 MWp of photovoltaic generation, 3.4 MVA hydro plant and 2.8 MW of base demand. The MV grid is connected with 1.5 MVA/2.5 MWh BESS that is controlled by the real-time controller, and monitored by 17 PMUs. The experimental results performed over a week (including clear-sky, cloudy, weekday and weekend days) show that the proposed two-layer MPC scheme always keeps the BESS SOC within flexible region as well as achieves better tracking compared to myopic single-layer MPC scheme. The proposed two-layer MPC scheme reduces the absolute energy tracking error and RMSE by half compared to the myopic single-layer MPC scheme. We also validated the grid model by comparing the modeled vs estimated states, concluding the error below 0.01 per unit in the nodal voltages/lines currents and below 0.2 kW in the grid losses.

This Part of the thesis (Chapters 2 and 3) developed control frameworks that assumed that grid models, i.e., topology and electrical line parameters, are known and referred to as model-based control schemes. However, the grid models might be unavailable, partially missing, or often incorrect in real life. Part two (Chapters 4 and 5) focuses on developing model-less or measurement-based control schemes where the network models are inferred from the measurements and then used in the control frameworks.

# **Model-less and Measurement-based Control of Active Distribution Networks**

## **Part II**



# Prelude

In Part I, we proposed control schemes that rely on the availability of models of the distribution network. They assume that the grid models (i.e., topology and electrical line parameters) are known, hence they are referred to as *model-based control schemes*. However, in real-life, the ADN models might be unavailable, partially missing, or often incorrect.

In this context, the second part of the thesis develops *model-less* or *measurement-based control schemes* where the network models are inferred from measurements and then used by the control framework.

In *Chapter 4*, we present two different measurement-based approaches for the estimation of the admittance matrix and power-flow sensitivity coefficients. In *Chapter 5*, the estimated models from the Chapter 4 are used to obtain measurement-based control schemes. The model-less control is demonstrated for voltage regulation by controlling the distributed energy resources in real-time. The proposed model-less/measurement-based control is validated on an actual microgrid hosted at the EPFL Distributed Electrical Systems Laboratory.



## 4 Data-driven Estimation of Compound Admittance Matrix and Power-Flow Sensitivity Coefficients

*The control schemes illustrated in the previous chapters rely on the true models of the grid. However, in real-life these models might not be easily available, often missing, or partially incorrect. To tackle this challenge, the Chapter presents methods to estimate these models. In particular, it presents schemes to estimate the power-flow sensitivity coefficients which can be used for formulating the linearised grid-aware control as in Chapter 2. The Chapter presents two estimation approaches. The first one estimates the compound admittance matrix of the ADN, which is then used to compute the power-flow sensitivity coefficients. It is referred to as the indirect estimation approach. For the estimation of the admittance matrix, we propose a linear estimator that uses measurements of the voltage and current phasors. It also proposes a pre-processing strategy to improve the estimation quality of regression-based methods such as least squares (LS) and total least squares (TLS). The uncertainty on the estimated admittance matrix and measurement noise on the grid states are propagated to the computed sensitivity coefficients by a proposed analytical error propagation tool. Second, a direct estimation of the sensitivity coefficients is proposed. It does a recursive estimation of the sensitivity coefficients using the measurements of the nodal power injections and grid states magnitudes. The direct estimation problem is solved in two stages: first a least square (LS)-based estimator obtains a rough estimate of the sensitivity coefficients, then a recursive LS (RLS) is used periodically to refine those LS estimates. Finally, both approaches are numerically validated for different CIGRE and IEEE networks and their performances compared.*

*This Chapter includes results of publication [95, 96, 97].*

### 4.1 Problem Statement

Let us consider a generic power distribution network equipped with measurement devices capable of providing high throughput measurements of nodal voltage and current phasors (e.g., phasor measurement units – PMUs). The objective is to estimate the grid's sensitivity coefficients concerning nodal voltages, lines currents and grid losses. The voltage magnitude



## Chapter 4. Data-driven Estimation of Compound Admittance Matrix and Power-Flow Sensitivity Coefficients

sensitivity coefficient<sup>22</sup> of the  $i$ -th node with respect to absorbed/injected power at node  $j$  is defined as

$$K_{ij}^p = \frac{\partial |v_i|}{\partial p_j}; K_{ij}^q = \frac{\partial |v_i|}{\partial q_j} \quad (4.1)$$

where,  $K_{ij}^p, K_{ij}^q$  are the sensitivity coefficients of the  $i$ -th nodal voltage magnitudes ( $|v_i|$ ) with respect to the active and reactive power injections  $p_j, q_j$  of node  $j$ .

As said, in this Chapter, we propose and develop two different methods to estimate the grid's sensitivity coefficients. Although the developed methods are generic for the estimation of all types of sensitivity coefficients (such as lines current magnitudes, grid losses), for the sake of brevity we demonstrate them only for the voltage sensitivity coefficients. The proposed method workflows are described below.

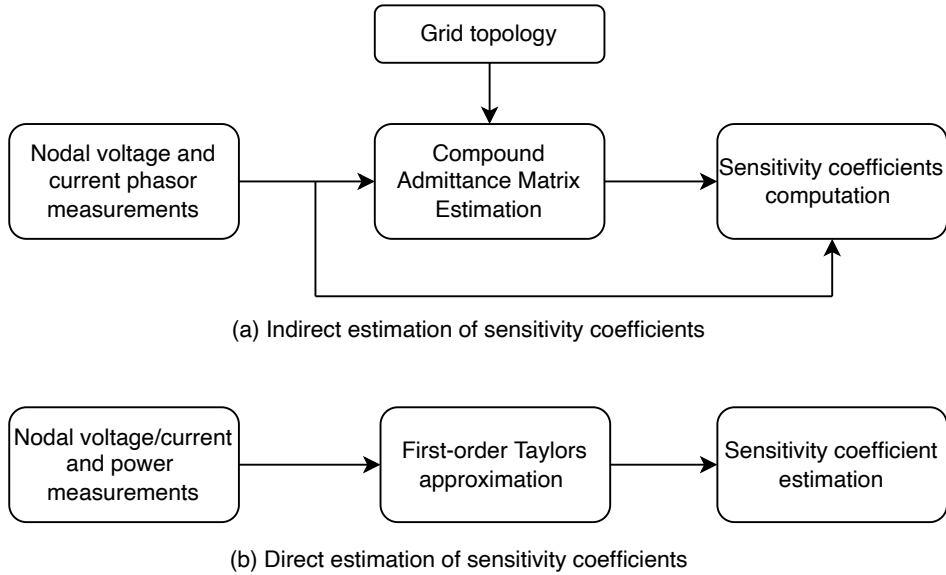


Figure 4.1: Schematic flow diagram for indirect and direct estimation of the sensitivity coefficients.

- **Indirect Method:** first it estimates the compound admittance matrix ( $\mathbf{Y}$ ) of the grid using nodal voltages and lines' current phasor measurements. Then the estimated  $\mathbf{Y}$  and the grid state measurements are used to compute the grid's sensitivity coefficients. The sensitivity coefficients are estimated by existing methods in the literature, for example [40]. The data-flow is shown in Fig. 4.1(a). Furthermore, to assess the uncertainty of the computed sensitivity coefficients, the Section presents an analytical error propagation tool that assess via uncertainty propagation the estimation error of  $\mathbf{Y}$  and measurement noise of grid states onto the sensitivity coefficients. Since the quality of the estimated

<sup>22</sup>Other sensitivity coefficients like those of branches currents magnitudes and grid losses can be obtained similarly.

coefficients directly depends on the estimation quality of  $\mathbf{Y}$ , we also develop a tool to improve the estimation of the  $\mathbf{Y}$  matrix. We propose a linear estimation model that uses phasor measurements of nodal voltages, injection currents, and branch currents. The estimation scheme is generic and applicable to any unbalanced three-phase network with shunt components. It also illustrates a pre-processing strategy to the PMU's raw measurements, which consists of grouping the raw measurements in clusters and using the averaged measurements from each cluster for  $\mathbf{Y}$  estimation. The proposed pre-processing step reduces the noise level and discards similar measurements from each cluster, ultimately improving the estimation quality of regression-based estimation methods such as least squares (LS) and total least squares (TLS).

- **Direct Method:** this method estimates the grid's sensitivity coefficients using nodal measurements of the grid's states (e.g., nodal voltage magnitudes) and active and reactive power injections. It relies on a first-order Taylors' approximation, allowing the deviation of the nodal voltages to be expressed as a linear function of the deviation of nodal power injections. The sensitivity coefficients (slope of the linear approximation between the grid states and nodal injected powers) are obtained by solving a regression-based estimation problem. The data flow is shown in Fig. 4.1(b).

The above two methods are different in terms of the required input data and estimates. The indirect method requires nodal voltage and line currents phasor measurements, whereas the direct method requires nodal voltage and power measurements. In addition to the sensitivity coefficients, the indirect method also estimates the admittance matrix. Since the admittance matrix does not change often, this estimation step could be performed once in a while. The estimated admittance from the indirect method could also be used to formulate relaxed OPF schemes (such as the AR-OPF). In contrast, the sensitivity coefficient from the direct method is only limited to the use of the linearized power flow model.

## 4.2 State-of-the-Art

Several data-driven approaches have been proposed in the literature for measurement-based estimation of the sensitivity coefficients. They consist of two main groups based on methods proposed for the sensitivity coefficients estimation: direct and indirect estimation.

### Direct Estimation of Sensitivity Coefficients

As defined, the direct methods refer to schemes which estimate the sensitivity coefficients directly from the nodal power injections and grid's measurements. These schemes rely on the assumption that the deviation of grid states can be approximated as a linear function of nodal power injection deviations using a first order Taylors' Approximation. The works in [98, 99] used weighted least squares (WLS) for the estimation of the voltage sensitivity coefficients. The work in [98] introduced a pre-filtering strategy to improve the conditionality of the estimation

## Chapter 4. Data-driven Estimation of Compound Admittance Matrix and Power-Flow Sensitivity Coefficients

---

problem. It also proposed to use a covariance matrix accounting for the correlation between the subsequent time steps. However, these methods do not work well in the case of collinear measurements (nodal injections with similar patterns at different nodes) as shown in [100]. The work in [101, 102] used ridge-regression and noise-assisted least-squares schemes to counter the collinearity problem. It added a constant term (also called ridge regression) in the LS gain matrix, equivalent to adding white Gaussian noise in the measurements. However, the method in [101, 102] suffers from high estimation biases in case of high measurement noise coming from real measuring instruments (whose noise are not necessarily white). The work in [103] proposed a two-stage estimation scheme where rough estimates of the coefficients are corrected by Recursive Least Squares (RLS) using recent measurements. However, the work did not analyse different approaches to solve the known covariance windup problem.

In this context, in this Chapter, we develop a two-stage estimation scheme where the first stage (offline LS) obtains rough estimates of the sensitivity coefficients. Then, in the second stage (online RLS), the sensitivity coefficients are updated recursively using recent measurements. The offline estimates from the first stage are used as initialization in the online estimation stage. Also, we evaluate different strategies to solve the covariance windup problem of the RLS scheme.

### Indirect Estimation of Sensitivity Coefficients via Compound Admittance Matrix

The other approach is estimating the line parameters of the grid: first the compound admittance matrix ( $\mathbf{Y}$ ) is estimated. Then an analytical approach (e.g., [40]) is used to compute the sensitivity coefficients. This method is referred to as **indirect estimation**, as the sensitivity coefficients are not estimated directly using the measurements, instead using an already estimated quantity ( $\mathbf{Y}$ ). This scheme involves propagating the uncertainty of the estimated  $\mathbf{Y}$  to the sensitivity coefficients by using the principle of error propagation.

The *admittance estimation problem* has been addressed by several works in the literature, and it can be broadly clustered into three categories focusing on different aspects of the estimation process: (i) assumptions on the measurement noise model, (ii) solution techniques used for the parameter estimation and (iii) approximations in the modelling of the grids. Estimating the grid parameters with PMU measurements was initially proposed in [104, 105]. The works in [106, 107, 108, 109, 110] proposed methods for line parameter estimation in transmission networks. The work in [111] formulated the problem to identify the admittance matrix directly from the synchronised measurements. However, it did not account for realistic noise model, and the proposed model is sensitive with respect to the measurement noise. The work in [112] formulated the problem for joint-estimation of line parameters and topology using a weighted total least squares (WTLS) method. The formulation is non-convex and is solved iteratively. The work assumes an unrealistic noise model by adding an offset noise from historical data lacking physical significance. The works in [113, 114, 115] accounted for the systematic error of the instrument transformers (ITs) in the parameter estimation problem and used realistic measurement noise in polar coordinates. The work in [116] considered the

noise in polar coordinates for three-phase systems and estimated an equivalent error model for positive sequence components. The use of LS is proposed for estimating the parameters in [106, 107, 108, 109, 111]. However, as shown in [117], it does not perform well when the measurements are corrupted with realistic measurement noise (in polar coordinates) as LS ignores noise in some variables. WLS-based parameter estimation was used in [113]. Some works have proposed using error-in-variable (EIV) methods, such as the TLS [112]. The TLS solution is equivalent to the maximum likelihood estimation (MLE) when the noise on the input and output variables is approximated by white Gaussian distribution, and is i.i.d. (independent and identically distributed). If these conditions are not met, the estimations can be worse than LS, even if the TLS formulation is statistically more comprehensive than the LS [117] with respect to appropriate noise models. It happens because TLS tries to estimate not only the estimation variables but also the true and unobserved values of the measurements. Also, when TLS is fed with a large number of measurements, its performance deteriorates due to the large dimension of measurement being de-noised. However, it is widely known that estimation methods achieve better performance when fed with inputs characterised by low measurement noise. For example, the work in [109] proposed a moving window averaging on the raw data for improving TLS-based line parameter estimation by reducing the noise level. The method was proposed for the estimation of a transposed and balanced line and used measurements of nodal powers along with currents and voltages. Although this work proposed an averaging strategy of raw PMU measurements, it did not fully use the fact that this step preserves the mathematical structure of the original formulation and improves the estimation performance. Furthermore, in most existing works, it is often assumed that the power networks are balanced and transposed three-phase systems (e.g., [106, 107, 108, 109, 110, 111, 112, 113]) with negligible shunt components. These assumptions do not hold at the same time for real distribution grids. For example, low voltage distribution networks are often untransposed [5, 118] and are characterised by negligible shunt parameters, whereas medium voltage systems have non-negligible shunt parameters [5] (especially in the presence of long coaxial cables) and are relatively transposed systems. The works in [119, 120, 121, 122] considered parameter estimation for three-phase unbalanced and untransposed systems, but their analysis is limited to the estimation of single line parameters instead of the whole compound admittance matrix and neglect shunt admittances. Estimating the whole compound admittance matrix is a complex problem as it requires to estimate all the branch parameters having different characteristics (e.g., short and long lines) within the network. Also these methods rely on measurements of line currents instead of injection currents which require twice the number of measuring instruments.

In this context, to improve the estimation of the grid's admittance matrix, this Chapter proposes:

1. A pre-processing strategy on the raw PMU measurements for improving the estimation performance of LS and TLS. The pre-processing consists of two main steps: first, the raw measurements are grouped into different clusters and, then, the averaged measurements

## Chapter 4. Data-driven Estimation of Compound Admittance Matrix and Power-Flow Sensitivity Coefficients

---

from each cluster are used for the admittance matrix estimation. This process reduces the noise level of measurements, ultimately improving the estimation performance of LS and TLS.

2. It proposes a PMU-based linear estimation model for estimating the whole admittance matrix for untransposed three-phase distribution networks (i.e. the so-called compound admittance matrix) taking into account both branch and shunt admittance matrices of the grid components (i.e. with no approximation on the grid model).

Compared to [106, 107, 108, 109, 115, 119, 120, 121, 122], the proposed method has the following features: (a) it estimates the whole compound admittance matrix including the presence of shunt admittances, (b) it uses a pre-processing strategy for reducing the noise level ultimately improving the estimation performance, and (c) it works with either injection or branch/line current measurements, the former requires half the number of measurements. Compared to [111, 112, 113], the proposed method can be applied to untransposed three-phase grids accounting for the presence of shunt parameters. It is worth noting that this work does not assume knowing the nominal values of the branch and shunt parameters compared to [113, 114].

Finally, the estimated  $\mathbf{Y}$  is used to compute the sensitivity coefficients. So, to calculate the uncertainty on the computed sensitivity coefficients through  $\mathbf{Y}$ , the Chapter also illustrates an analytical tool following the principle of error propagation.

The estimation models adopt realistic noise in polar coordinates, reflecting the accuracy class of ITs suitably projected onto the rectangular coordinates. The method is validated by performing numerical experiments on different CIGRE and IEEE benchmark networks for admittance estimation. Furthermore, we perform sensitivity analysis on the estimation performance with different noise-levels on the measurement data on the pre-processing strategy (cluster type and size) and availability of branch or injection currents measurements.

In the following, first we present the *indirect approach* to estimate the sensitivity coefficients which involves estimation of the admittance matrix. Then, the *direct method* to estimate the sensitivity coefficient is presented. Finally, two methods are compared.

### 4.3 Indirect Estimation of Sensitivity Coefficients via Estimation of Compound Admittance Matrix

In the following, first, we present a scheme for estimating the compound admittance matrix. Then, we show how the estimated admittance matrix is used to estimate the power-flow sensitivity coefficients indirectly. Finally, we present a technique to propagate the uncertainty of the estimated admittance matrix and grid state measurements to the power-flow sensitivity coefficients.

### 4.3 Indirect Estimation of Sensitivity Coefficients via Estimation of Compound Admittance Matrix

We consider the problem of estimating the parameters of the admittance matrix of a single- and three-phase distribution network (assuming that the topology is known) using a set of synchrophasor measurements that may include phase-to-ground nodal voltages, nodal injection currents and branch currents per phase.

In the following, we describe the poly-phase grid model, which is then used to formulate the parameter estimation problem for a generic transposed and untransposed three-phase system. We use the same nomenclature and hypothesis as in [123].

#### 4.3.1 Polyphase Grid Model

Consider the generic case of a ground-referenced<sup>23</sup> unbalanced and untransposed<sup>24</sup> polyphase power network with  $\mathcal{G} := \{0\}$  be the ground node, and  $\mathcal{P} := \{1, \dots, |\mathcal{P}|\}$  the phases,  $N_b$  buses and  $N_l$  branches. The polyphase nodes, shunts and branch indices are collected in the sets  $\mathcal{N} := \{1, \dots, N_b\}$ ,  $\mathcal{T} := \mathcal{N} \times \mathcal{G} = \mathcal{N}$  and  $\mathcal{L} := \{1, \dots, N_l\}$  respectively. Figure 4.2 shows the topology of compound electrical parameters of a polyphase electrical circuit of the grid. The polyphase terminals and wires are bundled into a line for the sake of clarity. The compound branch impedance matrices are denoted by  $\mathbf{Z}_l (l \in \mathcal{L})$  and shunt admittance matrices are denoted by  $\mathbf{Y}_t (t \in \mathcal{T})$  respectively.

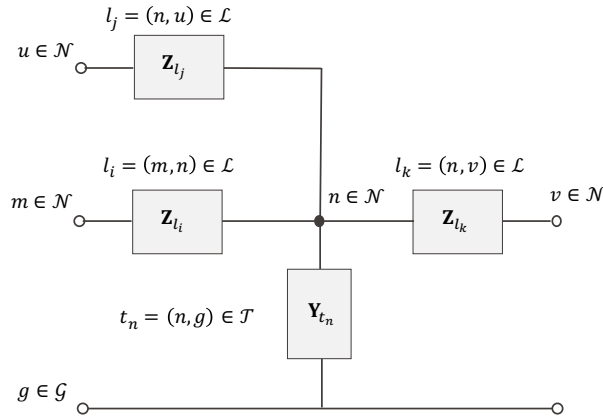


Figure 4.2: Compound electrical parameters of the overall electrical circuit of the grid: compound branch impedance matrices  $\mathbf{Z}_l (l \in \mathcal{L})$  and shunt admittance matrices  $\mathbf{Y}_t (t \in \mathcal{T})$ . The polyphase terminals and wires are bundled into single line for the sake of clarity.

**Hypothesis 4.1** *The grid consists of electrical components which are passive and linear. The coupling between the phases of the same component is significant, they can be represented by polyphase  $\Pi$ -section or T-section equivalent circuits.*

<sup>23</sup>We assume that there exists a reference node i.e., ground, used as a reference to measure the nodal phase-to-ground voltages.

<sup>24</sup>Therefore, branch impedances and shunt admittance matrices are not necessarily circular-symmetric and triplets of three-phase voltages and currents are unsymmetrical (i.e., their phase angle displacements are not equal) and unbalanced (i.e., the sum of phase quantities are not null.).

## Chapter 4. Data-driven Estimation of Compound Admittance Matrix and Power-Flow Sensitivity Coefficients

**Hypothesis 4.2** *The compound branch impedance matrices are symmetric ( $\mathbf{Z}_l = \mathbf{Z}_l^T$ ), invertible ( $\exists \mathbf{Y}_l = \mathbf{Z}_l^{-1}$ ), and lossy ( $\Re\{\mathbf{Z}_l\} \succ 0$ ),  $\forall l \in \mathcal{L}$ . The compound shunt admittance matrix  $\mathbf{Y}_t$  is also symmetric<sup>25</sup> ( $\mathbf{Y}_t = \mathbf{Y}_t^T$ ), invertible ( $\exists \mathbf{Z}_t = \mathbf{Y}_t^{-1}$ ). We assume that the shunts are lossless ( $\Re\{\mathbf{Y}_t\} = 0$ ),  $\forall t \in \mathcal{T}$ .*

Let  $v_{n,p}$  and  $i_{n,p}$  be the phasors of the nodal phase-to-ground voltage and the injected current for the phase  $p \in \mathcal{P}$  of the polyphase node  $n \in \mathcal{N}$ . The quantities defined for a polyphase node  $n \in \mathcal{N}$  as a whole are written as:

$$\mathbf{v}_n := \text{col}_{p \in \mathcal{P}}(v_{n,p}) \quad (4.2)$$

$$\mathbf{i}_n := \text{col}_{p \in \mathcal{P}}(i_{n,p}) \quad (4.3)$$

and for the grid as a whole as

$$\mathbf{v} := \text{col}_{n \in \mathcal{N}}(\mathbf{v}_n) \quad (4.4)$$

$$\mathbf{i} := \text{col}_{n \in \mathcal{N}}(\mathbf{i}_n) \quad (4.5)$$

where the operator "col" constructs a column vector.

From Ohm's law, the injection currents are related to the nodal voltage as:

$$\mathbf{i} = \mathbf{Y}\mathbf{v}, \quad (4.6)$$

where  $\mathbf{Y}$  is the compound admittance matrix defined as:

$$\mathbf{Y} = (\mathcal{A}^{\mathcal{P}})^T \mathbf{Y}_{\mathcal{L}} \mathcal{A}^{\mathcal{P}} + \mathbf{Y}_{\mathcal{T}} \quad (4.7)$$

where,

$$\mathbf{Y}_{\mathcal{L}} = \text{diag}_{l \in \mathcal{L}}(\mathbf{Y}_l) \quad (4.8)$$

$$\mathbf{Y}_{\mathcal{T}} = \text{diag}_{t \in \mathcal{T}}(\mathbf{Y}_t) \quad (4.9)$$

are the primitive compound branch and the primitive compound shunt admittance matrices respectively. The symbol  $\mathcal{A}^{\mathcal{P}}$  denotes the polyphase incidence matrix and is defined as

$$\mathcal{A}^{\mathcal{P}} = \mathcal{A} \otimes \text{diag}(\mathbf{1}_{|\mathcal{P}|}) \quad (4.10)$$

where  $(\mathbf{1}_{|\mathcal{P}|})$  is a vector of ones with length  $|\mathcal{P}|$ ,  $\otimes$  refers to the Kronecker product, and  $\mathcal{A}$  is the incidence matrix obtained from the graph comprising of network branches as in [123].

<sup>25</sup>It is worth pointing out that the symmetric property is a consequence of reciprocity of electromagnetism imposed by Maxwell's equation.

### 4.3 Indirect Estimation of Sensitivity Coefficients via Estimation of Compound Admittance Matrix

Using (4.6) and (4.7), the injected current can be re-written as

$$\mathbf{i} = ((\mathcal{A}^{\mathcal{P}})^T \mathbf{Y}_{\mathcal{L}} \mathcal{A}^{\mathcal{P}} + \mathbf{Y}_{\mathcal{T}}) \mathbf{v} \quad (4.11)$$

$$\mathbf{i} = (\mathcal{A}^{\mathcal{P}})^T \mathbf{i}_{\mathcal{L}} + \mathbf{i}_{\mathcal{T}} \quad (4.12)$$

where  $\mathbf{i}_{\mathcal{L}}$  and  $\mathbf{i}_{\mathcal{T}}$  refer to the branch and shunt current which are defined analogously as in (4.3) and (4.5).

In the following, we show how eqs. (4.2) - (4.12) can be used to derive linear models with branch and shunt parameters for transposed and untransposed distribution grids, which will be later used to estimate the compound admittance matrix.

#### Balanced and Transposed Three-Phase Case

A balanced and transposed system can be represented by a single-phase equivalent model, i.e.  $|\mathcal{P}| = 1$  or  $\mathcal{A}^{\mathcal{P}} = \mathcal{A}$ . Using the definitions (4.8) and (4.9) and (4.11) the injected current can be re-written as

$$\mathbf{i} = \left( \mathcal{A}^T \text{diag}_{l \in \mathcal{L}}(\mathbf{Y}_l) \mathcal{A} + \text{diag}_{t \in \mathcal{T}}(\mathbf{Y}_t) \right) \text{col}_{n \in \mathcal{N}}(\mathbf{v}_n) \quad (4.13)$$

$$\text{or, } \mathbf{i} = \mathcal{A}^T \text{diag}(\mathcal{A} \mathbf{v}) \text{col}_{l \in \mathcal{L}}(\mathbf{Y}_l) + \text{diag}_{n \in \mathcal{N}}(\mathbf{v}_n) \text{col}_{t \in \mathcal{T}}(\mathbf{Y}_t). \quad (4.14)$$

Similarly, the branch current can be expressed as

$$\mathbf{i}_{\mathcal{L}} = \text{diag}(\mathcal{A} \mathbf{v}) \text{col}_{l \in \mathcal{L}}(\mathbf{Y}_l) \quad (4.15)$$

Let us define the following matrices:

$$\mathbf{C} = \text{diag}(\mathcal{A} \Re\{\mathbf{v}\}) \quad (4.16a)$$

$$\mathbf{D} = \text{diag}(\mathcal{A} \Im\{\mathbf{v}\}) \quad (4.16b)$$

$$\mathbf{E} = \text{diag}(\Im\{\mathbf{v}\}) \quad (4.16c)$$

$$\mathbf{F} = \text{diag}(\Re\{\mathbf{v}\}) \quad (4.16d)$$

$$\mathbf{X}^G = \text{col}_{l \in \mathcal{L}}(\Re\{\mathbf{Y}_l\}) \quad (4.16e)$$

$$\mathbf{X}^B = \text{col}_{l \in \mathcal{L}}(\Im\{\mathbf{Y}_l\}) \quad (4.16f)$$

$$\mathbf{X}^T = \text{col}_{t \in \mathcal{T}}(\Im\{\mathbf{Y}_t\}) \quad (4.16g)$$

then, the injected and branch current can be re-written as

$$\begin{bmatrix} \Re\{\mathbf{i}\} \\ \Im\{\mathbf{i}\} \end{bmatrix} = \begin{bmatrix} \mathcal{A}^T \mathbf{C} & -\mathcal{A}^T \mathbf{D} & -\mathbf{E} \\ \mathcal{A}^T \mathbf{D} & \mathcal{A}^T \mathbf{C} & \mathbf{F} \end{bmatrix} \begin{bmatrix} \mathbf{X}^G \\ \mathbf{X}^B \\ \mathbf{X}^T \end{bmatrix}, \text{ and} \quad (4.17)$$



## Chapter 4. Data-driven Estimation of Compound Admittance Matrix and Power-Flow Sensitivity Coefficients

$$\begin{bmatrix} \Re\{\mathbf{i}_{\mathcal{L}}\} \\ \Im\{\mathbf{i}_{\mathcal{L}}\} \end{bmatrix} = \begin{bmatrix} \mathbf{C} & -\mathbf{D} \\ \mathbf{D} & \mathbf{C} \end{bmatrix} \begin{bmatrix} \mathbf{X}^{\mathbf{G}} \\ \mathbf{X}^{\mathbf{B}} \end{bmatrix} \quad (4.18)$$

respectively. Here,  $\Re(\cdot)$  and  $\Im(\cdot)$  refer to the real and imaginary part of a complex quantity.

### Unbalanced and Untransposed Three-Phase Case

In this case,  $|\mathcal{P}| = 3$ , the line and shunt parameters are matrices of dimension  $\mathbb{C}^{3 \times 3}$ . To express the line and shunt parameters in vector form, we propose transformations  $\Lambda$  and  $\Xi$  given below.

The line and shunt admittance parameters,  $\mathbf{Y}_l$  and  $\mathbf{Y}_t$  are symmetric (**Hypothesis 4.2**), we want to represent them by unique elements in a vector form. Let  $Y_l^{mn}(m, n = 1, 2, 3)$  be the unique elements of  $\mathbf{Y}_l$ , we propose the following transformation:

$$\Xi(\mathbf{Y}_l) = \Xi \left( \begin{bmatrix} Y_l^{11} & Y_l^{12} & Y_l^{13} \\ Y_l^{12} & Y_l^{22} & Y_l^{23} \\ Y_l^{13} & Y_l^{23} & Y_l^{33} \end{bmatrix} \right) = \begin{bmatrix} Y_l^{11} \\ Y_l^{22} \\ Y_l^{33} \\ Y_l^{12} \\ Y_l^{23} \\ Y_l^{13} \end{bmatrix}. \quad (4.19)$$

The same can be written for the shunt admittance parameters. To be able to express the branch and shunt parameters in vector form, the voltages need to be transformed as following:

$$f_{\gamma}(\mathbf{v}_n) = f_{\gamma} \left( \begin{bmatrix} v_{n,1} \\ v_{n,2} \\ v_{n,3} \end{bmatrix} \right) = \begin{bmatrix} v_{n,1} & 0 & 0 & v_{n,2} & 0 & v_{n,3} \\ 0 & v_{n,2} & 0 & v_{n,1} & v_{n,3} & 0 \\ 0 & 0 & v_{n,3} & 0 & v_{n,2} & v_{n,1} \end{bmatrix}. \quad (4.20)$$

Similarly, this transformation is applied to all the nodes by  $\Lambda(\mathbf{v}) = \text{col}_{n \in \mathcal{N}}(f_{\gamma}(\mathbf{v}_n))$ .

Using the above transformation on all phase voltages and branch and shunt parameters, eqs. (4.17) and (4.18) can be written for a three-phase unbalanced and untransposed system with the following definitions:

$$\mathbf{C} = \text{diag}_{l \in \mathcal{L}}(\mathcal{A}_l^{\mathcal{P}} \Re\{\Lambda(\mathbf{v})\}) \quad (4.21a)$$

$$\mathbf{D} = \text{diag}_{l \in \mathcal{L}}(\mathcal{A}_l^{\mathcal{P}} \Im\{\Lambda(\mathbf{v})\}) \quad (4.21b)$$

$$\mathbf{E} = \text{diag}_{n \in \mathcal{N}}(\Im\{f_{\gamma}(\mathbf{v}_n)\}) \quad (4.21c)$$

$$\mathbf{F} = \text{diag}_{n \in \mathcal{N}}(\Re\{f_{\gamma}(\mathbf{v}_n)\}) \quad (4.21d)$$

$$\mathbf{X}^{\mathbf{G}} = \text{col}_{l \in \mathcal{L}}(\Re\{\Xi(\mathbf{Y}_l)\}) \quad (4.21e)$$

$$\mathbf{X}^{\mathbf{B}} = \text{col}_{l \in \mathcal{L}}(\Im\{\Xi(\mathbf{Y}_l)\}) \quad (4.21f)$$

$$\mathbf{X}^{\mathbf{T}} = \text{col}_{t \in \mathcal{T}}(\Im\{\Xi(\mathbf{Y}_t)\}). \quad (4.21g)$$

### 4.3 Indirect Estimation of Sensitivity Coefficients via Estimation of Compound Admittance Matrix

Here,  $\mathcal{A}_l^{\mathcal{P}}$  is incidence matrix for  $l$ -th line, i.e. rows  $((l-1)|\mathcal{P}|+1)$  to  $l|\mathcal{P}|$  in  $\mathcal{A}^{\mathcal{P}}$ .

The problem considered is as follows. We assume that the incidence matrix  $\mathcal{A}^{\mathcal{P}}$  is known, and we have a collection of complex current  $\mathbf{i}$  and voltage  $\mathbf{v}$  measurements, from which the matrices  $\mathbf{C}, \mathbf{D}, \mathbf{E}$  and  $\mathbf{F}$  are immediately derived. The problem is then to estimate the unknown line and shunt parameters  $\mathbf{X}^G, \mathbf{X}^B$  and  $\mathbf{X}^T$  by regression techniques in (4.17) and (4.18).

#### 4.3.2 Estimation Model

**Hypothesis 4.3** *The line series impedances and shunt admittances are assumed to be constant during the period when measurements were collected. The change in these parameters due to temperature variations is neglected.*

**Hypothesis 4.4** *We assume that the nodal voltage, current and branch current phasor measurements are available at every node of the grid.*

Using equations (4.17)-(4.18) and **Hypotheses 4.3** and **4.4**, the estimation problem can be formulated and solved by using standard estimation techniques such as least squares (LS) and total least squares (TLS). In case of null measurement noise, Eq. (4.17) can be written for a time-index  $k$  as:

$$\mathcal{J}(k) = \mathcal{H}(k)\mathcal{X} \quad (4.22)$$

$$\text{where } \mathcal{H}(k) = \begin{bmatrix} \mathcal{A}^T \mathbf{C}(k) & -\mathcal{A}^T \mathbf{D}(k) & -\mathbf{E}(k) \\ \mathcal{A}^T \mathbf{D}(k) & \mathcal{A}^T \mathbf{C}(k) & \mathbf{F}(k) \end{bmatrix}, \mathcal{J}(k) = \begin{bmatrix} \Re\{\mathbf{i}(k)\} \\ \Im\{\mathbf{i}(k)\} \end{bmatrix}, \text{ and } \mathcal{X} = \begin{bmatrix} \mathbf{X}^G \\ \mathbf{X}^B \\ \mathbf{X}^T \end{bmatrix}.$$

If we have  $K$  measurements of voltage and current phasors, (4.22) can be expressed for all the  $K$  data-points to obtain an over-determined system of linear equations as,

$$\mathcal{J} = \mathcal{H}\mathcal{X} \quad (4.23)$$

where  $\mathcal{J} = [\mathcal{J}(1); \dots; \mathcal{J}(K)]$  and  $\mathcal{H} = [\mathcal{H}(1); \dots; \mathcal{H}(K)]$ .

The equality in (4.23) holds in case of null noise, which is not the case for real measurements. In presence of the measurement noise, the observations  $\mathcal{J}$  and  $\mathcal{H}$  are given as:

$$\mathcal{J} = \widehat{\mathcal{J}} + \Delta \mathcal{J}, \quad \Delta \mathcal{J} \sim \mathcal{N}(0, \mathbf{Q}_{\mathcal{J}}) \quad (4.24)$$

$$\mathcal{H} = \widehat{\mathcal{H}} + \Delta \mathcal{H}, \quad \Delta \mathcal{H} \sim \mathcal{N}(0, \mathbf{Q}_{\mathcal{H}}) \quad (4.25)$$

where,  $\widehat{\mathcal{J}}$  and  $\widehat{\mathcal{H}}$  are the true (unobservable) values,  $\Delta \mathcal{J}$  and  $\Delta \mathcal{H}$  are the measurement noises, and  $\mathbf{Q}_{\mathcal{J}}$  and  $\mathbf{Q}_{\mathcal{H}}$  represent the noise covariance matrices for  $\mathcal{J}$  and  $\mathcal{H}$  respectively.

## Chapter 4. Data-driven Estimation of Compound Admittance Matrix and Power-Flow Sensitivity Coefficients

---

It should be noted that the measurements on the branch currents (if available) can also be embedded in the estimation model using Eq. (4.18) in a similar way. In eq. (4.23),  $\mathcal{X}$  is the unknown parameter to be estimated, whereas  $\mathcal{H}$  and  $\mathcal{J}$  are obtained using the voltage and current measurements from PMUs. In the following section, we describe the estimation techniques to provide an estimate of  $\mathcal{X}$  in (4.23).

### 4.3.3 Estimation Techniques

In the following, we describe two estimation techniques which are used later to estimate the network parameters.

#### Least Squares (LS)

The LS method assumes that noise  $\Delta\mathcal{H}$  is negligible and the noise  $\Delta\mathcal{J}$  is homoscedastic (i.e. elements of  $\text{diag}(\mathbf{Q}_{\mathcal{J}})$  are all equal). The LS solution is:

$$\mathcal{X}_{LS}^* = (\mathcal{H}^T \mathcal{H})^{-1} \mathcal{H}^T \mathcal{J} \quad (4.26)$$

#### Total Least Squares (TLS)

In real measurement,  $\mathcal{H}$  contains measurement noise, LS solution is no longer optimal statistically. In [117], TLS was developed, trying to estimate the true (unobservable)  $\widehat{\mathcal{H}}$  and  $\widehat{\mathcal{J}}$  along with  $\mathcal{X}$ . This leads to a non-linear and non-convex problem and has too many unknowns to determine. The work in [117] derived an analytical approach relying on the assumption that noise terms  $\Delta\mathcal{J}, \Delta\mathcal{H}$  are Gaussian and i.i.d., using singular value decomposition (SVD). It is briefly summarized below.

Let the SVD of  $[\mathcal{H}|\mathcal{J}]$  be

$$[\mathcal{H}|\mathcal{J}] = \mathcal{U} \Sigma \mathcal{V}^T \quad (4.27)$$

$$\text{where, } \mathcal{V} = \begin{bmatrix} \mathcal{V}_{\mathcal{H},\mathcal{H}} & \mathcal{V}_{\mathcal{H},\mathcal{J}} \\ \mathcal{V}_{\mathcal{J},\mathcal{H}} & \mathcal{V}_{\mathcal{J},\mathcal{J}} \end{bmatrix}, \Sigma = \text{diag}(\overline{\sigma}, \dots, \underline{\sigma}). \quad (4.28)$$

The TLS solution is given as:

$$\mathcal{X}_{TLS}^* = -\mathcal{V}_{\mathcal{H},\mathcal{J}} \mathcal{V}_{\mathcal{J},\mathcal{J}}^{-1}. \quad (4.29)$$

Eq. (4.29) can be simplified when  $\mathcal{J}$  is vector, it is given as

$$\mathcal{X}_{TLS}^* = (\mathcal{H}^T \mathcal{H} - \underline{\sigma}^2 I)^{-1} \mathcal{H}^T \mathcal{J} \quad (4.30)$$

where,  $\underline{\sigma}$  refers to the smallest eigen value of  $[\mathcal{H}|\mathcal{J}]$  [124, 125]. Eq. (4.30) can be interpreted

### 4.3 Indirect Estimation of Sensitivity Coefficients via Estimation of Compound Admittance Matrix

as a method to remove the error covariance matrix (approximated by  $\sigma^2 I$ ).

When the TLS is fed with a large number of measurements (with non-negligible noise), it attempts to estimate large amount of variables. In our case these are true unobserved value of the measurements and admittance parameters. This results in poor estimates as reported in [117]. To tackle this issue, we propose a pre-processing strategy on the raw measurements: a linear transformation that reduces the dimension of the input measurements as well as the noise level while preserving the original structure of the problem. Due to this pre-processing, the TLS is now trying to estimate the average values of the measurements. This task is easier than the original because there are fewer data points and reduced noise. The pre-processing strategy is described as follows.

#### 4.3.4 Measurement Pre-processing by Cluster Averaging

Measurement noise of PMUs and sensing instruments impacts  $\mathcal{H}$  and  $\mathcal{J}$  observation matrices. Realistic instrument accuracy classes (e.g., 0.5 and 1.0) lead to poor estimation performance, further aggravated by the nonlinear transposition from polar to rectangular coordinates, as reported in [122]. We propose to pre-process the input measurements because, as it will be shown later, it is helpful to improve the estimation performance. The pre-processing strategy consists in, first grouping the raw measurements in a given number of clusters according to similarity features. Then measurements within the same cluster are averaged and used in the estimation process instead of the raw measurements. The considered similarity features are: nodal voltage magnitudes, current magnitudes, and for unbalanced and untransposed networks, sequence-domain voltage magnitudes and sequence-domain current magnitudes. The first group of features helps to detect different operating conditions in the grid due to large power variations and transient events (e.g., inrush currents), whereas the second, is more suitable for unbalanced conditions. The use of combinations of these features is discussed in the results section. Clustering and averaging the measurements achieve not only filtering out measurement noise but also reduce the number of similar measurements in the estimation process, improving the condition number of  $\mathcal{H}$  and estimation performance of LS and TLS. It is worth highlighting that since averaging is linear, it can be efficiently implemented by applying a linear transformation to Eq. (4.23).

The cluster-averaging procedure is illustrated **Algorithm 4.1**. The `kmeans` algorithm is used for clustering. Specifically, inputs to the `kmeans` are the raw voltage and current phasor measurements  $\{\mathbf{v}, \mathbf{i}\}$ , features (defined above) and number of clusters  $N_c$ , and the outputs are voltage and current phasor measurements grouped in different clusters  $[\{\mathbf{v}, \mathbf{i}\}_1, \dots, \{\mathbf{v}, \mathbf{i}\}_{N_c}]$ . After creating the clusters, the algebraic mean is computed for all the elements in the same cluster. We decide to use the `kmeans` as a clustering scheme as it is a widely used and effective method in unsupervised learning applications. Specifically, we use MATLAB built-in function which uses the `kmeans++` algorithm [126] regarding the clustering initialisation.

The similarity features, such as the magnitudes of the nodal voltages and currents, are used in

## Chapter 4. Data-driven Estimation of Compound Admittance Matrix and Power-Flow Sensitivity Coefficients

---

the kmeans algorithm to decide the basis of the grouping of the raw measurements. We choose magnitudes of the voltages and currents as clustering features because (i) as illustrated in [127, 128], the distribution of measurement noise is truly white in polar coordinates, (ii) magnitudes work well to identify the voltage and current imbalances in three-phase unbalanced systems and (iii) it results in a linear estimation model, which is preserved by the averaging. Sec. 4.3.7 shows how the cluster-averaging process affects the grouping of the raw-measurements and their characteristics. A naive averaging approach would be to perform block time-averaging of the measurements (**Algorithm 4.2**). However, this naive method has the disadvantage of losing important information associated to transients and unbalances contained in the raw measurements by averaging blindly time-contiguous data blocks. The advantage of cluster-averaging is that it groups and averages the data based on the similarity features and is independent of time. In the results section, we compare the estimation performance of the cluster-averaging vs the block-averaging method.

---

### Algorithm 4.1 Cluster-averaging

---

```
1: procedure CLUSTERAVG
2:   choose number of clusters =  $N_c$ 
3:    $\{\mathbf{v}, \mathbf{i}\}_1, \dots, \{\mathbf{v}, \mathbf{i}\}_{N_c} \leftarrow \text{kmeans}(\{\mathbf{v}, \mathbf{i}\}, \text{features}, N_c)$ 
4:   for  $l = 1 : N_c$  do
5:      $\{\tilde{\mathbf{v}}, \tilde{\mathbf{i}}\}_l = \text{mean}(\{\mathbf{v}, \mathbf{i}\}_l)$ 
6:   end for
7: end procedure
```

---

---

### Algorithm 4.2 Block-averaging

---

```
1: procedure BLOCKAVG
2:   choose block size =  $t_m$ 
3:   number of blocks,  $N_{\text{block}} = \text{data-length} / t_m$ ,
4:   Divide in  $N_{\text{block}}$  blocks:  $\{\{\mathbf{v}, \mathbf{i}\}_{1:t_m}, \dots, \{\mathbf{v}, \mathbf{i}\}_{((N_{\text{block}}-1)t_m+1):N_{\text{block}}t_m}\} \leftarrow \{\mathbf{v}, \mathbf{i}\}_{1:T}$ 
5:   for  $l = 1 : N_{\text{block}}$  do
6:      $\{\tilde{\mathbf{v}}, \tilde{\mathbf{i}}\}_l \leftarrow \text{mean}(\{\mathbf{v}, \mathbf{i}\}_{(l-1)t_m+1:lt_m})$ 
7:   end for
8: end procedure
```

---

In summary, the measurement pre-processing is to obtain a proper grouping of the raw measurements. After creating the clusters, the algebraic mean is computed for all the elements (both the magnitudes and phases of the voltages and currents) in the same cluster. The averaged values (both the magnitudes and phases) are then used in the admittance matrix estimation.

### 4.3 Indirect Estimation of Sensitivity Coefficients via Estimation of Compound Admittance Matrix

#### 4.3.5 Computation of Sensitivity Coefficients using Estimated Admittance Matrix and Error Propagation

As stated earlier in the Chapter, the estimated admittance matrix is used for the computation of the sensitivity coefficients. The method is referred to as *indirect*, as the sensitivity coefficients are not directly estimated using the measurements, instead utilizing an already estimated quantity ( $\mathbf{Y}$ ). In the following, we recall a method from the literature for computing the sensitivity coefficients. Then, we use it to develop an analytical approach to propagate the uncertainty on the admittance estimates and grid state measurements to the sensitivity coefficients.

##### Estimated Admittance Matrix to the Sensitivity Coefficients Computation

For the computation of the sensitivity coefficients, we rely on the method developed in [40, 55]. It uses the compound admittance matrix and grid states. The method computes the sensitivities by solving a set of linear equations and guarantees a unique solution, given that the Jacobian of the load flow solution is invertible [56]. The complex power<sup>26</sup> at node  $i$  can be expressed as

$$\underline{s}_i = p_i - jq_i = \underline{v}_i \sum_{j \in \mathcal{N}} Y_{ij} v_j \quad i \in \mathcal{N} \quad (4.31)$$

where,  $Y_{ij}$  refer to an element of  $\mathbf{Y}$ . Following the approach in [40, 55], we differentiate the equation in (4.31) with respect to active power and reactive power injections<sup>27</sup>  $p_l, l \in \mathcal{N}$ , we obtain the following relation:

$$\mathbb{1}_{\{i=l\}} = \frac{\partial \underline{v}_i}{\partial p_l} \sum_{j \in \mathcal{N}} Y_{ij} v_j + \underline{v}_i \sum_{j \in \mathcal{N}} Y_{ij} \frac{\partial v_j}{\partial p_l}, \quad (4.32)$$

$$-j \mathbb{1}_{\{i=l\}} = \frac{\partial \underline{v}_i}{\partial q_l} \sum_{j \in \mathcal{N}} Y_{ij} v_j + \underline{v}_i \sum_{j \in \mathcal{N}} Y_{ij} \frac{\partial v_j}{\partial q_l}. \quad (4.33)$$

where  $\frac{\partial \square}{\partial \square}$  refers to the partial derivatives. Rearranging the rows and columns of the eq. (4.32)-(4.33) for different nodes and stacking them, the set of linear equations can be written in matrix form as

$$\mathbf{z} = \mathbf{H}\mathbf{x} \quad (4.34)$$

where  $\mathbf{H} \in \mathbb{R}^{2(N_b-1) \times 2(N_b-1)}$  and  $\mathbf{z} \in \mathbb{R}^{2(N_b-1) \times (N_b-1)}$ . The elements of the matrix  $\mathbf{H}$  and vector  $\mathbf{z}$  are obtained using [55]. Here,  $\mathbf{x} \in \mathbb{R}^{2(N_b-1) \times (N_b-1)}$  is the vector of unknown sensitivities i.e.,  $\frac{\partial \underline{v}_i}{\partial p_l}$

<sup>26</sup>Conjugates of a complex number (e.g.  $z = |z|\exp(j\theta)$ ) is denoted by underlined symbol (e.g.  $\underline{z}$ ).

<sup>27</sup>Although the method proposed in [55] is generic enough to apply to any kind of buses, we only consider voltage independent and PQ buses in this work.

## Chapter 4. Data-driven Estimation of Compound Admittance Matrix and Power-Flow Sensitivity Coefficients

---

and  $\frac{\partial v_i}{\partial p_l}$ , where  $i, l \in \mathcal{N}$ . The  $\mathbf{x}$  can be obtained by

$$\mathbf{x} = \mathbf{H}^{-1} \mathbf{z}. \quad (4.35)$$

Once  $\frac{\partial v_i}{\partial p_l}$  and  $\frac{\partial v_i}{\partial p_l}$  are obtained, the sensitivity coefficient of the voltage magnitude can be obtained as

$$\frac{\partial |v_i|}{\partial p_l} = \frac{1}{|v_i|} \Re \left( v_i \frac{\partial v_i}{\partial p_l} \right) \quad (4.36)$$

It should be remarked that the expression in (4.35) depends on the value of the admittance matrix of the nodal voltage phasors. As both the admittance matrix and grid states are uncertain, we need to propagate the error into the computation of the sensitivity coefficients. This is described in the next section.

### Uncertainty Propagation: From Estimated Admittance Matrix to Sensitivity Coefficients

As mentioned earlier, the matrix  $\mathbf{H}$  in eq. (4.35) is uncertain due to the noise introduced by the measuring units and error on the estimates of the admittance matrix. To compute the uncertainty on  $\mathbf{x}$  in (4.35), the error on the  $\mathbf{Y}$  and grid state  $\mathbf{v}$  needs to be propagated.

Let  $[\sigma_{\mathbf{H}^{-1}}]$  be the variance of matrix  $\mathbf{H}^{-1}$ ,  $[\sigma_{\mathbf{H}^{-1}}]_{ij}$  be the variance of  $ij$ -th element of  $\mathbf{H}^{-1}$ ,  $[\sigma_{\mathbf{x}}]_i$  be the variance of  $i$ -th element of  $\mathbf{x}$ , and  $[\sigma_{\mathbf{z}}]_j$  be the variance of  $j$ -th element of  $\mathbf{z}$ . Using the principle of error propagation, variance on  $\mathbf{x}$  can be approximated as

$$[\sigma_{\mathbf{x}}]_i^2 \approx [\mathbf{H}^{-1}]_{ij}^2 [\sigma_{\mathbf{z}}]_j^2 + [\sigma_{\mathbf{H}^{-1}}]_{ij}^2 [\mathbf{z}]_j^2. \quad (4.37)$$

Since,  $\mathbf{z}$  in (4.34) is constant (as shown later in Sec. 4.3.5),  $\sigma_{\mathbf{z}} = 0$ , the expression in (4.37) reduces to

$$[\sigma_{\mathbf{x}}]_i^2 = [\sigma_{\mathbf{H}^{-1}}]_{ij}^2 [\mathbf{z}]_j^2. \quad (4.38)$$

In (4.38),  $[\sigma_{\mathbf{H}^{-1}}]$  is unknown, it can be computed by propagating the variances of element of  $\mathbf{H}$  by following relation (as described in [129]):  $[\sigma_{\mathbf{H}^{-1}}]_{mn}^2 =$

$$\text{cov}(\mathbf{H}_{mn}^{-1}, \mathbf{H}_{mn}^{-1}) = \sum_i \sum_j [\mathbf{H}^{-1}]_{mi}^2 [\sigma_{\mathbf{H}}]_{ij}^2 [\mathbf{H}^{-1}]_{jn}^2 \quad (4.39)$$

$$\text{cov}(\mathbf{H}_{mn}^{-1}, \mathbf{H}_{ab}^{-1}) = \sum_i \sum_j [\mathbf{H}^{-1}]_{mi} [\mathbf{H}^{-1}]_{ai} [\sigma_{\mathbf{H}}]_{ij}^2 [\mathbf{H}^{-1}]_{jn} [\mathbf{H}^{-1}]_{jb} \quad (4.40)$$

Eq. (4.39) and (4.40) refer to the self- and cross-correlations. It should be noted that the matrix inversion is a non-linear operation and the elements of the inverse matrix ( $\mathbf{H}^{-1}$ ) are statistically correlated. Thus, variance of each element of the matrix  $\mathbf{H}^{-1}$  is of size  $2(N_b - 1) \times 2(N_b - 1)$

### 4.3 Indirect Estimation of Sensitivity Coefficients via Estimation of Compound Admittance Matrix

itself. Therefore, the size of  $\sigma_{\mathbf{H}}$  is  $(4(N_b - 1)^2 \times 4(N_b - 1)^2)$ .

To understand error propagation from matrix to its inverse, we use a dummy example showing error propagation from a matrix  $\mathbf{H}$  to its inverse.

**Example of a Random Two-Dimensional Matrix:** let consider a random two-dimensional matrix

$$\mathbf{H} = \begin{bmatrix} \epsilon & \zeta \\ \eta & \xi \end{bmatrix} \quad (4.41)$$

with the matrix of respective variances as:

$$\sigma_{\mathbf{H}}^2 = \begin{bmatrix} \sigma_{\epsilon}^2 & \sigma_{\zeta}^2 \\ \sigma_{\eta}^2 & \sigma_{\xi}^2 \end{bmatrix} \quad (4.42)$$

Using the expression in (4.39)-(4.40), the covariance matrices for the elements of  $[\mathbf{H}^{-1}]$  are computed as

$$\begin{aligned} \text{cov}([\mathbf{H}^{-1}]_{11}, [\mathbf{H}^{-1}]_{ij}) &= \begin{bmatrix} \epsilon^4 \sigma_{\epsilon}^2 + \epsilon^2 \zeta^2 \sigma_{\eta}^2 + \epsilon^2 \eta^2 \sigma_{\delta}^2 + \zeta^2 \eta^2 \sigma_{\xi}^2 & \epsilon^3 \zeta \sigma_{\epsilon}^2 + \xi \eta \epsilon^2 \sigma_{\delta}^2 + \epsilon \zeta^3 \sigma_{\eta}^2 + \xi \eta \zeta^2 \sigma_{\xi}^2 \\ \epsilon^3 \eta \sigma_{\epsilon}^2 + \zeta \xi \epsilon^2 \sigma_{\eta}^2 + \epsilon \eta^3 \sigma_{\delta}^2 + \zeta \xi \eta^2 \sigma_{\xi}^2 & \epsilon^2 \zeta \eta \sigma_{\epsilon}^2 + \epsilon \zeta^2 \xi \sigma_{\eta}^2 + \epsilon \xi \eta^2 \sigma_{\delta}^2 + \zeta \xi^2 \eta \sigma_{\xi}^2 \end{bmatrix} \\ \text{cov}([\mathbf{H}^{-1}]_{12}, [\mathbf{H}^{-1}]_{ij}) &= \begin{bmatrix} \epsilon^3 \zeta \sigma_{\epsilon}^2 + \xi \eta \epsilon^2 \sigma_{\delta}^2 + \epsilon \zeta^3 \sigma_{\eta}^2 + \xi \eta \zeta^2 \sigma_{\xi}^2 & \epsilon^2 \zeta^2 \sigma_{\epsilon}^2 + \epsilon^2 \xi^2 \sigma_{\delta}^2 + \zeta^4 \sigma_{\eta}^2 + \zeta^2 \xi^2 \sigma_{\xi}^2 \\ \epsilon^2 \zeta \eta \sigma_{\epsilon}^2 + \epsilon \zeta^2 \xi \sigma_{\eta}^2 + \epsilon \xi \eta^2 \sigma_{\delta}^2 + \zeta \xi^2 \eta \sigma_{\xi}^2 & \zeta^3 \xi \sigma_{\eta}^2 + \epsilon \eta \zeta^2 \sigma_{\epsilon}^2 + \zeta \xi^3 \sigma_{\delta}^2 + \epsilon \eta \xi^2 \sigma_{\xi}^2 \end{bmatrix} \\ \text{cov}([\mathbf{H}^{-1}]_{21}, [\mathbf{H}^{-1}]_{ij}) &= \begin{bmatrix} \epsilon^3 \eta \sigma_{\epsilon}^2 + \zeta \xi \epsilon^2 \sigma_{\eta}^2 + \epsilon \eta^3 \sigma_{\delta}^2 + \zeta \xi \eta^2 \sigma_{\xi}^2 & \epsilon^2 \zeta \eta \sigma_{\epsilon}^2 + \epsilon \zeta^2 \xi \sigma_{\eta}^2 + \epsilon \xi \eta^2 \sigma_{\delta}^2 + \zeta \xi^2 \eta \sigma_{\xi}^2 \\ \epsilon^2 \xi^2 \sigma_{\eta}^2 + \epsilon^2 \eta^2 \sigma_{\epsilon}^2 + \xi^2 \eta^2 \sigma_{\delta}^2 + \eta^4 \sigma_{\delta}^2 & \xi^3 \eta \sigma_{\xi}^2 + \epsilon \zeta \xi^2 \sigma_{\eta}^2 + \xi \eta^3 \sigma_{\delta}^2 + \epsilon \zeta \eta^2 \sigma_{\epsilon}^2 \end{bmatrix} \\ \text{cov}([\mathbf{H}^{-1}]_{22}, [\mathbf{H}^{-1}]_{ij}) &= \begin{bmatrix} \epsilon^2 \zeta \eta \sigma_{\epsilon}^2 + \epsilon \zeta^2 \xi \sigma_{\eta}^2 + \epsilon \xi \eta^2 \sigma_{\delta}^2 + \zeta \xi^2 \eta \sigma_{\xi}^2 & \zeta^3 \xi \sigma_{\eta}^2 + \epsilon \eta \zeta^2 \sigma_{\epsilon}^2 + \zeta \xi^3 \sigma_{\delta}^2 + \epsilon \eta \xi^2 \sigma_{\xi}^2 \\ \xi^3 \eta \sigma_{\xi}^2 + \epsilon \zeta \xi^2 \sigma_{\eta}^2 + \xi \eta^3 \sigma_{\delta}^2 + \epsilon \zeta \eta^2 \sigma_{\epsilon}^2 & \zeta^2 \xi^2 \sigma_{\eta}^2 + \zeta^2 \eta^2 \sigma_{\epsilon}^2 + \xi^4 \sigma_{\delta}^2 + \xi^2 \eta^2 \sigma_{\delta}^2 \end{bmatrix} \end{aligned}$$

**Example for a Three Node System:** Furthermore, we present an example of error propagation for a simple three node power system. Let  $Y_{ij}^{re} = \Re(Y_{ij})$ ,  $Y_{ij}^{im} = \Im(Y_{ij})$  and  $v_i^{re} = \Re(v_i)$ ,  $v_i^{im} = \Im(v_i)$ . Using the formulation in (4.32)-(4.33), the elements of  $\mathbf{H}$  are given by

$$H_{11} = v_1^{re} Y_{21}^{re} - v_1^{im} Y_{21}^{im} - v_3^{im} Y_{32}^{im} - v_2^{re} + 2v_2^{re} Y_{22}^{re} + v_3^{re} Y_{32}^{re}, \quad (4.43a)$$

$$H_{12} = v_2^{im} Y_{32}^{im} + v_2^{re} Y_{32}^{re}, \quad (4.43b)$$

$$H_{13} = v_1^{im} Y_{21}^{re} + Y_{21}^{im} v_1^{re} + 2v_2^{im} Y_{22}^{re} + v_3^{im} Y_{32}^{re} + Y_{32}^{im} v_3^{re}, \quad (4.43c)$$

$$H_{14} = v_2^{im} Y_{32}^{re} - Y_{32}^{im} v_2^{re}, \quad (4.43d)$$

$$H_{21} = v_3^{im} Y_{32}^{im} + v_3^{re} Y_{32}^{re}, \quad (4.43e)$$

$$H_{22} = v_1^{re} Y_{31}^{re} - v_1^{im} Y_{31}^{im} - v_2^{im} Y_{32}^{im} - v_3^{re} + v_2^{re} Y_{32}^{re} + 2v_3^{re} Y_{33}^{re}, \quad (4.43f)$$

$$H_{23} = v_3^{im} Y_{32}^{re} - Y_{32}^{im} v_3^{re} \quad (4.43g)$$

$$H_{24} = v_1^{im} Y_{31}^{re} + Y_{31}^{im} v_1^{re} + v_2^{im} Y_{32}^{re} + Y_{32}^{im} v_2^{re} + 2v_3^{im} Y_{33}^{re}, \quad (4.43h)$$

$$H_{31} = v_1^{im} Y_{21}^{re} + Y_{21}^{im} v_1^{re} + 2Y_{22}^{im} v_2^{re} + v_3^{im} Y_{32}^{re} + Y_{32}^{im} v_3^{re}, \quad (4.43i)$$



## Chapter 4. Data-driven Estimation of Compound Admittance Matrix and Power-Flow Sensitivity Coefficients

$$H_{32} = Y_{32}^{im} v_2^{re} - v_2^{im} Y_{32}^{re} \quad (4.43j)$$

$$H_{33} = v_1^{im} Y_{21}^{im} + 2v_2^{im} Y_{22}^{im} + v_3^{im} Y_{32}^{im} - v_1^{re} Y_{21}^{re} - v_3^{re} Y_{32}^{re}, \quad (4.43k)$$

$$H_{34} = v_2^{im} Y_{32}^{im} + v_2^{re} Y_{32}^{re}, \quad (4.43l)$$

$$H_{41} = Y_{32}^{im} v_3^{re} - v_3^{im} Y_{32}^{re}, \quad (4.43m)$$

$$H_{42} = v_1^{im} Y_{31}^{re} + Y_{31}^{im} v_1^{re} + v_2^{im} Y_{32}^{re} + Y_{32}^{im} v_2^{re} + 2Y_{33}^{im} v_3^{re}, \quad (4.43n)$$

$$H_{43} = v_3^{im} Y_{32}^{im} + v_3^{re} Y_{32}^{re}, \quad (4.43o)$$

$$H_{44} = v_1^{im} Y_{31}^{im} + v_2^{im} Y_{32}^{im} + 2v_3^{im} Y_{33}^{im} - v_1^{re} Y_{31}^{re} - v_2^{re} Y_{32}^{re}. \quad (4.43p)$$

And, the elements of  $\mathbf{z}$  are

$$\mathbf{z} = \begin{bmatrix} 1 & 0 \\ 0 & 1 \\ 0 & 0 \\ 0 & 0 \end{bmatrix} \quad (4.44)$$

In (4.43), the variances of elements of  $\mathbf{Y}$  and  $v$  are known,<sup>28</sup> so to compute the variance of elements of  $\mathbf{H}$ , we use propagation of uncertainty for *multiplicative* and *additive* error propagation rules. They are

$$\sigma(\Theta + \Phi)^2 \approx \sigma_\Theta^2 + \sigma_\Phi^2 + 2\sigma_{\Theta\Phi}, \quad (4.45a)$$

$$\sigma(\Theta \times \Phi)^2 \approx \Theta^2 \Phi^2 (\sigma_\Theta^2 / \Theta^2 + \sigma_\Phi^2 / \Phi^2 + 2\sigma_{\Theta\Phi} / \Theta\Phi). \quad (4.45b)$$

Using these rules, the variances of the elements of  $\mathbf{H}$  are

$$\begin{aligned} [\sigma_{\mathbf{H}}]_{11} = & \sigma_{v_2^{re}}^2 + v_1^{im2} Y_{21}^{im2} (\sigma_{v_1^{im}}^2 / v_1^{im2} + \sigma_{Y_{21}^{im}}^2 / Y_{21}^{im2}) + v_3^{im2} Y_{32}^{im2} (\sigma_{v_3^{im}}^2 / v_3^{im2} + \\ & \sigma_{Y_{32}^{im}}^2 / Y_{32}^{im2}) + v_1^{re2} Y_{21}^{re2} (\sigma_{v_1^{re}}^2 / v_1^{re2} + \sigma_{Y_{21}^{re}}^2 / Y_{21}^{re2}) + 4v_2^{re2} Y_{22}^{re2} (\sigma_{v_2^{re}}^2 / v_2^{re2} + \\ & \sigma_{Y_{22}^{re}}^2 / Y_{22}^{re2}) + v_3^{re2} Y_{32}^{re2} (\sigma_{v_3^{re}}^2 / v_3^{re2} + \sigma_{Y_{32}^{re}}^2 / Y_{32}^{re2}), \end{aligned} \quad (4.46a)$$

$$[\sigma_{\mathbf{H}}]_{12} = v_2^{im2} Y_{32}^{im2} (\sigma_{v_2^{im}}^2 / v_2^{im2} + \sigma_{Y_{32}^{im}}^2 / Y_{32}^{im2}) + v_2^{re2} Y_{32}^{re2} (\sigma_{v_2^{re}}^2 / v_2^{re2} + \sigma_{Y_{32}^{re}}^2 / Y_{32}^{re2}), \quad (4.46b)$$

$$\begin{aligned} [\sigma_{\mathbf{H}}]_{13} = & v_1^{im2} Y_{21}^{re2} (\sigma_{Y_{21}^{re}}^2 / Y_{21}^{re2} + \sigma_{v_1^{im}}^2 / v_1^{im2}) + Y_{21}^{im2} v_1^{re2} (\sigma_{v_1^{re}}^2 / v_1^{re2} + \sigma_{Y_{21}^{im}}^2 / Y_{21}^{im2}) + \\ & 4v_2^{im2} Y_{22}^{re2} (\sigma_{Y_{22}^{re}}^2 / Y_{22}^{re2} + \sigma_{v_2^{im}}^2 / v_2^{im2}) + v_3^{im2} Y_{32}^{re2} (\sigma_{Y_{32}^{re}}^2 / Y_{32}^{re2} + \sigma_{v_3^{im}}^2 / v_3^{im2}) + \\ & Y_{32}^{im2} v_3^{re2} (\sigma_{v_3^{re}}^2 / v_3^{re2} + \sigma_{Y_{32}^{im}}^2 / Y_{32}^{im2}), \end{aligned} \quad (4.46c)$$

$$[\sigma_{\mathbf{H}}]_{14} = v_2^{im2} Y_{32}^{re2} (\sigma_{Y_{32}^{re}}^2 / Y_{32}^{re2} + \sigma_{v_2^{im}}^2 / v_2^{im2}) + Y_{32}^{im2} v_2^{re2} (\sigma_{v_2^{re}}^2 / v_2^{re2} + \sigma_{Y_{32}^{im}}^2 / Y_{32}^{im2}), \quad (4.46d)$$

$$[\sigma_{\mathbf{H}}]_{21} = v_3^{im2} Y_{32}^{im2} (\sigma_{v_3^{im}}^2 / v_3^{im2} + \sigma_{Y_{32}^{im}}^2 / Y_{32}^{im2}) + v_3^{re2} Y_{32}^{re2} (\sigma_{v_3^{re}}^2 / v_3^{re2} + \sigma_{Y_{32}^{re}}^2 / Y_{32}^{re2}), \quad (4.46e)$$

<sup>28</sup>Variance of  $\mathbf{Y}$  is obtained by propagating the estimation error on estimated lines and branch impedances as will be described later in (4.50). The variance of  $v$  is obtained from the measurement units specifications projected to the rectangular coordinates.

### 4.3 Indirect Estimation of Sensitivity Coefficients via Estimation of Compound Admittance Matrix

$$[\sigma_H]_{22} = \sigma_{v_3^{re}}^2 + v_1^{im^2} Y_{31}^{im^2} (\sigma_{v_1^{im}}^2 / v_1^{im^2} + \sigma_{Y_{31}}^{im^2} / Y_{31}^{im^2}) + v_2^{im^2} Y_{32}^{im^2} (\sigma_{v_2^{im}}^2 / v_2^{im^2} + \sigma_{Y_{32}}^{im^2} / Y_{32}^{im^2}) + v_1^{re^2} Y_{31}^{re^2} (\sigma_{v_1^{re}}^2 / v_1^{re^2} + \sigma_{Y_{31}}^{re^2} / Y_{31}^{re^2}) + v_2^{re^2} Y_{32}^{re^2} (\sigma_{v_2^{re}}^2 / v_2^{re^2} + \sigma_{Y_{32}}^{re^2} / Y_{32}^{re^2}) + 4v_3^{re^2} Y_{33}^{re^2} (\sigma_{v_3^{re}}^2 / v_3^{re^2} + \sigma_{Y_{33}}^{re^2} / Y_{33}^{re^2}), \quad (4.46f)$$

$$[\sigma_H]_{23} = v_3^{im^2} Y_{32}^{re^2} (\sigma_{Y_{32}}^{re^2} / Y_{32}^{re^2} + \sigma_{v_3^{im}}^2 / v_3^{im^2}) + Y_{32}^{im^2} v_3^{re^2} (\sigma_{v_3^{re}}^2 / v_3^{re^2} + \sigma_{Y_{32}}^{im^2} / Y_{32}^{im^2}), \quad (4.46g)$$

$$[\sigma_H]_{24} = v_1^{im^2} Y_{31}^{re^2} (\sigma_{Y_{31}}^{re^2} / Y_{31}^{re^2} + \sigma_{v_1^{im}}^2 / v_1^{im^2}) + Y_{31}^{im^2} v_1^{re^2} (\sigma_{v_1^{re}}^2 / v_1^{re^2} + \sigma_{Y_{31}}^{im^2} / Y_{31}^{im^2}) + v_2^{im^2} Y_{32}^{re^2} (\sigma_{Y_{32}}^{re^2} / Y_{32}^{re^2} + \sigma_{v_2^{im}}^2 / v_2^{im^2}) + Y_{32}^{im^2} v_2^{re^2} (\sigma_{v_2^{re}}^2 / v_2^{re^2} + \sigma_{Y_{32}}^{im^2} / Y_{32}^{im^2}) + 4v_3^{im^2} Y_{33}^{re^2} (\sigma_{Y_{33}}^{re^2} / Y_{33}^{re^2} + \sigma_{v_3^{im}}^2 / v_3^{im^2}), \quad (4.46h)$$

$$[\sigma_H]_{31} = v_1^{im^2} Y_{21}^{re^2} (\sigma_{Y_{21}}^{re^2} / Y_{21}^{re^2} + \sigma_{v_1^{im}}^2 / v_1^{im^2}) + Y_{21}^{im^2} v_1^{re^2} (\sigma_{v_1^{re}}^2 / v_1^{re^2} + \sigma_{Y_{21}}^{im^2} / Y_{21}^{im^2}) + 4Y_{22}^{im^2} v_2^{re^2} (\sigma_{v_2^{re}}^2 / v_2^{re^2} + \sigma_{Y_{22}}^{im^2} / Y_{22}^{im^2}) + v_3^{im^2} Y_{32}^{re^2} (\sigma_{Y_{32}}^{re^2} / Y_{32}^{re^2} + \sigma_{v_3^{im}}^2 / v_3^{im^2}) + Y_{32}^{im^2} v_3^{re^2} (\sigma_{v_3^{re}}^2 / v_3^{re^2} + \sigma_{Y_{32}}^{im^2} / Y_{32}^{im^2}), \quad (4.46i)$$

$$[\sigma_H]_{32} = v_2^{im^2} Y_{32}^{re^2} (\sigma_{Y_{32}}^{re^2} / Y_{32}^{re^2} + \sigma_{v_2^{im}}^2 / v_2^{im^2}) + Y_{32}^{im^2} v_2^{re^2} (\sigma_{v_2^{re}}^2 / v_2^{re^2} + \sigma_{Y_{32}}^{im^2} / Y_{32}^{im^2}), \quad (4.46j)$$

$$[\sigma_H]_{33} = v_1^{im^2} Y_{21}^{im^2} (\sigma_{v_1^{im}}^2 / v_1^{im^2} + \sigma_{Y_{21}}^{im^2} / Y_{21}^{im^2}) + 4v_2^{im^2} Y_{22}^{im^2} (\sigma_{v_2^{im}}^2 / v_2^{im^2} + \sigma_{Y_{22}}^{im^2} / Y_{22}^{im^2}) + v_3^{im^2} Y_{32}^{im^2} (\sigma_{v_3^{im}}^2 / v_3^{im^2} + \sigma_{Y_{32}}^{im^2} / Y_{32}^{im^2}) + v_1^{re^2} Y_{21}^{re^2} (\sigma_{v_1^{re}}^2 / v_1^{re^2} + \sigma_{Y_{21}}^{re^2} / Y_{21}^{re^2}) + v_3^{re^2} Y_{32}^{re^2} (\sigma_{v_3^{re}}^2 / v_3^{re^2} + \sigma_{Y_{32}}^{re^2} / Y_{32}^{re^2}), \quad (4.46k)$$

$$[\sigma_H]_{34} = v_2^{im^2} Y_{32}^{im^2} (\sigma_{v_2^{im}}^2 / v_2^{im^2} + \sigma_{Y_{32}}^{im^2} / Y_{32}^{im^2}) + v_2^{re^2} Y_{32}^{re^2} (\sigma_{v_2^{re}}^2 / v_2^{re^2} + \sigma_{Y_{32}}^{re^2} / Y_{32}^{re^2}), \quad (4.46l)$$

$$[\sigma_H]_{41} = v_3^{im^2} Y_{32}^{re^2} (\sigma_{Y_{32}}^{re^2} / Y_{32}^{re^2} + \sigma_{v_3^{im}}^2 / v_3^{im^2}) + Y_{32}^{im^2} v_3^{re^2} (\sigma_{v_3^{re}}^2 / v_3^{re^2} + \sigma_{Y_{32}}^{im^2} / Y_{32}^{im^2}), \quad (4.46m)$$

$$[\sigma_H]_{42} = v_1^{im^2} Y_{31}^{re^2} (\sigma_{Y_{31}}^{re^2} / Y_{31}^{re^2} + \sigma_{v_1^{im}}^2 / v_1^{im^2}) + Y_{31}^{im^2} v_1^{re^2} (\sigma_{v_1^{re}}^2 / v_1^{re^2} + \sigma_{Y_{31}}^{im^2} / Y_{31}^{im^2}) + v_2^{im^2} Y_{32}^{re^2} (\sigma_{Y_{32}}^{re^2} / Y_{32}^{re^2} + \sigma_{v_2^{im}}^2 / v_2^{im^2}) + Y_{32}^{im^2} v_2^{re^2} (\sigma_{v_2^{re}}^2 / v_2^{re^2} + \sigma_{Y_{32}}^{im^2} / Y_{32}^{im^2}) + 4Y_{33}^{im^2} v_3^{re^2} (\sigma_{v_3^{re}}^2 / v_3^{re^2} + \sigma_{Y_{33}}^{im^2} / Y_{33}^{im^2}), \quad (4.46n)$$

$$[\sigma_H]_{43} = v_3^{im^2} Y_{32}^{im^2} (\sigma_{v_3^{im}}^2 / v_3^{im^2} + \sigma_{Y_{32}}^{im^2} / Y_{32}^{im^2}) + v_3^{re^2} Y_{32}^{re^2} (\sigma_{v_3^{re}}^2 / v_3^{re^2} + \sigma_{Y_{32}}^{re^2} / Y_{32}^{re^2}), \quad (4.46o)$$

$$[\sigma_H]_{44} = v_1^{im^2} Y_{31}^{im^2} (\sigma_{v_1^{im}}^2 / v_1^{im^2} + \sigma_{Y_{31}}^{im^2} / Y_{31}^{im^2}) + v_2^{im^2} Y_{32}^{im^2} (\sigma_{v_2^{im}}^2 / v_2^{im^2} + \sigma_{Y_{32}}^{im^2} / Y_{32}^{im^2}) + 4v_3^{im^2} Y_{33}^{im^2} (\sigma_{v_3^{im}}^2 / v_3^{im^2} + \sigma_{Y_{33}}^{im^2} / Y_{33}^{im^2}) + v_1^{re^2} Y_{31}^{re^2} (\sigma_{v_1^{re}}^2 / v_1^{re^2} + \sigma_{Y_{31}}^{re^2} / Y_{31}^{re^2}) + v_2^{re^2} Y_{32}^{re^2} (\sigma_{v_2^{re}}^2 / v_2^{re^2} + \sigma_{Y_{32}}^{re^2} / Y_{32}^{re^2}). \quad (4.46p)$$

Here,  $\sigma_x$  refer to standard deviation of  $x$ . The developed error propagation in (4.46) is validated in Appendix B using Monte Carlo simulations. It is used for computation of the uncertainty on sensitivity coefficient using indirect method. The results for the uncertainty estimation using above proposed approach are discussed in Sec. 4.5.

### 4.3.6 Simulation Setup for the Admittance Matrix Estimation

#### Input data-set

To evaluate and compare the performance of the proposed methods, we estimate the admittance parameters of selected power grid benchmarks starting from noisy phasor measurements. First, load flows are solved to compute ground-truth values of voltage and current phasors. Then, these are corrupted with i.i.d. zero-mean Gaussian noise to simulate noisy measurements, as discussed in the next subsection. This procedure is described in **Algorithm 4.3**. The nodal active and reactive power injections in the load flows are from the experimental setup of the EPFL Distributed Electrical Systems Laboratory [72] (peak consumption of 350 kW with 95 kWp of PV generation). These measurements are rescaled according to the nominal power of the respective node of the test network. The rescaling is performed by first dividing the nodal demand/generation profiles of the original system in [72] by their nominal nodal powers and, then multiplying by the nominal nodal powers of the test network.

---

#### Algorithm 4.3 Raw-data generation

---

**Require:** Admittance:  $\mathbf{Y}$ , nodal power injections:  $\mathbf{p}, \mathbf{q}$

```

1: procedure GENDATA
2:   for  $k = 1 : K$  do
3:      $[\mathbf{v}(k), \mathbf{i}(k)] = \text{LoadFlow}(\mathbf{p}(k), \mathbf{q}(k), \mathbf{Y})$ 
4:     for  $\lambda = [\mathbf{v}(k), \mathbf{i}(k)]$  do
5:        $\delta_m = \mathcal{N}(0, \frac{\sigma^m}{3} |\lambda|)$ 
6:        $|\lambda| = |\lambda| + \delta_m$ 
7:        $\delta_\phi = \mathcal{N}(0, \frac{\sigma^p}{3})$ 
8:        $\arg(\lambda) = \arg(\lambda) + \delta_\phi$ 
9:        $\lambda = |\lambda| \exp(j \arg(\lambda))$ 
10:    end for
11:  end for
12: end procedure
```

---

#### Noise Model

The measurements of ITs are characterised by errors in polar coordinates (i.e., given in terms of phasors and magnitudes), not in rectangular coordinates. Therefore, we introduce noise in polar coordinates defined by the standard IEC IT class types [127, 128]. The voltage and current measuring instruments are characterized by a phase and magnitude error, specified by the manufactures in form of percentage  $\sigma^m$  for magnitudes and in radians  $\sigma^p$  for the phase error. The values of  $\sigma^m$  and  $\sigma^p$  are listed in the Table 4.1 as defined by [127, 128].

**Hypothesis 4.5** *The ITs do not have a bias, and they behave according to standards; the magnitude and phase angle error of the ITs are Gaussian. The noise introduced by the PMUs is negligible compared to the one of the ITs (e.g. [130, 131]).*

### 4.3 Indirect Estimation of Sensitivity Coefficients via Estimation of Compound Admittance Matrix

Table 4.1: Errors specifications for different class of Instrument Transformers.

IT class	Voltage transformers [128]		Current transformers [127]	
	mag. error ( $\sigma^m$ ) [%]	phase error $\sigma^p$ [rad.]	mag. error ( $\sigma^m$ ) [%]	phase error $\sigma^p$ [rad.]
0.1	0.1	1.5e-3	0.1	1.5e-3
0.2	0.2	3e-3	0.2	3e-3
0.5	0.5	6e-3	0.5	9e-3
1	1	12e-3	1	18e-3

We add a Gaussian and i.i.d. unbiased noise (**Hypothesis** (4.5)) to the voltage and current measurements in the polar coordinates, which is then projected onto the rectangular coordinates. Although Gaussian property may not be preserved upon the transformation, the transformed noise can be approximated as a Gaussian distribution for the IT classes<sup>29</sup> of Table 4.1 as shown in [122].

#### Performance Metrics for Admittance Estimation

We measure the performance of the estimation algorithm by the three following metrics.

- The Normalized Mean Square Error (NMSE) between the true ( $\hat{\mathbf{X}}$ ) and the estimated ( $\mathbf{X}^*$ ) quantities as:

$$\mathcal{E}(\mathbf{X}^*, \hat{\mathbf{X}}) = \mathcal{E}_{\mathbf{X}} = \frac{\|\hat{\mathbf{X}} - \mathbf{X}^*\|_2}{\|\hat{\mathbf{X}}\|_2} \quad (4.47)$$

$\mathcal{E}_{\mathbf{X}}$  is a dimensionless quantity, the value  $\mathcal{E}_{\mathbf{X}} = 0$  indicates a perfect estimation.

- Comparison in terms of per unit (pu) of the estimated and original parameters; per unit (pu) values are computed by dividing the parameter impedance/admittance by the base impedance/admittance. The base impedance/admittance is computed using the base power and base voltage of the system.
- Element-wise relative error of the estimated admittance. It is expressed for real and imaginary parts of each element of the compound admittance matrix defined as

$$\Delta \mathbf{Y} = \hat{\mathbf{Y}} - \mathbf{Y}^* = \Re(\Delta \mathbf{Y}) + j\Im(\Delta \mathbf{Y}) \quad (4.48)$$

where  $\hat{\mathbf{Y}}$  and  $\mathbf{Y}^*$  are true and estimated admittance matrices,  $\Delta \mathbf{Y}$  is the element-wise error on estimated admittance. We define the relative element-wise error of estimated

<sup>29</sup>According to [127, 128], the maximum measurement noise for a calibrated IT (i.e. without a bias) is associated to the magnitude and phase errors reported in Table 4.1.

admittance on real ( $\Delta_{\Re}\tilde{\mathbf{Y}}$ ) and imaginary ( $\Delta_{\Im}\tilde{\mathbf{Y}}$ ) elements as

$$\Delta_{\Re}\tilde{\mathbf{Y}} = \Re(\Delta\mathbf{Y}) \oslash \Re(\hat{\mathbf{Y}}) \quad (4.49a)$$

$$\Delta_{\Im}\tilde{\mathbf{Y}} = \Im(\Delta\mathbf{Y}) \oslash \Im(\hat{\mathbf{Y}}) \quad (4.49b)$$

where  $\oslash$  refers to Hadamard division (i.e., element-wise division of a matrix). Later, we show these relative component-wise errors on the real and imaginary part of the admittance matrix in a heatmap plots for the different strategies.  $\Delta_{\Re}\tilde{\mathbf{Y}}, \Delta_{\Im}\tilde{\mathbf{Y}}$  are dimensionless as they are relative errors (these relative errors are zero for a perfect estimation).

- Uncertainty of the estimated parameters: is computed by their variances. The variances of the estimates are given by

$$\sigma_{\mathbf{X}} = \sqrt{\sigma_r^2 \text{diag}((\mathbf{H}^T \mathbf{H})^{-1})} \quad (4.50)$$

where  $\sigma_r$  is estimated variance of the residuals in (4.23) post-estimation. We determine the uncertainty corresponding to 99% confidence interval approximated by  $\pm 3 \sigma_{\mathbf{X}}$ .

#### 4.3.7 Results and Discussion

We use the data sets from simulated experiments on different benchmark distribution grids, as described earlier, to estimate their admittance parameters. We compare the estimation performances using: *i*) the raw measurements (denoted by “Raw-data”), *ii*) the pre-processed data with block-averaging (denoted by “Block-averaging”) and *iii*) the pre-processed data with cluster-averaging (denoted by “Cluster-averaging”). Figure 4.3 summarizes the steps used for the estimation using cluster-averaged data. Raw measurements are directly used for the estimations in the “Raw-data” case. They are not subject to any pre-processing and all the measurements are used once for the estimation of the parameters. The results are reported for both LS and TLS techniques.

A sensitivity analysis with respect to different levels of measurement noise is presented. Then, a performance comparison is presented against different clustering strategy (such as cluster features, number of clusters). Finally, we compare the estimation performances with availability of branch and injection currents measurements.

#### Estimation Performance on Benchmark Test Cases

We present a detailed estimation performance analysis applied to the IEEE 4-bus benchmark network. It is an unbalanced and untransposed three-phase distribution system with artificially added shunt parameters. The details on the parameters, topologies and nominal demand can be found in [118]. The topology is shown in Fig. 4.4. The estimations are performed with an estimation model comprising of both the injection and branch currents measurements. We use a single day of simulated measurements of nodal voltages, branch, and

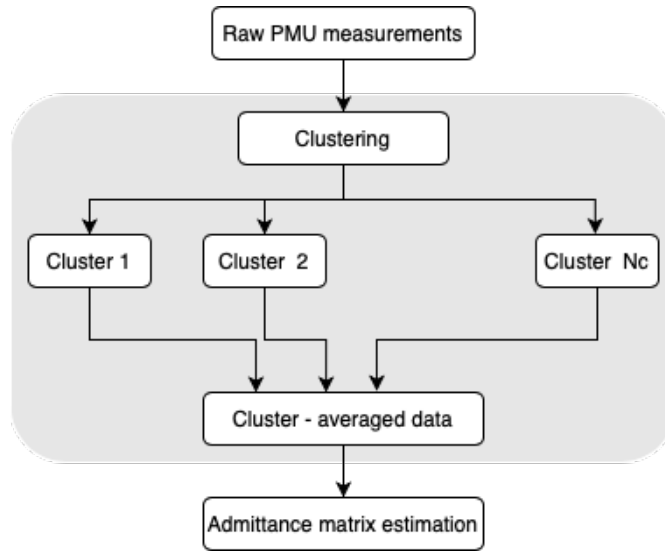


Figure 4.3: Flow diagram for the admittance matrix estimation using cluster-averaged data.

injection currents (**Algorithm 4.3**) at a 1-second resolution. We first consider instrument type of class 0.2 (Table 4.1). We compare the estimation performance when using directly the raw measurements (from **Algorithm 4.3**), block-averaging (first **Algorithm 4.3** then **Algorithm 4.2**) and cluster-averaging (first **Algorithm 4.3** then **Algorithm 4.1**). For the first one, we use all the measurements for the admittance estimation. For the last two, the estimations are compared using the same number of blocks as the number of clusters to have a fair comparison. We use 1-hour blocks in the block-averaging method of **Algorithm 4.2** and 24 clusters (24 clusters in a day according to block-averaging of 1-hour as blocks) in the cluster-averaging method of **Algorithm 4.1**. The corresponding averaged values of each cluster or block are used for the admittance matrix estimation. A sensitivity analysis with cluster size and features will be discussed later in the Chapter.

Table 4.2 shows the estimation performance for IEEE 4-bus unbalanced and untransposed three-phase network. It shows the NMSEs using LS and TLS techniques. The first, second and

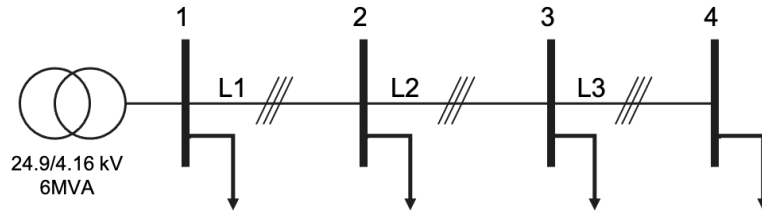


Figure 4.4: Topology of the adopted IEEE 4-bus network.

the third rows show estimations when using raw, block-averaged and cluster-averaged data, respectively. It shows the NMSEs for conductances, susceptances, shunts and compound admittance matrices denoted by  $\mathcal{E}_{X^G}$ ,  $\mathcal{E}_{X^B}$ ,  $\mathcal{E}_{X^T}$  and  $\mathcal{E}_Y$  respectively (as defined in (4.47)).

## Chapter 4. Data-driven Estimation of Compound Admittance Matrix and Power-Flow Sensitivity Coefficients

Table 4.2: Estimation performance for the IEEE 4-bus network.

Data	Method	$\mathcal{E}_{\mathbf{X}^G}$	$\mathcal{E}_{\mathbf{X}^B}$	$\mathcal{E}_{\mathbf{X}^T}$	$\mathcal{E}_Y$
Raw-data	LS	0.124	0.172	0.337	0.181
	TLS	0.027	0.035	0.147	0.038
Block-averaging (1-hour block)	LS	0.191	0.145	0.016	0.163
	TLS	0.229	0.117	0.021	0.137
Cluster-averaging (24 clusters)	LS	0.008	0.002	0.014	0.003
	TLS	0.008	0.002	0.014	0.003

As it can be seen, the estimations are poor using the raw data, whereas they improve significantly with cluster-averaged data and thus have better estimation of the admittance matrix. With the cluster-averaging policy, the NMSEs decreases by 2-3 orders of magnitude compared to the raw-data. The estimations using block-averaging are also poor compared to the cluster-averaging and slightly better than the raw-data case. The block-averaging method performs the worst with TLS.

Fig. 4.5 shows the plots of the true and estimated three-phase line and shunt parameters for the LS using the raw-data, block-averaging, and cluster-averaging cases. We also show the uncertainty of the estimates using error bars corresponding to 99 % confidence interval. The upper, middle and the bottom plots show the comparison for the true and estimated conductances, susceptances and shunts, respectively. The estimates are expressed in pu as described in Sec. 4.3.6 (we use respectively the base power and voltage of 6 MVA and 4.16 kV corresponding to a base admittance of 0.3467 S.) From the plots, it is clear that the estimation model with cluster-averaging successfully estimates the longitudinal and shunts parameters and has the least uncertainty of the parameter estimates, whereas the estimates using the raw-data and block-averaging have high biases and uncertainties. Also, it can be observed that the methods using the raw measurements and block-averaging fail to identify the parameters which are zero (line L2 and shunts for all the lines are assumed to have zero off-diagonal elements in the studied IEEE 4-bus test case). Indeed they are estimated to be non-zero, whereas cluster-averaging correctly estimates it.

We also show the heatmaps of the element-wise relative error for the real and imaginary part of the compound admittance matrix. Fig. 4.6(a-b), (c-d) and (e-f) shows the estimation error for LS with raw-data, block-averaging and cluster-averaging strategies, respectively. The heatmap plots have node indices of the network as  $x$ - and  $y$ - axes, whereas the color shows the element-wise estimation error on non-zero elements of the admittance matrix using (4.49). The heatmap has the dimension of 12 on  $x$ - and  $y$ -axis because we are dealing with a 3-phase 4 node system with an admittance matrix dimension of  $12 \times 12$ . The comparison shows that the estimations with raw-data and block-averaging have high errors with maximum error upto 200 %. In contrast, we obtain near-perfect estimations by using the cluster-averaging strategy with a maximum absolute element-wise error below 3 %.

### 4.3 Indirect Estimation of Sensitivity Coefficients via Estimation of Compound Admittance Matrix

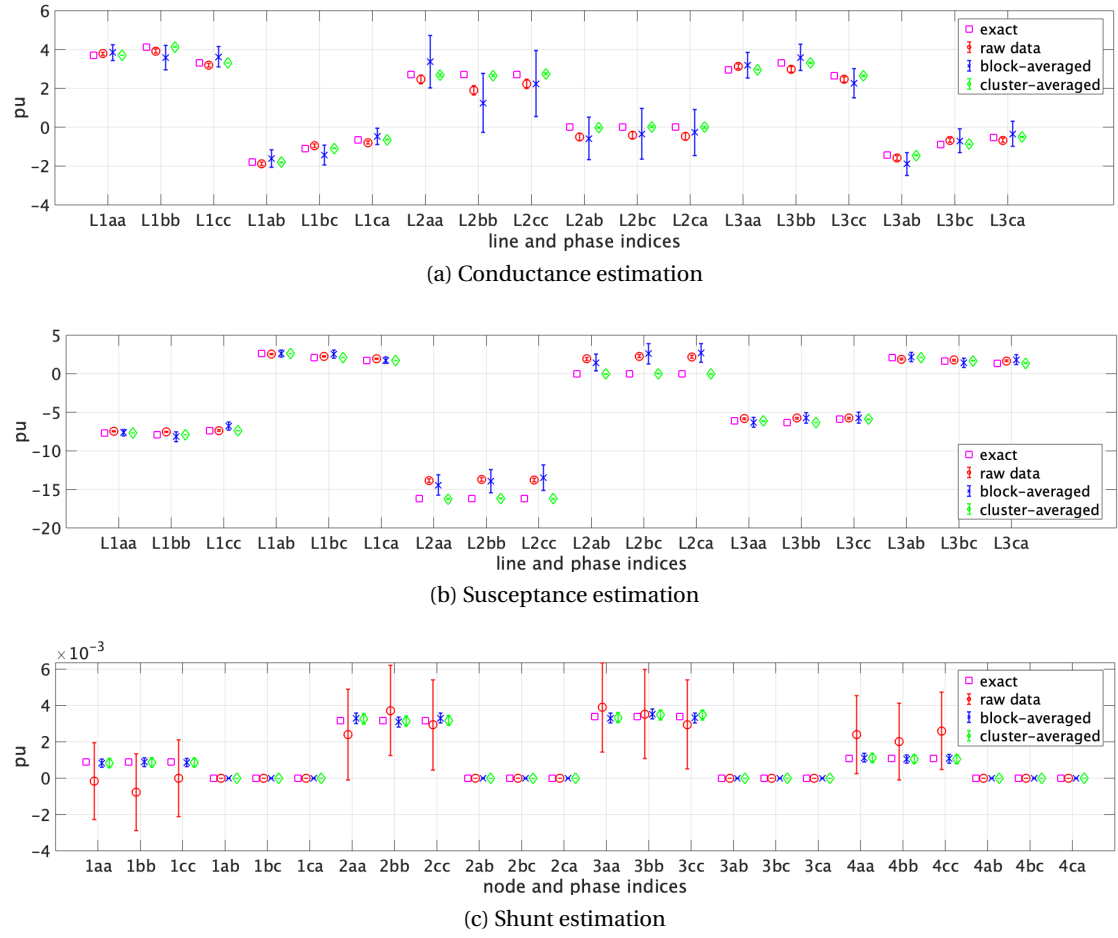


Figure 4.5: Estimation performance of the parameters (a) conductances (b) susceptance and (c) shunts of the IEEE 4-bus untransposed and unbalanced test network with raw measurements, block-averaged and with cluster-averaged data with LS. Error bars on top of each estimated value shows the uncertainty of the estimates (99 % confidence interval) using (4.50). L1, L2, L3 refer to different branches and a, b, c refer to different phases of the IEEE 4-bus system in Fig. 4.4.

In view of the above, we can conclude that the pre-processing on raw-data by cluster-averaging largely improves the estimation performance compared to using the raw-data directly or simple block-averaging.

#### Other Test Cases

We also perform estimation on several other networks (BT = balanced and transposed, UU = unbalanced and untransposed). The results are summarized in Table 4.3. We show the NMSEs on admittance estimation ( $\mathcal{E}_Y$ ) for different publicly available test cases.

From the comparison, it can be seen that the proposed method gives good estimations for all



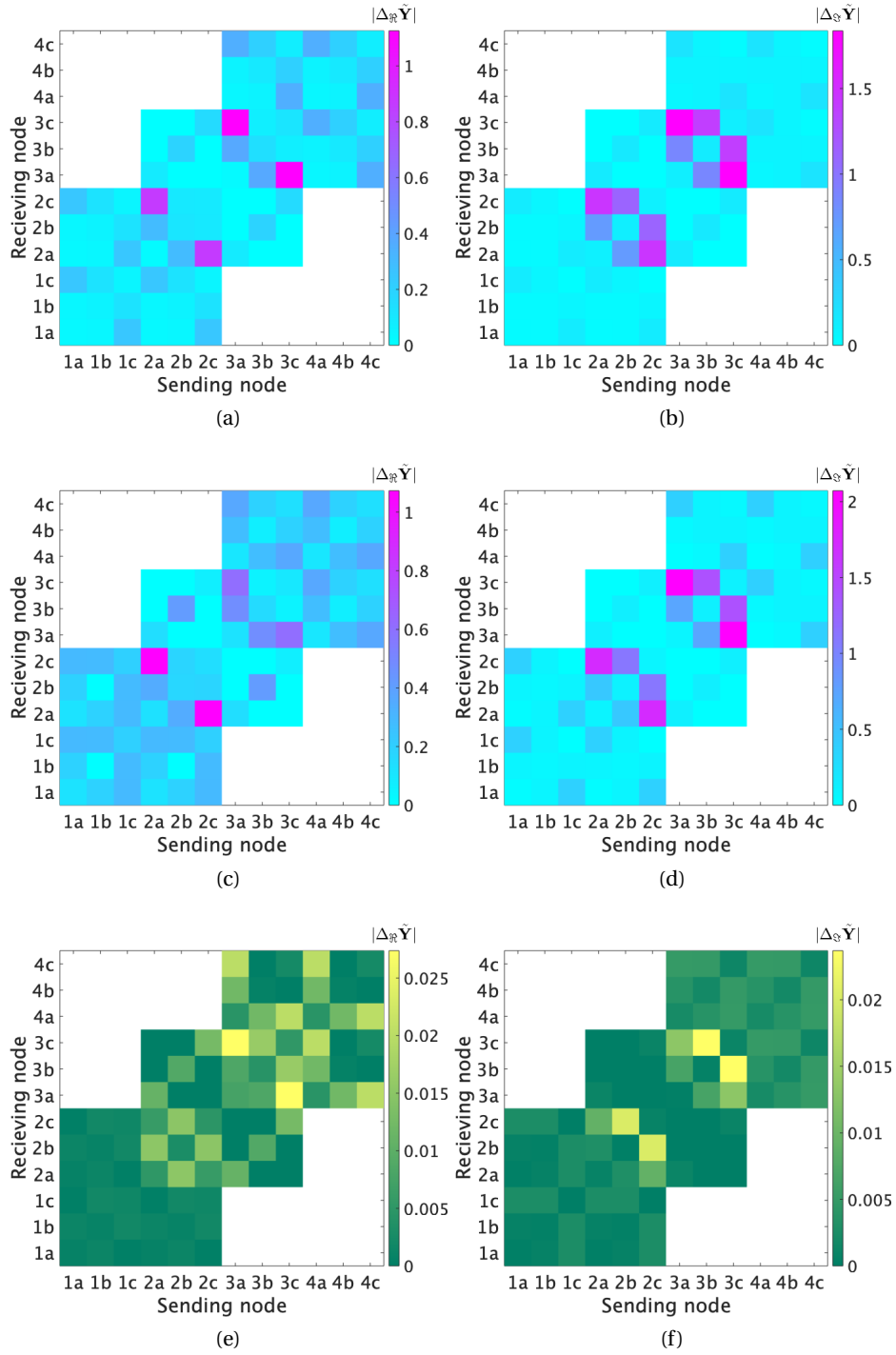


Figure 4.6: Element-wise relative error computed via (4.49) on real (left) and imaginary (right) part of the estimated compound admittance matrix for the IEEE 4-bus test network using the raw data in (a-b), using the block-averaging in (c-d) and using the cluster-averaged in (e-f) with LS.

### 4.3 Indirect Estimation of Sensitivity Coefficients via Estimation of Compound Admittance Matrix

Table 4.3: NMSE on admittance estimation for different networks.

Test-networks	Raw-data		Cluster-averaging	
	LS	TLS	LS	TLS
CIGRE MV (BT)	0.897	6.137	0.016	0.012
CIGRE LV (BT)	0.620	5.877	0.002	0.002
CIGRE LV (UU)	0.371	4.77	0.033	0.037
CIGRE microgrid (BT)	0.884	6.812	0.044	0.019
IEEE13 (UU)	0.585	2.961	0.060	0.056
IEEE123 (BT)	0.946	15.551	0.060	0.060

the tested networks. With TLS, we observe that the NMSEs are high in case of raw-data. This happens because the TLS tries to compensate for the original measurement noise estimating the true (unobservable)  $\hat{\mathbf{H}}$  and  $\hat{\mathbf{J}}$  along with the admittance parameters resulting in large number of estimation variables compared to the LS. This is mitigated by the cluster-averaging which reduces the noise level on the measurements and number of true measurements to be estimated.

#### Sensitivity Analysis

**Noise Level:** we perform estimations using simulated experiments with noise of the IT classes 0.1, 0.2, 0.5 and 1 (Table 4.1) according to **Algorithm 4.3**. The results are reported for IEEE 4-bus network. We use the same clustering features and  $N_c$  as in Sec 4.3.7. Table 4.4 shows the NMSEs on admittance estimation for LS and TLS with respect to noise level. As it can be seen, the NMSEs obtained using cluster-averaging is 2-3 order of magnitude better compared to the case without averaging, for all cases. The TLS method with cluster-averaging policy performs the best.

Table 4.4: NMSE on admittance estimation ( $\mathcal{E}_Y$ ) with different noise levels for IEEE 4-bus network.

IT class	Raw-data		Cluster-averaging	
	LS	TLS	LS	TLS
0.1	0.064	0.012	0.002	0.002
0.2	0.181	0.038	0.003	0.003
0.5	0.404	0.148	0.010	0.009
1	0.548	9.171	0.018	0.014

**Clustering Strategy:** we investigated different clustering strategies for the cluster-averaging policy. We vary the clustering features used in **Algorithm 4.1** and use them for admittance

## Chapter 4. Data-driven Estimation of Compound Admittance Matrix and Power-Flow Sensitivity Coefficients

estimation. The analysis is presented in terms of NMSEs on admittance estimation in Table 4.5 for IEEE 4-bus network with IT class 0.5. From the analysis, we conclude that the clustering features comprising of the magnitudes of the nodal voltages and currents perform the best.

Table 4.5: NMSE on admittance estimation ( $\mathcal{E}_Y$ ) with clustering features.

Clustering features	LS	TLS
Voltage magnitude	0.036	0.024
Current magnitude	0.021	0.021
Voltage and current magnitude	0.010	0.009
Sequence voltage magnitude	0.066	0.432
Sequence current magnitude	0.054	0.056
Sequence voltage and current magnitude	0.019	0.018

We also analysed the sensitivity on the estimation performance with the number of clusters in the cluster-averaging policy. The feature used for this simulation is the dominant feature inferred from the last analysis, namely, the magnitudes of voltages and currents together. The analysis is presented for the IEEE4 system with IT class of 0.5. We perform cluster averaging on the raw data of 86,400 data points (corresponding to per second single day measurement) with  $N_c = 25, 50, 100, 300, 500, 1000, 5000$  and 10,000 (refer to **Algorithm 4.1**). The NMSEs on estimated admittance matrix ( $\mathcal{E}_Y$ ) are plotted in Fig. 4.7 for LS and TLS techniques. As it can be observed, the estimation performance improves with decrease in number of clusters. This happens because the cluster-averaging scheme reduces the noise levels on the voltage and current measurements, leading to improvement in estimation quality. The estimations worsen slightly if we go below  $N_c = 100$ , this is because the number of input data points in the estimation model becomes smaller or comparable to the number of variables to be estimated. The optimal value of  $N_c$  is subject to future investigations as the NMSE metric is inaccessible for practical cases.

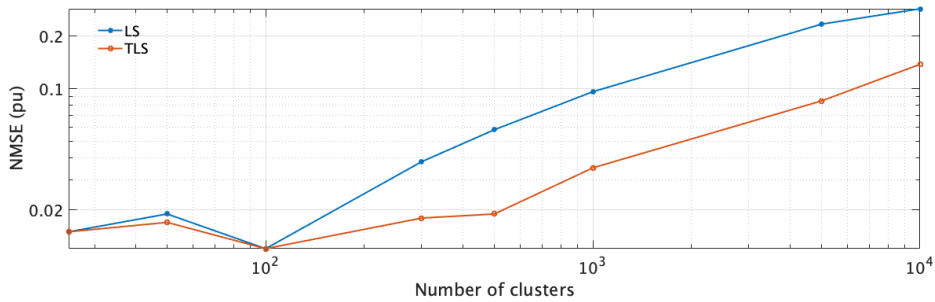


Figure 4.7: NMSE ( $\mathcal{E}_Y$ ) as a function of the cluster size for IEEE 4-bus network.

**Injection Current vs Branch Current Model vs Both:** we here compare the performance of the proposed estimation process when using: (i) injection currents and (ii) branch currents

### 4.3 Indirect Estimation of Sensitivity Coefficients via Estimation of Compound Admittance Matrix

along with injection currents. The comparison is done for the IEEE 4-bus system with IT class 0.2 in Table 4.6. The analysis is presented for LS. We use the same settings for the block- and cluster-averaging as in Sec 4.3.7. The comparison shows that the estimation using the cluster-averaging method is not affected significantly even without branch currents information, whereas the other two methods estimations deteriorate. It is worth noting that the use of the branch current measurements improves the estimation performance significantly, especially for the shunt admittances. This happens because the estimation variables are related to the branch current (as in (4.15)) individually and can be estimated in a decoupled way, whereas the estimation variables are interlinked to each other in the model relying on injection currents, and so they are not decoupled.

Table 4.6: Estimation performance for the IEEE 4-bus network with availability of measurements on injection current and branch currents.

Data	Current	$\mathcal{E}_{\mathbf{X}^G}$	$\mathcal{E}_{\mathbf{X}^B}$	$\mathcal{E}_{\mathbf{X}^T}$	$\mathcal{E}_{\mathbf{Y}}$
Raw-data	Injection	0.138	0.213	2.392	0.221
	Branch + Injection	0.124	0.172	0.337	0.181
Block-averaging (1-hour block)	Injection	0.381	0.201	0.101	0.239
	Branch + Injection	0.191	0.145	0.016	0.163
Cluster-averaging (24 clusters)	Injection	0.008	0.002	0.027	0.008
	Branch + Injection	0.008	0.002	0.014	0.003

#### Further Analysis

In this section, we show how the cluster-averaging method groups the raw-data in different clusters. This analysis gives an insight on why cluster-averaging improves the parameter estimation.

**Effect of Cluster Averaging on the Raw Measurement Data:** we show this analysis for the IEEE 4-bus test network (Fig. 4.4). We use the same clustering features (voltage and current magnitudes) and  $N_c$  as in Sec 4.3.7.

Fig. 4.8a shows the distribution of the 1-sec time-indices (86400-time steps) during the day in the 24 clusters as a result of `kmeans` clustering. In Fig. 4.8b and Fig. 4.8c, we also show the variation of the nodal voltage and current magnitudes respectively for the non-zero injection nodes which were used for the clustering. Fig. 4.8a  $y$ -axis (left) shows the cluster number, and the corresponding time-steps that fall into clusters are shown in black. In the same plot, we also include the number of elements per cluster on the right  $y$ -axis of Fig. 7(a). As it can be seen, the clustering does not group the data that is contiguous in time. Instead, data belonging to a given cluster is distributed throughout the day. In particular, the clustering scheme groups measurements with similar magnitudes (considering all the nodes and phases). For example,

## Chapter 4. Data-driven Estimation of Compound Admittance Matrix and Power-Flow Sensitivity Coefficients

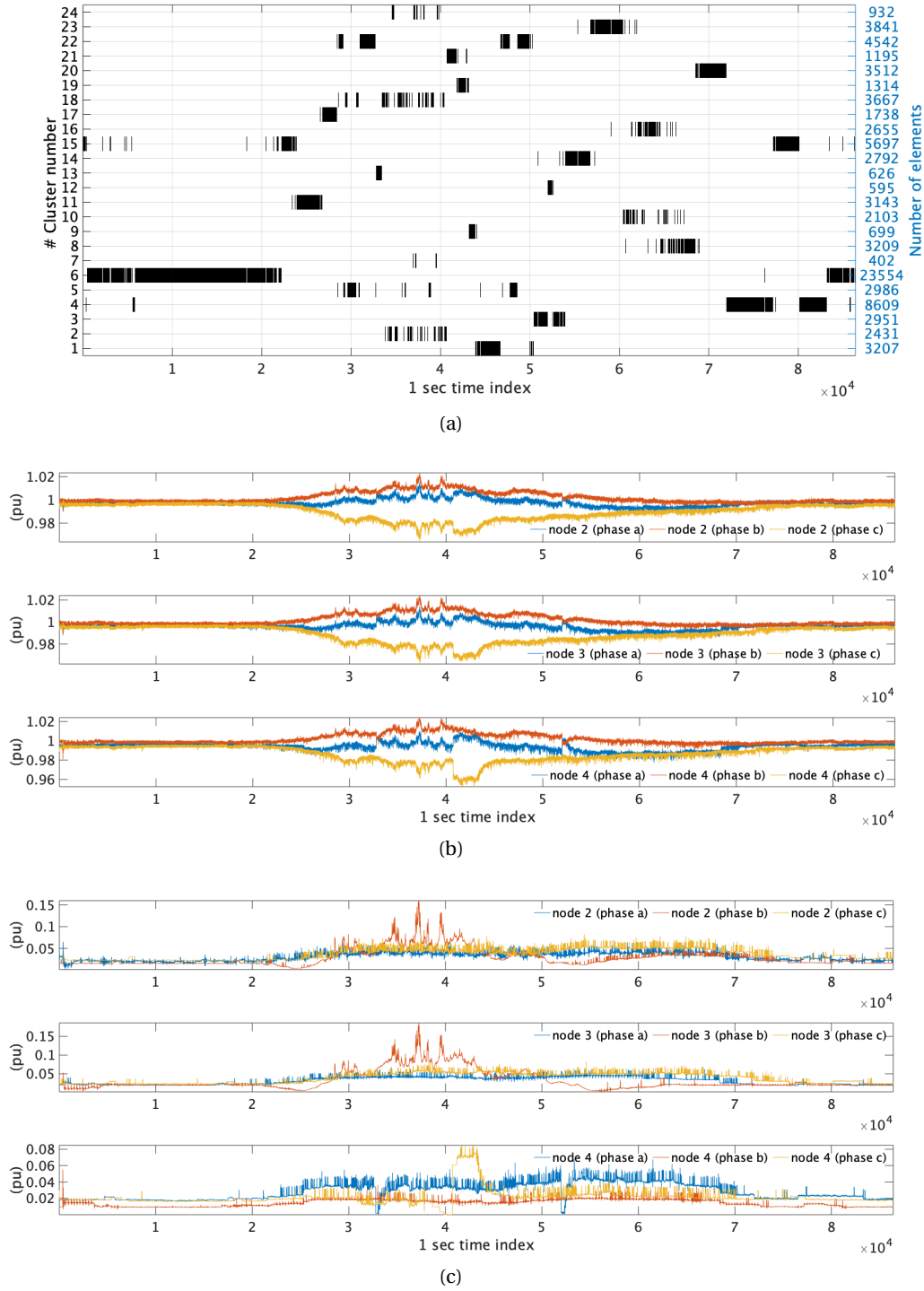


Figure 4.8: Distribution of the 86400 time steps during the day into 24 clusters as a result of cluster averaging: (a) measurements assigned to different clusters with number of elements (right) per cluster, (b) nodal voltage magnitudes (in pu) and (c) nodal current magnitudes (in pu) for all the nodes and phases (except slack node) for 24 hrs.

### 4.3 Indirect Estimation of Sensitivity Coefficients via Estimation of Compound Admittance Matrix

in cluster-6, most of the measurements are balanced among phases with voltage magnitudes close to 1 pu and current injections below 0.05 pu. Similarly, in clusters-9, 19, and 21, the measurements observing a sudden dip in the nodal voltages (caused by increased demand at node 4 phase c) are clustered together. Another example is cluster-12 and 13, which capture slight variation in the voltages due to a dip in demand at node 4 phase a. Clusters-2, 18, and 24 captures sharp generation peaks due to PV injections from node 2 (phase b) and node 3 (phase b).

Furthermore, to show the distribution of the data as a result of the averaging strategies, we show zero and negative sequence normalized by positive sequence component for all the nodes for each cluster in the bar plot of Fig. 4.9. They are defined as follows: **Neg. seq.** and **Zero seq.** are defined as the percentage of the negative and zero sequence components with respect to the positive sequence components, respectively. It is given as **Neg. seq.**

$$\frac{|\mathbf{v}_{\text{neg}}|}{|\mathbf{v}_{\text{pos}}|} \times 100\% \quad (4.51)$$

and **Zero seq.**

$$\frac{|\mathbf{v}_{\text{zero}}|}{|\mathbf{v}_{\text{pos}}|} \times 100\% \quad (4.52)$$

where  $\mathbf{v}_{\text{pos}}$ ,  $\mathbf{v}_{\text{neg}}$ ,  $\mathbf{v}_{\text{zero}}$  are positive, negative and zero sequence components respectively.

Fig 4.9(a) and 4.9(b) show the barplots corresponding to **Neg. seq.** and **Zero seq.**, respectively for block-averaged and cluster-averaged data. As seen from the figure, cluster-averaging produces clusters where the positive and negative sequence components are higher than in the block-averaging case.

Table 4.7 summarizes the mean and max of **Neg. seq.** and **Zero seq.** for all the clusters. In view of the above comparisons, it can be seen that the cluster averaging provides higher values of positive and negative sequence components compared to the ones obtained using the block averaging. This feature helps to take into account the contribution of off-diagonal elements of line impedance and shunt admittance matrices in the grid's compound admittance matrix.

Table 4.7: Percentage of negative and zero sequence components with respect to positive sequence components.

Method	Neg. seq. (%)		Zero seq. (%)	
	mean	max	mean	max
Block-averaging	0.32	0.80	0.69	2.04
Cluster-averaging	0.49	1.71	1.15	4.05

In this section, we only presented the estimation performance of the proposed  $\mathbf{Y}$  estimation scheme. The results of sensitivity computation using the estimated  $\mathbf{Y}$  (indirect approach) will be shown later in Sec. 4.5 after describing other proposed schemes for estimating sensitivity

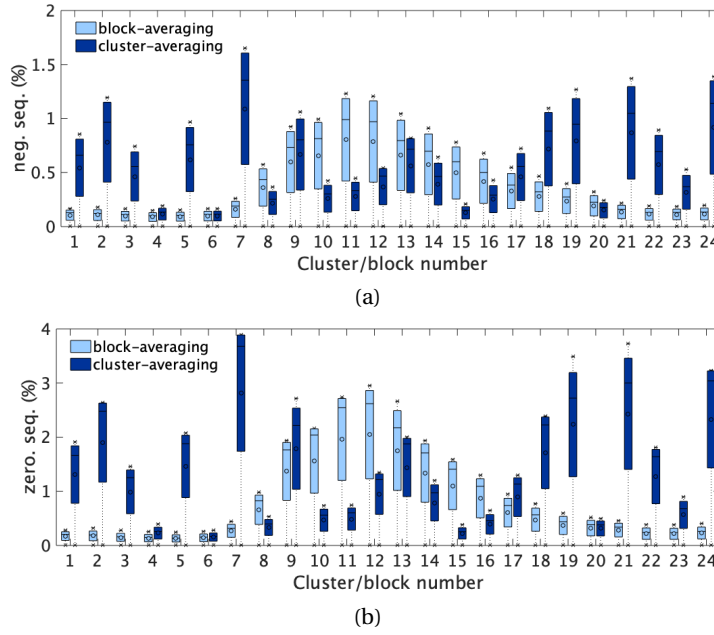


Figure 4.9: Distribution of negative and zero sequence components normalised by the positive sequence component after block-averaging and cluster averaging on raw-data.

coefficients, i.e., the direct estimation method. It allows a better performance comparison between the two methods, i.e., the indirect and direct methods.

## 4.4 Direct Estimation of Sensitivity Coefficients

In this section, we present the method for direct estimation of the sensitivity coefficients. First, we present an estimation model, then the proposed two-stage estimation scheme. Finally, we present the estimation performance. The objective is to estimate the voltage sensitivity coefficients and their uncertainties by using the measurements of nodal voltage magnitudes, active and reactive powers. The method is described as follows.

### 4.4.1 Estimation Model

We assume the following hypothesis to hold true.

**Hypothesis 4.6** *The operator does not know the network parameters, the topology, and the system state.*

**Hypothesis 4.7** *The network is equipped with measurements units providing the user with the measurements of voltage magnitudes, and active and reactive power injections at regular time intervals. The metering devices are aligned with a network time protocol (e.g. NTP [132]). The measurements are time-synchronised.*

**Hypothesis 4.8** *The system is in steady-state, and the power injection is subject to small dynamics that the first-order Taylor approximations can represent with sufficient accuracy [16, 17]. The sensitivity coefficients remain unchanged over a time window<sup>30</sup> (5 minutes in this case) which is used to collect adequate number of measurements in the estimation problem.*

Using the coefficient definition in (4.1), Hypothesis 4.8 and Taylor's first-order approximation, the magnitude deviation of the nodal voltages at time  $t_k$  for node  $i$  can be written as

$$\underbrace{|\Delta v|_{i,t_k}}_{\gamma_{t_k}} \approx \underbrace{[\Delta \mathbf{p}_{t_k} \ \Delta \mathbf{q}_{t_k}]}_{h_{t_k}} \underbrace{\begin{bmatrix} \mathbf{K}_{i,t_k}^p \\ \mathbf{K}_{i,t_k}^q \end{bmatrix}}_{\mathbf{X}} \quad (4.53)$$

where  $|v|_{i,t_k} - |v|_{i,t_{k-1}} = |\Delta v|_{i,t_k} \in \mathbb{R}$  is the deviation of nodal voltage magnitude of  $i$ -th node, vectors  $\mathbf{p}_{t_k} - \mathbf{p}_{t_{k-1}} = \Delta \mathbf{p}_{t_k}$ ,  $\mathbf{q}_{t_k} - \mathbf{q}_{t_{k-1}} = \Delta \mathbf{q}_{t_k} \in \mathbb{R}^{N_b}$  include deviations of active and reactive powers of all the nodes from timestep  $t_{k-1}$  to  $t_k$ . The vectors  $\mathbf{K}_{i,t_k}^p, \mathbf{K}_{i,t_k}^q \in \mathbb{R}^{N_b}$  include voltage sensitivity coefficients of  $i$ -th node with respect injections of nodes  $j \in \mathcal{N}$ . It should be noted that the approximation in (4.53) of the power-flow equations involves two errors: (i) the linearization and (ii) the measurement noise. In this work, we assume that the linearization error is negligible compared to the one due to the measurement noise. This assumption is reasonable if the state of the system is slow varying and the control is acting in quasi real-time. Assuming that we have measurements for time  $t = t_1 \dots, t_T$  and coefficients do not change for  $T$  timesteps (Hypothesis 4.8), Eq. (4.53) can be written as

$$\Gamma \approx \mathbf{H}\mathbf{X} \quad (4.54)$$

where,  $\Gamma \in \mathbb{R}^T = [\gamma_{t_1} \gamma_{t_2} \dots \gamma_{t_T}]^\top$ ,  $\mathbf{H} \in \mathbb{R}^{T \times 2N_b} = [h_{t_1} h_{t_2} \dots h_{t_T}]^\top$  and  $\mathbf{X} \in \mathbb{R}^{2N_b}$  includes  $\mathbf{K}_{i,t_k}^p$  and  $\mathbf{K}_{i,t_k}^q$ . Eq. (4.54) can be re-written assuming noise model to be white Gaussian (Hypothesis 4.5).

$$\Gamma = \mathbf{H}\mathbf{X} + \mathcal{W} \quad \mathcal{W} \in \mathcal{N}(\mathbf{0}, \Sigma), \quad (4.55)$$

$\Sigma$  refers to the noise covariance matrix.

#### 4.4.2 Estimation Technique

The linear model in (4.55) is typically solved for  $\mathbf{X}$  by minimizing the norm-2 difference of the residual, known as Least-Squares (LS). However, the LS method does not perform well in case of low excitation (nodal power injections are small) and suffers from the problem of multicollinearity (power injections at different nodes are very similar) [102, 103]. Also because the sensitivity coefficients vary as a function of network's states, it is necessary to use the most recent estimates during a real-time control. Thus, an online estimation scheme was used in

<sup>30</sup>We assume that there is no significant change in the network's operating conditions, such as topology or step change of the load/generation. If it happens, the fixed time window could be replaced by a variable time window where sensitivity coefficients are re-estimated.



## Chapter 4. Data-driven Estimation of Compound Admittance Matrix and Power-Flow Sensitivity Coefficients

[103, 133] that used recursive least square (RLS)-based estimation coupled with an offline LS.

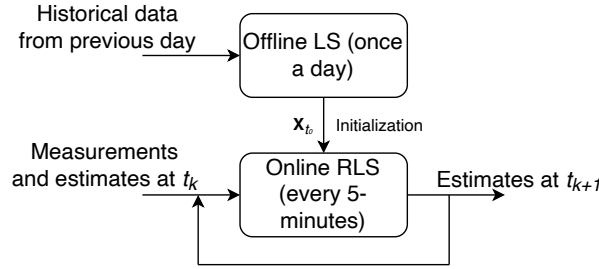


Figure 4.10: Flow diagram for two-stage estimation of sensitivity coefficients.

In this work, we use this scheme to estimate the sensitivity coefficients. Figure 4.10 shows the dataflow of the estimation process. First, the LS is used to get a rough estimate of the coefficients. Then, the RLS is used to refine the LS estimates by using the latest information on the voltage and power measurements. The LS is solved off-line using a large number of historical measurements. The RLS problem is solved at each time step using recent measurements where the LS estimation is used to initialize the RLS. Both the processes are described next.

### Offline LS

Offline LS problem is formulated as

$$\hat{\mathbf{X}} = \min_{\mathbf{X}} \|\Gamma - \mathbf{H}\mathbf{X}\|_2 + \lambda^{\text{reg}} \mathbf{X}^T \mathbf{X} \quad (4.56)$$

where  $\lambda^{\text{reg}}$  is a positive number that serves as a regularization parameter and is used to avoid ill-conditioned information matrix (i.e., in case of multi-collinearity nodal injections). The closed-form solution of (4.56) is obtained in view of its quadratic and unconstrained nature as,

$$\hat{\mathbf{X}}_{t_0} = (\mathbf{H}^T \mathbf{H} + \lambda^{\text{reg}} \mathbf{I})^{-1} \mathbf{H}^T \Gamma = (\mathbf{R}_{t_0} + \lambda^{\text{reg}} \mathbf{I}) \mathbf{H}^T \Gamma \quad (4.57)$$

where  $\mathbf{I}$  is the identity matrix. The covariance matrix is defined as inverse of the information matrix, i.e.  $\mathbf{P}_{t_0}^{\text{cov}} = \mathbf{R}_{t_0}^{-1} = (\mathbf{H}^T \mathbf{H})^{-1}$ .

### Online RLS

In this scheme, an online recursive estimation is performed using the most recent measurements. It utilizes the estimates from the previous time step and measurements at the current time step. RLS updates the estimates whenever the new data is available. LS solution ( $\hat{\mathbf{X}}_{t_0}$ ) in (4.57) is used to initialize the RLS stage. The use of exponential forgetting factor applied to the observations is advised to give less importance to previous measurements [134]. The

forgetting factor  $0 < \mu \leq 1$  is reflected in the covariance matrix update.

$$\mathbf{R}_{t_k} = \mu \mathbf{R}_{t_{k-1}} + h_{t_k}^T h_{t_k} \quad (4.58)$$

This results in the following iterative updates.

$$e_{t_k} = \gamma_{t_k} - h_{t_k}^T \hat{\mathbf{X}}_{t_{k-1}} \quad (4.59a)$$

$$\hat{\mathbf{X}}_{t_k} = \hat{\mathbf{X}}_{t_{k-1}} + \mathbb{G}_{t_k} e_{t_k} \quad (4.59b)$$

$$\mathbb{G}_{t_k} = \frac{\mathbf{P}_{t_{k-1}}^{\text{cov}} h_{t_k}^T}{\mu + h_{t_k}^T \mathbf{P}_{t_{k-1}}^{\text{cov}} h_{t_k}} \quad (4.59c)$$

$$\mathbf{P}_{t_k}^{\text{cov}} = (\mathbf{I} - \mathbb{G}_{t_k} h_{t_k}^T) \mathbf{P}_{t_{k-1}}^{\text{cov}} / \mu \quad (4.59d)$$

where,  $\mathbb{G}$  is the estimated gain and  $e$  the residual. In the following, this scheme is referred to as RLS-F.

As reported in [134, 135], the RLS-F scheme suffers from the windup problem of the covariance matrix. It may lead to very large covariances resulting in large estimates variances. Multiple schemes are proposed in the literature to solve this problem. They are briefly described next.

**Constant-Trace Scheme (RLS-CT):** in [136], it is discussed how to limit the windup problem of the co-variance matrix by setting an upper bound on the trace sum of the covariance matrix and adding an identity matrix  $\mathbf{I}$ . The scheme uses two different factors  $c_1$  and  $c_2$  such that  $c_1/c_2 = 10e3$ ;  $h_{t_k}^T h_{t_k}^T c_1 \gg 1$ . The covariance matrix is modified as:

$$\mathbf{P}_{t_k}^{\text{cov}} = c_1 \mathbf{P}_{t_k}^{\text{cov}} / \text{trace}(\mathbf{P}_{t_k}^{\text{cov}}) + c_2 \mathbf{I} \quad (4.60)$$

**Selective Forgetting (RLS-SF):** in [134] it is proposed to use selective forgetting factor, i.e., to use different forgetting factors for different eigenvalues of the covariance matrix. These forgetting factors are computed and updated iteratively to limit the windup problem of the covariance matrix. The gain and covariance matrix are updated as follows.

$$\mathbb{G}_{t_k} = \frac{\mathbf{P}_{t_{k-1}}^{\text{cov}} h_{t_k}^T}{1 + h_{t_k}^T \mathbf{P}_{t_{k-1}}^{\text{cov}} h_{t_k}} \quad (4.61a)$$

$$\mathbf{P}_{t_k}^{\text{cov}} = \sum_{i=1}^{2N_b} \frac{\tau_{i,t_k}}{\mu_i} u_{i,t_k}^T u_{i,t_k}. \quad (4.61b)$$

## Chapter 4. Data-driven Estimation of Compound Admittance Matrix and Power-Flow Sensitivity Coefficients

Here,  $u_{i,t_k}$  denotes the eigenvectors of  $\mathbf{P}_{t_k}^{\text{cov}}$  in Eq. (4.59d) and  $\tau_{i,t_k}$  the corresponding eigenvalues. It is proposed to limit  $\tau_{i,t_k}$  by a function  $f^{\text{SF}}$  that keeps it within bounds  $[\tau_{\min} \ \tau_{\max}]$ :

$$\tau_{i,t_k} = f^{\text{SF}}(\tau_{i,t_{k-1}}) \quad (4.61c)$$

$$f^{\text{SF}}(x) = \begin{cases} x, & x > \tau_{\max} \\ \tau_{\min} + (1 - \tau_{\min}/\tau_{\max})x & x \leq \tau_{\min} \end{cases} \quad (4.61d)$$

More information on the tuning of RLS-SF is in [134] and [136].

**Directional Forgetting (RLS-DF):** in [137, 138], a directional forgetting algorithm is proposed where the matrix  $\mathbf{R}$  is decomposed into two parts: the first part is fully propagated to the next time step, whereas the second part is propagated with a forgetting factor,  $\mu$ . This method was first proposed in [137] and termed as “directional forgetting” as the two parts of the gain matrix are orthogonal to each other. Theoretical development supporting this algorithm is in [138]. The iterative updates of RLS-DF are

$$\mathbb{G}_{t_k} = \mathbf{P}_{t_k}^{\text{cov}} h_{t_k}^T \quad (4.62a)$$

$$\bar{\mathbf{P}}_{t_{k-1}}^{\text{cov}} = \mathbf{P}_{t_{k-1}}^{\text{cov}} + \frac{1-\mu}{\mu} \frac{h_{t_k}^T h_{t_k}}{h_{t_k}^T \mathbf{R}_{t_k} h_{t_k}} \quad (4.62b)$$

$$\mathbf{P}_{t_k}^{\text{cov}} = \bar{\mathbf{P}}_{t_{k-1}}^{\text{cov}} - \frac{\bar{\mathbf{P}}_{t_{k-1}}^{\text{cov}} h_{t_k}^T h_{t_k} \bar{\mathbf{P}}_{t_{k-1}}^{\text{cov}}}{1 + h_{t_k}^T \bar{\mathbf{P}}_{t_{k-1}}^{\text{cov}} h_{t_k}} \quad (4.62c)$$

$$\mathbf{R}_{t_k} = [\mathbf{I} - \mathbf{M}_{t_k}] \mathbf{R}_{t_{k-1}} + h_{t_k}^T h_{t_k} \quad (4.62d)$$

$$\mathbf{M}_{t_k} = (1 - \mu) \frac{\mathbf{R}_{t_{k-1}} h_{t_k}^T h_{t_k}}{h_{t_k}^T \mathbf{R}_{t_{k-1}} h_{t_k}} \quad (4.62e)$$

The updates strategies for the covariance matrix directly affects the estimates and their uncertainties. The numerical performance of these schemes (i.e. RLS-F, RLS-CT, RLS-SF and RLS-DF) are assessed in the results section.

### Estimation of Uncertainties on Sensitivity Coefficients

In this work, we propose to account for the uncertainties of the estimated sensitivity coefficients to robustify the voltage control. The uncertainties are computed using the co-variance matrix given by

$$\sigma_{\mathbf{X}} = \sigma_r \sqrt{\text{diag}(\mathbf{P}^{\text{cov}})} \quad (4.63)$$

where  $\sigma_r$  is the estimated standard deviation of residuals inferred post-estimation. They are continuously updated during the RLS estimation stage. The uncertainty on the estimated coefficients are estimated to be  $\pm 3\sigma_{\mathbf{X}}$  corresponding to the 99 % confidence interval.

### 4.4.3 Simulation and Results

#### Test-case and Input data

For the validation of the proposed estimation scheme and the corresponding performance evaluation, we consider an IEEE4 benchmark network (where lines are transposed) [118]. The line parameters for the network are listed in Table 4.8. The network is 24.9/4.16 kV, 6 MVA 3-phase operating in balanced configuration as shown in Fig. 4.11. The nominal demands and the PV generation sites and sizes are also shown in Table 4.8. This network has been selected because of its short lines that result in a stiff response of nodal voltage variations with respect to the nodal injections making the sensitivity coefficient estimation particularly challenging.

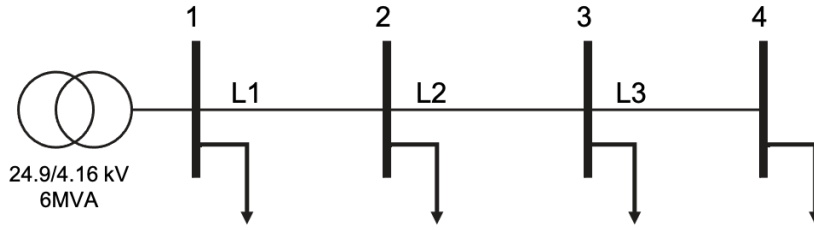


Figure 4.11: IEEE4 balanced system

Table 4.8: Line data and nodal injections for IEEE4 system in Fig. 4.11.

Line data					Load data			PV
Line (to -- from)	R ( $\Omega/\text{km}$ )	X ( $\Omega/\text{km}$ )	B ( $\mu\text{S}$ )	Length (km)	node #	Active (kW)	Reactive (kVAr)	MPP (kW)
1 -- 2	0.4013	1.4133	76	1	2	300	150	480
2 -- 3	0.4576	1.078	76	0.38	3	300	150	600
3 -- 4	0.4576	1.078	76	0.475	4	300	150	–

Figure 4.12a and 4.12b shows the nodal active and reactive power injections for 2 days sampled at 1-second resolution. To obtain the ground-truth measurements of the voltage magnitudes and power injections, we carry out simulated experiments performing load-flows by knowing the true admittance matrix of the grid. The resulting nodal voltage magnitudes are shown in Fig 4.12c. Then, the currents and voltages are corrupted with measurement noise characterized by the IT's uncertainty characteristics described in [127, 128]. This process is described in **Algorithm 4.4**. The algorithm introduces noise in polar coordinates (i.e., magnitudes and phase noise) on the voltage and currents, which is then used to compute the corrupted nodal active ( $\tilde{p}$ ) and reactive ( $\tilde{q}$ ) power magnitudes. The specifications of the ITs are listed in Table 4.1.

#### 4.4.4 Performance Metrics for Sensitivity Coefficient Estimation

This section defines the metrics used in the performance assessment. The first metric is the

## Chapter 4. Data-driven Estimation of Compound Admittance Matrix and Power-Flow Sensitivity Coefficients

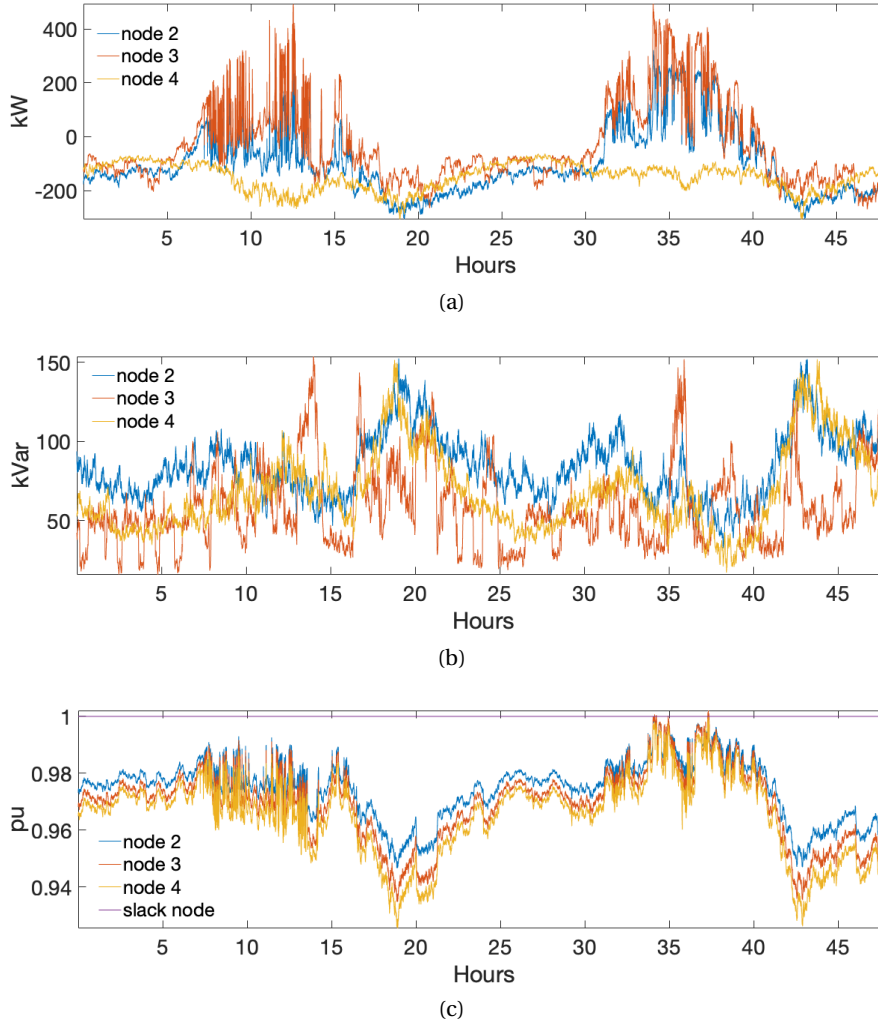


Figure 4.12: (a) Nodal active (in kW), (b) reactive (in kVar) power injections and (c) nodal voltage magnitudes for non-zero injection nodes.

root-mean-square-error (RMSE), defined as

$$\text{RMSE}(\hat{\mathbf{X}}) = \frac{\|\mathbf{X}^{\text{true}} - \hat{\mathbf{X}}\|_2}{\|\mathbf{X}^{\text{true}}\|_2}. \quad (4.64)$$

where,  $\mathbf{X}^{\text{true}}$ ,  $\hat{\mathbf{X}}$  are the true and estimated values of a (generic quantities a scalar or vector).

For the performance comparison on the estimation of the uncertainty intervals, we use metrics inspired by [139]: the first is the prediction interval coverage probability (PICP) that counts the number of instances realization falling within the uncertainty bounds for a given confidence

---

**Algorithm 4.4** Raw-data generation
 

---

**Require:** Admittance:  $\mathbf{Y}$ , nodal power injections:  $\mathbf{p}, \mathbf{q}$

```

1: procedure GENDATA
2:   for  $t_k = t_1 : t_N$  do
3:      $[\mathbf{v}(t_k), \mathbf{i}(t_k)] = \text{LoadFlow}(\mathbf{p}(t_k), \mathbf{q}(t_k), \mathbf{Y})$ 
4:      $[\tilde{\mathbf{v}}(t_k), \tilde{\mathbf{i}}(t_k)] =$ 
5:       for  $\beta = [\mathbf{v}(t_k), \mathbf{i}(t_k)]$  do
6:          $\delta^m = \mathbb{N}(0, \sigma^m |\beta|/3)$ 
7:          $|\beta| = |\beta| + \delta^m$ 
8:          $\delta^p = \mathbb{N}(0, \sigma^p/3)$ 
9:          $\arg(\beta) = \arg(\beta) + \delta^m$ 
10:         $\beta = |\beta| \exp(j \arg(\beta))$ 
11:      end for
12:       $\tilde{\mathbf{p}}(t_k) + j\tilde{\mathbf{q}}(t_k) = \tilde{\mathbf{v}}(t_k) \tilde{\mathbf{i}}(t_k)^*$ 
13:    end for
14: end procedure
    
```

---

interval (CI). It is

$$\text{PICP} = \frac{1}{T} \sum_{t_k=t_1}^{t_T} b_{t_k} \quad (4.65)$$

$$b_{t_k} = \begin{cases} 1 & \hat{K}_{ij,t_k}^p - \Delta K_{ij,t_k}^p \leq \hat{K}_{ij,t_k}^p \leq K_{ij,t_k}^p + \Delta K_{ij,t_k}^p \\ 0 & \text{otherwise.} \end{cases} \quad (4.66)$$

The second is the prediction interval normalized average width (PINAW):

$$\text{PINAW} = \frac{1}{T(K_{ij,\max}^p)} \sum_{t_k=t_1}^{t_T} (2\Delta K_{ij,t_k}^p). \quad (4.67)$$

Here,  $K_{ij,\max}^p$  being the maximum value of the coefficient in the series. The final metric is the coverage width-based criterion (CWC), which quantifies the trade-off between high PICP and small PINAW.

$$\text{CWC} = \text{PINAW}(1 + \eta(\text{PICP})e^{-(v(\text{PICP}-\text{CI}))}) \quad (4.68)$$

$$\eta = \begin{cases} 0, & \text{PICP} \leq \text{CI} \\ 1, & \text{otherwise} \end{cases} \quad (4.69)$$

The parameter  $v$  can be set based on a tradeoff between the interval width penalization. We chose it to be  $v = 50$ . The considered confidence CI is 99%.

#### 4.4.5 Estimation Results

We estimate  $\mathbf{K}^p, \mathbf{K}^q$  for the nodes where the controllable units (i.e., PV generation units) are connected, as these assets could be potentially used in grid-aware control applications, i.e.,  $K_{2,2}^p, K_{2,3}^p, K_{2,2}^q, K_{2,3}^q$ . The estimations plots are shown for IT measurements class of 0.5. The estimated coefficients are shown for the second day; the first day measurements are used to obtain initial LS estimates. For performance comparison among different estimation schemes, we report the estimations for LS, RLS-F, RLS-CT, RLS-SF, and RLS-DF as defined in Sec. 4.4.2. "LS" solves the LS algorithm and uses the measurements from last 5 minutes (sampled at 1-second, i.e., 300 samples) to estimate the sensitivity coefficients. For the methods based on the RLS, the first-day measurements (0 - 24 hours) are used to compute initial estimates (offline-LS). Then, they are updated each 5-minutes with the last timestep measurements in a recursive way. The forgetting factor  $\mu = 0.95$  is used in the simulations.

Figures 4.13 - 4.17 shows the estimations and prediction intervals with confidence interval coverage of 99%. The estimated coefficients,  $K_{2,2}^p, K_{2,3}^p, K_{2,2}^q, K_{2,3}^q$  are shown in Fig 4.13 - 4.17 (a), (b), (c) and (d) respectively. The plots in red show the estimated coefficients, and the grey area their corresponding uncertainty. The black line shows the true coefficients.

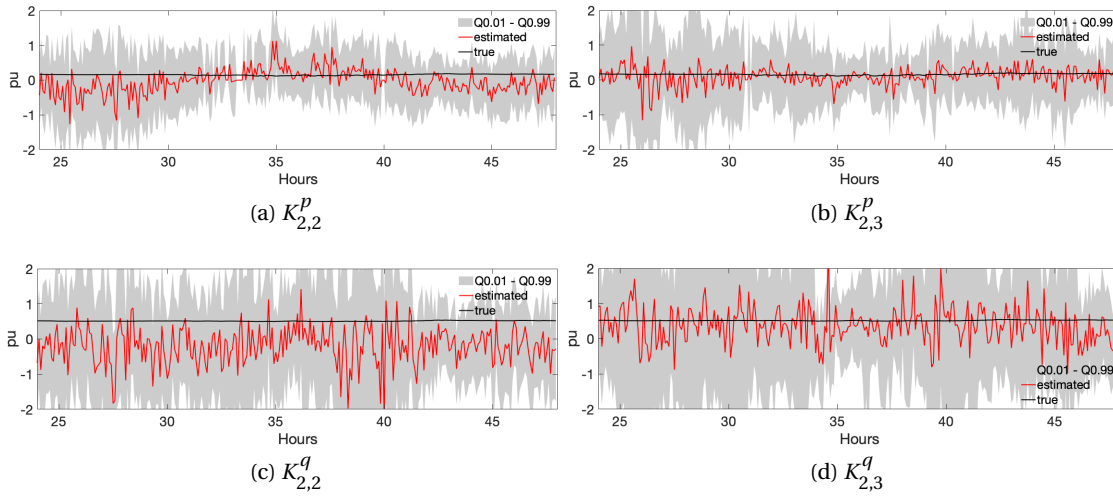


Figure 4.13: Coefficients estimates and their uncertainty using the LS.

As observed from the plot in Fig. 4.13, LS fails in reliably estimating the coefficients and suffers from biases and large variances. The RLS-F (Fig. 4.14) exhibits large uncertainty on the estimates. This is due to the windup problem in the covariance matrix, as reported in [134]. RLS-CT (Fig. 4.15), RLS-SF (Fig. 4.16), and RLS-DF (Fig. 4.17) do fix the windup problem using the strategies described in Sec. 4.4.2. However, the RLS-CT fails to reliably estimate for all the coefficients. RLS-SF and RLS-DF show similar performances. However, the former shows higher coverage width compared to the latter. To have a proper comparison, we report the RMSE and the PICP-PINAW-CWC for each of the coefficients  $K_{2,2}^p, K_{2,3}^p, K_{2,2}^q, K_{2,3}^q$  in

#### 4.4 Direct Estimation of Sensitivity Coefficients

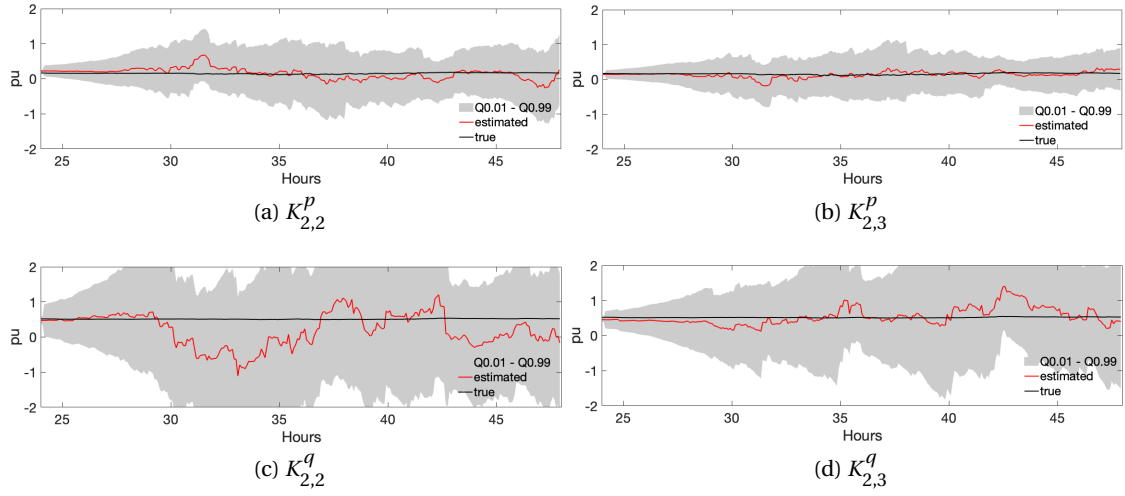


Figure 4.14: Coefficients estimates and their uncertainty using the RLS-F.

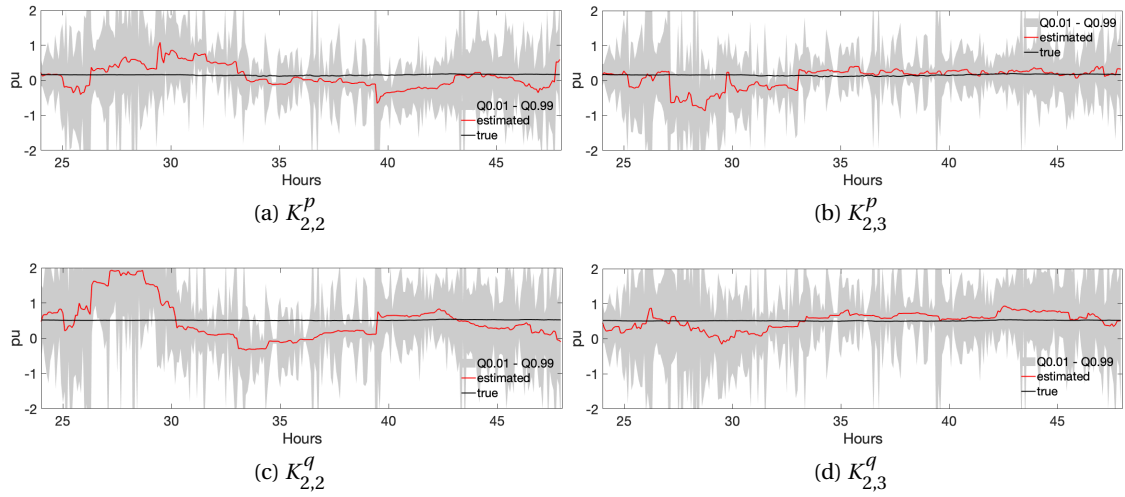


Figure 4.15: Coefficients estimates and their uncertainty using the RLS-CT.

Table 4.9: Performance comparison of different estimation techniques for  $K_{2,2}^p$  with different IT classes.

Method	IT 0.2		IT 0.5		IT 1.0	
	RMSE	PICP-PINAW-CWC	RMSE	PICP-PINAW-CWC	RMSE	PICP-PINAW-CWC
LS	0.97	0.93-4.21-7.81	2.58	0.93-9.73-18.04	8.78	0.69-17.07-28.19
RLS-F	0.31	0.99-5.08-5.08	1.03	0.99-7.49-7.49	1.98	1-13.71-13.71
RLS-CT	1.11	0.89-4.45-8.11	2.1	0.89-11.23-20.41	5.61	0.85-20.1-35.83
RLS-SF	0.2	0.99-2.39-2.39	0.69	0.99-5.74-5.74	1.55	1-10.78-10.78
RLS-DF	0.12	0.99-0.94-0.94	0.37	0.99-2.25-2.25	0.46	1-3.16-3.16

Table 4.9, 4.10, 4.11 and 4.12, respectively. It compares these metrics for different methods and with measurements characterized by other IT classes. From such a comparison, it can



## Chapter 4. Data-driven Estimation of Compound Admittance Matrix and Power-Flow Sensitivity Coefficients

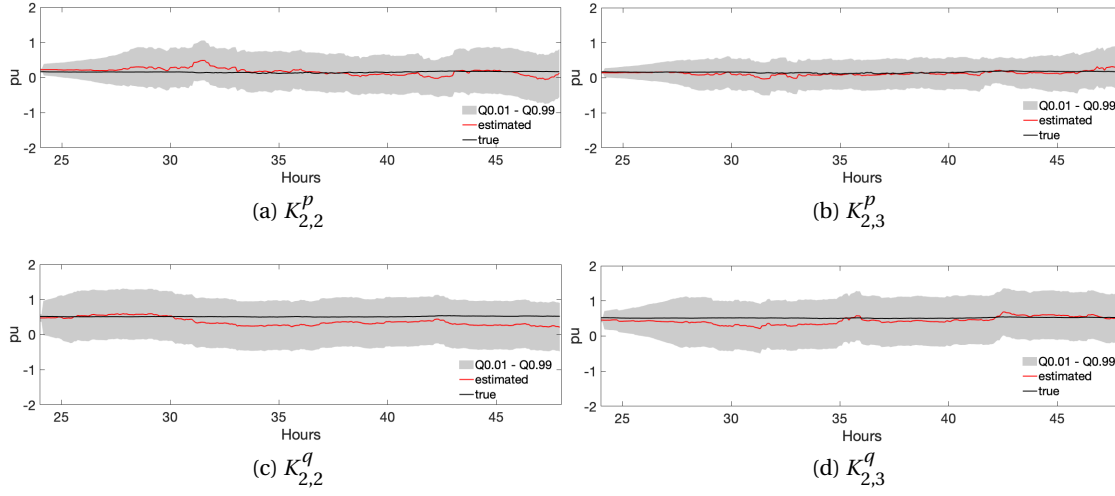


Figure 4.16: Coefficients estimates and their uncertainty using the RLS-SF

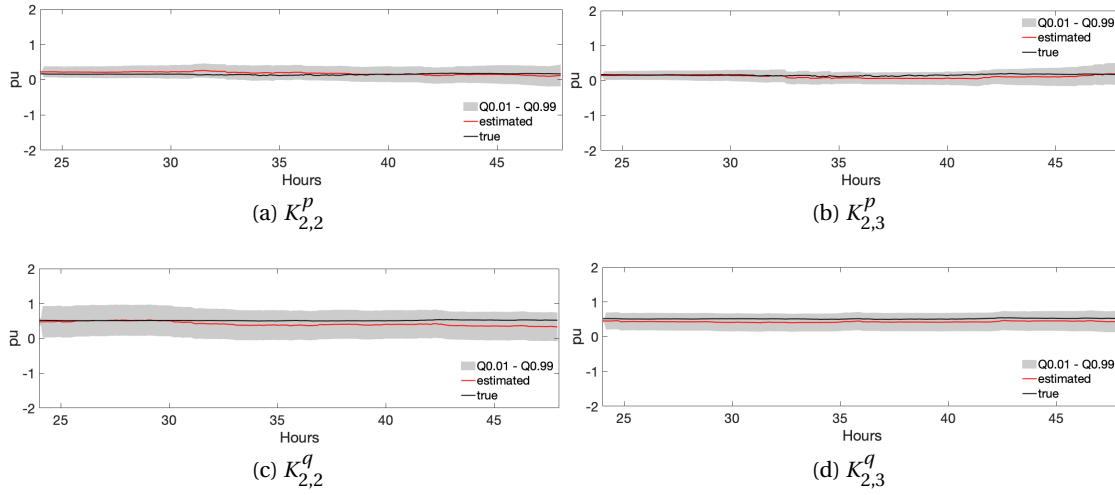


Figure 4.17: Coefficients estimates and their uncertainty using the RLS-DF

Table 4.10: Performance comparison of different estimation techniques for  $K_{2,3}^P$  with different IT classes.

	IT 0.2		IT 0.5		IT 1.0	
Method	RMSE	PICP-PINAW-CWC	RMSE	PICP-PINAW-CWC	RMSE	PICP-PINAW-CWC
LS	0.8	0.97-4.69-4.69	1.68	0.98-10.86-10.86	3.44	0.97-18.98-18.98
RLS-F	0.21	1-3.54-3.54	0.53	1-5.15-5.15	1.27	1-9.34-9.34
RLS-CT	0.73	0.94-3.43-6.37	1.82	0.91-8.72-16	2.15	0.92-15.7-28.94
RLS-SF	0.14	1-1.73-1.73	0.38	1-4.16-4.16	0.85	1-7.76-7.76
RLS-DF	0.12	1-0.77-0.77	0.37	1-1.85-1.85	0.29	1-2.62-2.62

be observed that the RLS-DF performs the best with respect to all the metrics, i.e., it has the lowest RMSE and good coverage. As expected, the RMSE increases with the increasing of the

#### 4.5 Performance Comparison of Direct and Indirect Methods for the Estimation of Sensitivity Coefficients

Table 4.11: Performance comparison of different estimation techniques for  $K_{2,2}^q$  with different IT classes.

	IT 0.2		IT 0.5		IT 1.0	
Method	RMSE	PICP-PINAW-CWC	RMSE	PICP-PINAW-CWC	RMSE	PICP-PINAW-CWC
LS	0.8	0.97-3.39-3.39	1.74	0.96-6.64-6.64	4.18	0.73-9.36-15.71
RLS-F	0.53	1-4.83-4.83	1.09	1-6.77-6.77	2.26	1-12.09-12.09
RLS-CT	0.37	0.85-1.95-3.47	1.1	0.86-4.87-8.71	1.38	0.88-8.73-15.82
RLS-SF	0.23	1-1.07-1.07	0.36	1-2.56-2.56	0.73	1-4.82-4.82
RLS-DF	0.16	1-0.65-0.65	0.22	1-1.54-1.54	0.48	1-2.05-2.05

Table 4.12: Performance comparison of different estimation techniques for  $K_{2,3}^q$  with different IT classes.

	IT 0.2		IT 0.5		IT 1.0	
Method	RMSE	PICP-PINAW-CWC	RMSE	PICP-PINAW-CWC	RMSE	PICP-PINAW-CWC
LS	0.78	0.99-4.97-4.97	1.05	1-8.49-8.49	1.93	0.99-10.76-10.76
RLS-F	0.29	0.99-3.23-3.23	0.46	0.99-4.69-4.69	0.98	0.99-8.32-8.32
RLS-CT	0.29	0.93-1.74-3.22	0.44	0.95-4.39-4.39	1.4	0.85-7.87-14.06
RLS-SF	0.15	0.98-1-1	0.24	0.99-2.4-2.4	0.61	0.99-4.52-4.52
RLS-DF	0.16	0.97-0.41-0.41	0.17	0.99-0.95-0.95	0.37	0.95-1.31-1.31

measurement noise. However, in all the cases related to this specific network, RLS-DF is the dominant estimation method.

#### 4.5 Performance Comparison of Direct and Indirect Methods for the Estimation of Sensitivity Coefficients

This section presents the performance comparison of sensitivity coefficients estimated using the indirect method (Sec. 4.3.5) and direct method (Sec. 4.4). The comparison is shown against the performance metrics defined in Sec. 4.3.6. For the indirect method, the admittance matrix is estimated using the method presented in Sec. 4.3; we consider both the raw and cluster-averaging (Sec. 4.3.4). For the direct method, we consider the dominant estimation scheme RLS-DF (recursive least squares with directional forgetting).

##### 4.5.1 Simulation Setup

The comparison is shown for two different test cases. For the first one, we consider the four-node system of the previous analysis (shown in Fig. 4.11) with line and load parameters of Table 4.8. For the second, we consider a *modified IEEE4* system by artificially increasing the line length in Table 4.8 by a factor of 6. As expected, a longer line length create weaker networks proportionally to the increase of longitudinal branches impedances. It is to study the performance for a weaker network. The same power profiles from Fig. 4.12a-4.12b are used for simulate the grid state measurements then, measurement noise is added using Algorithm 4.3 and 4.4. For the *indirect* method, the first-day measurements are used to

## Chapter 4. Data-driven Estimation of Compound Admittance Matrix and Power-Flow Sensitivity Coefficients

---

estimate the compound admittance matrix. Then the second day is used for the sensitivity coefficient estimation. For the *direct* method, the first-day measurements are used for first-stage LS estimates. Then the second day is used by RLS for online estimation of the sensitivity coefficients.

### 4.5.2 Performance Comparison

#### IEEE4 System

**Indirect (Using Raw-data vs. Cluster-averaged data):** first, we compare the estimation quality among two variants of indirect estimation methods, where the first raw-data is used for the admittance estimation and the second uses cluster-averaged data. We show the estimated coefficients,  $K_{2,2}^P, K_{2,3}^P, K_{2,2}^Q, K_{2,3}^Q$ . Fig. 4.18 and 4.19 shows the estimated coefficient, and the 99 % confidence interval (CI) uncertainty using indirect method using directly the *raw-data* and *cluster-averaged* data with 24 clusters. By comparing Fig. 4.18 and 4.19, it can be observed that the cluster-averaged based estimations exhibit smaller RMSE and narrower coverage widths. Using cluster-averaging, the true coefficient always lies within the confidence uncertainty of the estimates, whereas it is not true in the case of estimations with raw measurements. We also compare the RMSE and PICP-CWC-PINAW in Table 4.13 for coefficient  $K_{2,3}^P$ . These metrics are reported with measurement noise of IT 0.2, 0.5 and 1.0 classes. As seen from the comparison, the RMSE increases for higher measurement noises. However, for the cluster-averaged method, the coverage PICP always remains higher than 1 (i.e., achieving 100% coverage). The cluster averaging largely reduces the CWC. In the case of raw measurements, it shows PICP less than 1 (sometimes 0), meaning that the actual sensitivity coefficients are not fully covered by the computed uncertainties. In contrast, cluster-averaging achieves the best RMSE, and PICP close to 1. The coverage (quantified by CWC) increases with an increase in the measurement noise due to the increase in noise variance from the measuring instrument.

**Indirect (Cluster-averaged data) vs. Direct (RLS-DF):** now, we compare the estimates with the direct method. We only compare with RLS-DF (dominant method from the last analysis in Sec. 4.4.5). By comparing the estimations of the indirect scheme with those presented in Sec. 4.4.5 for the direct method, it can be concluded that the dominant indirect method (with cluster averaging) performs better than the corresponding dominant direct method (RLS-DF). By looking at the grey area around estimations in Fig. 4.19 and 4.17, it can be seen that the RLS-DF has higher CWC (higher variance). The same can be concluded by comparing the metrics in Table 4.13. The indirect method (with cluster averaging) performs almost 10 times better on RMSE. Although, they perform similarly on PICP, the CWC is almost twice for the case of the direct method. Therefore, the indirect method (with cluster averaging) is the best-performing estimation scheme for this specific test case.

#### 4.5 Performance Comparison of Direct and Indirect Methods for the Estimation of Sensitivity Coefficients

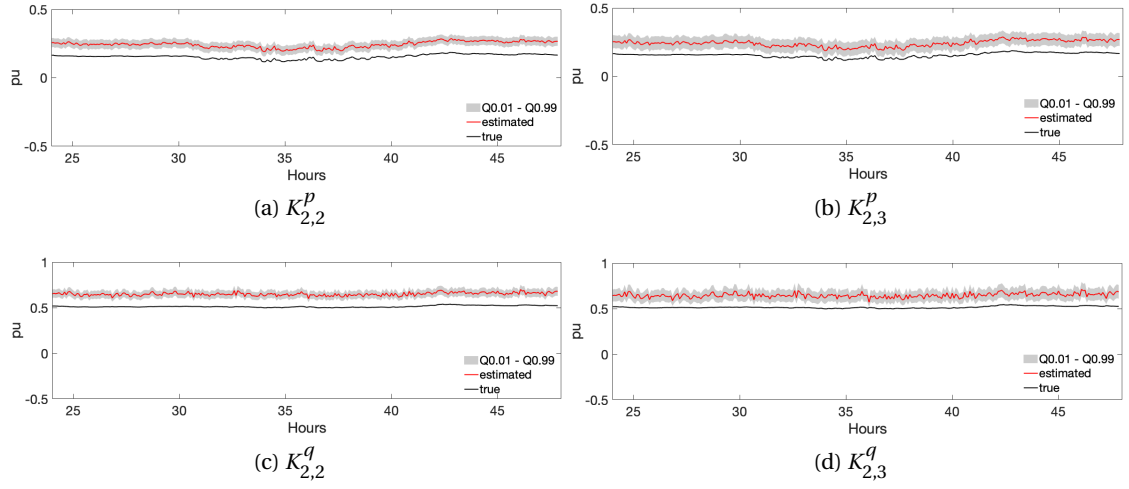


Figure 4.18: Coefficients estimates and their uncertainty using the *indirect method with raw data* for IT 0.5.

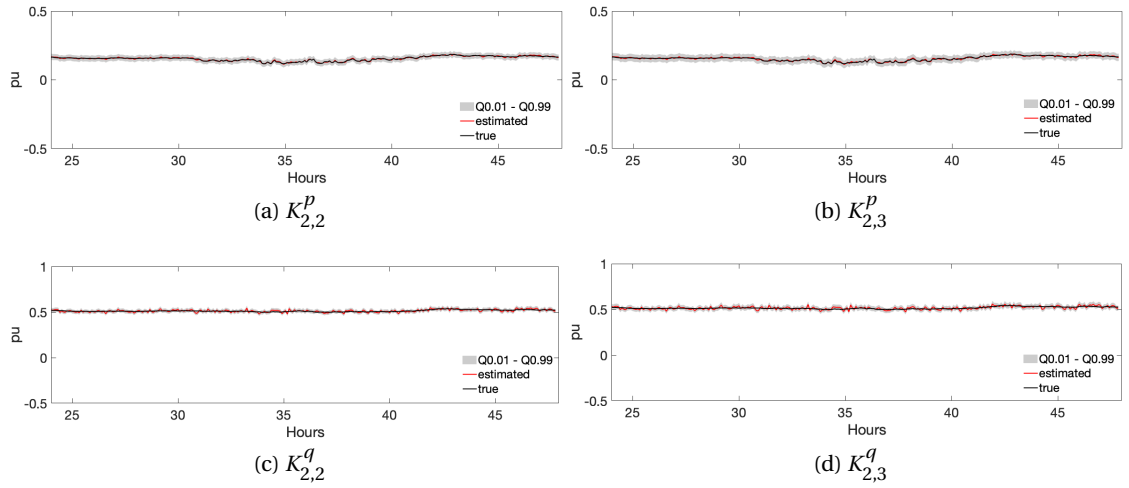


Figure 4.19: Coefficients estimates and their uncertainty using the *indirect method with cluster-averaging* for IT 0.5.

Table 4.13: Performance comparison of indirect and direct method for IEEE4 system (the coefficient  $K_{2,3}^p$ ).

Method	IT 0.2		IT 0.5		IT 1.0	
	RMSE	PICP-PINAW-CWC	RMSE	PICP-PINAW-CWC	RMSE	PICP-PINAW-CWC
<b>Indirect</b> (Raw data)	0.18	0.01-0.19-0.19	0.56	0-0.52-0.52	0.93	0-1.03-1.03
<b>Indirect</b> (Cluster-averaging)	0.01	1-0.1-0.1	0.03	1-0.29-0.29	0.06	1-0.59-0.59
<b>Direct</b> (RLS-DF)	0.12	1-0.77-0.77	0.37	1-1.85-1.85	0.29	1-2.62-2.62

## Chapter 4. Data-driven Estimation of Compound Admittance Matrix and Power-Flow Sensitivity Coefficients

### Modified IEEE4 System (Artificially Elongated Line-length)

Furthermore, we perform the same analysis for a network with long line parameters by artificially increasing the line length of the IEEE4 network in Table. 4.8 by a factor of 6. The comparison is shown in Table 4.14. Contrary to the previous test case, the uncertainty of the estimates using the indirect method is quite high as seen in the CWC values. It is due to the high variance of the  $\mathbf{Y}$  estimates as the elements of  $\mathbf{Y}$  are quite small in the case of a network with long line lengths. In contrast, the direct estimation scheme has a smaller estimation variance. However, in terms of RMSE, the indirect method is still better than the direct method.

Table 4.14: Performance comparison of indirect and direct method for *modified* IEEE4 system (the coefficient  $K_{2,3}^P$ ).

Method	IT 0.2		IT 0.5		IT 1.0	
	RMSE	PICP-PINAW-CWC	RMSE	PICP-PINAW-CWC	RMSE	PICP-PINAW-CWC
<b>Indirect</b> (Raw data)	0.22	1-5.46-5.46	0.65	1-12.69-12.69	1.1	1-20.73-20.73
<b>Indirect</b> (Cluster-averaging)	0.01	1-3.42-3.42	0.02	1-9.3-9.3	0.05	1-19.25-19.25
<b>Direct</b> (RLS-DF)	0.22	0.99-1.91-1.91	0.31	0.99-2.54-2.54	0.98	1-3.46-3.46

## 4.6 Discussion

This Chapter proposed two different schemes for the measurement-based estimation of the grid's sensitivity coefficients. The first relies on the estimation of the compound admittance matrix, which is then used to compute the sensitivity coefficients. The quality of the estimated sensitivity coefficients directly depends on the accuracy of the admittance matrix. So, we propose a pre-processing scheme on the raw measurements to improve the admittance estimation performance. The pre-processing scheme clusters the raw data by kmeans and averages them, before using them for the admittance estimation. Furthermore, we developed an error propagation tool to estimate the uncertainty from the estimated admittance matrix to the computed sensitivity coefficients. The second scheme estimates the sensitivity coefficients directly, using the nodal power and grid state measurements. In this scheme, an RLS-based estimator is used to refine previous estimates by the most recent measurements, whereas an offline-LS estimate is used as initialization to the RLS. The above two schemes are compared in terms of their inaccuracies and the uncertainty of the estimates.

The methods were validated by simulated experiments on various benchmark networks. From the comparison of the above two methods, it can be concluded that the pre-processing of data using cluster-averaging improves the admittance estimation performance by 2-3 orders of magnitude. Consequently, the sensitivity coefficients estimated using pre-processing strategies have the best performance in terms of RMSE and PICP-CWC-PINAW. Compared to directly using the raw measurements, this scheme achieves almost 10 times better RMSE.

For direct methods, the RLS-based scheme performs better than the offline LS. The windup problem of RLS is tackled best by the directional forgetting (RLS-DF) algorithm.

Finally, we compared the direct and indirect estimation methods for two different test cases. For the benchmark IEEE4 network, the indirect scheme attained better RMSE and PICP-CWC-PINAW, whereas, for the case with longer lines (still used in the IEEE4 network), the direct scheme outperforms the indirect method in terms of PICP-CWC-PINAW. However, in terms of RMSE, the indirect method is still better than the direct method. Therefore, we can conclude that the dominant estimation is grid-dependent.

Furthermore, a potential drawback of the indirect method is that it requires measuring instruments at all the nodes in the network, which might not be a feasible setup, especially in power distribution systems. In contrast, the direct method requires measurement instruments only at a few locations (preferable at the nodes with high sensitivity to the grid states, and where controllable resources are located). In this context, although the direct methods exhibit worse RMSE and coverage width, they might be economically feasible to implement in real distribution networks.

In the following chapter, we use the above-estimated sensitivity coefficients using the direct-method (RLS-DF) for measurement-based control of a distribution network.



## 5 Model-less Robust Control of ADNs using Measurements-based Estimated Sensitivity Coefficients

*Measurement-rich power distribution networks may enable distribution system operators (DSOs) to adopt model-less and measurement-based monitoring and control of distributed energy resources (DERs) for mitigating grid issues such as over/under voltages and lines congestion. However, measurement-based monitoring and control applications may lead to inaccurate control decisions due to error in the estimated models caused by measurement noise. In particular, estimation models relying on regression-based schemes result in significant errors in the estimates (e.g., nodal voltages) especially for measurement devices with high Instrument Transformer (IT) classes. The consequences are detrimental to control performance since this may lead to infeasible decisions. This work proposes a model-less robust voltage control accounting for the uncertainties of measurement-based estimated voltage sensitivity coefficients. The coefficients and their uncertainties are obtained using the estimation scheme as described in Chapter 4. This control formulation is applied to control distributed controllable photovoltaic (PV) generation as active power curtailment and reactive power regulation in a distribution network to restrict the voltage within prescribed limits. The proposed scheme is experimentally validated for controlling two PV inverters connected to a real microgrid, an exact replica of CIGRE benchmark microgrid network, at the EPFL Distributed Electrical Systems Laboratory.*

*The Chapter includes results of publication [96, 140].*

### 5.1 State-of-the-Art

Voltage control is one of the widely acknowledged control schemes to be adopted and improved in power distribution networks. Conventional voltage controls are based on volt-var schemes, where only the reactive power is controlled to regulate nodal voltages. However, as shown in [141], the sole reactive power control might not be enough especially for grids with high R/X ratio of branches longitudinal impedances, the control of both active and reactive powers may be needed. In the literature, this type of control can be broadly categorized into



## Chapter 5. Model-less Robust Control of ADNs using Measurements-based Estimated Sensitivity Coefficients

---

two kinds. The first relies on the network model (network topology, branch, and shunt parameters). These methods are also referred to as model-based methods. For example, in [17, 142], it is proposed a distributed control of PV inverters for regulating the nodal voltage magnitudes in a distribution grid where the grid constraints are modeled using the admittance matrix of the network. However, in many cases, the network parameters are either unavailable, partially missing, or outdated. Thanks to the increasing adoption of monitoring systems such as smart meters in present distribution networks, measurement-based/data-driven/model-less control schemes can be an alternative. This leads to the second kind of voltage control scheme often referred to as measurement-based schemes [99, 103, 133, 141, 143]. These schemes are used for real-time voltage control where the network model is inferred from the measurements (e.g. [95]). However, in all the reported model-less and measurement-based methods, the control or the estimation problem does not consider uncertainty on the estimated grid models (e.g., estimated sensitivity coefficients) and may result in wrong control decisions. The uncertainty on the measurement-based estimated model comes from the measurement noise of the instrument transformers (ITs). As reported in [101, 102], the estimated sensitivity coefficients suffer high biases due to measurement noise and fluctuating values due to collinearity in the measured data set.

In this context, this Chapter proposes a model-less robust voltage control that accounts for the uncertainty on the measurement-based estimated sensitivity coefficients ensuring safe and reliable operation of the distribution grid. The work comprises the estimation of the sensitivity coefficients and their uncertainties and use them to provide robustness against the inaccuracies of measurement-based estimated grid models [144]. The proposed voltage control problem consists of two stages: in the first stage, an estimation problem is solved to estimate the voltage sensitivity coefficients and their uncertainties. In the second stage, we solve a robust voltage control problem accounting for the uncertainties on the estimated coefficients.

First, the performance assessment is carried out by performing numerical experiments using the CIGRE LV [5] network interfacing multiple controllable PV units. To show the effectiveness of the proposed robust formulation, we compare it with a non-robust voltage control case when uncertainties are not considered. The performance is also bench-marked against model-based control. Then, we perform experimental validation of the control scheme on a real microgrid hosted at the EPFL Distributed Electrical Systems Laboratory (the same grid as described in Sec. 2.8). The microgrid is a low voltage distribution network which is an exact replica of the CIGRE microgrid benchmark network. It hosts two controllable PV inverters of capacities 13 kW and 16 kW respectively which are controlled by the proposed control scheme for voltage regulation.

## 5.2 Problem Statement

Let us consider a power distribution network equipped with measurement devices capable of providing high throughput measurements on nodal voltage magnitudes and active/reactive powers. Let  $N_b$  be the number of non-slack buses and the set  $\mathcal{N} = \{1, \dots, N_b\}$  defining the bus indices. The distribution network hosts multiple DERs (for example, PV generation units) that can be controlled to provide active and reactive power support to the grid. The objective is to control DERs in real-time (or quasi-real-time) such that grid constraints are always satisfied. The parameters and topology of the network are not known, so model-based controls could not be implemented. The control scheme solely relies on a model-less scheme, where the grid constraints (such as nodal voltages, lines, and transformer power flows) are accounted by models estimated from measurements. Although the model-less framework is generic and can be applied for various control schemes, this work focuses on the voltage control problem where the DERs are controlled in real-time to avoid or mitigate voltage problems. The key features of the proposed voltage control scheme are listed below.

- The control is formulated as a robust problem by accounting for the error on the estimated grid models (i.e., voltage sensitivity coefficients in this specific case).
- The control relies on both the active and reactive power control of the flexible resources (in contrast to volt-var controls).
- A performance comparison of different estimation techniques of measurement-based estimations of sensitivity coefficients for the proposed robust control is presented.

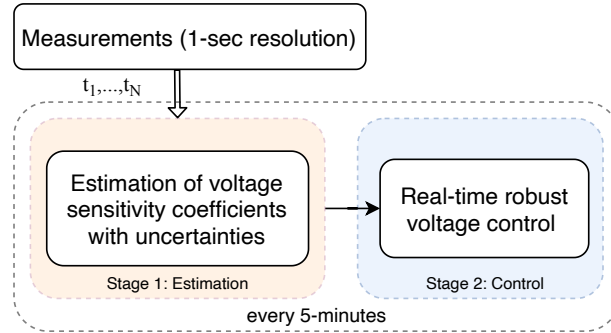


Figure 5.1: Flow-chart of the model-less/measurement-based robust voltage control framework.

Figure 5.1 shows the flow diagram illustrating the proposed two-stage scheme for the robust model-less control framework. The first stage (on the left) is composed of a measurement-based estimation loop that stores nodal voltage magnitudes, active and reactive power measurements and estimates the voltage sensitivity coefficients and their uncertainties. The estimation stage was described in Chapter 4. Then, the block on the right solves the constrained optimization problem for controlling distributed energy resources (DERs) to mitigate the voltage problems in the network. It is described as follows.

### 5.3 Problem Formulation

In the following, first we introduce the non-robust voltage control problem (i.e., the uncertainty on the coefficients estimates are not accounted), then we present its robust counterpart.

#### 5.3.1 Voltage Control Problem without Considering Uncertainty on the Estimates (Non-robust)

Let us consider a distribution network connected with controllable PV generation units such that their active and reactive power injections can be controlled. Let the set  $\mathcal{N}_{\text{pv}}$  includes indices of the PV units. The objective is to control active/reactive power injections  $(p_{j,t_k}^{\text{pv}}, q_{j,t_k}^{\text{pv}}, j \in \mathcal{N}_{\text{pv}})$  such that the nodal voltages are within the statutory bounds. Additionally, the local objective of the PV units is to minimize the curtailment of their active power generation and provide reactive power support, latter constrained by imposed power factor limits. The problem we solve at time  $t_k$  is to minimize curtailments of PV plants:

$$\underset{p_{j,t_k}^{\text{pv}}, q_{j,t_k}^{\text{pv}}, \forall j \in \mathcal{N}}{\text{minimize}} \sum_{j \in \mathcal{N}_{\text{pv}}} \left\{ (p_{j,t_k}^{\text{pv}} - \hat{p}_{j,t_k}^{\text{pv}})^2 + (q_{j,t_k}^{\text{pv}})^2 \right\} \quad (5.1a)$$

subject to the constraint on the PV generation limited by short-term MPP forecast  $\hat{p}_{j,t_k}^{\text{pv}}$ ,

$$0 \leq p_{j,t_k}^{\text{pv}} \leq \hat{p}_{j,t_k}^{\text{pv}} \quad j \in \mathcal{N}_{\text{pv}} \quad (5.1b)$$

the capability constraint of the converter rating  $S_{j,\text{max}}^{\text{pv}}$  (assumed to be AC and DC voltages independent),

$$0 \leq (p_{j,t_k}^{\text{pv}})^2 + (q_{j,t_k}^{\text{pv}})^2 \leq (S_{j,\text{max}}^{\text{pv}})^2 \quad j \in \mathcal{N}_{\text{pv}}, \quad (5.1c)$$

and the minimum power factor constraint

$$q_{j,t_k}^{\text{pv}} \leq p_{j,t_k}^{\text{pv}} \zeta \quad j \in \mathcal{N}_{\text{pv}} \quad (5.1d)$$

$$-q_{j,t_k}^{\text{pv}} \leq p_{j,t_k}^{\text{pv}} \zeta \quad j \in \mathcal{N}_{\text{pv}}. \quad (5.1e)$$

Here,  $\zeta = \sqrt{(1 - \text{PF}_{\text{min}}^2) / \text{PF}_{\text{min}}^2}$ ,  $\text{PF}_{\text{min}}$  being the minimum power-factor allowed for the PV operation of each PV plant. The final constraints are on the voltage magnitudes, which are bounded by  $[v^{\text{min}}, v^{\text{max}}]$ . The voltage magnitudes ( $|v_{i,t_k}|$ ) are modeled by the estimated voltage sensitivity coefficients as

$$v^{\text{min}} \leq |v_{i,t_{k-1}}| + \hat{\mathbf{K}}_{i,t_{k-1}}^p \Delta \mathbf{p}_{t_k} + \hat{\mathbf{K}}_{i,t_{k-1}}^q \Delta \mathbf{q}_{t_k} \leq v^{\text{max}} \quad \forall i \in \mathcal{N} \quad (5.1f)$$

Here,  $\mathbf{p}_{t_k} - \mathbf{p}_{t_{k-1}} = \Delta \mathbf{p}_{t_k}$ ,  $\mathbf{q}_{t_k} - \mathbf{q}_{t_{k-1}} = \Delta \mathbf{q}_{t_k}$  are deviations of nodal active and reactive power injections. The voltage sensitivity coefficients,  $\hat{\mathbf{K}}_{i,t_{k-1}}^p, \hat{\mathbf{K}}_{i,t_{k-1}}^q$ , are estimated online using one of the estimation scheme described in Sec. 4.4.2 utilizing latest measurements on voltages and

power magnitudes.

As described earlier, the non-robust problem in (5.1) does not account for the uncertainty on the estimates caused by measurement noise which might result in inaccurate control decisions leading to voltage violations.

### 5.3.2 Robust Voltage Control Problem

We here illustrate the robust voltage control by accounting for the uncertainty on the measurement-based estimated voltage sensitivity coefficients. The robust counterpart of (5.1) can be formulated by adding following constraints to (5.1)

$$\mathbf{K}_{i,t_k}^p \in [\hat{\mathbf{K}}_{i,t_k}^p - \Delta\mathbf{K}_{i,t_k}^p, \hat{\mathbf{K}}_{i,t_k}^p + \Delta\mathbf{K}_{i,t_k}^p] \quad \forall i \in \mathcal{N} \quad (5.1g)$$

$$\mathbf{K}_{i,t_k}^q \in [\hat{\mathbf{K}}_{i,t_k}^q - \Delta\mathbf{K}_{i,t_k}^q, \hat{\mathbf{K}}_{i,t_k}^q + \Delta\mathbf{K}_{i,t_k}^q] \quad \forall i \in \mathcal{N}. \quad (5.1h)$$

The respective voltage constraint in (6.10b) becomes

$$v^{\min} \leq |v_{i,t_{k-1}}| + \mathbf{K}_{i,t_{k-1}}^p \Delta \mathbf{p}_{t_k} + \mathbf{K}_{i,t_{k-1}}^q \Delta \mathbf{q}_{t_k} \leq v^{\max} \quad \forall i \in \mathcal{N} \quad (5.1i)$$

Here,  $\Delta\mathbf{K}_{i,t_k}^p, \Delta\mathbf{K}_{i,t_k}^q$  be the estimated uncertainty on  $\hat{\mathbf{K}}_{i,t_k}^p, \hat{\mathbf{K}}_{i,t_k}^q$ . As known, accounting for the interval constraints of (5.1g) and (5.1h) makes the problem non-tractable in its original form. Thus, it is reformulated using the technique proposed in [145, 146] summarized hereafter.

We introduce auxiliary variables  $z_i, g_{ij}, y_j^p, y_j^q, j \in \mathcal{N}_{pv}, i \in \mathcal{N}$ . We also introduce a parameter  $\xi_i \in [0, |\mathcal{N}_{pv}|]$  which provides a trade-off between the robustness and conservativeness of the solution as described in [145]. Considering these auxiliary variables and following the robust quadratic program with linear constraints in [146], the robust counterpart of the problem can be formulated as

$$\underset{p_{j,t_k}^{pv}, q_{j,t_k}^{pv}, \forall j \in \mathcal{N}}{\text{minimize}} \sum_{j \in \mathcal{N}_{pv}} \left\{ (p_{j,t_k}^{pv} - \hat{p}_{j,t_k}^{pv})^2 + (q_{j,t_k}^{pv})^2 \right\} \quad (5.2a)$$

subject to:

$$(5.1b), (5.1c), (5.1d), (5.1e). \quad (5.2b)$$

With the help of the auxiliary variables, the constraints on the nodal voltages (5.1i) are reformulated as follows.

$$|v_{i,t_{k-1}}| + \hat{\mathbf{K}}_{i,t_{k-1}}^p \Delta \mathbf{p}_{t_k} + \hat{\mathbf{K}}_{i,t_{k-1}}^q \Delta \mathbf{q}_{t_k} + z_i \xi_i + \sum_{j \in \mathcal{N}_{pv}} g_{ij} \leq v^{\max} \quad \forall i \in \mathcal{N} \quad (5.2c)$$

$$|v_{i,t_{k-1}}| + \hat{\mathbf{K}}_{i,t_{k-1}}^p \Delta \mathbf{p}_{t_k} + \hat{\mathbf{K}}_{i,t_{k-1}}^q \Delta \mathbf{q}_{t_k} - z_i \xi_i - \sum_{j \in \mathcal{N}_{pv}} g_{ij} \geq v^{\min} \quad \forall i \in \mathcal{N} \quad (5.2d)$$

$$-y_j^p \leq \Delta p_{j,t_k}^{pv} \leq y_j^p \quad \forall j \in \mathcal{N}_{pv} \quad (5.2e)$$

$$-y_j^q \leq \Delta q_{j,t_k}^{pv} \leq y_j^q \quad \forall j \in \mathcal{N}_{pv} \quad (5.2f)$$

$$z_i + g_{ij} \geq \Delta K_{ij,t_k}^p y_j^p \quad i \in \mathcal{N}, j \in \mathcal{N}_{pv} \quad (5.2g)$$

$$z_i + g_{ij} \geq \Delta K_{ij,t_k}^q y_j^q \quad i \in \mathcal{N}, j \in \mathcal{N}_{pv} \quad (5.2h)$$

$$y_j^p, y_j^q, z_i, g_{ij} \geq 0 \quad i \in \mathcal{N}, j \in \mathcal{N}_{pv}. \quad (5.2i)$$

The robust problem in (5.2) has a quadratic objective and linear constraints, hence it is convex and can be efficiently solved with any off-the-shelf solver.

## 5.4 Simulation and Results

To compare the performance of the above two control schemes, first, we perform numerical experiments for voltage control in a distribution network by controlling multiple PV units. Then, the dominant scheme from this analysis is used for the experimental validation in the next section.

### 5.4.1 Test-case and Input Data

For the performance evaluation, we consider a CIGRE benchmark low-voltage network [5]. The network is 20 kV/0.4 V, 400 kVA 3-phase balanced system as shown in Fig. 5.2. The

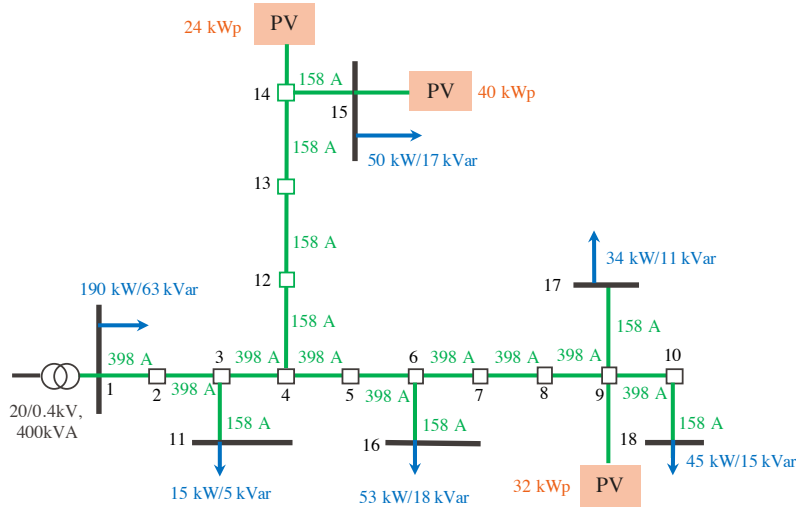


Figure 5.2: Topology of the CIGRE low-voltage system with distributed PV units.

nominal demands and the PV generation sites and sizes are also shown in the figure. In this case study, we assume a reduced load scenario such that the PV generation is causing over-voltages during the middle of the day.

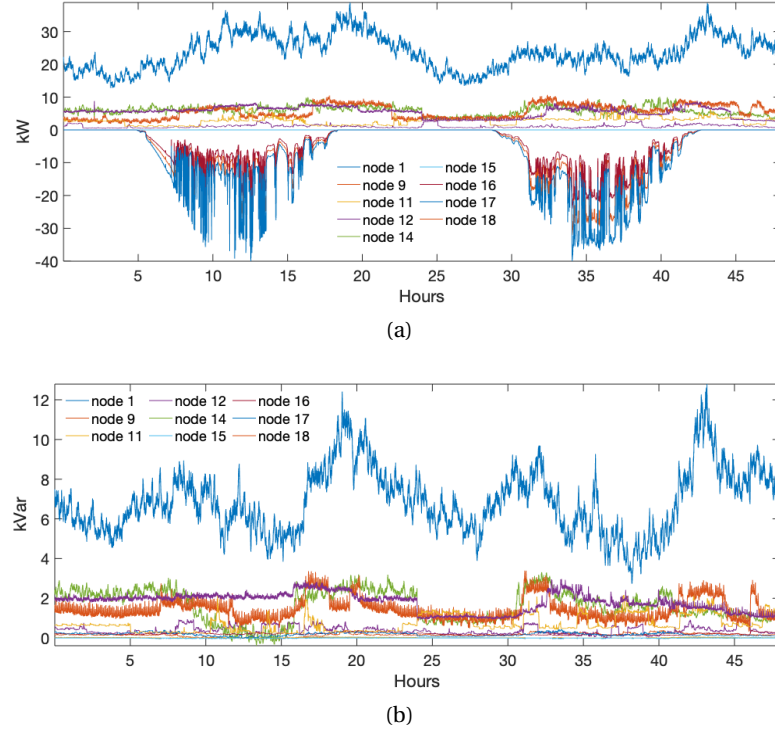


Figure 5.3: (a) Nodal active (in kW) and (b) reactive (in kVar) power injections for non-zero injection nodes.

Figure 5.3(a-b) shows the nodal active and reactive power injections. To obtain the ground-truth measurements of the voltage magnitudes and power injections, we carry simulated experiments performing load-flows by knowing the true admittance matrix of the grid. Then, the currents and voltages are corrupted with measurement noises characterized by the IT's specification described in [127, 128]. This process is described in **Algorithm 4.4**. The algorithm introduces noise in polar coordinates (i.e., magnitudes and phase noise) on the voltage and currents, which is then used to compute the corrupted nodal active ( $\tilde{\mathbf{p}}$ ) and reactive ( $\tilde{\mathbf{q}}$ ) power magnitudes. The specifications of the ITs are listed in Table 4.1.

### 5.4.2 Estimation Results

The sensitivity coefficients and their uncertainties are estimated via the RLS-based estimation technique proposed in Sec. 4.4. The analysis presented in Sec. 4.4.5 showed that RLS-DF and RLS-SF were the two top performing schemes among others. Here, we report sensitivity estimation for these two schemes in this section, and they will be used for the numerical and experimental validation of the proposed model-less control schemes.

Figs. 5.4a, 5.4b and 5.4c show the estimation of the sensitivity coefficients  $K_{15,15}^p$ ,  $K_{14,8}^p$  and  $K_{15,18}^q$  (nodes corresponding to PV plants locations) using RLS-SF and the plots in Figs. 5.5a, 5.5b and 5.5c using RLS-DF respectively. The estimated coefficients are shown for the 2nd

## Chapter 5. Model-less Robust Control of ADNs using Measurements-based Estimated Sensitivity Coefficients

day with peak PV production during 32–42 h (potentially causing over-voltages). It shows the estimates in red and the uncertainty in the shaded grey area. The estimations are compared against the true sensitivity coefficients shown in black. As it can be seen, the true coefficient lies within the estimated uncertainty for both the RLS-SF and RLS-DF, so they can be reliably used for the control. Although, the RLS-DF shows better performance than RLS-SF in covering the true sensitivity coefficients by estimated uncertainty bounds.

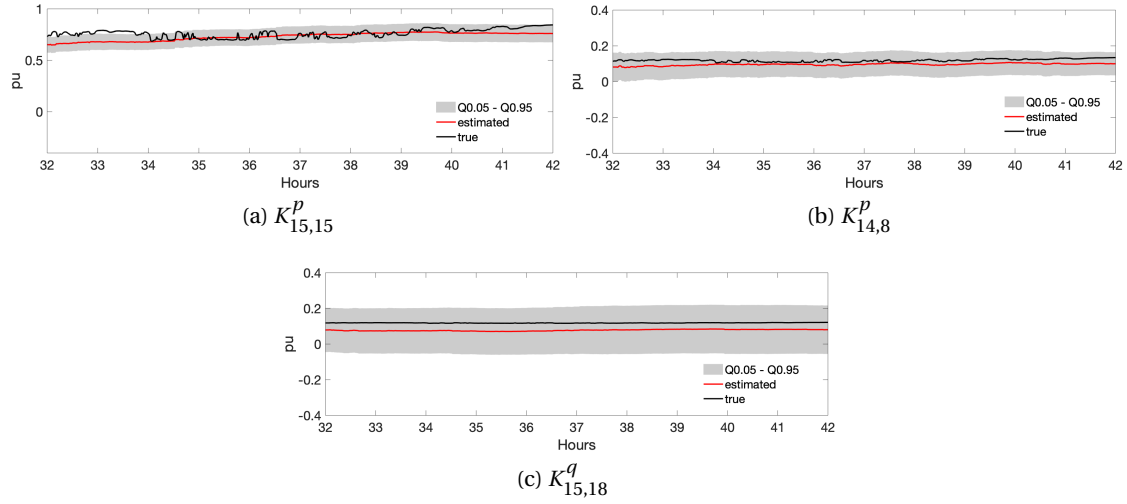


Figure 5.4: Coefficients estimates and their uncertainty using the RLS-SF.

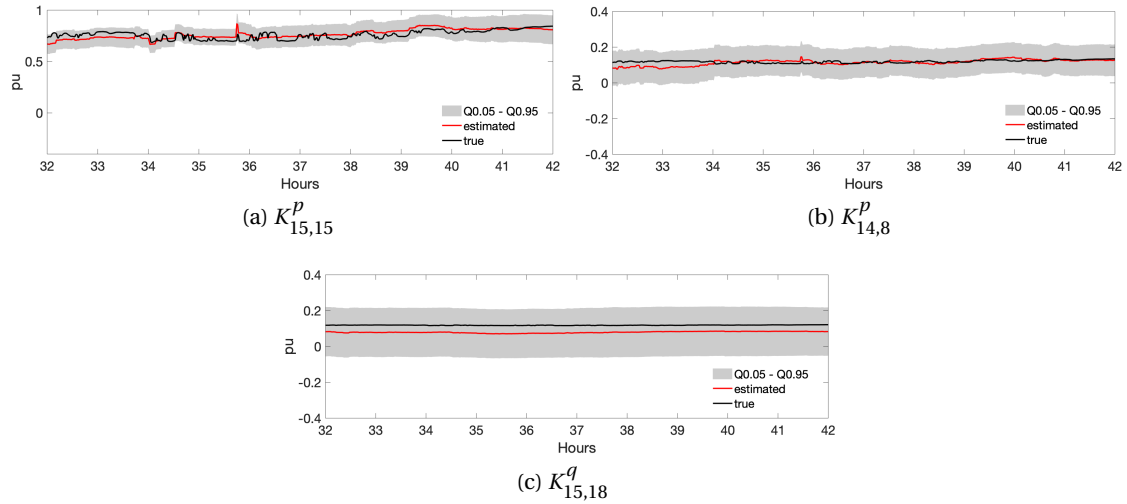


Figure 5.5: Coefficients estimates and their uncertainty using the RLS-DF.

### 5.4.3 Control Results

In the following, we present the voltage control results. We control all three PV plants using the robust and non-robust approaches described in Sec. 5.3. The objective is to restrict the voltage magnitudes within the bounds 0.97 - 1.03 pu. We show the results only using the dominant estimation schemes i.e., RLS-SF and RLS-DF from the last analysis. In this setup, the previous day measurements (0-24 hrs) are used to compute initial estimates (offline-LS) for the RLS. Then, the online-RLS refines these estimates every 5 minutes using the last measurements. The latest estimated coefficients and their uncertainties are then used for the voltage control. To compare the voltage violations produced by the different control schemes, the power set-points from these control schemes are fed to the non-linear AC power flow equations to obtain the actual nodal voltages.

**Non-robust Voltage Control:** Fig. 5.6a compares the daily boxplot post-control nodal voltage magnitudes for all the nodes using the non-robust control. The performance is also compared against *model-based* method, i.e., when the true sensitivity coefficients are known. As clear from the comparison, the non-robust control fails to restrict the voltage magnitudes of nodes 14 and 15 within imposed bounds by a large margin, irrespective of the estimation techniques. It should be noted that even the dominant estimation method (i.e., RLS-DF) fails to respect the upper voltage constraint in non-robust control.

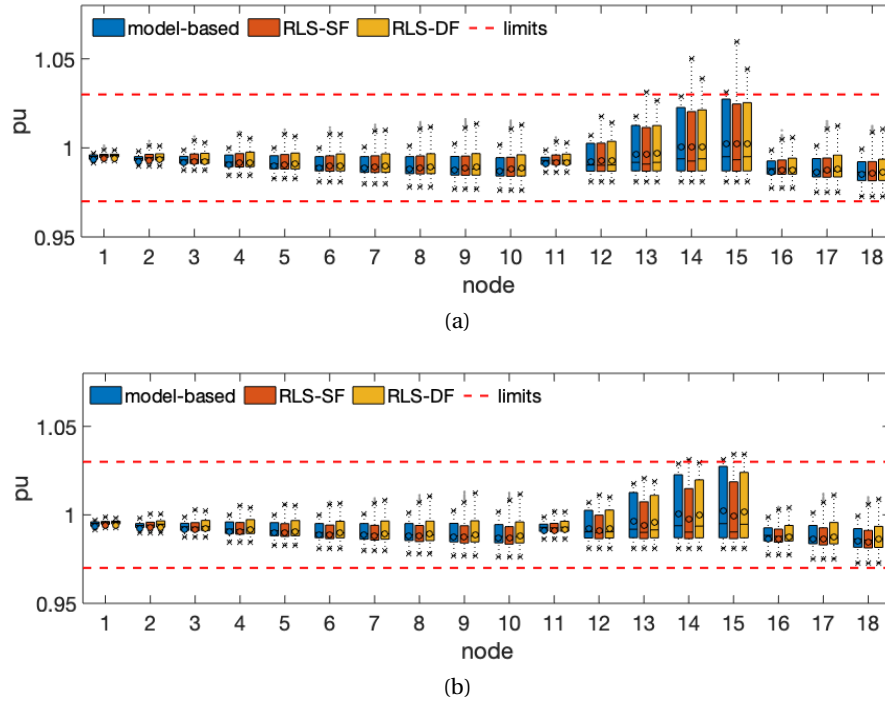


Figure 5.6: Distribution of daily nodal voltage magnitudes using (a) non-robust and (b) robust voltage control.



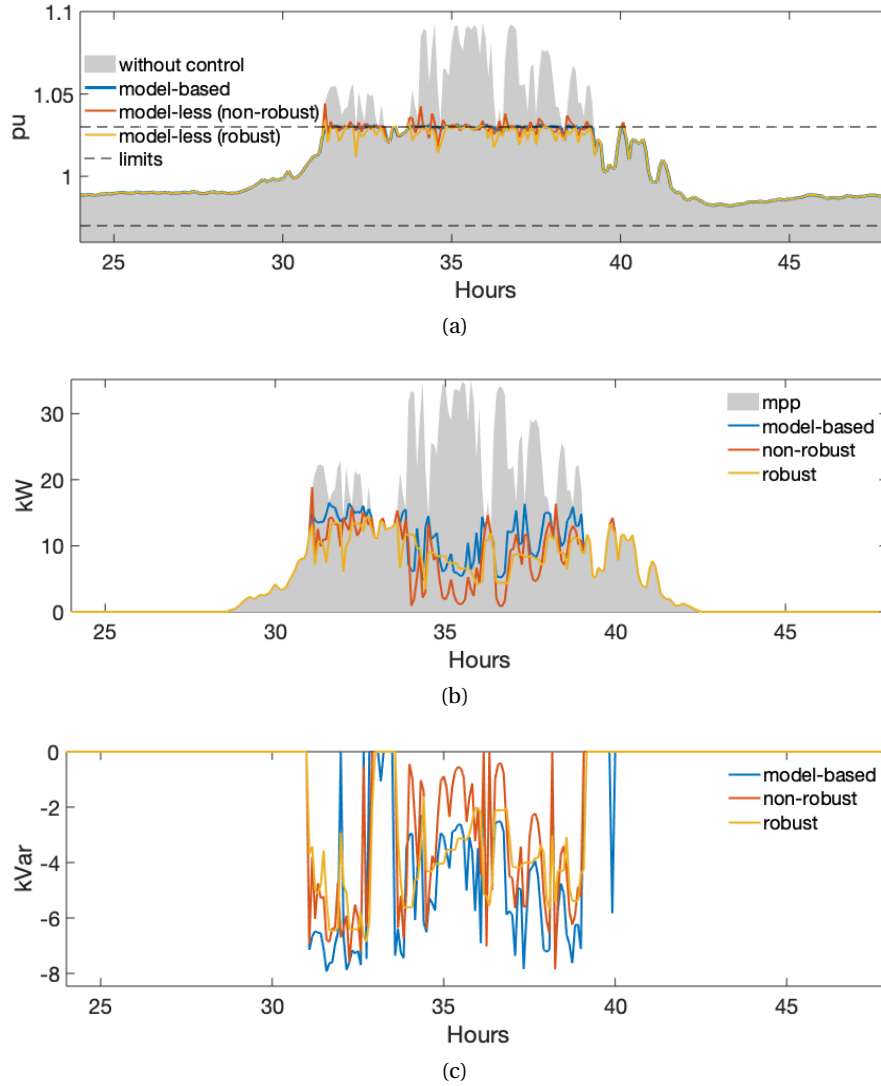


Figure 5.7: Control results using RLS-DF for robust, non-robust and model-based controls: (a) voltage magnitude, (b) active power and (c) reactive power for node 15.

**Robust Voltage Control:** Figure 5.6b compares the daily boxplot post-control nodal voltage magnitudes for all the nodes using the robust voltage control. As it can be seen, robust voltage control succeeds in reducing voltage violations. Robust voltage control using estimates from RLS-SF and RLS-DF perform similarly to the model-based controls (i.e., the maximum voltage magnitude is near the upper bound).

Figure 5.7 shows the control results for the RLS-DF, comparing model-less robust and non-robust methods against model-based control. Fig. 5.7a shows the voltage of node 15 under different control schemes. It can be observed that model-less robust control keeps the voltage within the imposed upper bound and close to the model-based approach, whereas the non-robust method has higher voltage violations. Fig. 5.7b shows the curtailed PV generation for

node 15, and it can be seen that model-less controls curtail more than model-based control. The model-based control curtails 86.5 kWh out of the total 210 kWh PV generation, whereas model-less non-robust and robust schemes curtail 106 and 104 kWh respectively. This is because they compute a more conservative solution to avoid voltage violations. Although the non-robust scheme curtails more, it fails to satisfy the voltage bounds due to inaccurate reactive power actuation. Finally, Fig. 5.7c shows the reactive power injections in three cases. Model-based and robust control follow a similar pattern, whereas non-robust provides less reactive power during the middle of the day.

Table 5.1: Performance comparison of different voltage control methods: maximum nodal voltage magnitude.

	IT 0.2		IT 0.5		IT 1.0	
Method	non-Robust	Robust	non-Robust	Robust	non-Robust	Robust
Model-based	1.031					
RLS-SF (model-less)	1.041	1.032	1.043	1.032	1.059	1.034
RLS-DF (model-less)	1.036	1.031	1.043	1.034	1.045	1.034

**Performance with Measurement Noise:** we also present a performance comparison when robust or non-robust control is subjected to different estimation techniques for different IT classes. The results are summarised in Table 5.1 that shows the maximum voltage magnitude violations resulting in different and the following observations: (i) non-robust control always results in voltage violations, even when the measurement noise is minimum; in contrast, robust control achieves negligible violations; (ii) RLS-SF and RLS-DF-based robust control performed the best with respect to maximum voltage violations, irrespective of the IT class.

## 5.5 Experimental Validation

The dominant scheme from the previous analysis (RLS-DF for the estimation, and robust voltage control) is used for experimental validation on a real micro-grid. It is described below.

### 5.5.1 Experimental Setup

We validate the proposed control scheme on a real microgrid at the Distributed Electrical Systems Laboratory at EPFL. The setup is similar to the one described in Sec. 2.8. For this control validation, we control two PV resources of nominal rating 13 kWp and 16 kWp capacities. Both can be controlled to curtail active power injection for voltage regulation by the developed robust voltage control scheme.

As was described in Sec. 2.8, the microgrid is equipped with 7 phasor measurement units (PMUs) which provide the measurements of nodal voltages and lines currents. Although the measurements are available at time sampling of 100 ms, we down-sample it to 1 second to demonstrate that the proposed model-less scheme doesn't require measurements at fast time

## Chapter 5. Model-less Robust Control of ADNs using Measurements-based Estimated Sensitivity Coefficients

sampling. Since the estimation using the direct approach (Sec. 4.4) requires power measurements, we compute the nodal powers using the voltage and current measurements from PMUs. The nodal voltages and currents are sensed by commercial LEM voltage transducer CV 3-1000 [147] and current transducer LF 205-S/SP3 [148] corresponding to IT measurement classes of 0.2 and 0.5 respectively.

In this setup, the control aims to keep the voltage within 0.96 - 1.04 per unit (pu) of the base voltage. The PV inverters are controlled with a time resolution of 30 seconds. This time resolution is chosen based on the time taken to execute the estimation, obtain a recent forecast of the PV production, and solve the robust control problem.

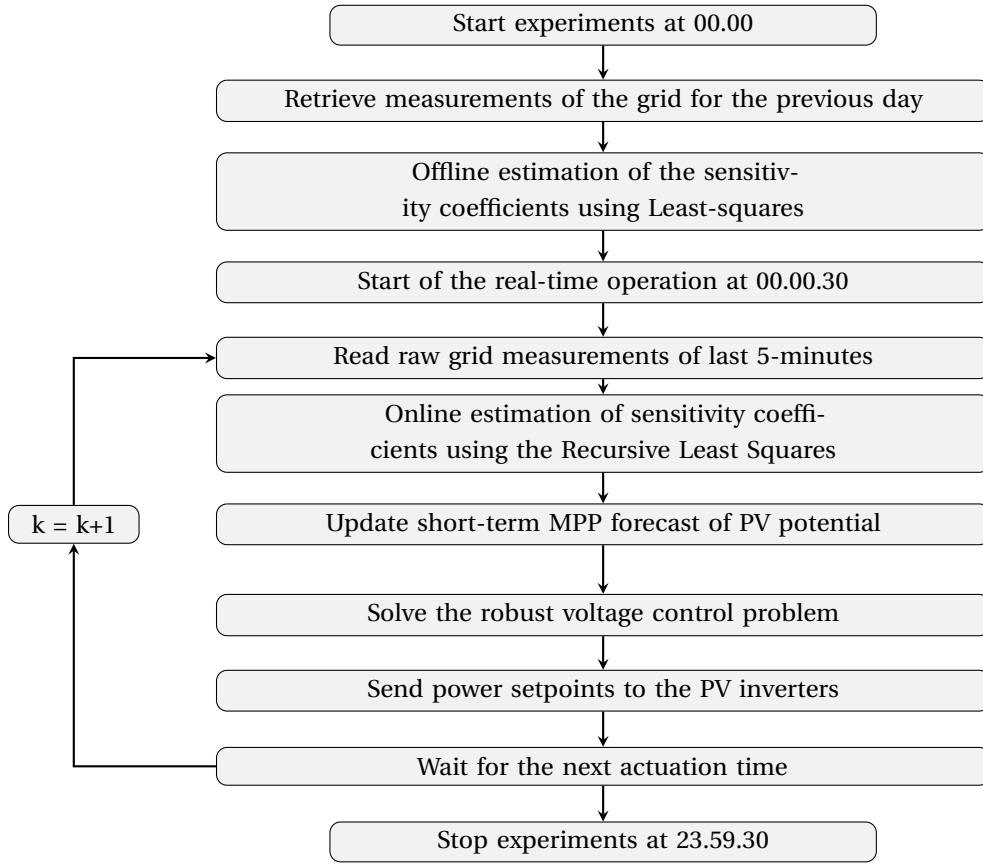


Figure 5.8: Flow-chart showing real-time operation during 24 hours.

The data flow during the real-time operation is shown in Fig. 5.8. The real-time operation starts at midnight 00.00 UTC. For the sensitivity coefficient estimation, we use the direct method (Sec. 4.4). It consist in obtaining offline estimation of the sensitivity coefficients by LS using the previous day measurements. Once these estimates are obtained, the real-time stage starts at 00.00.30. Using the recent 5-minutes measurements (sampled per second), it updates the estimation of the sensitivity coefficients. In the next step, we update the MPP (maximum power potential) forecasts of the PV generation using measurements on the solar irradiances and air temperature (using the weather-box as described in Sec. 3.5.1) and PV model from

[68]. Using the updated sensitivity coefficients estimates and the MPP forecast, the robust voltage control problem is solved. The power setpoints from the controller is then sent to the PV inverters. Their cycles are repeated every 30 seconds till end of the day's operation.

### 5.5.2 Experimental Results

We present the experimental results for two days of different types. The first corresponds to a weekend day (Saturday), whereas the second corresponds to a weekday (Monday). Both days are characterised by show clear sky irradiance patterns. In the following, we show the estimation and control results for these two days of experiments.

#### Day 1: Saturday (16 - July - 2022)

**Estimation Results:** the estimation results are shown in Fig. 5.9. We show the estimation results for nodes with controllable PV plant (node 9 and 11), i.e.,  $K_{11,11}^p$ ,  $K_{11,3}^p$ ,  $K_{9,9}^p$ , and  $K_{9,3}^p$ . The estimates are shown in red, and the uncertainty on the estimates are shown in shaded grey. They are compared against the true values (in black) those are obtained by model-based computation of the sensitivity coefficients [40]. As, it can be seen that the true coefficients fall within the estimated uncertainty bounds, therefore it can be used reliably for the real-time voltage control. The key metrics on the RMSE, and PICP-CWC-PINAW (defined earlier in Sec. 4.4.4) are shown in Table. 5.2.

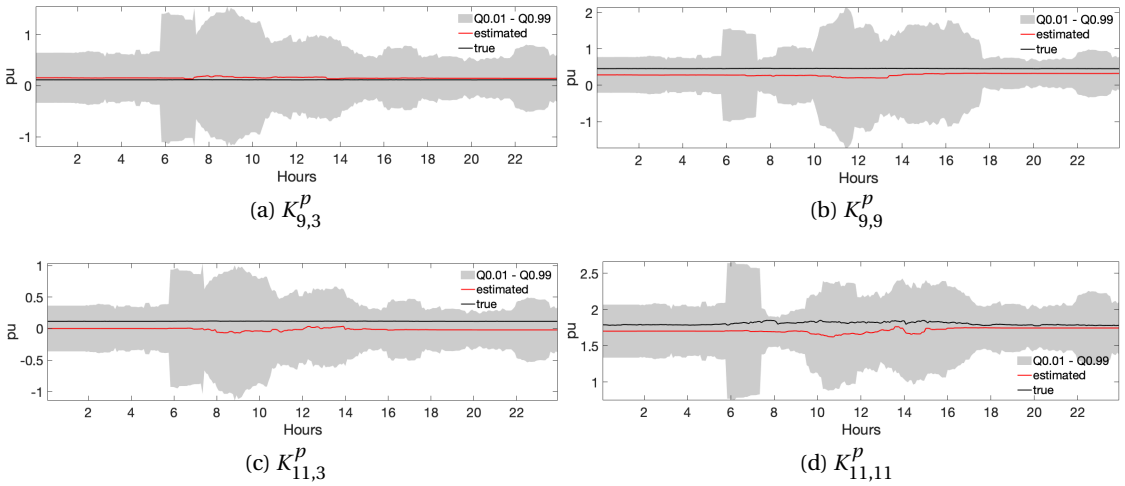


Figure 5.9: Coefficients estimates and their uncertainty for day 1.

**Control Results:** are shown in Fig. 5.10. The plot on top panel (Fig. 5.10a) shows the voltage measurements of different nodes: line plots show the voltage magnitude with the robust

## Chapter 5. Model-less Robust Control of ADNs using Measurements-based Estimated Sensitivity Coefficients

Table 5.2: Estimation performance on day 1.

Coefficients	RMSE	PICP-CWC-PINAW
$K_{9,3}^p$	0.34	1 - 11.27 - 11.27
$K_{9,9}^p$	0.38	1 - 3.48 - 3.48
$K_{11,3}^p$	1.12	1 - 8.47 - 8.47
$K_{11,11}^p$	0.03	1 - 0.74 - 0.74

control. We also show the plots when the robust control is removed<sup>31</sup>; it is shown in the shaded grey area. From the plots, it can be observed that the nodal voltage magnitudes of all the nodes are kept within the imposed limit of 1.04 pu using the proposed robust control scheme. In contrast, the voltage goes beyond the limit when there isn't any control. The control curtails PV generation from the two PV plants to keep the voltage within the imposed limit. Fig 5.10b and 5.10c shows the curtailed PV and the estimated maximum power potential (MPP) of each of the PV plant; MPP is estimated using the measurements of the solar irradiance, air temperature and the PV generation model from [68]. Fig. 5.10d and 5.10e shows the active and reactive power injections of the uncontrollable nodes. By looking at the experimental results, following observation can be made

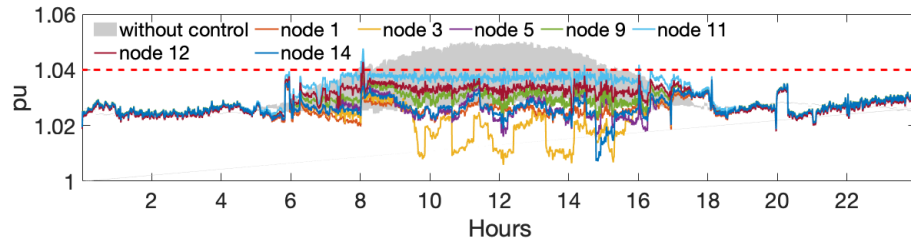
- The curtailment on the PV plant at node 11 is higher compared to the PV plant at node 9, as the former is hosted at the end of the feeder and causes overvoltage across all the nodes with its excess PV generation.
- PV plant starts curtailing at 8.00hrs due to a sudden rise in the voltage imposed at the slack node. Then, when the voltage goes down, PV starts increasing its generation.
- At around 11.00 hrs, 14 hrs, and 15 hrs there is generation at node 5 (shown in Fig. 5.10d), which leads to curtailments in PV generation at those intervals.
- An increase in demand at node 3 at around 11 hrs, and 13 hrs leads to an increase in the PV generations.

### Day 2: Monday (18 - July - 2022)

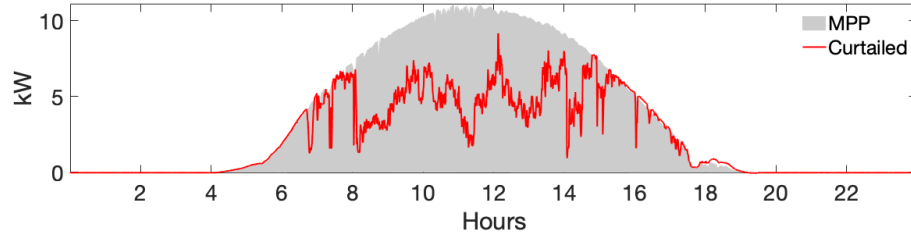
Similar to the day 1, the offline estimates are obtained by solving offline LS using previous day measurements. The estimation results and control results during the real-time operations are reported below.

**Estimation Results:** The estimations for day 2 are shown in Fig. 5.11. Again, the true sensitivities shown in black are covered by the estimation uncertainty i.e., by the shaded grey region.

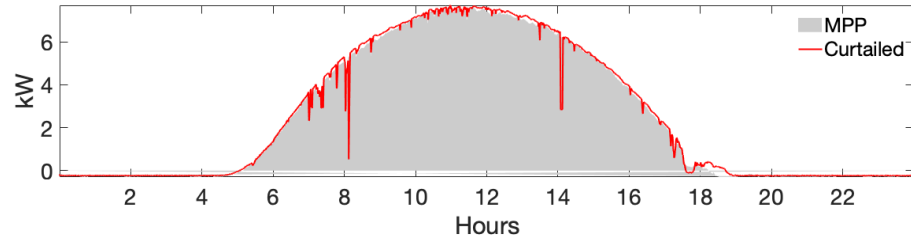
<sup>31</sup>The plot is obtained by simulating AC load flow by imposing the maximum power potential of the PV plants as the same experiment can not be repeated.



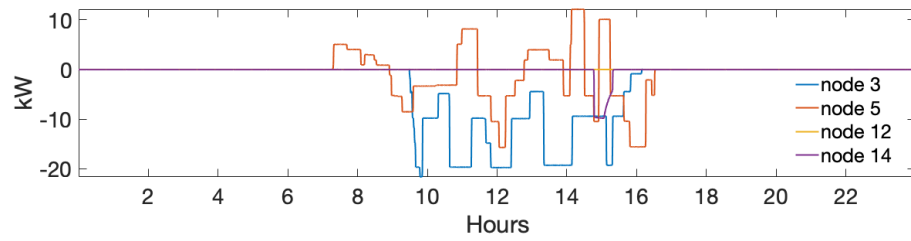
(a) Nodal voltage magnitudes with control (line plot) and without control (shaded grey).



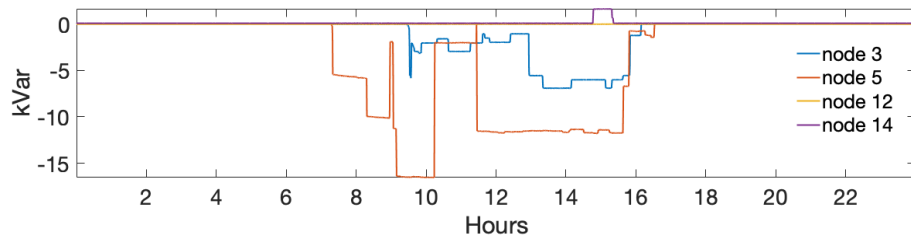
(b) PV plant at node 11: curtailed generation (line plot) and MPP (shaded grey).



(c) PV plant at node 9: curtailed generation (line plot) and MPP (shaded grey).



(d) Uncontrollable active power injections.



(e) Uncontrollable reactive power injections.

Figure 5.10: Experimental validation results for day 1: (a) voltage magnitude, (b) PV at node 11 (c) PV at node 9 and uncontrollable (d) active power (e) reactive powers at other nodes.

## Chapter 5. Model-less Robust Control of ADNs using Measurements-based Estimated Sensitivity Coefficients

The metrics listed in Table 5.3 show that, for all the coefficients, 100 % coverage is obtained. However, the coverage width in all cases is very high.

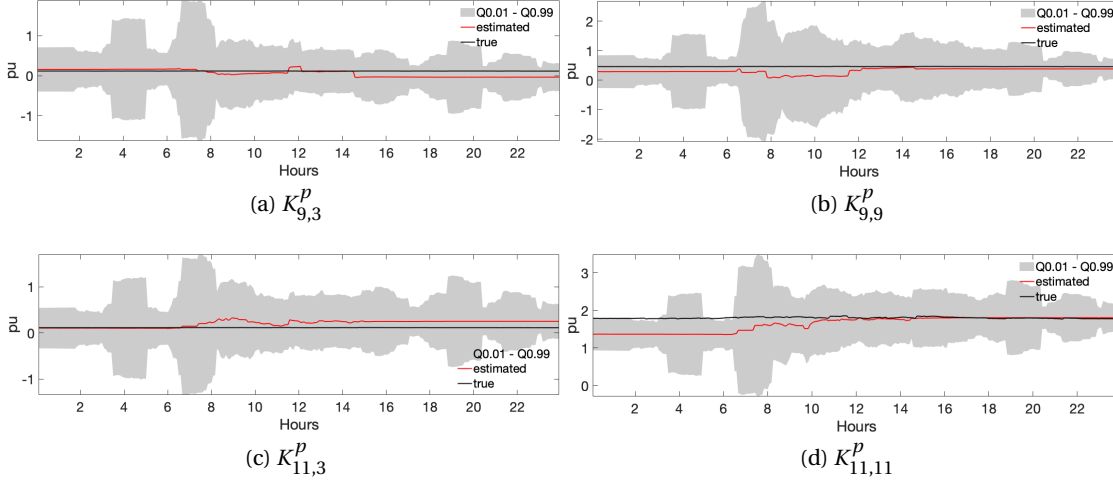


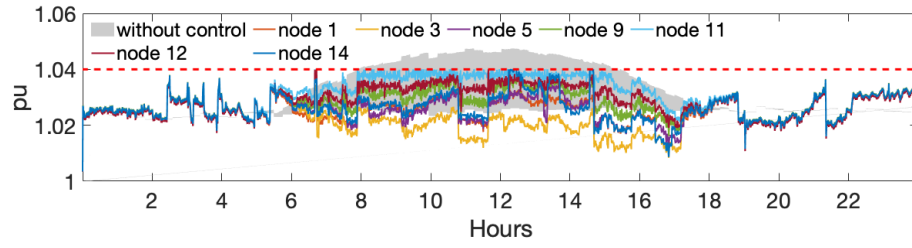
Figure 5.11: Coefficients estimates and their uncertainty for day 2.

Table 5.3: Estimation performance on day 2.

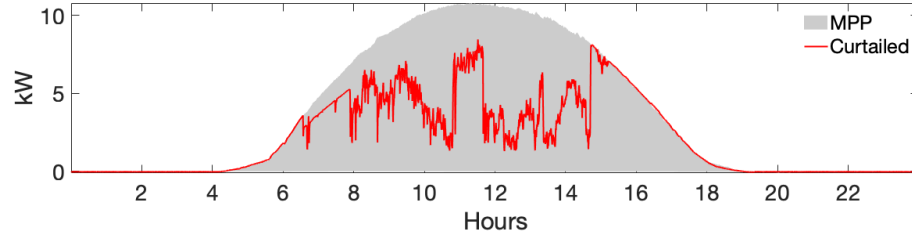
Coefficients	RMSE	PICP-CWC-PINAW
$K_{9,3}^p$	0.88	1 - 11.75 - 11.75
$K_{9,9}^p$	0.37	1 - 3.60 - 3.60
$K_{11,3}^p$	0.95	1 - 11.03 - 11.03
$K_{11,11}^p$	0.13	0.9 - 0.78 - 1.44

**Control Results:** as seen from the nodal voltage plots in Fig. 5.12, it can be concluded that the control scheme manages to keep the nodal voltage within the imposed limit, thanks to the curtailment of the PV generation in two PV plants. Again, most of the curtailments have happened on the PV plant at node 11. Day 2 experienced higher curtailments compared to day 1. It is because the voltage imposed by the upstream network is higher (on average) on day 2 compared to day 1. By looking at these plots, the following observation can be made:

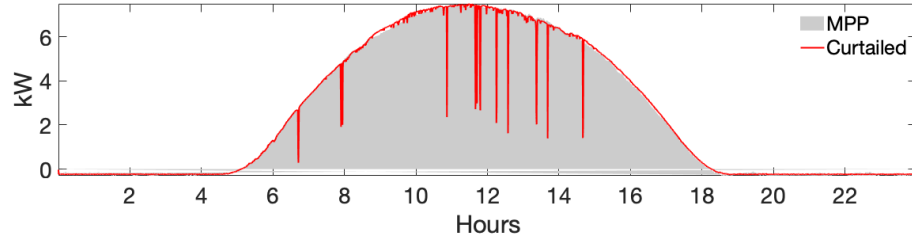
- PV plant starts curtailment slowly from 9 hrs to 11 hrs due to an increase in the nodal voltage at the slack (imposed by the upstream medium voltage network).
- PV production rises sharply at 11 hrs and after 14 hrs due to a sudden drop in the voltage at the slack (node 1). This might be due to a tap change on the primary side of the transformer connecting the upstream medium voltage network.
- PV generation is curtailed again just before 12 hrs due to an increase in the voltage at the slack.



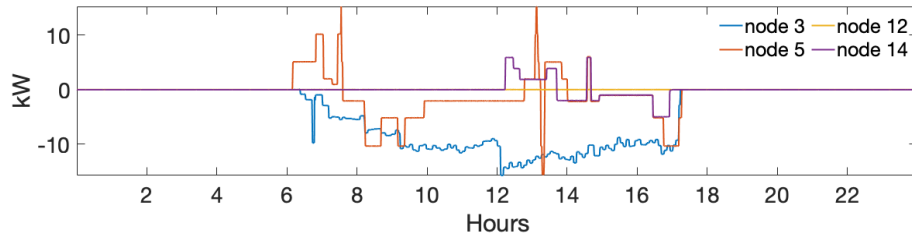
(a) Nodal voltage magnitudes with control (line plot) and without control (shaded grey).



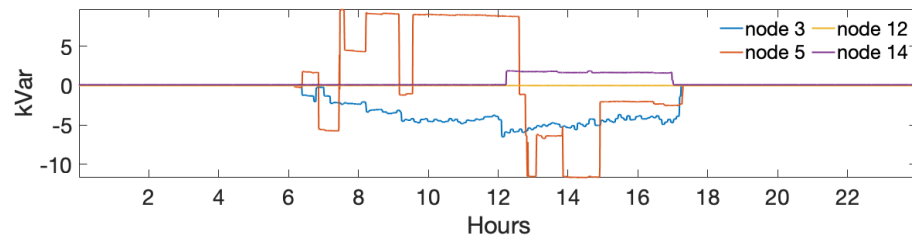
(b) PV plant at node 11: curtailed generation (line plot) and MPP (shaded grey).



(c) PV plant at node 9: curtailed generation (line plot) and MPP (shaded grey).



(d) Uncontrollable active power injections.



(e) Uncontrollable reactive power injections.

Figure 5.12: Experimental validation results for day 2: (a) voltage magnitude, (b) PV at node 11 (c) PV at node 9 and uncontrollable (d) active power (e) reactive powers at other nodes.



### Computation Time

Table 5.4 lists statistics on computation time lapsed for estimation, forecasting and solving robust control problem. It shows the average and maximum computation time. As seen, they are below the control actuation time of 30 seconds.

Table 5.4: Computation time

	Mean (seconds)	Max (seconds)
<b>Day 1</b>	14.7	24.8
<b>Day 2</b>	12.8	25.6

## 5.6 Discussion

This chapter proposed a model-less robust voltage control scheme accounting for the uncertainty on the sensitivity coefficients which are estimated from measurements. The robust control scheme relies on measurement-based estimated voltage sensitivity coefficients and their uncertainties. The voltage sensitivity coefficients are estimated using a recursive estimation algorithm, the dominant measurement-based estimation method from Chapter 4.

First, the scheme is validated numerically for controlling active/reactive power injections from distributed PV generation units connected to the CIGRE low-voltage benchmark network. The results show that the non-robust voltage controls fail to satisfy the voltage constraint (i.e., when uncertainty on the estimated coefficients are not accounted for). The proposed robust control scheme always satisfies the voltage control limits even for the highest instrument class producing the largest measurement noise. The performance comparison with respect to different estimation schemes shows that an online estimation scheme with directional forgetting performs the best.

Finally, the proposed control scheme is experimentally validated on a real microgrid which is a replica of the CIGRE benchmark micro-grid at the EPFL Distributed Electrical Systems Laboratory. The control results are shown for two different days of experiments where the PV inverters were controlled each 30 seconds. The results show that the proposed robust control scheme succeeds to keep the nodal voltage magnitudes within the imposed limits thanks to the curtailment action on the PV plants given by the proposed model-less robust voltage control scheme.

**Countrywide Impact of Large Renewable Deployment on the Planning of Active Distribution Networks**

**Part III**



## Prelude

*In parts I and II of this thesis, we presented control and scheduling frameworks for ADNs. The control algorithms were formulated to tackle the problem of local network constraint violations (such as nodal voltage violations and line and transformer congestion) and to provide ancillary support (such as dispatching) to the upper-level transmission grid. All the proposed control schemes rely on the availability of flexible distributed energy resources (DERs). As a matter of fact, the performance of such control schemes directly depends on the quantity of (i) the controllable (or flexible) resources and (ii) uncontrollable stochastic resources hosted by the ADN. Therefore, it is essential to compute the hosting capacity of the distribution networks, i.e., the amount of local stochastic generation (e.g., PV plants) that can be connected to the distribution system before reaching the violation of the grid operational constraints. Furthermore, it is worthwhile to investigate how much controllable flexibility is required when PV installation exceeds the grids' hosting capacity.*

*In this context, in this part III of this thesis we propose a countrywide planning scheme to assess the potential of PV and controllable resources, e.g., battery energy storage system (BESS) when the whole grid is forced to host PV plants beyond its hosting capacity. In particular, we develop a method to (i) assess the hosting capacity of ADNs concerning PV plants and ii) plan controllable assets as an alternative to the grid reinforcement. The analysis is carried out on a country scale. However, since countrywide models of the distribution grids are generally unavailable, we estimate realistic synthetic models of power distribution networks using public data sets. We focus mainly on medium voltage distribution networks because, in general, they account for the most significant part of the total grid upgrade costs associated to large PV generation deployment. Then, we propose a convex grid-aware planning problem to evaluate the PV hosting capacity of the estimated MV distribution networks. PV hosting of the whole country is determined by running the PV hosting capacity problem for all the inferred synthetic models of the distribution networks. Furthermore, we develop an optimal planning problem of BESSs for the distribution networks to increase their hosting capacity. As a final contribution, we derive cost-optimal plans for the countrywide deployment of PV generation and BESS considering the MV power distribution infrastructure's technical limitations. The method is applied to Switzerland as a case study.*



## 6 Countrywide Synthetic Network Estimation, Computation of PV Hosting Capacity and Battery Energy Storage Requirements for Power Distribution Networks

*Renewable energy resources (RERs) such as Photovoltaic (PV) plants are typically connected to power distribution networks. Historically, these networks are not designed to host large stochastic electricity generation. Given the prominent role of RERs in energy transition pathways, modelling the power distribution infrastructure's constraints is critical for its reliable techno-economical analysis and planning. However, power distribution grid data are generally confidential due to distribution system operators (DSOs) concerns and security. Publicly available test networks are minimal and can not applied to analyse a large region such as a whole country. In this context, this Chapter presents a method to estimate grid topologies and characteristics from public data sets. In particular, an unsupervised approach is proposed to infer the grid's topology and characteristics starting from publicly available locations of the Extra High Voltage (EHV) substations and geo-referenced socio-economic data such as population density maps and heat demand maps. The proposed method is applied to model the medium voltage distribution network of the whole Switzerland, and is made publicly available. Using the estimated synthetic power distribution networks, the Chapter presents a method to estimate the PV hosting capacity of those networks along with the cost-optimal sizing of battery energy storage systems (BESSs) for different levels of PV deployment. In particular, we develop an optimal planning schemes to size PV and BESS units in distribution grids. The formulation uses the linearized optimal power flow model (from Chapter 2) to model the grid constraints. Finally, we derive cost-optimal plans for countrywide deployment of PV generation and energy storage systems considering the MV power distribution infrastructure's technical limitations. The distributed PV generation potential is modeled with high-spatially resolved capacity factors, and the analysis is carried out countrywide using Switzerland as a case study.*

*The Chapter includes results of publication [149].*

## **6.1 Problem Statement**

We consider a geographical area for which we are interested in evaluating the renewable energy resources (RERs) hosting capacity. Since RERs are typically connected to power distribution networks, the evaluation requires networks' realistic models. However, these data are often not publicly available. In this context, the objective is to generate realistic synthetic models of power distribution networks in a given geographical area. In this Chapter, we propose an unsupervised method to infer the most likely grid topology and characteristics from publicly available information, i.e., locations of the Extra High Voltage (EHV) substations and geo-referenced energy demand data at high spatial resolution. The method uses the locations of the EHV substations to approximate their region of operation, referred to as EHV areas. Then, each EHV area uses the spatial distribution of the electricity demand to locate high voltage (HV) substations. The same process is applied to the HV substation location to approximate the areas and locations of the medium voltage (MV) substations. Finally, we use a routing scheme (based on common DSO practices) to estimate the topology and line parameters of the MV grids.

Once the network models are estimated, the Chapter presents a method to compute their PV hosting capacities, i.e., the amount of PV generation which can be connected to each distribution network without creating any grid violations such as min/max nodal voltages, max line ampacities, and max transformer power flows. Then, it also presents a scheme to optimize the sizes and sites of energy storage systems (BESSs) when the grid hosts PV generation higher than the estimated capacity. The problem accounts for the investment costs for the BESSs and PV plants. Grid constraints (i.e., nodal voltages, lines, and substation transformer limits) are modeled by linearized power flow equations (Chapter 2) to keep the problem formulation tractable. Finally, we derive cost-optimal plans for countrywide deployment of PV generation and BESSs considering the MV power distribution infrastructure's technical limitations. The distributed PV generation potential is modelled with high-spatially resolved capacity factors, and the analysis is carried out countrywide using Switzerland as a case study.

## **6.2 State-of-the-Art**

Assessing the generation potential of distributed PV has attracted significant attention in the recent literature. For example, [150] proposes a rule-based estimations and [151] a geographic information system (GIS) approach to assess PV deployment potential for a large part of Europe considering the land availability. The considered spatial scales go from city to subcontinental levels, as in [152, 153, 154, 155, 156, 157] and [158], respectively. The works above mentioned focus on estimating the PV generation potential without considering the impact on the power distribution systems. Distributed PV generation, such as rooftop PV plants installed either on urban industry or rural environments, are typically connected to distribution grids, which, however, are designed to primarily deliver power to consumers and, as a matter of fact, can interface a limited amount of power generation. The main limitation is due to the DSO's

requirements to satisfy the physical constraints of the power grid assets (other limiting factors are associated to protections adoption and dispatching of DSO grids). The amount of PV generation that a distribution grid can connect without violations of the grid constraints is called *PV hosting capacity*. Power distribution systems are an important asset of the electrical infrastructure and upgrade costs to increase their generation hosting capacity are substantial [159]. Therefore, a reliable techno-economical assessment of the distributed PV generation potential should be done in conjunction with an accurate assessment of the PV hosting capacity of the existing distribution grids. The PV hosting capacity of distribution grids is typically assessed for MV and LV distribution systems with probabilistic load flows applying the Monte Carlo method [160, 161, 162, 163], or by less computationally intensive variations [164], or OPF models [165, 166]. Load flow- and OPF-based approaches require the knowledge of the grid topology, lines characteristics (length, physical parameters, buried/aerial type), and demand and PV generation profiles. Due to the large diversity of distribution grids in terms of topology and demand patterns, it is generally not possible to extend the results from a few known networks to the level of a country, which, depending on its size, might have thousands of MV distribution grids with different features.

Concerning synthetic network data generation, different methods have been proposed depending on the availability of public data sets. Broadly, these methods can be categorized in two different types: (i) *supervised* and (ii) *unsupervised* methods. The *supervised* methods use data from existing grid models to estimate information of unobserved grids [167, 168, 169, 170, 171]. The work in [167] use statistical properties such as topological characteristics (sparsity), nodal degree distribution (number of outgoing and incoming nodes from a parent node) and line impedances derived from known power grids. The work in [168] proposes a random growth model for power grids based on parameters such as degree distribution and average shortest path length derived from existing power network models. The work in [169] uses Gaussian Mixture Model (GMM) to estimate the density of the node positions and generates a set of nodes with a similar spatial distribution. It also uses average path length, clustering coefficient, degree of distribution of the nodes, and length of the lines as extra features. The work in [170] presents a set of validation criteria based on data from existing power grids. These structural properties include connectivity of the nodes, Delaunay triangulation overlap [172], DC power flow analysis, and geographic intersection rates [170]. It proposes a scheme to locate and connect the power substations to match the above-listed structural properties. *Unsupervised* methods use socio-economic data, like population density maps and electricity demand to generate distribution network models without prior knowledge of the power grids characteristics [173, 174, 175, 176]. The work in [173] uses population density data to cluster geographical regions into rural and urban areas and further classified into small, medium, and large areas based on the size of the population. The method uses a heuristic approach to locate and route the medium and low-voltage substations. The work in [174] proposed an open-source tool named *Distribution Network GeneratOr* (DINGO) that uses available GIS-referenced demand data from *OpenEnergy Platform (OEM)* [177] which also partitions areas into medium-voltage and low-voltage grid districts. The scheme in [174] uses the Capacitated



## Chapter 6. Countrywide Synthetic Network Estimation, Computation of PV Hosting Capacity and Battery Energy Storage Requirements for Power Distribution Networks

---

Vehicle Routing Problem (CVRP) for the routing of these load areas. [175] uses OSM data for modeling the sub-transmission high voltage power grids of the state of Schleswig-Holstein in Germany. The work in [176] used a similar approach as [174] but for the HV and EHV grid of Germany. [171] contains a survey of different modeling approaches using publicly available data from OpenStreetMap (OSM) in conjugation with other open-source software tools. [178] developed the tool *SciGRID* which used OSM power data, filters them, and connects them by standard lines impedances from benchmark networks. A similar approach was adopted in *osmTGmod* [179]. All the above works require a database of existing power networks to derive some structural properties from being used in the generation model. Also, most of these studies are focused on modeling transmission systems and can not be used to infer detailed power distribution network models.

Given the above discussed limitations of existing literature, and due to the lack of availability of a large public dataset on existing power networks, in this Chapter, we propose an unsupervised approach to generate the synthetic power distribution networks. With respect to existing unsupervised methods in [173, 174, 175, 176] described above, our approach relies on less information, requiring only the location of the EHV substations and the spatial distribution of the demand. After the synthetic networks are obtained, we estimate the PV hosting capacity of each network with a tractable OPF based on linearized grid models, including also how to optimally deploy BESSs to increase the grids' PV hosting capacity. Finally, we determine the countrywide cost-optimal deployment of PV generation and BESSs to achieve a target level of PV installed capacity accounting for the spatial information on the capacity factor of PV generation. In summary, the main contributions of this Chapter are listed below.

- Propose an unsupervised method to estimate MV grids synthetic models starting from publicly available information.
- Formulate a tractable convex OPF-based tool to estimate the PV hosting capacity and optimal planning of BESS in distribution grids.
- Propose a tractable convex optimization problem to determine countrywide cost-efficient PV and BESS deployments plans to accommodate a target PV generation level accounting for the capacity factor of PV generation.

Compared to the works in [150, 180] that report country-specific analyses of the PV potential and works in [156, 157, 181, 182, 183] that specifically refer to Switzerland, we estimate, for the first time in the literature, the PV generation potential for a whole country subject to the limitations of the existing distribution networks infrastructure. Compared to the works in [160, 161, 162, 163] that evaluates the PV hosting capacity of small systems, we propose a method that can be extended to large areas, that estimates grid data and includes the deployment of BESSs to increase the PV hosting capacity.

## 6.3 Estimation of Countrywide Models of Medium Voltage Power Distribution Networks: the Case of Switzerland

In this section, we describe the procedure to estimate the countrywide models of MV distribution grids. The procedure is graphically represented in Fig. 6.1 and summarized next. Starting from the locations of the EHV substations, we approximate the geographical region that each substation serves by partitioning the country with Voronoi diagrams [184] (as described in subsection 6.3.1). We call these partitions EHV areas. Then, for each EHV area, we process the geographical distribution of the electricity demand to infer the position of the HV substations (subsection 6.3.2). By re-applying these two steps using the HV substation positions as input, we first identify the areas served by each HV substation, called HV areas. Finally, we find the locations of the MV substations (subsection 6.3.3). Once the location of the MV nodes are known, a routing scheme is used to estimate the topology and cable parameters of the relevant MV grids (subsection 6.3.4).

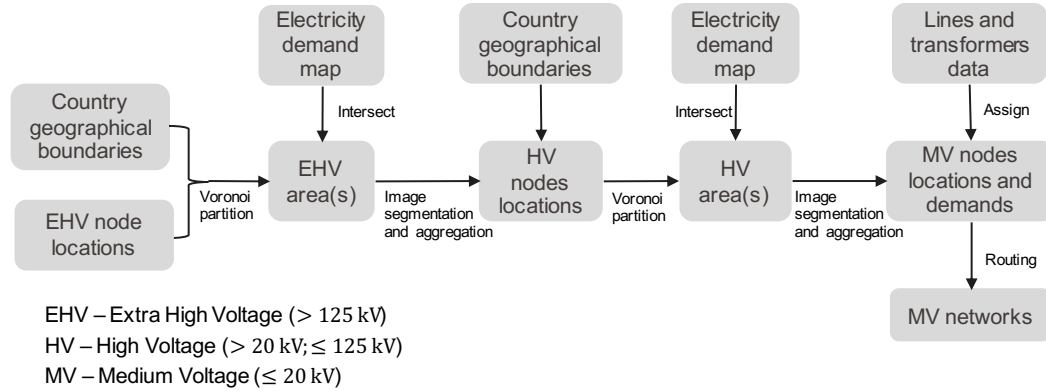


Figure 6.1: Flow chart for the estimation of countrywide models of medium voltage power distribution networks.

In order to exemplify the description of the proposed algorithms, in the following of this Chapter we specifically refer to the case of Switzerland.

### 6.3.1 Identification of EHV Areas

EHV/HV substations adapt the power grid voltage level from a value suitable for transmission over long distances to a more practical value for short-distance transmission and more suitable to be transformed by primary and secondary substations to the final level at which electricity is consumed. As opposed to the substations at the distribution level, the locations of the primary substation are available in public databases (e.g. [185]). We use them as the first step to infer the rest of the network.

In total, we consider 148 georeferenced EHV substations. The locations of the EHV nodes

## Chapter 6. Countrywide Synthetic Network Estimation, Computation of PV Hosting Capacity and Battery Energy Storage Requirements for Power Distribution Networks

are from the dataset [186], that is derived from ENTSOE information. These locations were verified by visual inspection from satellite images and it was found that not all the locations from [186] correspond to real ones (as also acknowledged on the ENTSOE website<sup>32</sup>). The inaccurate locations were corrected, when possible, by considering the locations reported in the collaborative dataset,<sup>33</sup> which were found accurate after being verified one by one on aerial images. The locations of the EHV nodes are shown in Fig. 6.2a.

Starting from the locations of the EHV substations, we apply Voronoi diagrams to approximate the region that each EHV node serves. Given an image and a collection of coordinates within that image, a Voronoi diagram (one per set of coordinates) is the closest (in terms of geographical distance) locus of points to those coordinates. The adoption of the Voronoi diagrams is justified as we may reasonably assume that the electrical demand in a certain area is served by the closest substation. This modeling choice is also proposed in [174, 187, 188, 189]. The result of the Voronoi partitioning is shown in Fig. 6.2b.

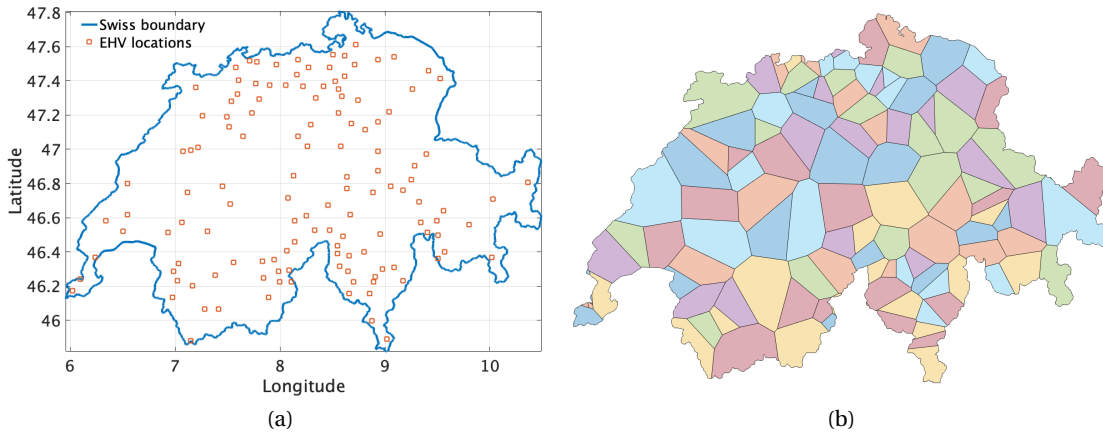


Figure 6.2: Identification of EHV areas: (a) locations of the considered 148 EHV's substations in Switzerland and (b) approximated regions served by each substation after Voronoi partitioning.

### 6.3.2 Identification of HV/MV Primary Substation: Locations and Characteristics

#### Distribution of the Electrical Demand

Power distribution systems were designed to deliver electricity to end customers. Therefore, we expect their topology and power ratings to reflect the geographical distribution of the demand for electricity. We leverage this notion and start from the distribution of the electricity demand over the country to infer the topology of distribution systems. First we estimate the low-level geographical distribution of the electricity demand as described next.

<sup>32</sup><https://www.entsoe.eu/data/map/>

<sup>33</sup>[https://en.wikipedia-on-ipfs.org/wiki/List\\_of\\_EHV-substations\\_in\\_Switzerland](https://en.wikipedia-on-ipfs.org/wiki/List_of_EHV-substations_in_Switzerland)

### 6.3 Estimation of Countrywide Models of Medium Voltage Power Distribution Networks: the Case of Switzerland

The work in [190] reports the statistics of the sectorial (industrial, commercial and residential) electricity consumption for each canton in Switzerland. This information gives already a comprehensive overview of the countrywide distribution of the electricity demand. However, since power distribution systems extend far deep into local regions, higher spatially resolved data are needed to estimate their topology. The Swiss Federal Office for Topography<sup>34</sup> has mapped the heat demand for space heating and cooling for industrial, commercial, and residential buildings with a resolution of 100x100 meters. Since the heat demand follows the building distribution and that buildings are also large consumer of electricity (due to various electrical equipment, besides the obvious case of electric space heating [191, 192], that reinforces the correlation among the two), we assume that the electricity and heat demands follow the same spatial distribution. With this assumption, we model the electricity demand map by rescaling heat demand map by appropriate coefficients. These coefficients are computed separately for the residential, commercial and industrial demands using the values of electricity consumption (Table 6.1). The estimated countrywide electricity demand map is shown in Fig. 6.3a. Fig. 6.3b is an illustrative example of the electrical demand distribution within a single Voronoi cell. The geographical area each Voronoi cell is supplied by the substation corresponding to that cell.

Table 6.1: Composition of electricity demand in different sectors for Switzerland for 2014.

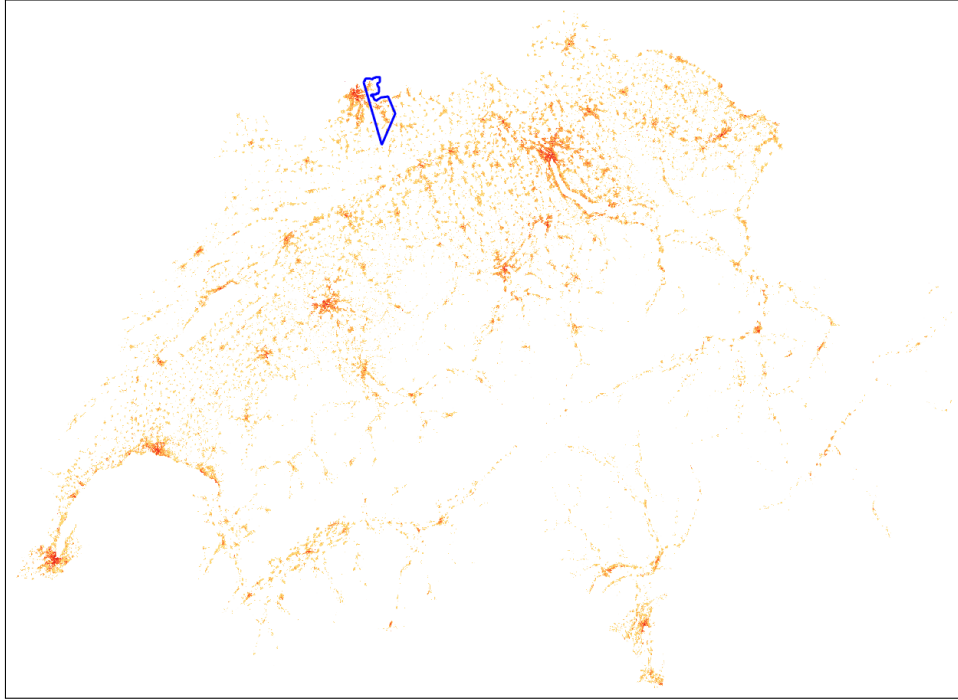
Sector	Electricity demand (GWh)
Residential	18'333
Commercial	17'531
Industrial	19'028

#### Identification of the HV/MV Primary Substations

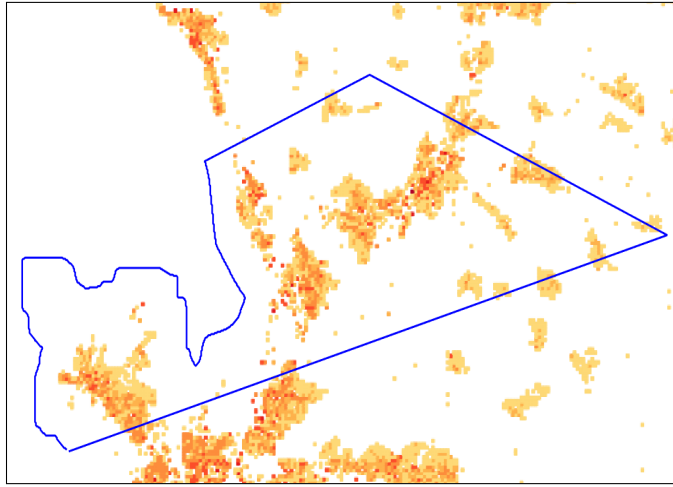
The location of the HV/MV primary substation is determined by analyzing the electrical demand map within each EHV area according to the following procedure.

1. Identify clusters with contiguous demand. To do so, we first derive a binary image from the electrical demand map, where boolean true pixels denote non-zero electrical demand, and vice-versa. Then, to identify clusters with contiguous demand, we apply binary image segmentation, that partitions the input binary map into clusters containing pixels of the same kind (true or false) only. For the binary image segmentation, we use the `bwboundaries` Matlab function [193]. The result of this process for the example EHV area of Fig. 6.3b) is shown in Fig. 6.4a;
2. On the one hand, clusters with total demand exceeding a pre-established threshold are recursively partitioned into smaller clusters using **Algorithm 6.1**. On the other hand, neighbour small clusters are aggregated until their total power demand reaches the

<sup>34</sup><http://map.geo.admin.ch/>



(a)



(b)

Figure 6.3: Estimated electricity demand map of: (a) Switzerland and (b) a single EHV area. The blue polygon refers to an EHV area obtained using Voronoi partition.

threshold and so as to justify the presence of a secondary substation. The result of this step is illustrated in Fig. 6.4b. Threshold  $\bar{L}$  in **Algorithm 6.1** is an informed estimated computed as

$$\frac{\text{average power demand}}{\text{number of EHV substation} \cdot 5} = \frac{63 \text{ TWh}/8760 \text{ h}}{148 \cdot 5} \approx 10 \text{ MW}, \quad (6.1)$$

### 6.3 Estimation of Countrywide Models of Medium Voltage Power Distribution Networks: the Case of Switzerland

where 63 TWh is the total electricity demand in Switzerland in 2015 [194] and 5 is the estimated average number of HV/MV nodes served by each EHV/HV substation.

3. The location of each secondary substation is chosen at the geographical center of the convex-envelope<sup>35</sup> encompassing the respective aggregated cluster, as shown in Fig. 6.4c.

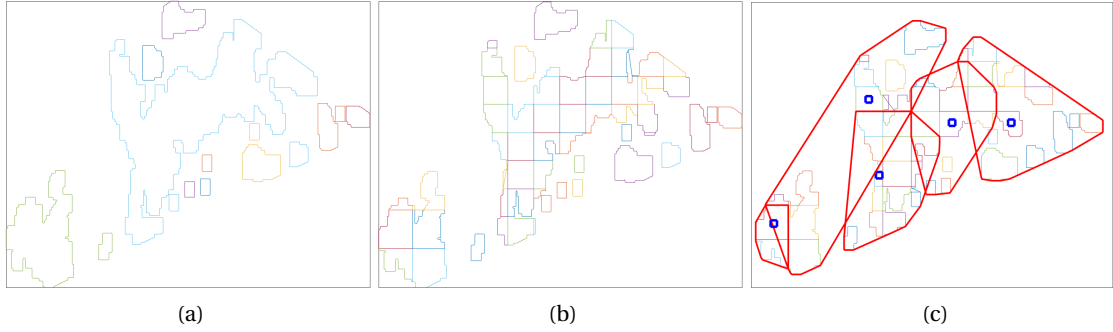


Figure 6.4: Identification of the substations locations: (a) the EHV area is divided into clusters, (b) large clusters are divided into smaller ones, (c) convex hull of the aggregated clusters (in red) and final locations of the HV substations (in blue).

---

#### Algorithm 6.1 Partition cluster

---

**Require:**  $\text{Poly}_{\text{cluster}} :=$  original cluster,  $L_c :=$  cluster's total demand, demand threshold  $\bar{L}$ ,  $\mu :=$  Divide factor (<sup>36</sup>)

- 1: **if**  $(L_c > \bar{L})$  **then**
- 2:    $n = \text{ceil}(L/\bar{L}/\mu)$ ,  $n_x = \text{ciel}(\sqrt{n})$ ,  $n_y = \text{ciel}(n/n_x)$ ,  $\tilde{n} = n_x n_y$
- 3:   Find the bounding box of  $\text{Poly}_{\text{cluster}}$  defined  
by  $(\text{Poly}_{\text{bbox}} = \{(x, y) : \underline{x} \leq x \leq \bar{x}, \underline{y} \leq y \leq \bar{y}\})$
- 4:   Partition: obtain  $[\text{Poly}_{\text{div}}^1, \dots, \text{Poly}_{\text{div}}^{\tilde{n}}]$
- 5:   **for**  $(i = 1, \dots, n_x)$  **do**
- 6:      $a^i = \underline{x} + \frac{(i-1)(\bar{x}-\underline{x})}{n_x}$ ,  $c^i = \underline{x} + \frac{(i)(\bar{x}-\underline{x})}{n_x}$ ,
- 7:     **for**  $(j = 1, \dots, n_y)$  **do**
- 8:       $b^j = \underline{y} + \frac{(j-1)(\bar{y}-\underline{y})}{n_y}$ ,  $d^j = \underline{y} + \frac{(j)(\bar{y}-\underline{y})}{n_y}$
- 9:       $\text{Poly}_{\text{div}}^k = \{(x, y) : a^i \leq x \leq c^i, b^j \leq y \leq d^j\}$
- 10:       $\text{Poly}_{\text{div}}^k = \leftarrow \text{Poly}_{\text{cluster}} \cap \text{Poly}_{\text{div}}^k$  ▷ Intersection
- 11:       $k + 1 \leftarrow k$
- 12:    **end for**
- 13:   **end for**
- 14:   Compute the demand of each small polygon:  $[L_{\text{div}}^1, \dots, L_{\text{div}}^{\tilde{n}}]$
- 15:   Save  $[\text{Poly}_{\text{div}}^1, \dots, \text{Poly}_{\text{div}}^{\tilde{n}}]$ ,  $[L_{\text{div}}^1, \dots, L_{\text{div}}^{\tilde{n}}]$
- 16: **end if**

---

<sup>35</sup>The convex envelope allows efficient computation of its centroid and distance with other convex-envelopes.

<sup>36</sup>Divide factor is chosen appropriately ( $\leq 0.5$ ) to obtain polygons with demands smaller than  $L_{\text{thres}}$ .

## Chapter 6. Countrywide Synthetic Network Estimation, Computation of PV Hosting Capacity and Battery Energy Storage Requirements for Power Distribution Networks

Fig. 6.5a shows the cumulative distribution function (CDF) of the demand interfaced by the various primary substations, and the first row of Table 6.2 reports its mean and maximum value. It can be observed that, even if a static threshold of 10 MW is used to generate the clusters, the demand within each cluster is finally spread around this value. On the one hand, larger values of the total demand happen because when merging multiple clusters, their aggregated demand might exceed the threshold. On the other hand, smaller values are because certain areas have low demand.

### 6.3.3 Identification of MV/LV Secondary Substation: Location and Characteristics

Once the locations of the primary substations are found, we apply the Voronoi partitioning and cluster-aggregation procedures of subsections 6.3.1 and 6.3.2 to identify the HV areas and the MV/LV secondary substations. For the latter step, we use a threshold value for the total power within each cluster of 400 kW. This value has been chosen because it is the average power rating of the nodes of the CIGRE benchmark grid for MV european systems [5]. The distribution of the demand interfaced by the secondary substation and its statistics are reported in Fig. 6.5b and Table 6.2. Similarly to the previous case, the demand within each cluster is spread around the static threshold.

Table 6.2: Statistics on HV and MV substations

Type	Number	Mean Demand	Max Demand
HV substations	776	9.3 MW	24.7 MW
MV substations	17,844	0.41 MW	0.97 MW

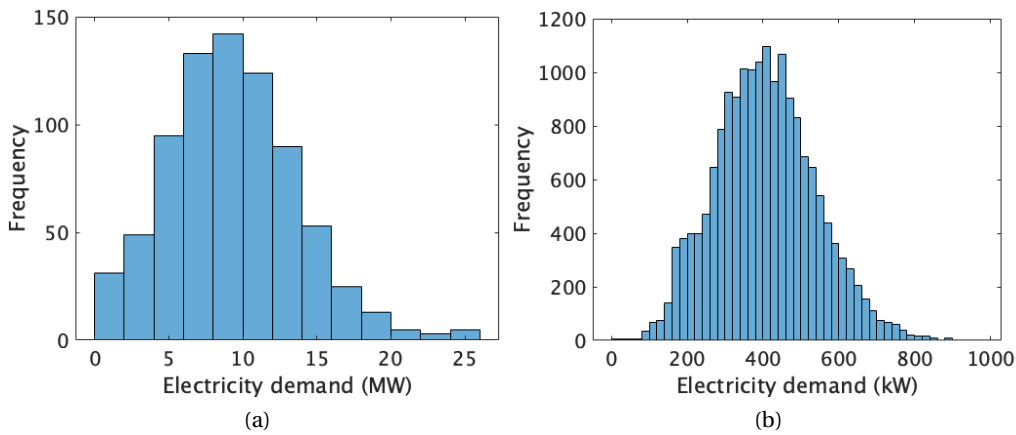
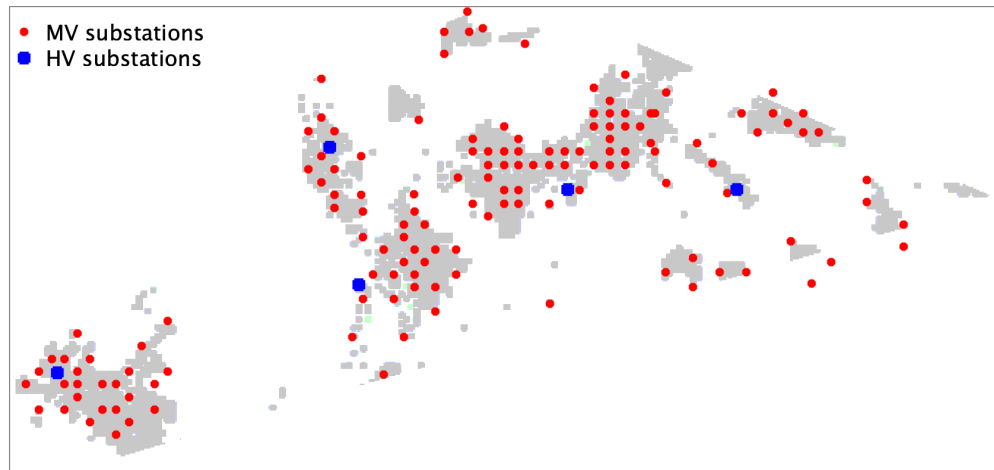


Figure 6.5: Probability density function (PDF) plots of estimated electricity demands for (a) HV and (b) MV substations.

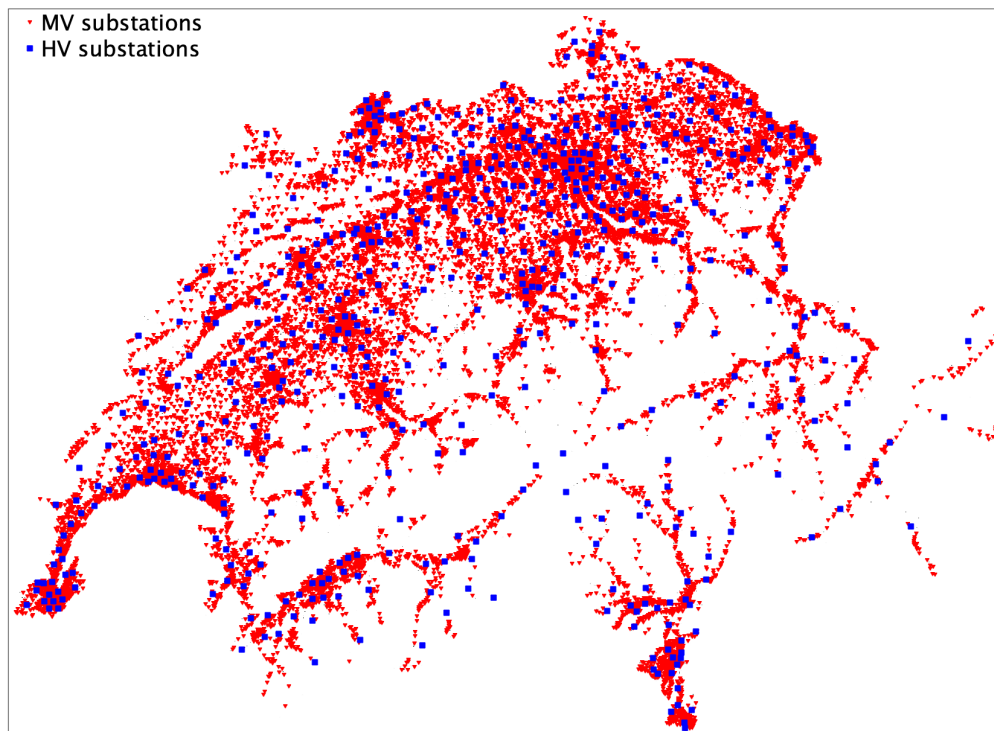
Fig. 6.6a shows the identified locations of the substations for the example EHV area of Fig. 6.3b, where 5 HV/MV and 142 MV/LV substations were identified. This process is repeated for all

### 6.3 Estimation of Countrywide Models of Medium Voltage Power Distribution Networks: the Case of Switzerland

EHV areas so as to estimate the locations of HV/MV and MV/LV substations for the whole country. For Switzerland, the model estimated 776 HV/MV nodes and 17'844 MV/LV, whose locations are shown in Fig 6.6b.



(a)



(b)

Figure 6.6: Identified HV/MV and MV/LV substations for (a) the example EHV area (5 and 142, respectively) and (b) Switzerland (776 and 17'844)



### **6.3.4 Power Networks Routing**

#### **Routing Algorithm**

Once the locations of the MV substations are identified, we use a routing scheme to determine the connections and topologies of the corresponding grids. Several routing methods were proposed in the literature, as discussed in the review paper [195]. For example, the work in [196] uses a genetic algorithm and minimum spanning tree, works in [197, 198, 199] apply evolutionary algorithms such as simulated annealing and ant-colony. The work in [200, 201] proposes the branch-exchange method, and the work in [202] applies dynamic programming.

In this Chapter, we use the routing scheme based on the steepest gradient descent proposed in [203, 204] because of the faster convergence and increased tractability compared to the above-listed methods. The method accounts for the grid operational constraints on voltage magnitudes and lines ampacities. It enforces the radiality of the final system because the MV networks are generally operated radially (as opposed to HV systems, that are typically meshed and operated as such). Although some MV network might have a meshed configuration (useful, e.g., for networks temporary operations in case of outages), they are usually operated radially to enable the effective operations of protection systems [205]. The method works by finding the grid topology that minimizes the invested capital cost into the grid, given by the investment cost for the power cables. In the routing scheme, we require voltage deviations to be up to  $\pm 3\%$  of the nominal voltage according to Swiss grid code [206]) and line currents below 80% of the respective cable ampacity, to reproduce a realistic scenario where grids operate with a safety margin from physical limits. The electrical characteristics of the lines and transformer used for the routing procedure are given in Tables 6.3 and 6.4, respectively. The rating of transformer is assumed 150 % of the total nominal demand to reflect the typical planning scenario where operators allow equipments to operate with a safety margin from their maximum ratings.

The routing scheme starts from a base topology where each substation node is connected to the 6 nearest ones (a value taken from the work in [167] to define an upper bound on the connections to/from a node in a typical power grid). Then, the following steps are performed:

1. run the routing scheme in **Algorithm 6.2** by selecting high-ampacity type-4 cables (from Table 6.3) for all the lines;
2. replace the type-4 cables (since they are most expensive ones according to their ampacity) with ones with lower ampacity according to the criterion reported in Table 6.5. For example, if the maximum line current in the first-stage routing is less than 10 % of the type-4 cable's ampacity, it is replaced with a type-1 cable. Once each single cable is replaced, we perform a load flow to verify voltage and current conditions and, if they are not satisfied, the original cable is restored.

Figure 6.7 shows the step-by-step routing results for an example EHV area. Fig. 6.7b shows the

### 6.3 Estimation of Countrywide Models of Medium Voltage Power Distribution Networks: the Case of Switzerland

Table 6.3: Cable ratings from a commercial source.

Cable Type	Section [mm <sup>2</sup> ]	Resistance [Ohm/km]	Reactance [Ohm/km]	Capacitance [ $\mu$ F/km]	Ampacity [A]
1	50	0.495	0.13	0.19	228
2	70	0.344	0.13	0.21	284
3	95	0.248	0.12	0.23	346
4	120	0.198	0.12	0.25	399

Table 6.4: Transformer rating.

HV voltage [kV]	MV voltage [kV]	Short-circuit impedance [Ohms]	Power rating [MVA]
110	20	$0.016 + j1.92$	25

---

#### Algorithm 6.2 Routing

---

**Require:** Base topology, line parameters, lines set

- 1: **while** Routing is successful (the network is connected and feasible) **do**
  - 2:   Remove the most expensive line (by length) from the lines set
  - 3:   Proceed to step 4 if connected else go to step 7
  - 4:   Compute admittance matrix, perform load flow, proceed to step 5 if converged else go to step 7
  - 5:   Proceed to step 6 if the voltage and currents are within bounds else go to 7
  - 6:   Save the network, update the lines set and go to step 2
  - 7:   Keep the previous network, remove this line from the lines set, go to step 2.
  - 8: **end while**
- 

Table 6.5: Replacement scheme for lines.

Current range (pu)	Cable type
$0 < 0.1$	1
$0.1 \leq 0.2$	2
$0.2 \leq 0.4$	3

initial routing, which is obtained by connecting each node with the nearest 6 nodes. Fig 6.7c shows an intermediate stage of the routing, where some of the redundant lines have been removed. The final topology is shown in Fig. 6.7d, where the color of the lines denotes their ampacities. **Algorithm 6.2** works by iteratively removing the expensive (i.e., long) lines to minimize the cost of grid routing. The routing cost, expressed in terms of the total lines length, is shown in Fig. 6.7e for an example grid. It features a decreasing value before reaching a steady value after 300 iterations. In this example, the initial and final iterations correspond to 67 km and 10.5 km, respectively, of deployed lines.

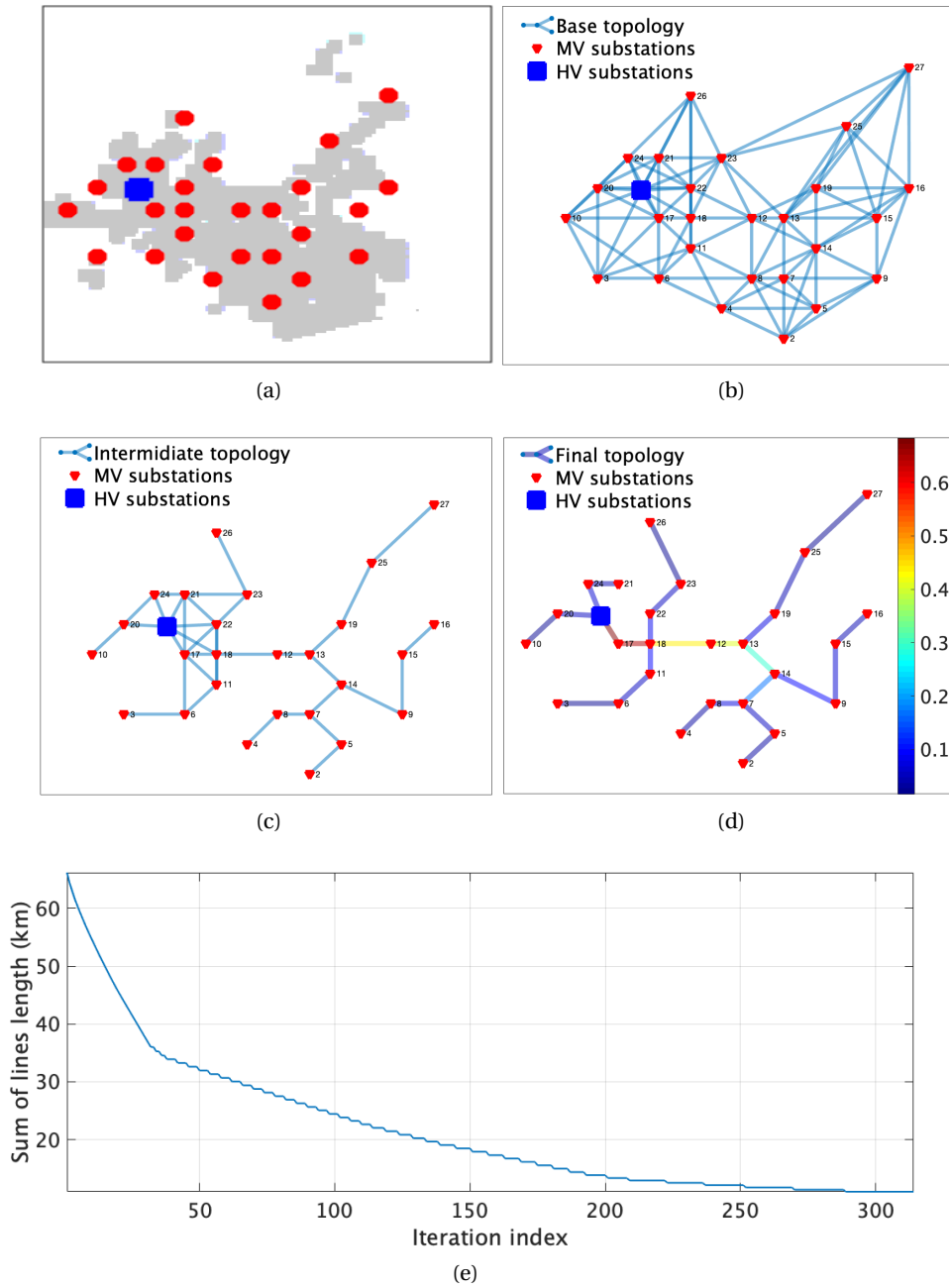


Figure 6.7: Routing procedure:(a) example EHV area with HV and MV substations, (b) highly-connected base topology, (c) meshed grid topology at an intermediate stage of the procedure, (d) final topology highlighting the current levels in the cables, and (e) total capital cost (expressed in km for length of cables used) as a function of the iteration.

### Re-routing Unsuccessful Networks

In certain cases, the routing by **Algorithm 6.2** might fail. This happens when a subset of the nodes in the given region is very distant in space to the rest of the nodes requiring very long

### 6.3 Estimation of Countrywide Models of Medium Voltage Power Distribution Networks: the Case of Switzerland

cables. It either results in violations on voltage and currents or convergence issues while solving load-flows or requires a meshed topology with single or multiple rings to be feasible. These networks are labelled as *unsuccessful* networks. To solve this issue, we propose a re-routing procedure, where we divide the region further using a clustering method. The steps are described in **Algorithm 6.3**. An example is shown in Fig. 6.8, where on the left figure, we see a meshed network to enable it to be routed due to current and voltage violations, whereas the right figure shows that the network is divided into two separate radial networks.

---

#### Algorithm 6.3 Re-routing

---

**Require:** Substations' geographical locations

- 1: **while** The network is connected and feasible **do**
  - 2:   Split the *unsuccessful* networks into two areas using k-means clustering with locations as features
  - 3:   Place HV substations at the centroid of two areas, re-route both the areas using **algorithm 6.2**
  - 4:   Proceed to step 5 if network routing is successful else go to 2
  - 5:   Save the networks.
  - 6: **end while**
- 

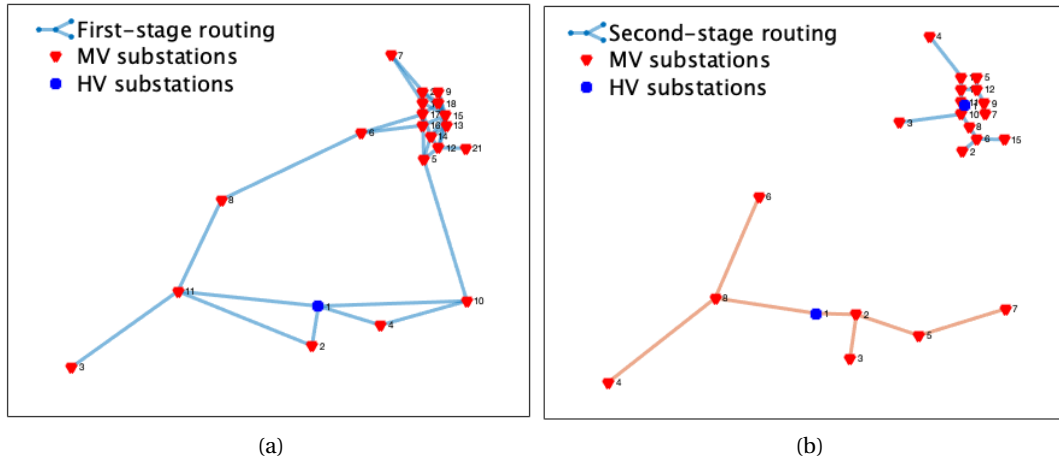


Figure 6.8: Re-routing: (a) routed network using algorithm 6.2 resulting in a meshed network, (b) routed network using algorithm 6.3 which divides it into two radial networks.

The final routing results for the example EHV region is shown in Fig. 6.9. Statistics on the routed networks for the whole Switzerland are listed in the Table 6.6. The distributions of the nodal voltages and the lines currents are shown in Fig. 6.10 and denote that design requirements are met. More discussion on the validation of the estimated MV networks is presented in Sec. 6.6.2.

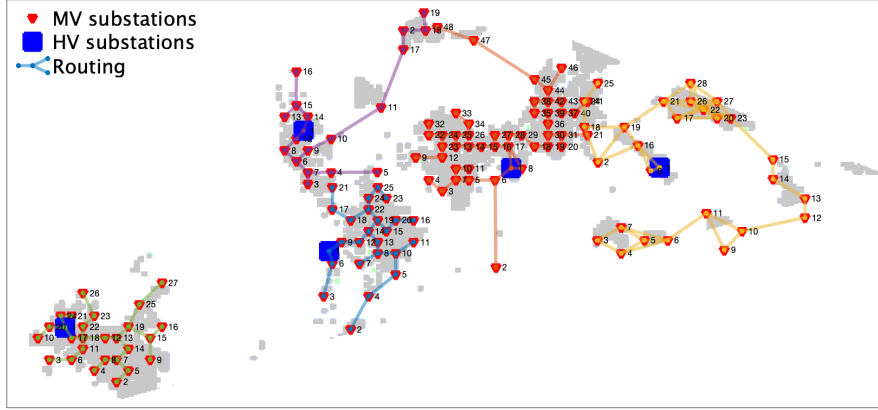


Figure 6.9: Routed MV networks for the example EHV area.

Table 6.6: Number of identified grid components.

Equipment	Number of elements
HV-MV transformers	776
MV-LV transformers	17'844 x 2 (for redundancy)
MV cables and overhead lines	1342.2 km

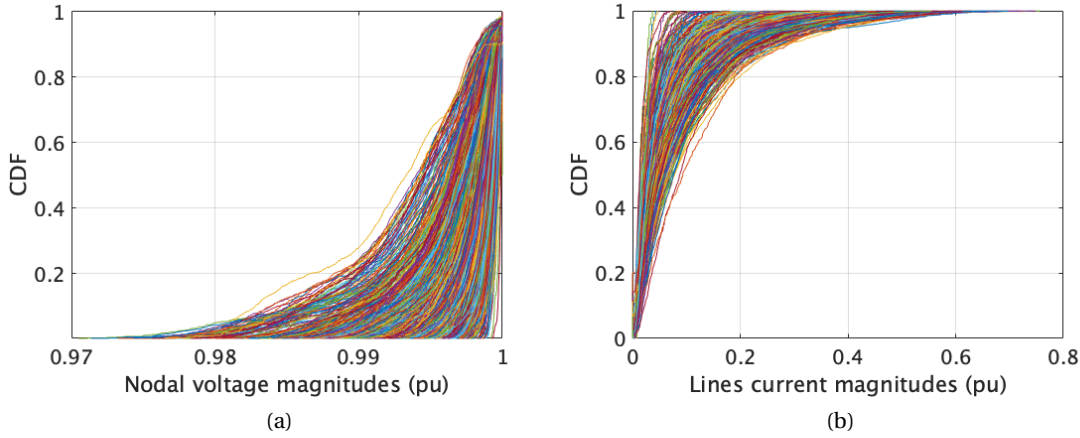


Figure 6.10: CDF plots (a) nodal voltages and (b) lines currents of estimated networks shown in different colors.

## 6.4 PV hosting Capacity and Energy Storage Requirements for Power Distribution Networks

The PV hosting capacity of a distribution grid is the maximum amount of PV generation that the grid can accommodate without violations of the its operational constraints. In this section, we describe the PV hosting capacity problem for distribution grids and, then, how to increase it with distributed energy storage systems [207]. Finally, we discuss the optimal deployment of PV power plants and BESSs to achieve the largest production at the minimum cost for the

## 6.4 PV hosting Capacity and Energy Storage Requirements for Power Distribution Networks

whole country. We first discuss the input data that are used in the problem formulation.

### 6.4.1 Input Data

#### Capacity Factor of PV Production

PV capacity factors (total actual generation to the total generation at the nominal plant capacity over one year) for all locations across the country are used to compare the suitability for hosting PV generation. Capacity factors are from the PVGIS database [208] considering optimal panel locations (south-facing and 38° tilt for the case of Switzerland). They are based on satellite information at a 3x3 km (at Nadir) resolution and are corrected for the shading induced by topographical features on the horizon. We query this information for the whole Switzerland with a resolution of 1.5x1.5 km. Figure 6.11a shows the distribution of the capacity factors across the country. The capacity factor varies from 0.06 to 0.16 showing variation that can vary up to a factor of 3.

#### Land-use Constraints for PV generation

We evaluate land allocation to identify suitable locations for PV power plants. We use a 100x100 m resolution land-use map<sup>37</sup> from the Swiss Federal Office for Topography, shown in Fig. 6.12, reporting settlement (residential, commercial, industrial and recreational) and agricultural areas. For the area corresponding to each MV grid, we consider that 10% of the settlement areas can host PV generation, for a total surface of 210 km<sup>2</sup> for the whole country. Considering this available surface, the yearly capacity factors from PVGIS [208], and an average PV conversion efficiency of 15 % in standard conditions [209], the yearly total PV generation for Switzerland with these assumption is of 33 TWh. Both the available area for PV deployment and total generation are in-line with the estimates reported in the existing literature [181, 182, 183, 210] as summarized in Table 6.7. Differences among the various estimations (more remarkably for PV generation) can be explained by different input data sets and methods, however they all seem to agree on the same order of magnitude. Fig. 6.11b shows the distribution of the PV installed capacity potential (solely based on land availability) across all the MV grids of the country. Its mean and maximum values are 2 and 13.1 MW. The total PV installed capacity potential with the above assumptions is of 30 GW. It is worth noting that larger capacity values are possible with higher usage of available land and PV conversion efficiency.

#### Time Series of the PV Generation and Demand

Solving the PV hosting capacity problem does require time series of PV generation and demand to model the loading conditions of the grid. We consider a scenario with high PV generation and low demand to reproduce cases where excess PV generation might cause violations of

<sup>37</sup><https://map.geo.admin.ch/?layers=ch.bfs.arealstatistik-hintergrund&lang=en&topic=ech&bgLayer=ch.swisstopo.pixelkarte-farbe>

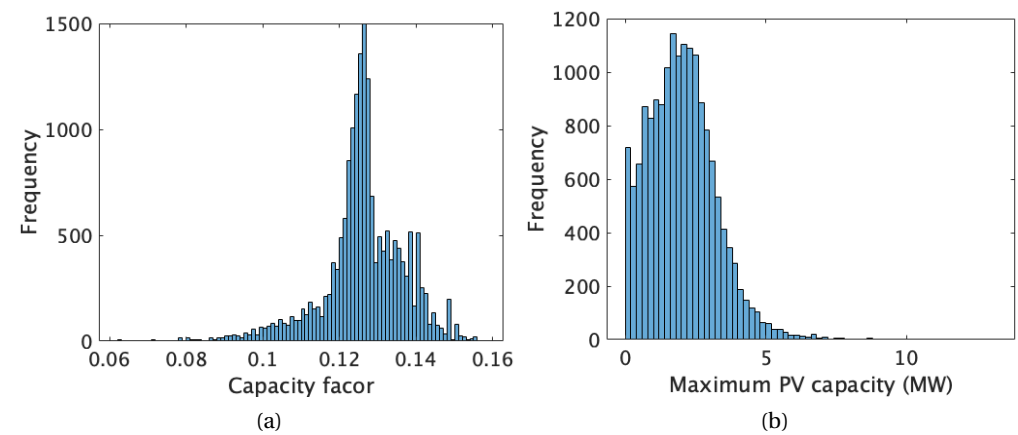


Figure 6.11: Distribution of (a) capacity factor and (b) maximum PV capacity per MV node due to land constraint.

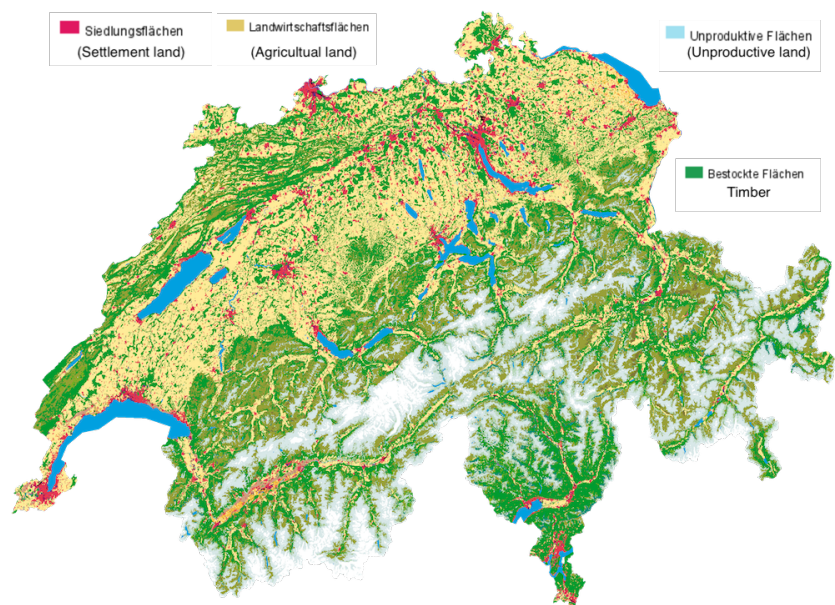


Figure 6.12: Simplified land-use map of Switzerland.

Table 6.7: A comparison of the PV generation potential.

Reference	Area [km <sup>2</sup> ]	Estimated PV generation [TWh]
[181]	328	17.86
[182]	252	16.29
[210]	485	41.32
[183]	267	24 ± 9
This work	210	33

## 6.4 PV hosting Capacity and Energy Storage Requirements for Power Distribution Networks

the grid constraints. In this respect, PV generation is modelled considering uniform clear-sky conditions over the whole power distribution network and considering the day of the year with the largest PV generation. We use a clear-sky model to compute the global-horizontal irradiance (GHI) as a function of the location, that we denote by  $n$ . The plane-of-array (POA) irradiance  $\mathcal{G}_{t,n}$  (kW/m<sup>2</sup>) is determined by transposing the GHI as a function of the plant tilt and azimuth, and time of the day. The POA irradiance is finally converted to PV generation ( $\hat{p}_{t,n}^{\text{PV}}$ ) for a plant with  $P^{\text{PV}}$  capacity (in kW) with the following model  $g^{\text{PV}}(t, n, P^{\text{PV}})$ :

$$\hat{p}_{t,n}^{\text{PV}} = g^{\text{PV}}(t, n, P^{\text{PV}}) = \mathcal{G}_{t,n} (1 + \eta_1 (T_{t,n}^{\text{air}} + \eta_2 \mathcal{G}_{t,n} - 25)) P^{\text{PV}} \quad (6.2)$$

where  $T_t^{\text{air}}$  is the air temperature (°C),  $\eta_1 = -0.0043$  and  $\eta_2 = 0.038$  are empirical parameters as in [68] for open-rack PV plants.

Demand profiles are obtained by scaling the residential, commercial and industrial demand profiles specified in the CIGRE benchmark grid for MV systems [5], shown in Fig. 6.13a, for the coefficients extracted from the demand map computed in subsection 6.3.2. To reproduce a scenarios with dominant PV generation over the demand, we halve the nominal demand profile to reflect a day with low electricity consumption. We assume ideal correlation among the loads. As the focus of the Chapter on modeling the impact of PV generation on the grid hosting capacity, modeling spatial diversity of the loads is not of special interest. We consider voltage- and frequency-independent loads. Figure 6.13b shows the PV and the load profiles considered for the PV and battery sizing.

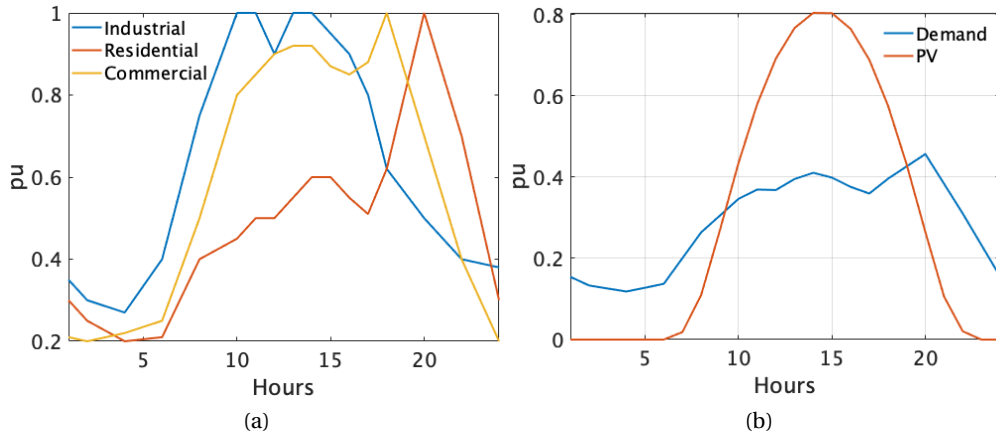


Figure 6.13: Demand and PV scenarios: (a) standard load profiles for different sector, (b) scenario considered for the PV and battery sizing problem.

### 6.4.2 The PV Hosting Capacity Problem

The objective of this problem is determining the maximum PV installed capacity that a grid can host at its nodes without violations of grid constraints. We consider a generic distribution grid



## Chapter 6. Countrywide Synthetic Network Estimation, Computation of PV Hosting Capacity and Battery Energy Storage Requirements for Power Distribution Networks

with  $N_b$  nodes and  $N_l$  lines with index  $n \in \mathcal{N} = \{1, \dots, N_b\}$  and  $l \in \mathcal{L} = \{1, \dots, N_l\}$ , respectively. The installed PV capacity at node  $n$ , that is an unknown of the problem, is denoted by  $P_n^{\text{pv}}$  <sup>(38)</sup>. As discussed in Section 6.4.1, the installed capacity is limited by the land availability, so we say that  $P_n^{\text{pv}} \leq \bar{P}_n^{\text{pv}}$ , where the right-hand-side upper-bound is derived from the land availability map.

### Grid Model

Active and reactive nodal injections at the various nodes of the grid are collected in vectors <sup>(39)</sup>  $\mathbf{p}_t, \mathbf{q}_t$  given by the variable injections, i.e., nodal PV generation  $\mathbf{p}_t^{\text{pv}}, \mathbf{q}_t^{\text{pv}}$  since they are decision variables in the planning problem.

$$\mathbf{p}_t = -\mathbf{p}_t^{\text{pv}} \quad t \in \mathcal{T} \quad (6.3)$$

$$\mathbf{q}_t = -\mathbf{q}_t^{\text{pv}} \quad t \in \mathcal{T} \quad (6.4)$$

We assume that PV plants operate at unitary power factor, as this is typical for small/medium size PV plants, i.e.,

$$\mathbf{q}_t^{\text{pv}} = \mathbf{0} \quad t \in \mathcal{T} \quad (6.5)$$

PV generation is computed by applying the model  $g^{\text{pv}}(\cdot)$  in (6.2). We impose load  $\mathbf{p}_t^{\text{load}}$  and  $\mathbf{q}_t^{\text{load}}$  as uncontrollable injections.

Let  $|\mathbf{v}|_t \in \mathbb{R}^{N_b-1}$  and  $|\mathbf{i}|_t \in \mathbb{R}^{N_l}$  the vector of magnitudes of the nodal voltage and line current, respectively. The symbols  $p_t^l$  and  $q_t^l$  are the active and reactive grid losses. Using the power-flow sensitivity coefficients-based linear model from Sec. 2.3, Chapter 2, the  $|\mathbf{v}|_t, |\mathbf{i}|_t, p_t^l$  and  $q_t^l$  are expressed as linear function of nodal power injections  $\mathbf{p}_t, \mathbf{q}_t$ . The linearized models are

$$|\mathbf{v}|_t = \mathbf{A}_t^v \begin{bmatrix} \mathbf{p}_t \\ \mathbf{q}_t \end{bmatrix} + \mathbf{b}_t^v \quad (6.6)$$

$$|\mathbf{i}|_t = \mathbf{A}_t^i \begin{bmatrix} \mathbf{p}_t \\ \mathbf{q}_t \end{bmatrix} + \mathbf{b}_t^i \quad (6.7)$$

$$\begin{bmatrix} p_t^l \\ q_t^l \end{bmatrix} = \mathbf{A}_t^l \begin{bmatrix} \mathbf{p}_t \\ \mathbf{q}_t \end{bmatrix} + \mathbf{b}_t^l \quad (6.8)$$

where  $\mathbf{A}$  and  $\mathbf{b}$  are the linear mapping parameters defined in Chapter 2. They are iteratively updated with newly sized battery and PV injections. An accuracy analysis of the modeled linear power flow is included in 6.6.1.

<sup>38</sup>For generality, if a node cannot host PV generation, we can add in the following formulation a constraint of the kind  $P_n^{\text{pv}} = 0$ .

<sup>39</sup>The bold-typeface notation refers to vectors.

## 6.4 PV hosting Capacity and Energy Storage Requirements for Power Distribution Networks

The symbols  $p_t^{\text{gcp}}, q_t^{\text{gcp}}$  denotes the active and reactive power at the GCP expressed as

$$p_t^{\text{gcp}} = \mathbf{1}^\top \mathbf{p}_t + p_t^l + \mathbf{1}^\top \mathbf{p}_t^{\text{load}} \quad t \in \mathcal{T} \quad (6.9a)$$

$$q_t^{\text{gcp}} = \mathbf{1}^\top \mathbf{q}_t + q_t^l + \mathbf{1}^\top \mathbf{q}_t^{\text{load}} \quad t \in \mathcal{T}. \quad (6.9b)$$

### Optimization Problem

The problem consists in maximizing the installed capacity of PV generation while subject to grid constraints. To foster the deployment of the PV plants in nodes with the highest irradiance availability, the installed capacity is weighted by the local capacity factor  $\gamma_n$ <sup>(40)</sup>, estimated previously in Sec. 6.4.1. The problem formulation is:

$$\underset{\{P_n^{\text{pv}} \in \mathbf{R}^+, n \in \mathcal{N}\}}{\text{maximize}} \left\{ \sum_{n \in \mathcal{N}} \gamma_n P_n^{\text{pv}} \right\} \quad (6.10a)$$

subject to nodal injections model and grid constraints

$$v^{\min} \leq \mathbf{A}_t^v \begin{bmatrix} \mathbf{p}_t \\ \mathbf{q}_t \end{bmatrix} + \mathbf{b}_t^v \leq v^{\max} \quad t \in \mathcal{T} \quad (6.10b)$$

$$\mathbf{0} \leq \mathbf{A}_t^i \begin{bmatrix} \mathbf{p}_t \\ \mathbf{q}_t \end{bmatrix} + \mathbf{b}_t^i \leq \mathbf{i}^{\max} \quad t \in \mathcal{T}, \quad (6.10c)$$

$$0 \leq (p_t^{\text{gcp}})^2 + (q_t^{\text{gcp}})^2 \leq \bar{S}^2 \quad t \in \mathcal{T}, \quad (6.10d)$$

where nodal voltage magnitudes and line currents limits are denoted by  $v^{\min}, v^{\max}$ , and line ampacities  $\mathbf{i}^{\max}$ , respectively. Similarly, the apparent power at the substation transformer should be less than the substation's transformer rating  $\bar{S}$ . The constraint (6.10d) is approximated by piece-wise linear functions to keep the optimization problem linear.

Other constraints include PV generation model and land-availability constraint  $\overline{P_n^{\text{pv}}}$ :

$$\hat{p}_{n,t}^{\text{pv}} = g^{\text{pv}}(t, n, P_n^{\text{pv}}) \quad t \in \mathcal{T}, n \in \mathcal{N} \quad (6.10e)$$

$$P_n^{\text{pv}} \leq \overline{P_n^{\text{pv}}} \quad n \in \mathcal{N}. \quad (6.10f)$$

<sup>40</sup>We include the capacity factor because, even if derived from satellite estimations with coarser resolution than that of the grid nodes, the topographical shading is at a higher resolution and could impact on the suitability of certain nodes.

### 6.4.3 Increasing the PV Hosting Capacity with BESSs

#### Problem Formulation

The objective of this problem is to determine the optimal location of PV plants to host a target level of total PV generation capacity, that we denote by  $P^*$ . However, values of  $P^*$  above the grid's PV hosting capacity cannot be accommodated because they would lead to violations of grid constraints. For this reason, this problem also determines an optimal configuration of BESSs (location, converter power ratings, and energy capacities) to relieve grid constraints and enabling the further integration of PV generation in the grid. The results of this process are discussed at the end of this section.

It is worth highlighting that, even if we consider BESSs, the formulation can be extended to other forms of energy storage systems or other resources capable of providing grid support, like flexible demand [211, 212]. It is also worth highlighting the parallel with PV self-consumption strategies, which can indirectly mitigate the impact of excess PV generation on grid constraints by promoting the direct consumption of locally generated electricity, see e.g. [213, 214]. PV self-consumption is typically provided on a best-effort basis by end consumers and is typically unaware of global grid conditions, thus does not offer reliable performance guarantees. Compared to PV self-consumption, we provide robust guarantees on grid control performance and optimized energy storage requirements considering the whole grid and not a single consumer.

**BESSs Model:** We use similar model as defined in Chapter 2. BESSs' active power is denoted by  $p_{n,t}^{\text{bess}}$ , and reactive by  $q_{n,t}^{\text{bess}}$ . We model the evolution of the BESS state-of-energy (SOE) with

$$\text{SOE}_{n,t} = \text{SOE}_{n,t-1} - p_{n,t}^{\text{bess}} \Delta t, \quad (6.11)$$

where  $\Delta t$  is the sampling time. Charging and discharging efficiency is accounted for by integrating the BESS equivalent resistance in the load flow problem as proposed in [215]. If load flow equations are linearized, this modeling choice retains the convexity of the problem without requiring the use of additional variables as, for example, in [216]. Since battery sizes are the decision variables, the optimization problem is solved multiple times taking account the updated equivalent resistances in proportion to their converter ratings. To implement a safety margin from zero-SOE and full charge, we implement the following constraint

$$aE_n^{\text{bess}} \leq \text{SOE}_{n,t} \leq (1-a)E_n^{\text{bess}} \quad (6.12)$$

where  $0 \leq a \leq 0.5$  is a design parameter (chosen as 0.1) and  $E_n^{\text{bess}}$  is the BESS energy capacity. BESS injections should respect the capability curve of its four quadrant power converter (the constraint is approximated by piece-wise linear functions). This reads as:

$$0 \leq (p_{n,t}^{\text{bess}})^2 + (q_{n,t}^{\text{bess}})^2 \leq (P_n^{\text{bess}})^2. \quad (6.13)$$

## 6.4 PV hosting Capacity and Energy Storage Requirements for Power Distribution Networks

**Capital Investment for BESSs and PV Plants:** the capital investment for installing a PV plant with generation capacity  $P_n^{\text{pv}}$ , and a BESS with energy capacity  $E_n^{\text{bess}}$  and power rating  $P_n^{\text{bess}}$  at node  $n$  is:

$$J(P_n^{\text{pv}}, P_n^{\text{bess}}, E_n^{\text{bess}}) = \mathcal{C}^{\text{pv}} P_n^{\text{pv}} + \mathcal{C}_P^{\text{bess}} P_n^{\text{bess}} + \mathcal{C}_E^{\text{bess}} E_n^{\text{bess}}, \quad (6.14)$$

where  $\mathcal{C}^{\text{pv}}$ ,  $\mathcal{C}_P^{\text{bess}}$ , and  $\mathcal{C}_E^{\text{bess}}$  are the unitary costs for PV, power converter rating, and energy capacity, respectively. Costs are reported in Table 6.8. They are derived from current market figures.

Table 6.8: Costs of PV and BESSs.

Component	Unit	Value
Turn-key PV system ( $\mathcal{C}^{\text{pv}}$ )	USD(\$)/kWp	1020
BESS converter rating ( $\mathcal{C}_P^{\text{bess}}$ )	USD(\$)/kVA	200
BESS energy capacity ( $\mathcal{C}_E^{\text{bess}}$ )	USD(\$)/kWh	300

**Formulation of the Decision Problem:** the decision variables of the problem are the installed PV capacity, the BESS power rating and the BESS energy capacity at all the nodes of the grid, which we collect in the set  $\chi = \{P_n^{\text{pv}}, P_n^{\text{bess}}, E_n^{\text{bess}} \in \mathbb{R}^+, \forall n \in \mathcal{N}\}$ . Without losing generality, nodes that cannot host PV generation or BESS can be excluded by properly subsetting the nodes index. The problem consists in locating and sizing BESS to accommodate a target level  $P^*$  of installed PV generation capacity while minimizing the total capital investment (6.14) for all the nodes of the grid. The BESSs' optimal location is determined by the battery nodal injections that are different than zeros at certain nodes. Similarly to before, to favour the locations with large PV capacity factors, we weight the installed PV capacity at each node with the factor  $\bar{\gamma}/\gamma_n$ , where  $\bar{\gamma}$  is the average among all the capacity factors  $\gamma_n, n \in \mathcal{N}$  in the network. Finally, the problem is:

$$\underset{\chi}{\text{minimize}} \left\{ \sum_{n \in \mathcal{N}} J(\bar{\gamma}/\gamma_n \cdot P_n^{\text{pv}}, P_n^{\text{bess}}, E_n^{\text{bess}}) \right\} \quad (6.15a)$$

subject to nodal injections (now with BESSs demand too) and grid constraints

$$\mathbf{p}_t = -\mathbf{p}_t^{\text{pv}} + \mathbf{p}_t^{\text{bess}} \quad t \in \mathcal{T} \quad (6.15b)$$

$$\mathbf{q}_t = -\mathbf{p}_t^{\text{pv}} + \mathbf{q}_t^{\text{bess}} \quad t \in \mathcal{T} \quad (6.15c)$$

$$(6.9), (6.10b) - (6.10d), \quad (6.15d)$$

BESS model and constraints

$$\text{SOE}_{n,t} = \text{SOE}_{n,t-1} - p_{n,t}^{\text{bess}} \Delta t \quad t \in \mathcal{T}, n \in \mathcal{N} \quad (6.15e)$$

$$0 \leq (p_{n,t}^{\text{bess}})^2 + (q_{n,t}^{\text{bess}})^2 \leq (P_n^{\text{bess}})^2 \quad t \in \mathcal{T}, n \in \mathcal{N} \quad (6.15f)$$

$$aE_n^{\text{bess}} \leq \text{SOE}_{n,t} \leq (1-a)E_n^{\text{bess}} \quad t \in \mathcal{T}, n \in \mathcal{N} \quad (6.15g)$$

## Chapter 6. Countrywide Synthetic Network Estimation, Computation of PV Hosting Capacity and Battery Energy Storage Requirements for Power Distribution Networks

and PV model and target PV capacity  $P^*$  to install in the grid:

$$(6.10e) - (6.10f) \tag{6.15h}$$

$$\sum_{n \in \mathcal{N}} P_n^{\text{pv}} = P^*. \tag{6.15i}$$

### Results on BESS Sizing

For each estimated MV grid, first, we solve the PV problem (6.10) to obtain the PV hosting capacity, then, we solve the BESS sizing problem (6.15) by varying  $P^*$  in (6.15i) from 25% to 300% (with increments of 25%) of the grid PV hosting capacity. It should be noted that both the problems (6.10) and (6.15) are solved multiple times to correct the grid linearization (by updating the injections of newly sized PV and battery installations) and updating battery equivalent resistances (for the battery loss model as previously mentioned). With this procedure, we determine the BESSs requirements for PV configurations below (25-100%) and above (125-300%) the grid hosting capacity. The results of this process for are shown in Fig. 6.14 and are now discussed. Figures 6.14a and 6.14b show the cost curves for 10 randomly chosen distribution networks, whereas Figures 6.14c and 6.14d show the distribution along the grids with symmetric quantiles. Figure 6.14a shows the total investment for PV systems and BESSs as a function of the installed PV generation capacity. We can make two key observations:

1. Networks reach a different level of maximum PV installed capacity. This is due to the different values of land availability.
2. The total investment grows at two different rates because the investment below the hosting capacity is given by PV units only, whereas above by BESSs and PVs plants together.

Figure 6.14b shows the marginal cost of increasing the level of installed PV generation capacity. We define the marginal cost of each grid as the total cost of the PV-BESS system over the total PV yearly production accounting for the capacity factor as:

$$\text{Marginal cost} = \sum_{n \in \mathcal{N}} \frac{J(\hat{P}_n^{\text{pv}}, \hat{P}_n^{\text{bess}}, \hat{E}_n^{\text{bess}})}{\hat{P}_n^{\text{pv}} \cdot 365 \cdot 24 \cdot \gamma_n}, \tag{6.16}$$

where  $\hat{P}_n^{\text{pv}}, \hat{P}_n^{\text{bess}}, \hat{E}_n^{\text{bess}}$  denote the solution of problem (6.15). It can be seen from Fig. 6.14a and 6.14b that, below the hosting capacity, the marginal cost is constant because it corresponds to the unitary cost of PV, whereas above, it increases because progressively larger BESSs are required. Figure 6.14c and 6.14d shows the density plot of the cost curves derived for all estimated MV networks in Switzerland. They show the distribution of the total and marginal costs among different networks. As it can be seen in Fig. 6.14a and 6.14b, different networks have different PV hosting capacities, therefore the marginal costs of the various systems have different patterns.

## 6.4 PV hosting Capacity and Energy Storage Requirements for Power Distribution Networks

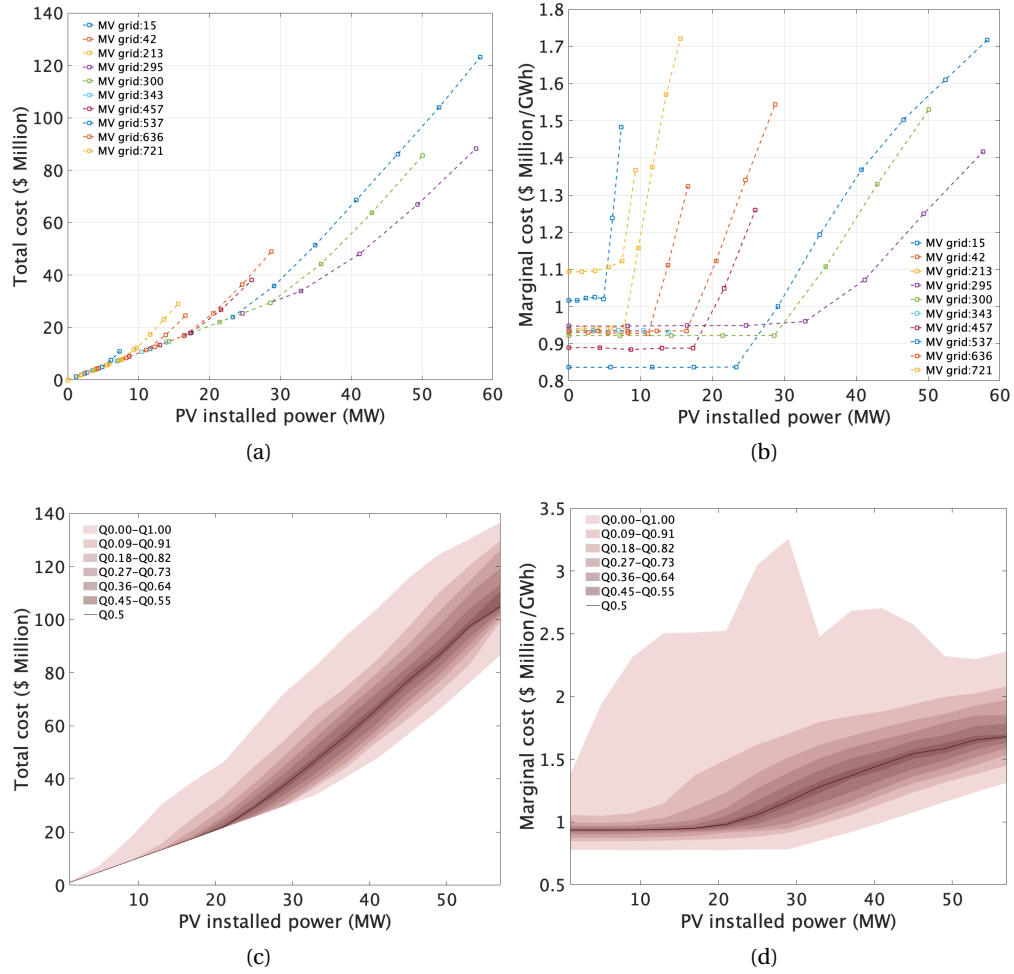


Figure 6.14: Investments to achieve a target level of installed PV generation capacity: (a, c) total cost, and (b, d) marginal cost. Top: for randomly chosen 10 MV networks, bottom: for all estimated MV networks in Switzerland (distribution with symmetric quantiles).

### 6.4.4 Optimal Allocation of PV and BESSs

In the former subsection, we have discussed a method to determine the optimal deployment of PV installations and BESSs within a network to accommodate a target level of installed PV capacity. We have applied it to all identified grids of Sec. 6.3 and derived, for each of them, marginal costs for installing increasing levels of installed PV capacity. The estimated marginal costs are key results as they allow us to compare the costs of installing PV generation in various networks across the country, and they will be the fundamental input of the problem discussed in this section. The objective of this problem is to determine the installed PV capacity in each network in order to achieve a countrywide objective for total PV generation at the lowest capital cost.

We denote the curves of Fig. 6.14b with the function  $\zeta_m(P_m^*)$ , where  $m \in \mathcal{M} = \{1, \dots, M\}$  is

## Chapter 6. Countrywide Synthetic Network Estimation, Computation of PV Hosting Capacity and Battery Energy Storage Requirements for Power Distribution Networks

the index for the identified MV networks and  $P_m^*$  is the installed capacity in grid  $m$ . We approximate the curves  $\zeta_m$  with a piece-wise linear function. The domain of  $\zeta_m$  is  $[\underline{P}_m^*, \bar{P}_m^*]$ , derived from Fig. 6.14b. The problem consists in finding the variables  $P_1^*, \dots, P_M^*$  at the minimum total cost and such that the total installed capacity equals the countrywide PV installation target  $P^{\text{target}}$ . The problem is:

$$\underset{\{P_m^* \in \mathbb{R}^+, m \in \mathcal{M}\}}{\text{minimize}} \left\{ \sum_{m \in \mathcal{M}} P_m^* \zeta_m(P_m^*) \right\} \quad (6.17a)$$

subject to the domains of the variables and the PV installation target:

$$\underline{P}_m^* \leq P_m^* \leq \bar{P}_m^* \quad m \in \mathcal{M} \quad (6.17b)$$

$$\sum_{m \in \mathcal{M}} P_m^* = P^{\text{target}}. \quad (6.17c)$$

The results are discussed in the next section.

## 6.5 Results and Discussion

### 6.5.1 Case Study

In the previous sections, we have presented a modeling toolchain that determines an economically optimal deployment of PV plants and BESSs to achieve a target level of installed PV generation while accounting for the capacity factor spatial distribution, grids constraints and how they can be relieved by BESSs (as an alternative to the grid reinforcement) when the PV generation capacity exceeds the grid's PV hosting capacity. It is worth highlighting that the problem's essence is not only about achieving an optimal deployment of PV generation based on its countrywide potential but also extending with distributed energy storage the PV hosting capacity of grids with large PV generation potential if this leads to more economically convenient configurations. For example, as shown in this section, it is more convenient to invest in BESSs to extend the hosting capacity of a grid with a large generation potential and installing here additional PV generation rather than in grids with lower generation potential.

In this section, we compare this approach (that we call **Case 1**) against the case where the same level of installed PV generation capacity is deployed uniformly in the distribution grids (**Case 0**). For an illustrative comparison between Case 0 and 1, we refer to Fig. 6.14d: for a given value of total PV generation capacity, Case 0 involves selecting, for each network, an installed PV generation capacity (x-axis) that is proportional to the grid area and regardless of its cost (y-axis). Case 1 involves placing PV generation starting from the grid with the lowest cost (y-axis), and saturating its potential (sweeping the x-axis) before moving to the second cheapest grid.

### 6.5.2 Deployment of PV Plants

Figure 6.15 shows the distribution of installed PV generation capacity across Switzerland for increasing (from top to bottom) levels of total installed capacity and for Case 0 (left column) and Case 1 (right). The difference between the two deployment policies is evident by comparing the plots in the first row: in the left plot (Case 0), PV plants are installed uniformly in the grids,<sup>41</sup> whereas in the right plot (Case 1) PV is installed prioritizing regions with higher irradiance availability, which appear to be Ticino, Leman and Neuchatel regions, and west Valais. For increasing values of installed PV capacity (second and third rows of Fig. 6.15), it can be observed that Case 0 and Case 1 feature increasingly similar geographical distribution patterns. This is due to land-use limitations, and the activation of the associated constraint in (6.10f). In other words, once Case 1 saturates the available locations for PV deployment in regions with high irradiance potential, it starts installing PV generation in second-choice grids. The distribution of the BESS follows the same pattern as of PV.

### 6.5.3 Deployment of PV Plants and BESSs for Case 0 and Case 1

Table 6.9 shows the PV installed capacity, the yearly production, the BESS power rating and energy capacity, and the total cost (i.e., investments for PV plants and BESSs) for 10 scenarios (A-J) of PV generation deployment for Case 0 and Case 1. Scenarios A, B, C to J correspond to allocating PV generation in 5, 10, 20 to 90% (with increments of 10%), respectively, of the available surface. We remind that the available surface for PV is 10% of the settlement areas, as discussed in section 6.4.1. The energy transition scenario for Switzerland reported in [217] estimates a yearly PV production potential from roof-top PV around 25 TWh, that corresponds to our scenarios H-J.

From Table 6.9 we can make the following observations.

- Case 1/Scenario A achieves a 0.21 TWh increase in yearly production compared to the same scenario of Case 0 thanks to installing PV generation in distribution grids with larger PV generation potential first. For increasing values of installed capacity (scenarios from B to J), the yearly production of the two cases converges to the same values due to land-use limitations, as discussed in 6.5.2;
- Case 0 requires BESSs starting from Scenario C, whereas Case 1 has mild needs in Scenario B already. This denotes that it is more cost effective to invest in BESS to increase the hosting capacity of high PV-generation-potential grids rather than connecting that same PV capacity in other grids with less PV generation potential.
- Connecting PV generation above Scenario C in Case 0 requires progressively larger values of energy storage capacity and power rating. For example, doubling its installed

<sup>41</sup>Non-uniform spatial distribution over the country of PV generation is because grids are not uniformly distributed.



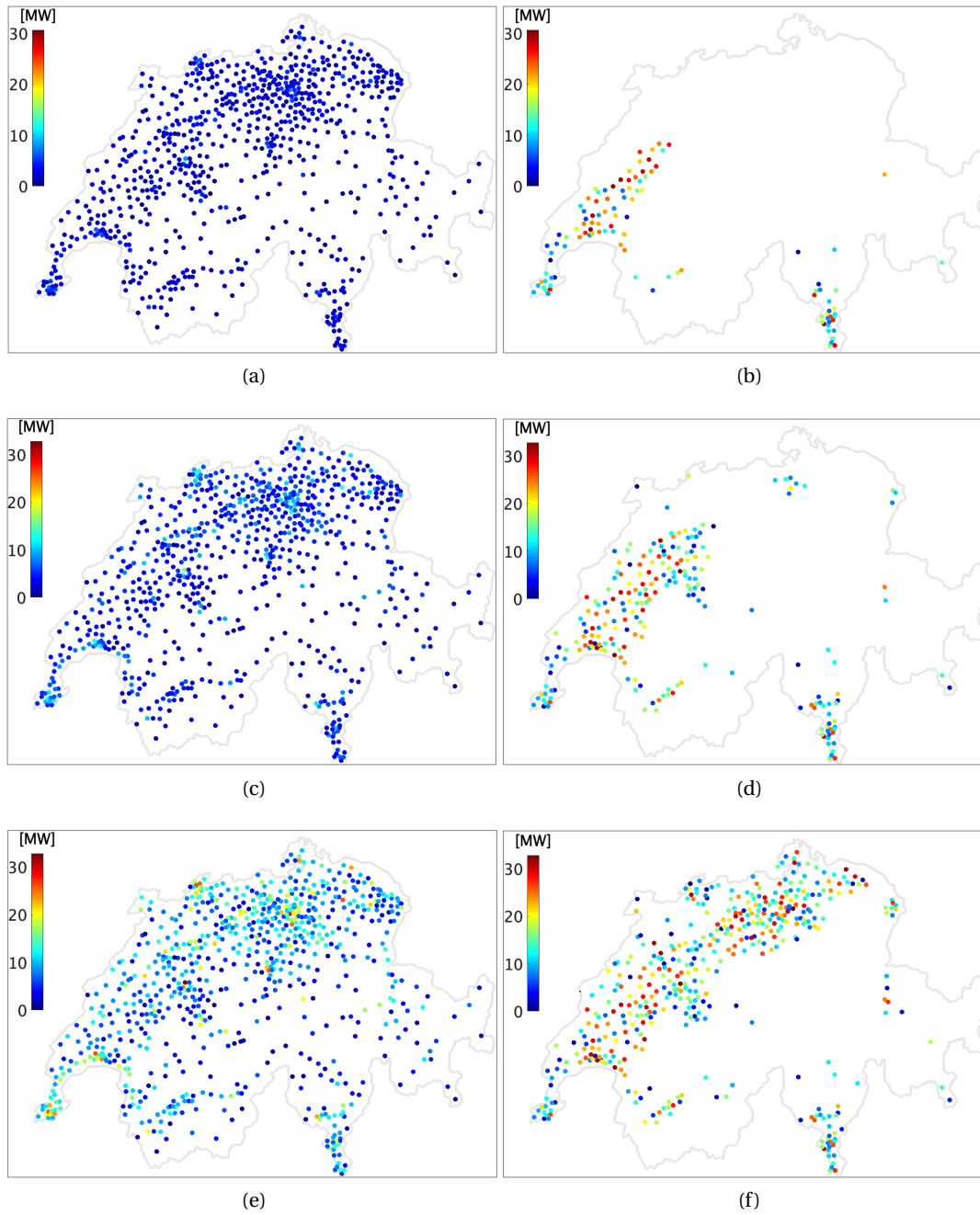


Figure 6.15: Installed PV generation capacity (in MW) across Switzerland for scenario A in (a) and (b), scenario B in (c) and (d), and scenario C in (e) and (f), for Case 0 and Case 1, respectively. Scenarios refer to the installed capacity of PV generation and are defined in Table 6.9.

capacity (from 6.85 to 13.70 GW) requires nearly 40 times the energy storage capacity (from 0.14 to 5.73 GWh). It is worth noting that the needs for BESSs increases sharper for Case 0 than Case 1. This is because the latter problem optimizes the locations of

BESSs and PV across all the grids attaining a minimum costs, whereas Case 0 scales PV capacity regardless of grid properties and irradiance potential. Costs are discussed next.

Table 6.9: Deployment of PV and BESS in the two cases.

Scenario	PV installed capacity (GWp)	PV production (TWh/y)		BESS Power (GW)		BESS Capacity (GWh)		Total cost Billions \$	
		Case 0	Case 1	Case 0	Case 1	Case 0	Case 1	Case 0	Case 1
A	1.71	1.90	2.11	0.00	0.00	0.00	0.00	1.76	1.77
B	3.43	3.81	4.09	0.00	0.00	0.00	0.01	3.53	3.53
C	6.85	7.62	7.87	0.03	0.01	0.14	0.01	7.11	7.07
D	10.28	11.42	11.46	0.46	0.04	1.31	0.05	11.07	10.61
E	13.70	15.23	15.25	1.74	0.51	5.73	0.68	16.18	14.42
F	17.02	18.92	18.99	3.64	3.08	14.74	7.88	22.68	20.51
G	20.11	22.36	22.43	5.87	5.67	26.83	21.26	29.94	28.23
H	22.89	25.44	25.46	8.10	7.94	39.90	36.20	37.17	36.03
I	25.42	28.24	28.25	10.18	10.08	53.41	51.00	44.25	43.50
J	27.57	30.61	30.61	12.07	12.00	65.87	65.04	50.57	50.31

#### 6.5.4 Cost Comparison

Figure 6.16 compares the marginal cost (i.e., total cost divided by the PV yearly production for the respective scenarios) of the two cases using results from Table 6.9. Case 1 (optimal

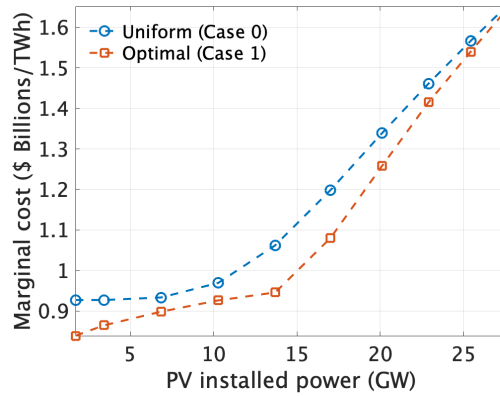


Figure 6.16: Cost per TWh of PV energy production for the two cases.

allocation) always achieves a lower unitary cost compared to Case 0. This is because the optimal allocation problem places the PV plants at locations with the higher irradiance potential first, whereas Case 0 (uniform PV allocation) places the PV plants proportionally to the available area. This shows the effectiveness of the optimal allocation algorithm. However, for higher values of installed PV generation capacity, the costs converge to the same value due to land-use limitations in most PV-favourable grids.

Fig. 6.17a shows the BESS energy capacity and power rating requirements for the optimal case as a function of the installed PV generation capacity using the results from Table 6.9. The

## Chapter 6. Countrywide Synthetic Network Estimation, Computation of PV Hosting Capacity and Battery Energy Storage Requirements for Power Distribution Networks

energy storage requirements are mild, before increasing sharply after 14 GW<sup>42</sup>). It can be noted that mitigating with BESSs the impact of excess PV generation on distribution grids is an energy-intensive application, with power-rating-to-energy-capacity ratios (i.e., C-rates) around 1/5. As current BESSs technologies can safely operate up to 2-3C, the spare power rating can be conveniently used to provide additional ancillary services, such as primary frequency control and grid synchronization services, that are mostly power-intensive [29]. Fig. 6.17b shows the corresponding system cost and cost breakdown and shows that the cost of the PV panels is largely dominant.

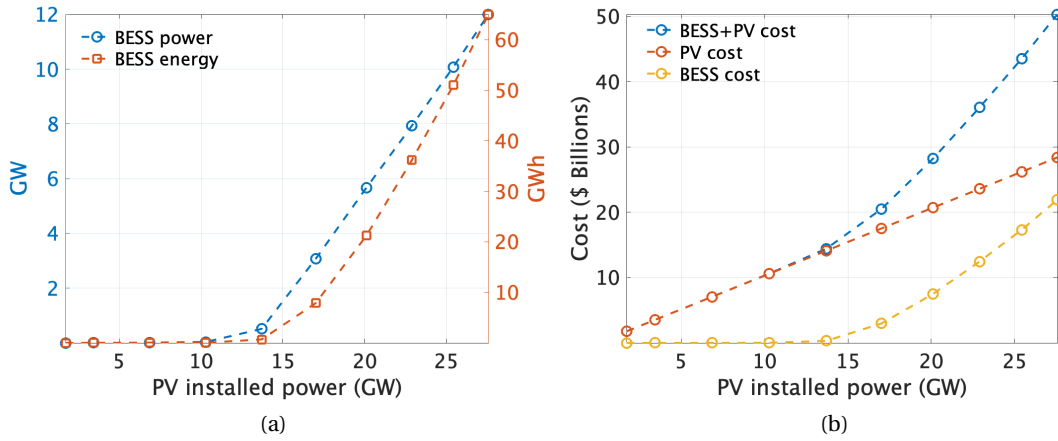


Figure 6.17: (a) BESS cost and size: (a) BESSs power rating and energy capacity and (b) system cost breakdown for Case 1 for different levels of installed PV generation capacity.

## 6.6 Further Analysis

### 6.6.1 Verification of Optimal Power Flow Results

We compare the voltage and current magnitudes computed by the linearized OPF model of Sec. 6.4.2 and 6.4.3 against ground-truth values from an AC load flow. The analysis is done for one of the synthetically generated network for which, the topology (with line parameters) and the nominal injections are shown in Fig. 6.18 and Table 6.10 respectively. As mentioned in Sec 6.4.3, the OPFs are solved by successively linearizing the model accounting for the updated BESS and PV injections to correct the linearization error until the cost of the problem converges. Fig. 6.19a and Fig. 6.19b show the power and energy ratings and the respective costs determined by the OPF of Sec. 6.4.3, respectively. Results settle in 7 iterations. After convergence is reached, we check the accuracy of the linear grid model against non-linear AC power flow using the BESS and PV injections from OPF problem. Fig. 6.20 shows the CDF plots of error of the nodal voltage magnitude and currents modeled by the linear OPF and the

<sup>42</sup>This value of hosting capacity is in-line with the countrywide hosting capacity obtained by solving the problem in Section 6.4.2.

AC power flow. Table 6.11 shows the maximum, absolute mean and mean error for the voltage and current modeling. They show that the voltage and current modeling errors are below 0.5 % and 1.75 % respectively. This proves that the voltage and current constraints modeling using sensitivity-based linear grid model is close to the non-linear AC power flow.

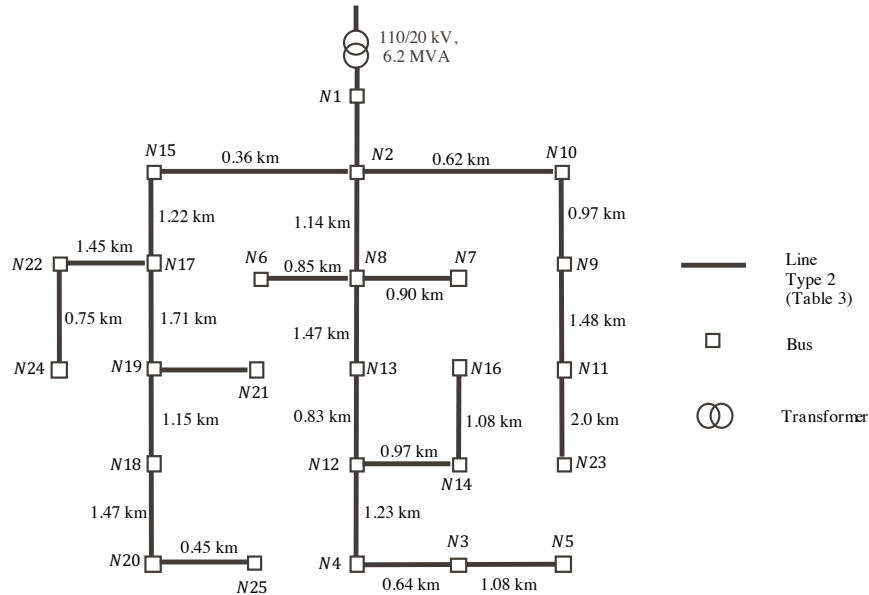


Figure 6.18: One of synthetically generated network as test case for the verification of linear grid model.

Table 6.10: Nominal Load and PV per node

Node	Load [MW]	PV [MWp]	Node	Load [MW]	PV [MWp]
N1	-	-	N14	0.17	-
N2	-	1.05	N15	0.18	0.35
N3	0.22	-	N16	0.19	-
N4	0.15	-	N17	0.17	0.44
N5	0.14	-	N18	0.20	-
N6	0.21	1.75	N19	0.21	-
N7	0.17	1.90	N20	0.22	-
N8	0.19	0.87	N21	0.16	-
N9	0.20	1.16	N22	0.18	1.00
N10	0.19	0.70	N23	0.26	1.81
N11	0.14	-	N24	0.23	1.17
N12	0.17	-	N25	0.02	-
N13	0.17	-			

Table 6.11: Accuracy of the linear power flow.

	Max	SD	Mean
Nodal voltage error	4.2e-3	1.8e-3	1.1e-3
Lines currents error	1.75e-2	4.1e-3	4.8e-4

## Chapter 6. Countrywide Synthetic Network Estimation, Computation of PV Hosting Capacity and Battery Energy Storage Requirements for Power Distribution Networks

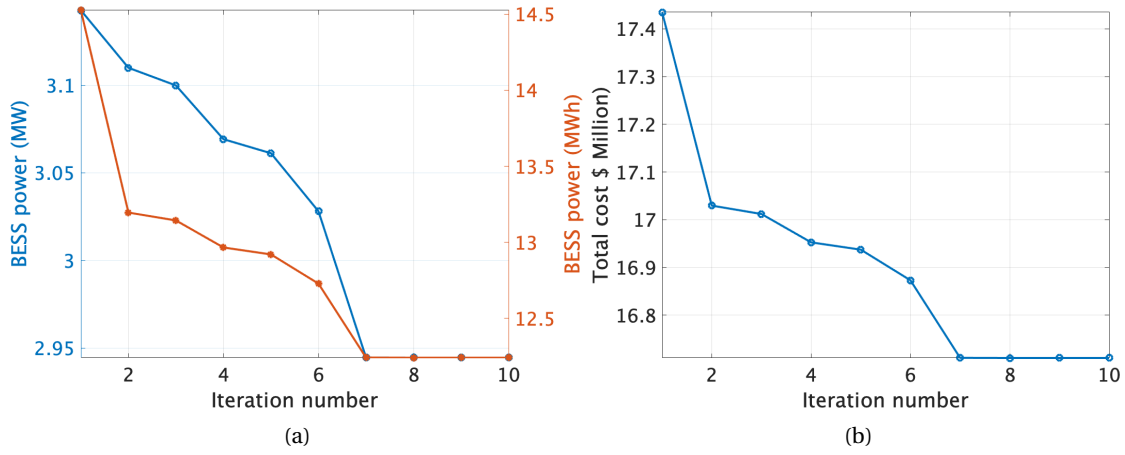


Figure 6.19: Plots showing convergence of the BESS sizes and the objective by correcting the linear power flow coefficients with newest battery injections from previous iteration: (a) BESS power and energy size and (b) Cost of the PV-BESS system.

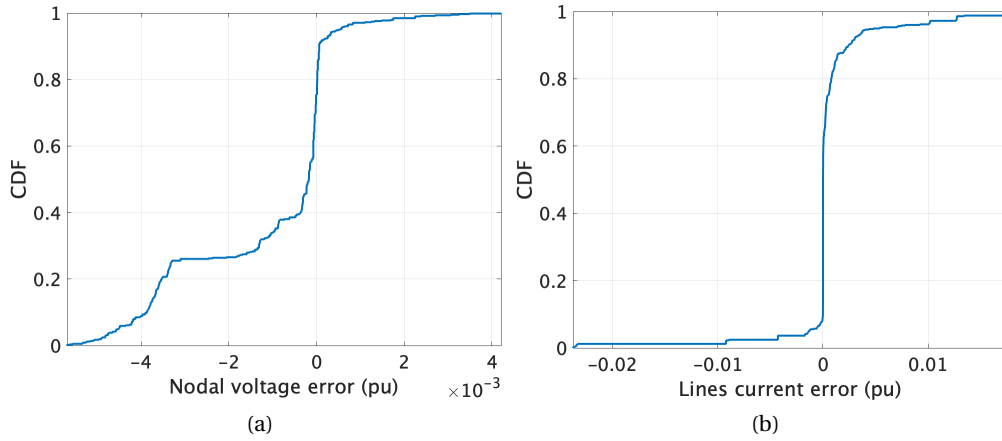


Figure 6.20: CDF plots (a) nodal voltages error and (b) branch current error.

### 6.6.2 Validation of Synthetically Generated MV Networks

We compare two estimated grids from our model with a real distribution network in Aigle, Switzerland, for which it was possible to access the topology and grid data. It is a three-phase 21 kV/6 MVA, a 55-bus network. The two synthetically generated networks are picked from a region near Aigle. The validation refers to comparing the “loadability” of the network, namely evaluating the CDFs of the voltage and line current magnitudes at different load conditions. For the comparison, we use the load profiles shown in Fig. 6.13a. Fig. 6.21 shows the CDFs of the voltage and current magnitudes of the original and estimated networks. The maximum, mean and the minimum values are reported in the Table 6.12. The numerical comparison and the CDFs show a good match among the networks. In particular, it emerges that the voltage and current magnitudes of the estimated networks fall in the same ranges as the one of the

real grid.

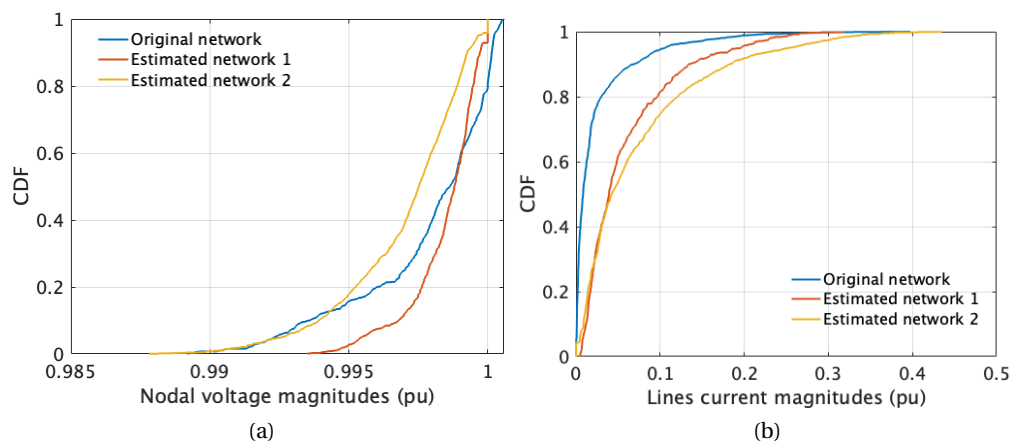


Figure 6.21: CDF plots: (a) nodal voltages and (b) lines currents of original network and the estimated networks shown in different colors.

Table 6.12: Comparison of actual and estimated networks.

Networks	Nodal voltage magnitudes			Lines current magnitudes		
	Max	SD	Mean	Max	SD	Mean
Actual	1.0006	0.0025	0.9978	0.3974	0.0420	0.0237
Estimated case 1	1.0000	0.0013	0.9985	0.3181	0.0570	0.0593
Estimated case 2	1.0000	0.0022	0.9970	0.4346	0.0782	0.0732

## 6.7 Discussion

PV generation will be key in achieving the energy transition targets, in Switzerland and other countries. As PV plants are connected to the power distribution system, it is important to consider the generation hosting capacity of existing distribution grids, which is typically limited due to grid operators' requirements to keep voltage levels within statutory limits, respect the lines ampacities and rating of the substation transformer.

The main obstacle to analyzing the PV hosting capacity of existing distribution grids is that their topology and line characteristics are confidential information owned by different DSOs. For this reason, we have first developed a method to estimate likely distribution grids starting from publicly available georeferenced data. Relying on the fact that existing distribution grids interface electrical demand, we use the countrywide geographical distribution of the electrical demand to infer the HV and MV electrical nodes' locations and connect them with a routing procedure from the existing literature. We then present a computationally tractable method based on a linearized OPF problem to compute the PV hosting capacity of distribution grids,

## **Chapter 6. Countrywide Synthetic Network Estimation, Computation of PV Hosting Capacity and Battery Energy Storage Requirements for Power Distribution Networks**

---

including how to host PV generation beyond prescribed limits with adequately located and sized distributed energy storage systems for relieving grid constraints violations.

Finally, we propose a specific planning problem that determines a cost-efficient allocation of PV power across the whole country, accounting for the technical limitations of the distribution grids (including adding energy storage, if conducive to lower system costs) and the distributed potential of PV generation, modeled with highly resolved PV capacity factors from the PVGIS database. We also consider land-use constraints to identify the sites where it is possible to install PV generation. The “cost-efficiency” notion for installing PV and energy storage systems includes two factors. First, cost efficiency is higher when installing PV plants where their capacity factor is larger. Second, it may be more cost-efficient to invest in distributed energy storage to extend the PV hosting capacity of highly insulated distribution grids rather than installing PV plants where their capacity factor is low.

The impact of this Chapter is twofold. On the one hand, it provides to distribution system operator a mathematically tractable and interpretable method to assess the PV generation hosting capacity of distribution grids, including how to cost optimally extend it with battery energy storage systems as an alternative to the grid reinforcement. On the other hand, developed methods provide actionable indications to national policymakers on the level of PV generation that a country can host and, on its techno-economical optimal deployment.

## 7 Conclusion

In this Thesis, we proposed, developed, and experimentally validated different methods for the grid-aware operation and the planning of active distribution networks (ADNs). In particular, the Thesis developed reliable grid-aware real-time controls and planning schemes that can be deployed in real-life ADNs. The key features of the developed methods are here summarized: (i) accounting for different kinds of uncertainties in ADNs operation and planning stages, (ii) accounting for the grid operational constraints (i.e., limits on the nodal voltages, branches, and transformer capacities) by convex optimal power flow models, (iii) leverage extensive experimental validations on real-life ADNs hosting large amount of stochastic generations and (iv) assessing the impact of a large scale deployment of stochastic renewable energy resources on the planning of ADNs.

First, the Thesis presented a control and scheduling framework for dispatching heterogeneous DERs in ADNs. The framework consisted of two stages. First, a day-ahead stage solves a stochastic optimization problem to compute the dispatch plan where the uncertainties of the prosumption are modeled by scenarios. Second, a real-time stage solves a MPC problem to optimally control flexible DERs, i.e., BESS, curtailable PV plants, in order to track the day-ahead dispatch plan, in real-time, with high accuracy. The control and scheduling stages were grid-aware, i.e., they both account for the grid operational constraints. To make these schemes computationally tractable, we investigated two different OPF approximations in view of real-time actuation deadlines. The first one linearizes the non-linear power-flow equations via well-known power-flow sensitivity coefficients. In this respect, we investigated and compared different approaches to update the sensitivity coefficients for the real-time control scheme. The second formulation uses the AR-OPF: an exact convex relaxation of the AC-OPF. We also compared the linearized OPF and AR-OPF with respect to their accuracy and computational performance. The control schemes associated to the above two OPF approximations were deployed and bench-marked on real-life ADNs hosting a large amount of stochastic generation. The ADNs were equipped with state-of-the-art monitoring and communication infrastructures



along with a state estimator process. Numerical and experimental validations, carried out with a single controllable BESS with time sampling of 30 seconds and MPC optimization horizon of 5 minutes, showed that the proposed scheme using AR-OPF attains better accuracy than the linearized OPF regarding the computation of the grid state variables. More specifically, the linearized OPF has a RMSE of voltage magnitudes/branch currents of  $3.8\text{e-}5\%$ / $0.38\%$  in comparison to  $2\text{e-}3\%$ / $0.14\%$  achieved by the AR-OPF. The linearized- and the AR-OPF-based real-time controls required average/max computation time of 1.32/2.49 and 1.39/2.56 seconds respectively.

Furthermore, for the cases when the installed controllable resource was insufficient to cover the uncertainties caused by the RERs' stochastic injections, the Thesis proposed a two-layer MPC scheme by adding an extra MPC layer to the existing real-time control. In the proposed two-layer MPC, the upper-layer (acting at a slower pace) leverages a forecast of the prosumption along the whole day to optimize the use of the controllable resources used by the lower-layer (acting at a faster pace). This scheme was experimentally validated on a real-life MV ADN hosting 3.2 MWp of photovoltaic generation, 3.4 MVA hydro-power generation, and 2.8 MW of base demand. The MV grid monitored by 17 PMUs was connected with a 1.5 MVA/2.5 MWh BESS controlled by the proposed two-layer MPC. An extensive experimental campaign has been carried out to assess the performance of the proposed control scheme with respect to different types of solar irradiations (and associated uncertainties). These conditions included: clear-sky, cloudy, weekday, and weekend days. The results showed that the proposed two-layer MPC scheme always kept the BESS SOC within an adequate range of operation and achieved better dispatch tracking compared to the single-layer MPC scheme. In particular, the proposed two-layer MPC scheme reduced by half the absolute-energy tracking error, maximum absolute error, and the RMSE, compared to the single-layer MPC scheme.

Second, to deploy the above control schemes on an ADN whose network model (line parameters) was unknown, the Thesis presented a set of model-less/measurement-based data-driven estimation and control schemes. Using PMU measurements on nodal voltages and branch currents, a linear estimator was developed to reliably estimate the parameters of the compound admittance matrix. The Thesis also developed a pre-processing strategy on the measured data set to improve the performance of LS and TLS-based admittance estimators. The numerical validation carried out on CIGRE and IEEE distribution test feeders showed that the pre-processing step improved estimation results by two to three orders of magnitude. The sensitivity analysis with measurements' noise levels showed that the pre-processing method works even with a low accuracy class of IT (i.e., class 1.0). Then, estimated admittance matrix was used to calculate the power flow-sensitivity coefficients, referred to as the indirect approach. The Thesis presented a tool to quantify the uncertainty of the computed sensitivity coefficients derived from the estimated admittance matrix. Still on the same topic, the Thesis investigated an alternative method for the estimation of the sensitivity coefficients, referred to as the direct scheme relying on nodal voltages and power measurements. We investigated the use of recursive-LS (RLS) techniques to estimate the sensitivity coefficients and compared different approaches to solve the usual covariance windup problem. The proposed estimation

---

scheme worked even with collinear power injections (i.e., when the power injections at different nodes are correlated). The numerical validation performed on the CIGRE benchmark network confirmed that the windup problem of RLS is tackled by the directional forgetting (RLS-DF) algorithm that exhibited the best RMSE and the least variance. The performance comparison between the direct and indirect schemes was carried out on two versions of the IEEE-4 network characterized by actual parameters and artificially modified ones corresponding to longer lines. This performance comparison allowed to conclude that the dominant method for the measurement-based estimation of sensitivity coefficients depends on the grid parameters. In particular, for a stiff network (shorter lines), the indirect method showed the least RMSE and variance, whereas, for a weak network (longer lines), the direct scheme showed the least estimation variance (even if it showed a higher RMSE).

The estimated sensitivity coefficients were then used for developing a model-less robust voltage control scheme accounting for the uncertainty of the sensitivity coefficients. The numerical validation on the CIGRE benchmark network showed that the non-robust voltage control failed to satisfy the voltage constraint (i.e., when uncertainty on the estimated coefficients is not accounted for). The proposed robust control scheme always satisfied the operational limits of the nodal voltages even for the highest IT class producing the largest measurement noise. The control scheme was experimentally validated on an actual microgrid that is a replica of the CIGRE benchmark microgrid at the EPFL Distributed Electrical Systems Laboratory. The experiments showed that the proposed robust control scheme kept the nodal voltage magnitudes within the imposed limits thanks to the optimally determined curtailment on the PV plants.

Finally, the Thesis presented a planning tool to analyze the impact of large-scale integration of stochastic renewable resources on the planning of countrywide ADNs. In this respect, the Thesis presented a tool to generate countrywide synthetic power distribution networks based on publicly available geo-referenced data on electricity demand and locations of the power grid extra high voltage substations, and made publicly available. Then, via a proposed linear-OPF-based planning approach, we computed the PV hosting capacity of the MV distribution grids of the whole country. We also computed sizes of BESS when the PV installations are above the ADN's hosting capacity. Also, a specific planning scheme was developed for cost-efficient allocation of PV power plants across the whole country, accounting for the technical limitations of the distribution grids (including adding BESS units, in case this option produces lower system costs) and the distributed potential of PV generation, modeled with highly resolved PV capacity factors from the PVGIS database. Based on our simulations, we concluded that investing in distributed BESS units may be more cost-efficient to increase the PV hosting capacity of distribution grids located in regions with high GHI rather than installing PV plants where their capacity factor is low. This developed tool could provide DSO and decision makers with a mathematically tractable and interpretable method to assess the distribution grid's PV hosting capacity, including how to cost optimally extend it with BESS units.

### Future works

As demonstrated by the experimental validation on real-life ADNs, the methods developed in this Thesis can be directly deployed in real-life power distribution networks. However, more research is required to extend the results to generic networks. The following points are suggested for further investigations.

- Validation of the proposed control schemes on unbalanced and untransposed systems.
- Formulation of grid-aware control problem for multiple provision of ancillary services such as dispatching, primary/secondary frequency control, voltage support to the upstream transmission grid etc.
- Better methods for forecasting the stochastic resources from intra-day to the day-ahead.
- Optimal planning scheme for grid reinforcement competing with BESS installation in ADNs.
- Validation of the measurement-based control scheme demonstrating lines' current congestion management along with voltage regulation.
- Development of distributed optimization schemes considering communication delays.
- Deriving fallback strategies in case of non-convergence of distributed schemes.
- Optimal planning of distributed energy resources with different operational objectives such as dispatching, peak-shaving etc.

## Appendix Part



# A Performance Comparison of RT-MPC using Linearized *vs.* AR-OPF

To find the dominant OPF model, we compare the performance of RT-MPC using the two models: (i) Linear OPF (used in Chapter 2) and ii) AR-OPF (used in Chapter 3), concerning their accuracy and computational speed. In the following, they are referred to as **L-OPF-MPC** and **AR-OPF-MPC** respectively. For the sake of simplicity, the comparison is performed using **Single-layer MPC**, i.e., solving the lower-layer MPC problem (eq. 3.4) but without SOE budget from upper layer MPC. The comparison is performed against the true quantities obtained by solving the non-linear load flow *a posteriori*. The results are compared by looking at the root-mean-square-error (RMSE) and maximum absolute error (MAE) in the voltage, current magnitudes, and grid losses.

## A.1 Accuracy of the Grid Model:

Here, we compare the grid states, i.e., nodal voltages, lines currents, and losses computed by the L-OPF and AR-OPF models. They are compared against true values by solving non-linear AC power flow using the setpoint of BESS. Fig. A.1a and A.1b show the nodal voltages using L-OPF and AR-OPF, respectively. The plot in the upper panel shows the voltage computed by the OPF models, whereas the lower panel shows error (in %) against true voltage. Similarly, Figs. A.1c and A.1d show the lines' current magnitudes (upper panel) and corresponding error (lower panel) using L-OPF and AR-OPF, respectively. Finally, Figs A.1e and A.1f show the net grid losses (upper panel) and corresponding error (lower panel) with L-OPF and AR-OPF, respectively. Fig. A.1g compares the CDF of the error in nodal voltages, lines currents, and grid losses using L-OPF and AR-OPF. Table A.1 compares the two models in terms of maximum absolute error (MAE) and RMSE errors of the nodal voltages, lines currents and grid losses. The comparisons show that the AR-OPF model performs better on the lines' current magnitude and grid losses by 87% and 90% on MAE. The error on the voltage magnitudes is slightly higher for AR-OPF; however, below  $5.5e-3\%$  on maximum magnitude error.

## Appendix A. Performance Comparison of RT-MPC using Linearized *vs.* AR-OPF

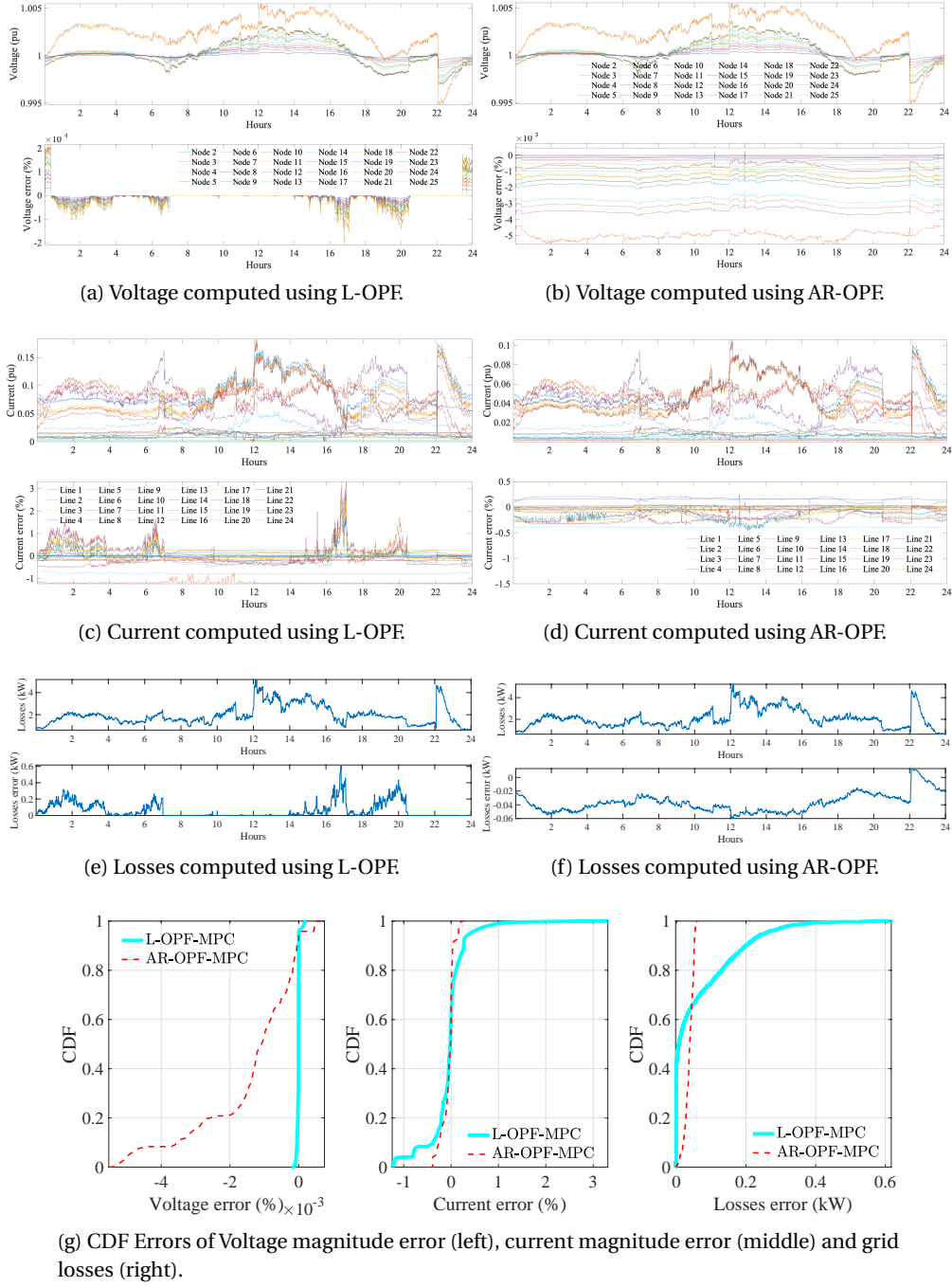


Figure A.1: Performance comparison of MPC using L-OPF and AR-OPF as grid models.

### A.2 Computational Performance:

We also compare the computation time using the two schemes. The comparison is shown in Table in terms of mean, and maximum computation time. The MPCs were run on a MacBook

### A.3 Control Performance:

Table A.1: Error on the modeled voltage, currents and grid losses.

MPC	Voltage error		Current error		Losses error	
	RMSE (%)	MAE (%)	RMSE (%)	MAE (%)	RMSE (kW)	MAE (kW)
L-OPF-MPC	3.8e-5	2.2e-4	0.38	3.31	0.11	0.62
AR-OPF-MPC	2e-3	5.5e-3	0.14	0.45	0.04	0.06

Pro with a 2.7 GHz Quad-Core Intel Core i7 and 16 GB of Memory. Both the schemes achieve computation time below 30 seconds which is the time resolution of the MPC.

Table A.2: Computation time

MPC	Mean time (sec)	Max time (sec)
L-OPF-MPC	1.32	2.49
AR-OPF-MPC	1.39	2.56

### A.3 Control Performance:

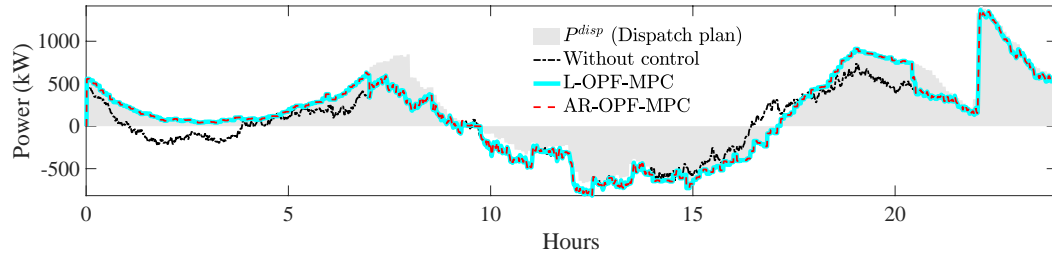
In this section, we compare the dispatch tracking performance of the L-OPF-MPC and AR-OPF-MPC schemes. Fig. A.2a shows dispatch plan, realization with and without MPC. Fig. A.2b shows the BESS active power and its state of charge (SOC) evolution for the two cases. Fig A.2c shows the CDF of the dispatch error for the two cases. As it can be seen, the dispatch plan tracking via both MPCs (L-OPF-MPC and AR-OPF) are similar. The same can be deduced from the comparison in Table A.3. It reports the maximum-absolute-error (MAE), absolute-energy-error (AEE), and root-mean-square-error (RMSE) of the dispatch error using different controls, concluding that both grid models perform similarly in terms of the control performance. The MPC schemes reduce the tracking error in RMSE and AEE by 35% and 60 %, respectively.

Table A.3: Dispatch tracking error

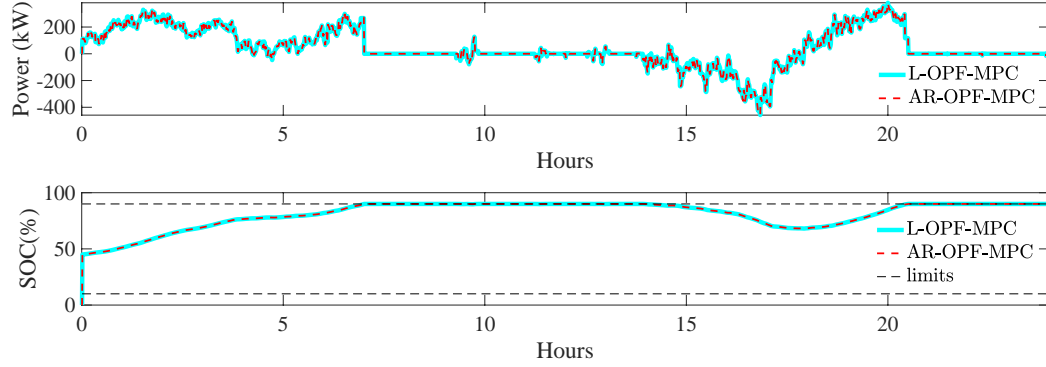
MPC	Dispatch error		
	MAE (kW)	RMSE (kW)	AEE (kWh)
Without MPC	1.2e3	190	3.6e3
L-OPF-MPC	1.2e3	125	1.4e3
AR-OPF-MPC	1.2e3	125	1.4e3



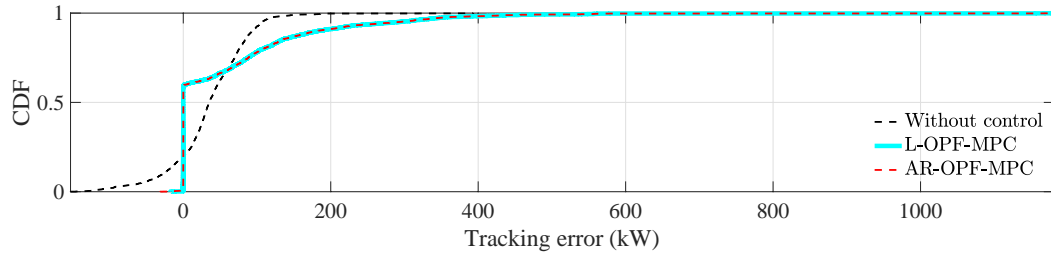
## Appendix A. Performance Comparison of RT-MPC using Linearized *vs.* AR-OPF



(a) GCP power tracking the dispatch plan with different control schemes.



(b) SOC of the BESS with different control schemes.



(c) CDF plot of the dispatch tracking error with different control schemes.

Figure A.2: (a-c) Dispatch plan computation for day 1 (22-Mar.-2022).

The above performance comparison shows that the AR-OPF models attain better accuracy than the Linearized OPF. The AR-OPF achieves higher accuracy in modeling the lines' currents and grid losses. Both the AR-OPF and L-OPF-based MPCs performed similarly on the control performance metrics.

## B Validation of Error Propagation using Monte-Carlo Simulations

The error propagation scheme developed in Sec. 4.3.5 is numerically validated by performing Monte-Carlo (MC) simulations. For this, we use the IEEE 4-bus system as shown in Fig. 4.11. The parameters of the branches are shown in Table 4.8. The nominal nodal injections are also listed in Table 4.8. To perform MC simulation, we assume different variances on the admittance matrix (to mimic uncertainty arising from the estimation process) and measurement noises of different classes according to IT standards [128]. The steps for MC simulation are described below.

1. Random noise is introduced on the voltage magnitudes and phase angles using IT class specifications as described in Table 4.1. The noise is then projected to rectangular coordinates using the approach described in [122].
2. Random error is introduced on the elements of the admittance matrix.
3. Compute matrix  $\mathbf{H}$  using the equations in (4.43). Compute its inverse  $\mathbf{H}^{-1}$ .
4. Compute the sensitivity coefficients  $\mathbf{x}$  using (4.35).
5. Repeat steps 1 – 4  $N_{\text{mc}}$  times, store the estimated sensitivity coefficients in  $\mathcal{X}(k) = \mathbf{x}$
6. Compute variance of each element of  $\mathbf{x}$ .

The variances computed using the analytical approach of (4.38) is compared with the ones computed using the MC scheme. The comparison is shown in Table B.1. We present this comparison for different values of  $N_{\text{mc}}$ . Here, we consider IT class 0.5 for the measurement noise on voltage phasors and 1 % error on the admittance matrix. For the sake of brevity, the comparisons are only shown for six different coefficients, as listed in Table B.1. As it can be observed, for the simulations with  $N_{\text{mc}}$  higher than 100, the standard deviation computed by the analytical approach and MC simulation matches. Hence, it can be concluded that the proposed analytical approach for error propagation works properly.

## Appendix B. Validation of Error Propagation using Monte-Carlo Simulations

Table B.1: Performance comparison with number of samples in Monte-Carlo simulations.

		$\Re(\frac{\partial v_3}{\partial p_2})$	$\Re(\frac{\partial v_3}{\partial p_4})$	$\Re(\frac{\partial v_4}{\partial p_4})$	$\Im(\frac{\partial v_3}{\partial p_2})$	$\Im(\frac{\partial v_3}{\partial p_3})$	$\Im(\frac{\partial v_4}{\partial p_4})$
	Nominal value	0.0071	0.0152	0.0239	0.0077	0.0176	0.0288
	Variance (Analytical)	0.0006	0.0012	0.0018	0.0006	0.0011	0.0016
	$N_{mc}$						
Variance (Monte-Carlo)	10	0.0009	0.0016	0.0021	0.0006	0.0012	0.0018
	100	0.0007	0.0013	0.0020	0.0007	0.0013	0.0019
	1000	0.0007	0.0014	0.0020	0.0007	0.0013	0.0019
	10000	0.0007	0.0014	0.0020	0.0007	0.0013	0.0019

Furthermore, we vary the error of the admittance matrix from 0.5 %, 1 %, and 2 %, respectively, to determine the corresponding standard deviations. From the comparison shown in Table B.2, it is concluded that the error propagation works well for the 0.5 % and 1 %. However, it differs slightly for case of 2 % error; the difference can be explained due to assumptions made on error propagation in Sec. 4.3.5 might not hold well for high standard deviations.

Table B.2: Performance comparison with respect to uncertainty on the admittance matrix.

		$\Re(\frac{\partial v_3}{\partial p_2})$	$\Re(\frac{\partial v_3}{\partial p_4})$	$\Re(\frac{\partial v_4}{\partial p_4})$	$\Im(\frac{\partial v_3}{\partial p_2})$	$\Im(\frac{\partial v_3}{\partial p_3})$	$\Im(\frac{\partial v_4}{\partial p_4})$
$\sigma_Y$ (% of $Y$ )	Nominal value	0.0071	0.0152	0.0239	0.0077	0.0176	0.0288
0.5	Variance (Monte-Carlo)	0.337e-3	0.666e-3	0.986e-3	0.338e-3	0.659e-3	0.938e-3
	Variance (Analytical)	0.334e-3	0.662e-3	0.991e-3	0.316e-3	0.628e-3	0.900e-3
1	Variance (Monte-Carlo)	0.0007	0.0014	0.0020	0.0007	0.0013	0.0019
	Variance (Analytical)	0.0006	0.0012	0.0018	0.0006	0.0011	0.0016
2	Variance (Monte-Carlo)	0.0015	0.0030	0.0044	0.0014	0.0028	0.0040
	Variance (Analytical)	0.0013	0.0026	0.0033	0.0010	0.0021	0.0030

# Bibliography

- [1] CAISO, *Frequency Response Phase 2*, 2016.
- [2] AEMO, *Review of the Black System South Australia Report – System Event of 28 September 2016*, 2017.
- [3] J. Morren and S. De Haan, “Impact of distributed generation units with power electronic converters on distribution network protection,” *IET*, 2008.
- [4] E. Coster and D. Van Houwelingen, “Integration of dg in mv-grids: Challenges encountered by the grid operator,” in *2009 CIGRE/IEEE PES Joint Symposium*. IEEE, 2009, pp. 1–9.
- [5] CIGRE’ Task Force C6.04.02, *Benchmark Systems for Network Integration of renewable and Distributed Energy Resources*, July 2009.
- [6] N. Hatziargyriou, J. Amantegui, B. Andersen, M. Armstrong, P. Boss, B. Dalle, G. De-Montravel, A. Negri, C. A. Nucci, and P. Southwell, “Cigre wg “network of the future” electricity supply systems of the future,” *ELECTRA*, vol. No 256, pp. 42–49, 06 2011.
- [7] C. D’Adamo, S. Jupe, and C. Abbey, “Global survey on planning and operation of active distribution networks-update of cigre c6. 11 working group activities,” in *CIGRE 2009-20th International Conference and Exhibition on Electricity Distribution-Part 1*. IET, 2009, pp. 1–4.
- [8] F. Pilo, S. Jupe, F. Silvestro, K. El Bakari, C. Abbey, G. Celli, J. Taylor, A. Baitch, and C. Carter-Brown, “Planning and optimisation of active distribution systems-an overview of cigre working group c6. 19 activities,” 2012.
- [9] NASPI Distribution Task Team, *Synchrophasor Monitoring for Distribution Systems Technical Foundations and Applications [White paper]*, 2018.
- [10] A. Angioni, G. Lipari, M. Pau, F. Ponci, and A. Monti, “A low cost pmu to monitor distribution grids,” in *2017 IEEE International Workshop on Applied Measurements for Power Systems (AMPS)*. IEEE, 2017, pp. 1–6.

- [11] P. Romano, M. Paolone, T. Chau, B. Jeppesen, and E. Ahmed, "A high-performance, low-cost pmu prototype for distribution networks based on fpga," in *2017 IEEE Manchester PowerTech*. IEEE, 2017, pp. 1–6.
- [12] D. Schofield, F. Gonzalez-Longatt, and D. Bogdanov, "Design and implementation of a low-cost phasor measurement unit: A comprehensive review," in *2018 Seventh Balkan Conference on Lighting (BalkanLight)*. IEEE, 2018, pp. 1–6.
- [13] B. Mohandes, M. S. E. Moursi, N. Hatziaargyriou, and S. E. Khatib, "A review of power system flexibility with high penetration of renewables," *IEEE Transactions on Power Systems*, vol. 34, no. 4, pp. 3140–3155, 2019.
- [14] M. Paolone, "Editorial," *Sustainable Energy, Grids and Networks*, vol. 1, pp. A1–A3, 2015. [Online]. Available: <https://www.sciencedirect.com/science/article/pii/S2352467715000089>
- [15] M. Nick, R. Cherkaoui, J.-Y. Le Boudec, and M. Paolone, "An exact convex formulation of the optimal power flow in radial distribution networks including transverse components," *IEEE Transactions on Automatic Control*, vol. 63, no. 3, pp. 682–697, 2017.
- [16] R. Gupta, F. Sossan, and M. Paolone, "Performance Assessment of Linearized OPF-based Distributed Real-time Predictive Control," in *IEEE PowerTech 2019*, Milan, Italy, Jun. 2019.
- [17] —, "Grid-aware distributed model predictive control of heterogeneous resources in a distribution network: Theory and experimental validation," *IEEE Transactions on Energy Conversion*, vol. 36, no. 2, p. 1392 – 1402, 2021.
- [18] A. Nottrott, J. Kleissl, and B. Washom, "Energy dispatch schedule optimization and cost benefit analysis for grid-connected, photovoltaic-battery storage systems," *Renewable Energy*, vol. 55, pp. 230–240, 2013.
- [19] E. Reihani, S. Sepasi, L. R. Roose, and M. Matsuura, "Energy management at the distribution grid using a battery energy storage system (bess)," *IJEPES*, vol. 77, pp. 337–344, 2016.
- [20] R. Palma-Behnke, C. Benavides, F. Lanas, B. Severino, L. Reyes, J. Llanos, and D. Sáez, "A microgrid energy management system based on the rolling horizon strategy," *IEEE Transactions on Smart Grid*, vol. 4, no. 2, pp. 996–1006, June 2013.
- [21] M. Abu Abdullah, K. Muttaqi, D. Sutanto, and A. Agalgaonkar, "An effective power dispatch control strategy to improve generation schedulability and supply reliability of a wind farm using a battery energy storage system," *Sustainable Energy, IEEE Transactions on*, vol. 6, 2015.
- [22] M. He et al., "Multiple timescale dispatch and scheduling for stochastic reliability in smart grids with wind generation integration," in *2011 Proceedings IEEE INFOCOM*. IEEE, 2011, pp. 461–465.

- [23] F. Sossan, E. Namor, R. Cherkaoui, and M. Paolone, "Achieving the dispatchability of distribution feeders through prosumers data driven forecasting and model predictive control of electrochemical storage," *IEEE Trans. on Sust. Energy*, vol. 7, no. 4, pp. 1762–1777, 2016.
- [24] A. Lorca and X. A. Sun, "Adaptive robust optimization with dynamic uncertainty sets for multi-period economic dispatch under significant wind," *IEEE Transactions on Power Systems*, vol. 30, no. 4, pp. 1702–1713, 2014.
- [25] E. Namor, F. Sossan, R. Cherkaoui, and M. Paolone, "Load leveling and dispatchability of a medium voltage active feeder through battery energy storage systems: Formulation of the control problem and experimental validation," in *2016 IEEE PES Innovative Smart Grid Technologies Conference Europe (ISGT-Europe)*. IEEE, 2016, pp. 1–6.
- [26] K. Christakou, D.-C. Tomozei, J.-Y. Le Boudec, and M. Paolone, "Gecn: Primary voltage control for active distribution networks via real-time demand-response," *IEEE Transactions on Smart Grid*, vol. 5, no. 2, pp. 622–631, 2013.
- [27] A. Bernstein, L. Reyes-Chamorro, J.-Y. L. Boudec, and M. Paolone, "A composable method for real-time control of active distribution networks with explicit power set-points. part i: Framework," *Electric Power Systems Research*, 2015.
- [28] R. Gupta, F. Sossan, E. Scolari, E. Namor, L. Fabietti, C. Jones, and M. Paolone, "An admm-based coordination and control strategy for pv and storage to dispatch stochastic prosumers: Theory and experimental validation," in *2018 Power Syst. Comput. Conf.*, June 2018, pp. 1–7.
- [29] E. Namor, F. Sossan, R. Cherkaoui, and M. Paolone, "Control of battery storage systems for the simultaneous provision of multiple services," *IEEE Transactions on Smart Grid*, vol. 10, no. 3, pp. 2799–2808, 2018.
- [30] D. Espín-Sarzosa, R. Palma-Behnke, and O. Núñez-Mata, "Energy management systems for microgrids: Main existing trends in centralized control architectures," *Energies*, vol. 13, no. 3, p. 547, 2020.
- [31] D. Kourounis, A. Fuchs, and O. Schenk, "Toward the next generation of multiperiod optimal power flow solvers," *IEEE Transactions on Power Systems*, vol. 33, no. 4, pp. 4005–4014, 2018.
- [32] A. Venzke, S. Chatzivasileiadis, and D. K. Molzahn, "Inexact convex relaxations for ac optimal power flow: Towards ac feasibility," *Electric Power Systems Research*, vol. 187, p. 106480, 2020.
- [33] D. K. Molzahn, I. A. Hiskens *et al.*, "A survey of relaxations and approximations of the power flow equations," *Now Publishers*, 2019.

- [34] R. A. Jabr, "Radial distribution load flow using conic programming," *IEEE transactions on power systems*, vol. 21, no. 3, pp. 1458–1459, 2006.
- [35] L. Gan, N. Li, U. Topcu, and S. H. Low, "Exact convex relaxation of optimal power flow in radial networks," *IEEE Transactions on Automatic Control*, vol. 60, no. 1, pp. 72–87, 2014.
- [36] A. Bernstein, C. Wang, E. Dall'Anese, J.-Y. Le Boudec, and C. Zhao, "Load flow in multi-phase distribution networks: Existence, uniqueness, non-singularity and linear models," *IEEE Transactions on Power Systems*, vol. 33, no. 6, pp. 5832–5843, 2018.
- [37] R. A. Jabr, "High-order approximate power flow solutions and circular arithmetic applications," *IEEE Transactions on Power Systems*, vol. 34, no. 6, pp. 5053–5062, 2019.
- [38] J.-H. Teng, "A direct approach for distribution system load flow solutions," *IEEE Trans. Power Del.*, vol. 18, no. 3, pp. 882–887, 2003.
- [39] P. Fortenbacher, A. Ulbig, and G. Andersson, "Optimal placement and sizing of distributed battery storage in low voltage grids using receding horizon control strategies," *IEEE Trans. Power Syst.*, vol. 33, no. 3, pp. 2383–2394, 2018.
- [40] K. Christakou, J.-Y. LeBoudec, M. Paolone, and D.-C. Tomozei, "Efficient computation of sensitivity coefficients of node voltages and line currents in unbalanced radial electrical distribution networks," *IEEE Transactions on Smart Grid*, vol. 4, no. 2, pp. 741–750, 2013.
- [41] E. Perez, H. Beltran, N. Aparicio, and P. Rodriguez, "Predictive power control for pv plants with energy storage," *IEEE Transactions on Sustainable Energy*, vol. 4, no. 2, pp. 482–490, 2012.
- [42] D. Halamay, M. Antonishen, K. Lajoie, A. Bostrom, and T. K. Brekken, "Improving wind farm dispatchability using model predictive control for optimal operation of grid-scale energy storage," *Energies*, vol. 7, no. 9, pp. 5847–5862, 2014.
- [43] S. Teleke, M. E. Baran, A. Q. Huang, S. Bhattacharya, and L. Anderson, "Control strategies for battery energy storage for wind farm dispatching," *Energy Conversion, IEEE Transactions on*, vol. 24, 2009.
- [44] Y. Zheng, S. Li, and R. Tan, "Distributed model predictive control for on-connected microgrid power management," *IEEE Transactions on Control Systems Technology*, vol. 26, no. 3, pp. 1028–1039, 2017.
- [45] Y. Du, J. Wu, S. Li, C. Long, and I. C. Paschalidis, "Distributed mpc for coordinated energy efficiency utilization in microgrid systems," *IEEE Transactions on Smart Grid*, vol. 10, no. 2, pp. 1781–1790, 2017.
- [46] M. R. Almassalkhi and I. A. Hiskens, "Model-predictive cascade mitigation in electric power systems with storage and renewables—part i: Theory and implementation," *IEEE Transactions on Power Systems*, vol. 30, no. 1, pp. 67–77, 2014.

- [47] J. A. Martin and I. A. Hiskens, "Corrective model-predictive control in large electric power systems," *IEEE Transactions on Power Systems*, vol. 32, no. 2, pp. 1651–1662, 2016.
- [48] J. Abrell, "The swiss wholesale electricity market," *tech. rep., wiss Competence Center for Energy Research*, 2016.
- [49] R. Gurram and B. Subramanyam, "Sensitivity analysis of radial distribution network–adjoint network method," *International Journal of Electrical Power & Energy Systems*, vol. 21, no. 5, pp. 323–326, 1999.
- [50] J. Bandler and M. El-Kady, "A unified approach to power system sensitivity analysis and planning, part i: Family of adjoint systems," in *Proc. IEEE Int. Symp. Circuits Syst*, 1980, pp. 681–687.
- [51] Q. Zhou and J. Bialek, "Simplified calculation of voltage and loss sensitivity factors in distribution networks," in *Proc. 16th Power Syst. Comput. Conf. (PSCC2008)*, 2008.
- [52] S. Conti, S. Raiti, and G. Vagliasindi, "Voltage sensitivity analysis in radial mv distribution networks using constant current models," in *2010 IEEE International Symposium on Industrial Electronics*. IEEE, 2010, pp. 2548–2554.
- [53] D. K. Khatod, V. Pant, and J. Sharma, "A novel approach for sensitivity calculations in the radial distribution system," *IEEE transactions on Power Delivery*, vol. 21, no. 4, pp. 2048–2057, 2006.
- [54] S. Maharjan, A. M. Khambadkone, and J. C.-H. Peng, "Enhanced z-bus method for analytical computation of voltage sensitivities in distribution networks," *IET Generation, Transmission & Distribution*, vol. 14, no. 16, pp. 3187–3197, 2020.
- [55] S. Fahmy and M. Paolone, "Analytical computation of power grids' sensitivity coefficients with voltage-dependent injections," in *2021 IEEE Madrid PowerTech*. IEEE, 2021, pp. 1–6.
- [56] M. Paolone, J.-Y. Le Boudec, K. Christakou, and D.-C. Tomozei, "Optimal voltage control processes in active distribution networks," *The Institution of Engineering and Technology-IET, Tech. Rep.*, 2015.
- [57] R. Gupta, S. Fahmy, and M. Paolone, "Coordinated day-ahead dispatch of multiple power distribution grids hosting stochastic resources: An admm-based framework," *Electric Power Systems Research*, vol. 212, p. 108555, 2022.
- [58] S. Haben, S. Arora, G. Giasemidis, M. Voss, and D. V. Greetham, "Review of low voltage load forecasting: Methods, applications, and recommendations," *Applied Energy*, vol. 304, p. 117798, 2021.
- [59] F. Sossan *et al.*, "Unsupervised disaggregation of photovoltaic production from composite power flow measurements of heterogeneous prosumers," *IEEE Trans. Ind. Inf.*, vol. 14, no. 9, pp. 3904–3913, 2018.



## Bibliography

---

- [60] *Solar radiation data (SoDa)*. [Online]. Available: [www.soda-pro.com/soda-products/ai-forecast](http://www.soda-pro.com/soda-products/ai-forecast)
- [61] B. Espinar *et al.*, “Helioclim-3: a near-real time and long-term surface solar irradiance database,” in *Workshop on Remote Sensing Measurements for Renewable Energy*, 2012.
- [62] M. Lefevre *et al.*, “Mcclear: a new model estimating downwelling solar radiation at ground level in clear-sky conditions,” *Atmospheric Measurement Techniques*, vol. 6, no. 9, pp. 2403–2418, 2013.
- [63] W. Holmgren, C. Hansen, and M. Mikofski, “pvlib python: A python package for modeling solar energy systems,” *Journal of Open Source Software*, vol. 3, no. 29, p. 884, 2018.
- [64] E. Stai *et al.*, “Dispatching stochastic heterogeneous resources accounting for grid and battery losses,” *IEEE Trans. on Smart Grid*, vol. 9, no. 6, pp. 6522–6539, 2018.
- [65] E. Dall’Anese, S. V. Dhople, B. B. Johnson, and G. B. Giannakis, “Decentralized optimal dispatch of photovoltaic inverters in residential distribution systems,” *IEEE Transactions on Energy Conversion*, vol. 29, no. 4, pp. 957–967, Dec 2014.
- [66] S. e. a. Boyd, “Distributed optimization and statistical learning via the alternating direction method of multipliers,” *Foundations and Trends in Machine Learning*, vol. 3, 2011.
- [67] S. Wang and L. Liao, “Decomposition method with a variable parameter for a class of monotone variational inequality problems,” *Journal of optimization theory and applications*, vol. 109, no. 2, pp. 415–429, 2001.
- [68] F. Sossan, E. Scolari, R. Gupta, and M. Paolone, “Solar irradiance estimations for modeling the variability of photovoltaic generation and assessing violations of grid constraints: A comparison between satellite and pyranometers measurements with load flow simulations,” *Journal of Renewable and Sustainable Energy*, vol. 11, no. 5, p. 056103, 2019.
- [69] J. D. Lara, D. E. Olivares, and C. A. Cañizares, “Robust energy management of isolated microgrids,” *IEEE Systems Journal*, vol. 13, no. 1, pp. 680–691, 2018.
- [70] F. Valencia, J. Collado, D. Sáez, and L. G. Marín, “Robust energy management system for a microgrid based on a fuzzy prediction interval model,” *IEEE Transactions on Smart Grid*, vol. 7, no. 3, pp. 1486–1494, 2015.
- [71] M. Hosseinzadeh and F. R. Salmasi, “Robust optimal power management system for a hybrid ac/dc micro-grid,” *IEEE Transactions on Sustainable Energy*, vol. 6, no. 3, pp. 675–687, 2015.
- [72] M. Pignati *et al.*, “Real-time state estimation of the epfl-campus medium-voltage grid by using pmus,” in *Conf. Innovative Smart Grid Technologies (ISGT)*, no. 1-5, 2015.

- [73] S. Fahmy, "Efficient methods for the operation of active distribution networks in un-symmetric and uncertain states," Ph.D. dissertation, Dept. Electrical Engineering, Ecole Polytechnique Federal De Lausanne, 2022.
- [74] S. Papathanassiou, N. Hatziargyriou, and K. e. a. Strunz, "A benchmark low voltage microgrid network," in *Proceedings of the CIGRE symposium: power systems with dispersed generation*. CIGRE, 2005, pp. 1–8.
- [75] L. e. a. Reyes-Chamorro, "Experimental validation of an explicit power-flow primary control in microgrids," *IEEE Trans. Ind. Informat.*, vol. 14, no. 11, pp. 4779–4791, 2018.
- [76] A. Derviškić, P. Romano, M. Pignati, and M. Paolone, "Architecture and experimental validation of a low-latency phasor data concentrator," *IEEE Transactions on Smart Grid*, vol. 9, no. 4, pp. 2885–2893, 2016.
- [77] A. M. e. a. Kettner, "Sequential discrete kalman filter for real-time state estimation in power distribution systems: Theory and implementation," *IEEE Trans. Inst. Meas.*, vol. 66, no. 9, pp. 2358–2370, 2017.
- [78] R. Gupta, V. Sovljanski, F. Sossan, and M. Paolone, "Performance comparison of alternating direction optimization methods for linear-opf based real-time predictive control," in *2021 IEEE Madrid PowerTech*. IEEE, 2021, pp. 1–6.
- [79] R. Gupta, A. Zecchino, J.-H. Yi, and M. Paolone, "Reliable dispatch of active distribution networks via a two-layer grid-aware model predictive control: Theory and experimental validation," *IEEE Open Access Journal of Power and Energy*, 2022.
- [80] M. Bozorg *et al.*, "Influencing the bulk power system reserve by dispatching power distribution networks using local energy storage," *Electric Power System Research*, vol. 163, pp. 270–279, 2018.
- [81] T. G. Paul *et al.*, "A quadratic programming based optimal power and battery dispatch for grid-connected microgrid," *IEEE Trans. Ind. App.*, vol. 54, no. 2, pp. 1793–1805, 2017.
- [82] F. Arrigo, E. Bompard, M. Merlo, and F. Milano, "Assessment of primary frequency control through battery energy storage systems," *IJEPES*, vol. 115, p. 105428, 2020.
- [83] M. Zeraati *et al.*, "Distributed control of battery energy storage systems for voltage regulation in distribution networks with high pv penetration," *IEEE Trans. Smart Grid*, vol. 9, no. 4, pp. 3582–3593, 2016.
- [84] C. Straub *et al.*, "Congestion management within a multi-service scheduling coordination scheme for large battery storage systems," in *2019 IEEE Milan PowerTech*. IEEE, 2019, pp. 1–6.
- [85] H. W. Dommel and W. F. Tinney, "Optimal power flow solutions," *IEEE Trans. Power App. Syst.*, no. 10, pp. 1866–1876, 1968.

## Bibliography

---

- [86] M. Huneault and F. D. Galiana, "A survey of the optimal power flow literature," *IEEE Trans. Power Syst.*, vol. 6, no. 2, pp. 762–770, 1991.
- [87] S. P. Torres and C. A. Castro, "Expansion planning for smart transmission grids using ac model and shunt compensation," *IET Generation, Transmission & Distribution*, vol. 8, no. 5, pp. 966–975, 2014.
- [88] E. Mohagheghi, M. Alramlawi, A. Gabash, and P. Li, "A survey of real-time optimal power flow," *Energies*, vol. 11, no. 11, p. 3142, 2018.
- [89] Y. Tang, K. Dvijotham, and S. Low, "Real-time optimal power flow," *IEEE Transactions on Smart Grid*, vol. 8, no. 6, pp. 2963–2973, 2017.
- [90] Y. Liu *et al.*, "Distributed real-time optimal power flow control in smart grid," *IEEE Trans. Power Syst.*, vol. 32, no. 5, pp. 3403–3414, 2016.
- [91] J. G. Robertson, G. P. Harrison, and A. R. Wallace, "Opf techniques for real-time active management of distribution networks," *IEEE Transactions on power systems*, vol. 32, no. 5, pp. 3529–3537, 2016.
- [92] L. E. R. Chamorro, *Real-time control framework for active distribution networks theoretical definition and experimental validation*, 2016.
- [93] *Guide for phasor data concentrator requirements for power system protection, control, and monitoring*.
- [94] M. ApS, "Mosek optimization toolbox for matlab," *User's Guide and Reference Manual, Version*, vol. 4, 2019.
- [95] R. K. Gupta, F. Sossan, J.-Y. Le Boudec, and M. Paolone, "Compound admittance matrix estimation of three-phase untransposed power distribution grids using synchrophasor measurements," *IEEE Transactions on Instrumentation and Measurement*, vol. 70, pp. 1–13, 2021.
- [96] R. Gupta, F. Sossan, and M. Paolone, "Model-less robust voltage control in active distribution networks using sensitivity coefficients estimated from measurements," *Electric Power Systems Research*, vol. 212, p. 108547, 2022. [Online]. Available: <https://www.sciencedirect.com/science/article/pii/S0378779622006277>
- [97] R. Gupta, "Quantifying uncertainty on the power-flow sensitivity coefficients from uncertain branches parameters and noisy grid-state measurements," *In preparation*, 2022.
- [98] C. Mugnier, K. Christakou, J. Jatton, M. De Vivo, M. Carpita, and M. Paolone, "Model-less/measurement-based computation of voltage sensitivities in unbalanced electrical distribution networks," in *2016 PSCC*. IEEE, 2016, pp. 1–7.

- [99] M. Carpita, A. Dassatti, M. Bozorg, J. Jatón, S. Reynaud, and O. Mousavi, "Low voltage grid monitoring and control enhancement: The grideye solution," in *2019 ICCEP*. IEEE, 2019, pp. 94–99.
- [100] G. Valverde, T. Zufferey, S. Karagiannopoulos, and G. Hug, "Estimation of voltage sensitivities to power injections using smart meter data," in *2018 ENERGYCON*. IEEE, 2018, pp. 1–6.
- [101] J. Zhang, Z. Wang, X. Zheng, L. Guan, and C. Chung, "Locally weighted ridge regression for power system online sensitivity identification considering data collinearity," *IEEE Trans. Power Syst.*, vol. 33, no. 2, pp. 1624–1634, 2017.
- [102] J. Zhang, C. Chung, and L. Guan, "Noise effect and noise-assisted ensemble regression in power system online sensitivity identification," *IEEE Trans. Ind. Info.*, vol. 13, no. 5, pp. 2302–2310, 2017.
- [103] E. L. da Silva, A. M. N. Lima, M. B. de Rossiter Corrêa, M. A. Vitorino, and L. T. Barbosa, "Data-driven sensitivity coefficients estimation for cooperative control of pv inverters," *IEEE Transactions on Power Delivery*, vol. 35, no. 1, pp. 278–287, 2019.
- [104] R. P. Schulz, L. S. VanSlyck, and S. H. Horowitz, "Applications of fast phasor measurements on utility systems," in *Conference Papers Power Industry Computer Application Conference*. IEEE, 1989, pp. 49–55.
- [105] I. W. Slutsker, S. Mokhtari, and K. A. Clements, "Real time recursive parameter estimation in energy management systems," *IEEE Transactions on power systems*, vol. 11, no. 3, pp. 1393–1399, 1996.
- [106] I.-D. Kim and R. K. Aggarwal, "A study on the on-line measurement of transmission line impedances for improved relaying protection," *Int. J. Elect. Power & Energy Syst.*, vol. 28, no. 6, pp. 359–366, 2006.
- [107] C. Indulkar and K. Ramalingam, "Estimation of transmission line parameters from measurements," *International Journal of Electrical Power & Energy Systems*, vol. 30, no. 5, pp. 337–342, 2008.
- [108] D. Shi, D. J. Tylavsky, K. M. Koellner, N. Logic, and D. E. Wheeler, "Transmission line parameter identification using pmu measurements," *European Transactions on Electrical Power*, vol. 21, no. 4, pp. 1574–1588, 2011.
- [109] L. Ding, T. Bi, and D. Zhang, "Transmission line parameters identification based on moving-window tls and pmu data," in *Int. Conf. APAP*, vol. 3. IEEE, 2011, pp. 2187–2191.
- [110] H. Zhang, Z. Diao, and Y. Cui, "Identification of Power Network Branch Parameters Based on State Space Transformation," *IEEE Access*, vol. 7, pp. 91 720–91 730, 2019.
- [111] Y. Yuan, O. Ardakanian, S. Low, and C. Tomlin, "On the inverse power flow problem," *arXiv preprint arXiv:1610.06631*, 2016.

## Bibliography

---

- [112] J. Yu, Y. Weng, and R. Rajagopal, "Patopa: A data-driven parameter and topology joint estimation framework in distribution grids," *IEEE Transactions on Power Systems*, vol. 33, no. 4, pp. 4335–4347, 2018.
- [113] P. A. Pegoraro, K. Brady, P. Castello, C. Muscas, and A. von Meier, "Line impedance estimation based on synchrophasor measurements for power distribution systems," *IEEE Transactions on Instrumentation and Measurement*, vol. 68, no. 4, pp. 1002–1013, 2018.
- [114] P. A. Pegoraro *et al.*, "Compensation of systematic measurement errors in a pmu-based monitoring system for electric distribution grids," *IEEE Transactions on Instrumentation and Measurement*, vol. 68, no. 10, pp. 3871–3882, 2019.
- [115] H. Goklani, G. Gajjar, and S. Soman, "Instrument transformer calibration and robust estimation of transmission line parameters using pmu measurements," *IEEE Transactions on Power Systems*, 2020.
- [116] C. Wang, V. A. Centeno, K. D. Jones, and D. Yang, "Transmission lines positive sequence parameters estimation and instrument transformers calibration based on pmu measurement error model," *IEEE Access*, vol. 7, pp. 145 104–145 117, 2019.
- [117] G. H. Golub and C. F. Van Loan, "An analysis of the total least squares problem," *SIAM journal on numerical analysis*, vol. 17, no. 6, pp. 883–893, 1980.
- [118] W. H. Kersting, "Radial distribution test feeders," in *2001 IEEE Power Engineering Society Winter Meeting. Conference Proceedings*, vol. 2. IEEE, 2001, pp. 908–912.
- [119] V. Milojević, S. Čalića, G. Rietveld, M. V. Ačanski, and D. Colangelo, "Utilization of pmu measurements for three-phase line parameter estimation in power systems," *IEEE Transactions on Instrumentation and Measurement*, vol. 67, no. 10, pp. 2453–2462, 2018.
- [120] P. K. Mansani, A. Pal, M. Rhodes, and B. Keel, "Estimation of transmission line sequence impedances using real pmu data," in *2018 North American Power Symposium (NAPS)*. IEEE, 2018, pp. 1–6.
- [121] R. S. Singh, S. Babaev, V. Cuk, S. Cobben, and H. van den Brom, "Line parameters estimation in presence of uncalibrated instrument transformers," in *2019 2nd International Colloquium on Smart Grid Metrology (SMAGRIMET)*. IEEE, 2019, pp. 1–8.
- [122] A. Wehenkel, A. Mukhopadhyay, J.-Y. Le Boudec, and M. Paolone, "Parameter estimation of three-phase untransposed short transmission lines from synchrophasor measurements," *IEEE Transactions on Instrumentation and Measurement*, vol. 69, no. 9, pp. 6143–6154, 2020.
- [123] A. M. Kettner and M. Paolone, "On the properties of the compound nodal admittance matrix of polyphase power systems," *IEEE Transactions on Power Systems*, vol. 34, no. 1, pp. 444–453, 2018.

- [124] S. Van Huffel and P. Lemmerling, *Total least squares and errors-in-variables modeling: analysis, algorithms and applications*. Springer Science & Business Media, 2013.
- [125] I. Markovsky and S. Van Huffel, "Overview of total least-squares methods," *Signal processing*, vol. 87, no. 10, pp. 2283–2302, 2007.
- [126] D. Arthur and S. Vassilvitskii, "k-means++: The advantages of careful seeding," Stanford, Tech. Rep., 2006.
- [127] *Instrument Transformers*; "Additional requirements for electronic current transformers," *Standard IEC*, pp. 61 869–7, 2014.
- [128] *Instrument Transformers*; "Additional requirements for electronic voltage transformers," *Standard IEC*, pp. 61 869–8, 2011.
- [129] M. Lefebvre, R. Keeler, R. Sobie, and J. White, "Propagation of errors for matrix inversion," *Nuclear Instruments and Methods in Physics Research Section A: Accelerators, Spectrometers, Detectors and Associated Equipment*, vol. 451, no. 2, pp. 520–528, 2000.
- [130] P. Romano and M. Paolone, "Enhanced interpolated-dft for synchrophasor estimation in fpgas: Theory, implementation, and validation of a pmu prototype," *IEEE Transactions on Instrumentation and Measurement*, vol. 63, no. 12, pp. 2824–2836, 2014.
- [131] M. Paolone, J.-Y. Le Boudec, S. Sarri, and L. Zanni, "Static and recursive pmu-based state estimation processes for transmission and distribution power grids," IET, Tech. Rep., 2015.
- [132] D. L. Mills, "Internet time synchronization: the network time protocol," *IEEE Trans. comm.*, vol. 39, no. 10, pp. 1482–1493, 1991.
- [133] S. Nowak, Y. C. Chen, and L. Wang, "Measurement-based optimal der dispatch with a recursively estimated sensitivity model," *IEEE Transactions on Power Systems*, vol. 35, no. 6, pp. 4792–4802, 2020.
- [134] J. Parkum, N. K. Poulsen, and J. Holst, "Recursive forgetting algorithms," *International Journal of Control*, vol. 55, no. 1, pp. 109–128, 1992.
- [135] A. Vahidi, A. Stefanopoulou, and H. Peng, "Recursive least squares with forgetting for online estimation of vehicle mass and road grade: theory and experiments," *Vehicle System Dynamics*, vol. 43, no. 1, pp. 31–55, 2005.
- [136] T. Fortescue, L. S. Kershenbaum, and B. E. Ydstie, "Implementation of self-tuning regulators with variable forgetting factors," *Automatica*, vol. 17, no. 6, pp. 831–835, 1981.
- [137] L. Cao and H. M. Schwartz, "A novel recursive algorithm for directional forgetting," in *Proceedings of the 1999 American Control Conference (Cat. No. 99CH36251)*, vol. 2. IEEE, 1999, pp. 1334–1338.

## Bibliography

---

- [138] S. Bittanti, P. Bolzern, and M. Campi, “Exponential convergence of a modified directional forgetting identification algorithm,” *Systems & Control Letters*, vol. 14, no. 2, pp. 131–137, 1990.
- [139] A. Khosravi, S. Nahavandi, and D. Creighton, “Prediction intervals for short-term wind farm power generation forecasts,” *IEEE Transactions on sustainable energy*, vol. 4, no. 3, pp. 602–610, 2013.
- [140] R. Gupta and M. Paolone, “Experimental validation of model-less robust voltage control using measurement-based estimated voltage sensitivity coefficients,” *In preparation*, 2022.
- [141] K. Christakou, “Real-time optimal controls for active distribution networks: from concepts to applications,” Ph.D. dissertation, Ph. D. dissertation, Dept. Information and communications, Univ. École ..., 2015.
- [142] Y. P. Agalgaonkar, B. C. Pal, and R. A. Jabr, “Distribution voltage control considering the impact of pv generation on tap changers and autonomous regulators,” *IEEE Transactions on Power Systems*, vol. 29, no. 1, pp. 182–192, 2013.
- [143] H. Su, P. Li, X. Fu, L. Yu, and C. Wang, “Augmented sensitivity estimation based voltage control strategy of active distribution networks with pmu measurement,” *IEEE Access*, vol. 7, pp. 44 987–44 997, 2019.
- [144] D. Bertsimas, D. B. Brown, and C. Caramanis, “Theory and applications of robust optimization,” *SIAM review*, vol. 53, no. 3, pp. 464–501, 2011.
- [145] K. Christakou, M. Paolone, and A. Abur, “Voltage control in active distribution networks under uncertainty in the system model: a robust optimization approach,” *IEEE Transactions on Smart Grid*, vol. 9, no. 6, pp. 5631–5642, 2017.
- [146] D. Bertsimas and M. Sim, “The price of robustness,” *Operations research*, vol. 52, no. 1, pp. 35–53, 2004.
- [147] *LEM Voltage Transducer CV 3-1000*. [Online]. Available: [https://www.lem.com/sites/default/files/products\\_datasheets/cv\\_3-1000.pdf](https://www.lem.com/sites/default/files/products_datasheets/cv_3-1000.pdf)
- [148] *LEM Current Transducer LF 205-S/SP3*. [Online]. Available: [https://www.lem.com/sites/default/files/products\\_datasheets/lf\\_205-s\\_sp3.pdf](https://www.lem.com/sites/default/files/products_datasheets/lf_205-s_sp3.pdf)
- [149] R. Gupta, F. Sossan, and M. Paolone, “Countrywide pv hosting capacity and energy storage requirements for distribution networks: The case of switzerland,” *Applied Energy*, vol. 281, p. 116010, 2021.
- [150] International Energy Agency, PVPS T7-4, *Potential for building integrated photovoltaics*, 2002.

- 
- [151] C. P. Castillo, F. B. e Silva, and C. Lavallo, "An assessment of the regional potential for solar power generation in eu-28," *Energy policy*, vol. 88, pp. 86–99, 2016.
  - [152] L. Wiginton, H. T. Nguyen, and J. M. Pearce, "Quantifying rooftop solar photovoltaic potential for regional renewable energy policy," *Computers, Environment and Urban Systems*, vol. 34, no. 4, pp. 345–357, 2010.
  - [153] K. Orehounig, G. Mavromatidis, R. Evins, V. Dorer, and J. Carmeliet, "Towards an energy sustainable community: An energy system analysis for a village in switzerland," *Energy and Buildings*, vol. 84, pp. 277–286, 2014.
  - [154] G. Mavromatidis, K. Orehounig, and J. Carmeliet, "Evaluation of photovoltaic integration potential in a village," *Solar Energy*, vol. 121, pp. 152–168, 2015.
  - [155] R. Singh and R. Banerjee, "Estimation of rooftop solar photovoltaic potential of a city," *Solar Energy*, vol. 115, pp. 589–602, 2015.
  - [156] N. Mohajeri, G. Upadhyay, A. Gudmundsson, D. Assouline, J. Kampf, and J.-L. Scartezzini, "Effects of urban compactness on solar energy potential," *Renewable Energy*, vol. 93, pp. 469–482, 2016.
  - [157] N. Mohajeri, A. Gudmundsson, T. Kunckler, G. Upadhyay, D. Assouline, J. Kampf, and J. Scartezzini, "A solar-based sustainable urban design: The effects of city-scale street-canyon geometry on solar access in geneva, switzerland," *Applied Energy*, vol. 240, pp. 173–190, 2019.
  - [158] K. Bódis, I. Kougias, A. Jäger-Waldau, N. Taylor, and S. Szabó, "A high-resolution geospatial assessment of the rooftop solar photovoltaic potential in the European Union," *Renewable and Sustainable Energy Reviews*, vol. 114, p. 109309, 2019.
  - [159] R. Cossent, L. Olmos, T. Gómez, C. Mateo, and P. Frías, "Distribution network costs under different penetration levels of distributed generation," *European Transactions on Electrical Power*, vol. 21, no. 6, pp. 1869–1888, 2011.
  - [160] A. Navarro, L. F. Ochoa, and D. Randles, "Monte carlo-based assessment of pv impacts on real uk low voltage networks," in *2013 IEEE Power Energy Society General Meeting*, 2013, pp. 1–5.
  - [161] A. Navarro, L. F. Ochoa, and D. Randles, "Monte carlo-based assessment of pv impacts on real uk low voltage networks," in *2013 IEEE Power & Energy Society General Meeting*. IEEE, 2013, pp. 1–5.
  - [162] A. Arshad, M. Lindner, and M. Lehtonen, "An analysis of photo-voltaic hosting capacity in finnish low voltage distribution networks," *Energies*, vol. 10, no. 11, p. 1702, 2017.
  - [163] F. Ebe, B. Idlbi, J. Morris, G. Heilscher, and F. Meier, "Evaluation of pv hosting capacity of distribuion grids considering a solar roof potential analysis—comparison of different algorithms," in *2017 IEEE Manchester PowerTech*. IEEE, 2017, pp. 1–6.



- [164] H. Al-Saadi, R. Zivanovic, and S. F. Al-Sarawi, "Probabilistic hosting capacity for active distribution networks," *IEEE Transactions on Industrial Informatics*, vol. 13, no. 5, pp. 2519–2532, 2017.
- [165] F. Sossan, J. Darulova, M. Paolone, A. Kahl, S. J. Bartlett, and M. Lehning, "Large scale deployment of pv units in existing distribution networks: Optimization of the installation layout," in *2016 Power Systems Computation Conference (PSCC)*. IEEE, 2016, pp. 1–6.
- [166] A. Fuchs, T. Demiray, E. Panos, R. Kannan, T. Kober, C. Bauer, W. Schenler, P. Burgherr, and S. Hirschberg, "Ischess–integration of stochastic renewables in the swiss electricity supply system," ETH Zurich, Tech. Rep., 2017.
- [167] Z. Wang, A. Scaglione, and R. J. Thomas, "Generating statistically correct random topologies for testing smart grid communication and control networks," *IEEE transactions on Smart Grid*, vol. 1, no. 1, pp. 28–39, 2010.
- [168] P. Schultz, J. Heitzig, and J. Kurths, "A random growth model for power grids and other spatially embedded infrastructure networks," *The European Physical Journal Special Topics*, vol. 223, no. 12, pp. 2593–2610, 2014.
- [169] S. Soltan and G. Zussman, "Generation of synthetic spatially embedded power grid networks," in *2016 IEEE Power and Energy Society General Meeting (PESGM)*. IEEE, 2016, pp. 1–5.
- [170] A. B. Birchfield, T. Xu, K. M. Gegner, K. S. Shetye, and T. J. Overbye, "Grid structural characteristics as validation criteria for synthetic networks," *IEEE Transactions on power systems*, vol. 32, no. 4, pp. 3258–3265, 2016.
- [171] W. Medjroubi, U. P. Müller, M. Scharf, C. Matke, and D. Kleinhans, "Open data in power grid modelling: new approaches towards transparent grid models," *Energy Reports*, vol. 3, pp. 14–21, 2017.
- [172] V. J. Tsai, "Delaunay triangulations in tin creation: an overview and a linear-time algorithm," *International Journal of Geographical Information Science*, vol. 7, no. 6, pp. 501–524, 1993.
- [173] H. Rui, M. Arnold, and W. H. Wellssow, "Synthetic medium voltage grids for the assessment of smart grid techniques," in *2012 3rd IEEE PES Innovative Smart Grid Technologies Europe (ISGT Europe)*. IEEE, 2012, pp. 1–8.
- [174] J. Amme, G. Pleßmann, J. Bühler, L. Hülk, E. Kötter, and P. Schwaegerl, "The ego grid model: An open-source and open-data based synthetic medium-voltage grid model for distribution power supply systems," in *Journal of Physics: Conference Series*, vol. 977, no. 1, 2018.
- [175] U. P. Müller, I. Cusmann, C. Wingenbach, and J. Wendiggensen, "AC power flow simulations within an open data model of a high voltage grid," in *Advances and New Trends in Environmental Informatics*. Springer, 2017, pp. 181–193.

- [176] U. P. Müller, L. Wienholt, D. Kleinhans, I. Cußmann, W.-D. Bunke, G. Pleßmann, and J. Wendiggensen, "The ego grid model: An open source approach towards a model of german high and extra-high voltage power grids," in *Journal of Physics: Conference Series*, vol. 977, no. 1. IOP Publishing, 2018, p. 012003.
- [177] L. Hülk, L. Wienholt, I. Cußmann, U. P. Müller, C. Matke, and E. Kötter, "Allocation of annual electricity consumption and power generation capacities across multiple voltage levels in a high spatial resolution," *International Journal of Sustainable Energy Planning and Management*, vol. 13, pp. 79–92, 2017.
- [178] W. Medjroubi, C. Matke, and D. Kleinhans, "Scigird: an open source reference model of european transmission networks for scientific analysis," 2014.
- [179] *osmTGmod*, 2016. [Online]. Available: <https://github.com/wupperinst/osmTGmod>
- [180] International Renewable Energy Agency, *Future of Solar Photovoltaic: Deployment, investment, technology, grid integration and socio-economic aspects*, 2019.
- [181] D. Assouline, N. Mohajeri, and J.-L. Scartezzini, "Quantifying rooftop photovoltaic solar energy potential: A machine learning approach," *Solar Energy*, vol. 141, pp. 278–296, 2017.
- [182] —, "Large-scale rooftop solar photovoltaic technical potential estimation using random forests," *Applied energy*, vol. 217, pp. 189–211, 2018.
- [183] A. Walch, R. Castello, N. Mohajeri, and J.-L. Scartezzini, "Big data mining for the estimation of hourly rooftop photovoltaic potential and its uncertainty," *Applied Energy*, vol. 262, 2020.
- [184] F. Aurenhammer, "Voronoi diagrams—a survey of a fundamental geometric data structure," *ACM Computing Surveys (CSUR)*, vol. 23, no. 3, pp. 345–405, 1991.
- [185] *ENTSO-E Transmission System Map*, 2019. [Online]. Available: <https://www.entsoe.eu/data/map/>
- [186] B. Wiegmanns, "Gridkit extract of entso-e interactive map," jun 2016. [Online]. Available: <https://doi.org/10.5281/zenodo.55853>
- [187] S. Wang, Z. Lu, S. Ge, and C. Wang, "An improved substation locating and sizing method based on the weighted voronoi diagram and the transportation model," *Journal of Applied Mathematics*, vol. 2014, 2014.
- [188] Y. Chen, S. Wang, J. Yu, W. Li, X. Shi, and W. Yang, "Optimal weighted voronoi diagram method of distribution network planning considering city planning coordination factors," in *2017 4th International Conference on Systems and Informatics (ICSAI)*. IEEE, 2017, pp. 335–340.

## Bibliography

---

- [189] Y. Yan, F. Wang, K. Zhou, S. Chen, J. Huang, and B. Wen, "Substation sower supply area division based on voronoi diagram and road grid," in *IOP Conference Series: Materials Science and Engineering*, vol. 677, no. 4. IOP Publishing, 2019, p. 042101.
- [190] L. Eymann, J. Rohrer, and M. Stucki, "Energieverbrauch der schweizer kantone: Endenergieverbrauch und mittelabfluss durch den energie-import," *ZHAW Zürcher Hochschule für Angewandte Wissenschaften*, 2014.
- [191] K. Wojdyga, "An influence of weather conditions on heat demand in district heating systems," *Energy and Buildings*, vol. 40, no. 11, pp. 2009–2014, 2008.
- [192] S. Avdakovic, A. Ademovic, and A. Nuhanovic, "Correlation between air temperature and electricity demand by linear regression and wavelet coherence approach: UK, Slovakia and Bosnia and Herzegovina case study," *Archives of Electrical Engineering*, vol. 62, no. 4, 2013.
- [193] R. C. Gonzalez, R. E. Woods, and S. L. Eddins, *Digital image processing using MATLAB*. Pearson Education India, 2004.
- [194] Swiss Federal Office of Energy, *Statistique Suisse de L'électricité 2015*, 2016.
- [195] P. S. Georgilakis and N. D. Hatziaargyriou, "A review of power distribution planning in the modern power systems era: Models, methods and future research," *Electric Power Systems Research*, vol. 121, pp. 89–100, 2015.
- [196] S. Najafi, S. H. Hosseinian, M. Abedi, A. Vahidnia, and S. Abachezadeh, "A framework for optimal planning in large distribution networks," *IEEE Transactions on Power Systems*, vol. 24, no. 2, pp. 1019–1028, 2009.
- [197] J. Gomez, H. Khodr, P. De Oliveira, L. Ocque, J. Yusta, R. Villasana, and A. Urdaneta, "Ant colony system algorithm for the planning of primary distribution circuits," *IEEE Transactions on power systems*, vol. 19, no. 2, pp. 996–1004, 2004.
- [198] E. Diaz-Dorado, J. Cidrás, and E. Míguez, "Application of evolutionary algorithms for the planning of urban distribution networks of medium voltage," *IEEE Transactions on Power Systems*, vol. 17, no. 3, pp. 879–884, 2002.
- [199] S. Afifi, D.-C. Dang, and A. Moukrim, "A simulated annealing algorithm for the vehicle routing problem with time windows and synchronization constraints," in *International Conference on Learning and Intelligent Optimization*. Springer, 2013, pp. 259–265.
- [200] S. Goswami, "Distribution system planning using branch exchange technique," *IEEE Transactions on Power Systems*, vol. 12, no. 2, pp. 718–723, 1997.
- [201] G. Peponis and M. Papadopoulos, "New dynamic, branch exchange method for optimal distribution system planning," *IEE Proceedings-Generation, Transmission and Distribution*, vol. 144, no. 3, pp. 333–339, 1997.

- 
- [202] N. G. Boulaxis and M. P. Papadopoulos, "Optimal feeder routing in distribution system planning using dynamic programming technique and gis facilities," *IEEE Transactions on Power Delivery*, vol. 17, no. 1, pp. 242–247, 2002.
- [203] J. M. Nahman and D. M. Peric, "Optimal planning of radial distribution networks by simulated annealing technique," *IEEE Transactions on Power Systems*, vol. 23, no. 2, pp. 790–795, 2008.
- [204] J. M. Nahman and D. M. Perić, "Radial distribution network planning under uncertainty by applying different reliability cost models," *International Journal of Electrical Power & Energy Systems*, vol. 117, p. 105655, 2020.
- [205] F. Pilo, S. Jupe, F. Silvestro, K. El Bakari, C. Abbey, G. Celli, J. Taylor, A. Baitch, and C. Carter-Brown, "Planning and optimisation of active distribution systems-an overview of cigre working group c6. 19 activities," *IET*, 2012.
- [206] EN 50160, "Voltage characteristics of electricity supplied by public distribution systems," *European standard*, 1999.
- [207] M. Nick, R. Cherkaoui, and M. Paolone, "Optimal planning of distributed energy storage systems in active distribution networks embedding grid reconfiguration," *IEEE Transactions on Power Systems*, vol. 33, no. 2, pp. 1577–1590, 2017.
- [208] *JRC Photovoltaic Geographical Information System (PVGIS) - European Commission*, 2016. [Online]. Available: [https://re.jrc.ec.europa.eu/pvg\\_tools/en/tools.html](https://re.jrc.ec.europa.eu/pvg_tools/en/tools.html)
- [209] A. Walch, N. Mohajeri, and J.-L. Scartezzini, "A critical comparison of methods to estimate solar rooftop photovoltaic potential in switzerland," in *Journal of Physics: Conference Series*, vol. 1343, no. 1. IOP Publishing, 2019, p. 012035.
- [210] R. Buffat, S. Grassi, and M. Raubal, "A scalable method for estimating rooftop solar irradiation potential over large regions," *Applied energy*, vol. 216, pp. 389–401, 2018.
- [211] F. Sossan, "Equivalent electricity storage capacity of domestic thermostatically controlled loads," *Energy*, vol. 122, pp. 767–778, 2017.
- [212] L. Fabietti, T. T. Gorecki, E. Namor, F. Sossan, M. Paolone, and C. N. Jones, "Enhancing the dispatchability of distribution networks through utility-scale batteries and flexible demand," *Energy and Buildings*, vol. 172, pp. 125–138, 2018.
- [213] F. Sossan, A. M. Kosek, S. Martinenas, M. Marinelli, and H. W. Bindner, "Scheduling of domestic water heater power demand for maximizing pv self-consumption using model predictive control," in *2013 4th IEEE PES Innovative Smart Grid Technologies Europe*. IEEE, 2013.
- [214] R. Luthander, J. Widén, D. Nilsson, and J. Palm, "Photovoltaic self-consumption in buildings: A review," *Applied Energy*, vol. 142, 2015.

## Bibliography

---

- [215] E. Stai, F. Sossan, E. Namor, J. Y. L. Boudec, and M. Paolone, “A receding horizon control approach for re-dispatching stochastic heterogeneous resources accounting for grid and battery losses,” *Electric Power Systems Research*, vol. 185, 2020.
- [216] M. Kraning, Y. Wang, E. Akuiyibo, and S. Boyd, “Operation and configuration of a storage portfolio via convex optimization,” in *Proceedings of the 18th IFAC World Congress*, vol. 18, 2011, pp. 10 487–10 492.
- [217] C. Bauer and S. Hirschberg, “Potentiale kosten und umweltauswirkungen von stromproduktionsanlagen,” *PSI-Paul Scherrer Institut, Bundesamt für Energie BFE*, pp. 1–10, 2017.

# Rahul K. Gupta

ELL 037, Station 11, EPFL, Lausanne, Switzerland 1015

[rahul.gupta@epfl.ch](mailto:rahul.gupta@epfl.ch), +41-762858528, [GoogleScholar](#)|[ResearchGate](#)|[LinkedIn](#)|[Orcid](#).

---

## EDUCATION

- **Ph.D. in Electrical Engineering**, 09/2018 - 12/2022  
Distributed Electrical Systems Laboratory,  
École Polytechnique Fédérale de Lausanne (EPFL), Switzerland  
Thesis title: “*Methods for Grid-aware Operation and Planning of Active Distribution Networks*”  
Thesis directors: Prof. Mario Paolone (EPFL), Prof. Fabrizio Sossan (ParisTech MINES, Nice, France).
- **M.Sc. in Electrical Engineering**, 09/2016 - 07/2018  
Smart Grids Science and Technology Orientation,  
École Polytechnique Fédérale de Lausanne, Switzerland  
Thesis title: “*Optimal Planning of Distributed Energy Resources in Distribution Networks*”  
Thesis director: Prof. Mario Paolone. Final grade: 5.75/6.
- **B.Tech in Electrical Engineering**, 07/2010 - 07/2014  
National Institute of Technology, Rourkela, India  
Final grade: 9.66/10.

## EXPERIENCE

**Doctoral Researcher, Distributed Electrical Systems Laboratory, EPFL, Switzerland** 09/2018 - present

- Optimal Power Flow (OPF)-based grid-aware scheduling and control frameworks for the active distribution networks (ADNs). Stochastic optimization-based dispatch plan computation considering uncertainties on demand and generation by scenarios. Real-time model predictive control of stochastic and energy storage units.
- Measurement-based/data-driven estimation and control frameworks for distribution networks. Recursive estimation of power-flow sensitivity coefficients for robust voltage control. Estimation of compound admittance matrix of an untransposed distribution network using voltage and branch currents measurements.
- Distributed control and optimization of ADNs with heterogeneous distributed energy resources (batteries, curtailable photovoltaic plants, electrolyzers, fuel cells, etc.) using a method such as ADMM and its variants.
- Experimental validation of the above control schemes on real-life low-voltage microgrid (hosted at the Distributed Electrical Systems Laboratory, EPFL) and medium-voltage distribution networks (in Aigle, Switzerland).

**Visiting Doctoral Researcher, ParisTech MINES, Nice, France**

09/2019 - 01/2020

- Development of countrywide planning tool for the estimation of photovoltaic (PV) hosting capacity and battery energy storage requirements (as alternative to grid reinforcement) of power distribution networks.
- Synthetic distribution network generation for countrywide planning and operation study for power distribution networks, and made publicly available.

**Student Assistant, Distributed Electrical Systems Laboratory, EFPL, Switzerland** 02/2018 - 06/2018

- Optimal planning of battery energy storage systems in distribution networks with different planning horizons.
- Probabilistic load flow (PLF)-based assessment of PV hosting capacity of distribution networks.
- Performance assessment of grid violation using satellite- and pyranometer-based solar irradiance estimation of PV generation connected to distribution grids.

**Intern, ABB Corporate Research Centre, Baden, Switzerland** 08/2017 - 01/2018

- Planning and acquisition of high voltage, high precision DC conductivity and surface potential measurements.
- Aging experiments on metallized film capacitors with temperature.

**Research Engineer, NUS lab of Sensors, National University of Singapore, Singapore** 01/2015 - 07/2016

- Design and fabrication of spring-based hybrid vibration energy harvester using triboelectric and electromagnetic mechanisms.

**Management Trainee at SAIL, India** 09/2014 – 12/2014

- Supervision on maintenance of electrical drives responsible for proper operation of ladle furnaces, casting machines, and the rolling mills.

## PUBLICATIONS

### Journal Articles (published)

1. **Rahul Gupta**, Antonio Zecchino, Ji-Hyun Yi, and Mario Paolone. Reliable dispatch of active distribution networks via a two-layer grid-aware model predictive control: Theory and experimental validation. *IEEE Open Access Journal of Power and Energy*, 2022. [Publisher Link](#).
2. **Rahul Gupta**, Sherif Fahmy, and Mario Paolone. Coordinated day-ahead dispatch of multiple power distribution grids hosting stochastic resources: An admm-based framework. *Electric Power Systems Research*, 212:108555, 2022. [Publisher Link](#).
3. **Rahul Gupta**, Fabrizio Sossan, and Mario Paolone. Model-less robust voltage control in active distribution networks using sensitivity coefficients estimated from measurements. *Electric Power Systems Research*, 212:108547, 2022. [Publisher Link](#).
4. Francesco Gerini, Yihui Zuo, **Rahul Gupta**, Antonio Zecchino, Zhao Yuan, Elena Vagnoni, Rachid Cherkaoui, and Mario Paolone. Optimal grid-forming control of battery energy storage systems providing multiple services: Modeling and experimental validation. *Electric Power Systems Research*, 212:108567, 2022. [Publisher Link](#).
5. **Rahul Gupta**, Fabrizio Sossan, Jean-Yves Le Boudec, and Mario Paolone. Compound admittance matrix estimation of three-phase untransposed power distribution grids using synchrophasor measurements. *IEEE Transactions on Instrumentation and Measurement*, 70:1–13, 2021. [Publisher Link](#).
6. **Rahul Gupta**, Fabrizio Sossan, and Mario Paolone. Countrywide pv hosting capacity and energy storage requirements for distribution networks: The case of switzerland. *Applied Energy*, 281:116010, 2021. [Publisher Link](#).

7. **Rahul Gupta**, Fabrizio Sossan, and Mario Paolone. Grid-aware distributed model predictive control of heterogeneous resources in a distribution network: Theory and experimental validation. *IEEE Transactions on Energy Conversion*, 36(2):1392–1402, 2020. [Publisher Link](#).
8. Sherif Fahmy, **Rahul Gupta**, and Mario Paolone. Grid-aware distributed control of electric vehicle charging stations in active distribution grids. *Electric Power Systems Research*, 189:106697, 2020. [Publisher Link](#).
9. Fabrizio Sossan, Enrica Scolari, **Rahul Gupta**, and Mario Paolone. Solar irradiance estimations for modeling the variability of photovoltaic generation and assessing violations of grid constraints: A comparison between satellite and pyranometers measurements with load flow simulations. *Journal of Renewable and Sustainable Energy*, 11(5):056103, 2019. [Publisher Link](#).

#### Journal Articles (under review)

1. **Rahul Gupta**, Fabrizio Sossan, and Mario Paolone. Optimal sizing and siting of energy storage systems considering curtailable photovoltaic generation in power distribution network. *[Submitted to Applied Energy]*, 2022

#### Conference Papers

1. **Rahul Gupta**, Vladimir Sovljanski, Fabrizio Sossan, and Mario Paolone. Performance comparison of alternating direction optimization methods for linear-opf based real-time predictive control. In *2021 IEEE Madrid PowerTech*, pages 1–6. IEEE, 2021. [Publisher Link](#).
2. **Rahul Gupta**, Fabrizio Sossan, and Mario Paolone. Performance assessment of linearized opf-based distributed real-time predictive control. In *2019 IEEE Milan PowerTech*, pages 1–6. IEEE, 2019. [Publisher Link](#).
3. **Rahul Gupta**, Fabrizio Sossan, Enrica Scolari, Emil Namor, Luca Fabietti, Colin Jones, and Mario Paolone. An admm-based coordination and control strategy for pv and storage to dispatch stochastic prosumers: Theory and experimental validation. In *2018 Power Systems Computation Conference (PSCC)*, pages 1–7. IEEE, 2018. [Publisher Link](#).

#### Papers (in preparation)

1. Rahul Gupta. Quantifying uncertainty on the power-flow sensitivity coefficients from uncertain branches parameters and noisy grid-state measurements. *In preparation*, 2022
2. Rahul Gupta and Mario Paolone. Experimental validation of model-less robust voltage control using measurement-based estimated voltage sensitivity coefficients. *In preparation*, 2022

#### HONORS AND AWARDS

1. **Zanelli: technologie et développement durable prize 2018** for the best master project in the field of sustainable development: environment, economy or society, EPFL, Switzerland.
2. **J.N. Tata Endowment Award** and **K. C. Mahindra Scholarship** for financing master studies at EPFL.
3. **Ashim Choudhury Memorial Gold Medal** for overall academic topper among all the undergraduate Electrical Engineering Students of 2014 batch, NIT Rourkela.
4. **Institute Silver Medal** for academic topper among Students of 2014 batch, NIT Rourkela, India.
5. **Sugat Kishore Mall Memorial Award** for the best graduate in electrical engineering batch of 2014, NIT Rourkela, India.
6. **DAAD WISE-2013 Scholarship** (Deutscher Akademischer Austausch Dienst), (German Academic Exchange Service) for an internship at University of Bremen, Germany.



## PRESENTATIONS

### Oral

1. *XXII PSCC, Porto, Portugal*: Coordinated Day-ahead Dispatch of Multiple Power Distribution Grids hosting Stochastic Resources: An ADMM-based Framework, Gupta, R., Fahmy, S., Paolone, M. 2022.
2. *XXII PSCC, Porto, Portugal*: Model-less Robust Voltage Control in Active Distribution Networks using Sensitivity Coefficients Estimated from Measurements, Gupta, R., Sossan, F., Paolone, M. 2022.
3. *14<sup>th</sup> PowerTech Conference, Madrid, Spain*: Performance Comparison of Alternating Direction Optimization Methods for Linear-OPF based Real-time Predictive Control, Gupta, R., Sossan, F., Paolone, M. 2021.
4. *13<sup>th</sup> PowerTech Conference, Milan, Italy*: Performance assessment of linearized opf-based distributed real-time predictive control, Gupta, R., Sossan, F., Paolone, M. 2019.
5. *XX PSCC, Dublin, Ireland*: An admm-based coordination and control strategy for pv and storage to dispatch stochastic prosumers: Theory and experimental validation, Gupta, R., Sossan, F., Scolari, E., Namor, E., Fabietti, L., Jones, C., Paolone, M., 2018.

### Poster

1. *PATHFNDR Workshop, Bern, Switzerland*: Coordinated Day-ahead Dispatch of Multiple Power Distribution Grids hosting Stochastic Resources, Gupta, R., Paolone, M., 2022.
2. *PATHFNDR Workshop, Bern, Switzerland*: Model Predictive Control of Multi-Energy Systems in a Microgrid, Gupta, R., Fernando, S., Paolone, M., 2022.
3. *SCCER-FURIES Annual Conference, EPFL, Lausanne, Switzerland*: Linearized-OPF based Distributed Real-time Predictive Control of Distribution Networks, Gupta, R., Sossan, F., Paolone, M. 2019.
4. *SCCER-FURIES Annual Conference, EPFL, Lausanne, Switzerland*: Optimal Planning of Energy Storage Systems in Electrical Distribution Grids using Receding Horizon Control Strategies, Gupta, R., 2018.

### Invited

1. *The 7th Purple Mountain Forum Panel Session - Advanced Optimization and Control Methods towards a Carbon Neutral Energy Internet, Nanjing China (Virtual)*: Grid aware Model Predictive Control of Distributed Energy Resources in a Distribution network Theory and Experimental Validation, Gupta, R., 2022.

## EXPERTISE

- Operation and planning of power distribution grids, optimal power flow.
- Robust and stochastic-based optimization for control and scheduling of power distribution networks.
- Model Predictive control, distributed control, measurement-based/data-driven control.
- Admittance matrix estimation, parameter estimation, model-identification.
- Convex optimization, convexification methods (linearization, relaxation etc.).
- Hands-on experience in operating grid-scale battery storage, photovoltaic plants, electrolyzers, fuel-cells and supercapacitors in a real-life distribution grid.
- Intra-day and day-ahead forecasting of stochastic resources such as PV generation and demand.
- **Softwares**: Matlab, Python, Julia (learning), LabVIEW, C++, EMTP-RV, pyomo, pypower, MATPOWER.

## INVOLVEMENT IN RESEARCH PROJECTS

### SWEET PATHFINDER

2020 - 2023

- Modeling and control of multi-energy systems.
- Validation of multi-grid dispatch framework.

### SCCER-FURIES REEL Demonstrator

2019 - 2022

- Validation of OPF-based real-time control algorithm on a real-life medium voltage distribution network in Aigle, Switzerland hosting 2.5MWh/1.5MW battery storage capacity, 3.2MWP photovoltaic, 3.4 MVA hydro and 2.8MW base demand.
- Development of the software for operation of the battery energy storage system for real-time control.

### Joint Activity Scenario and Modelling

2017 - 2022

- Providing a set of robust scenarios for the realization of the Swiss Energy Strategy 2050.
- Assessment of photovoltaic generation hosting capacity for the power distribution networks of Switzerland.
- Computing cost-optimal placement of energy storage systems for different levels of photovoltaic generation.

## TEACHING ACTIVITIES

- Teaching assistant for the “Smart Grids Technologies” course, M.Sc. in electrical engineering, EPFL, 2020-present.

## SUPERVISED STUDENT PROJECTS

1. Model Predictive Control of Multi-Energy Systems in a Microgrid, Master Thesis Project, Mr. Sooria Fernando, EPFL, Spring 2022.
2. Day-ahead Grid-aware Dispatcher for Active Distribution Networks Embedding Stochastic Electric Vehicle Charging Stations, Master Thesis Project, Mr. Max Chevron, Spring 2021.
3. Optimal Planning of Electric Vehicle Charging Stations and Photovoltaic Generation in a Distribution Network, Master Thesis Project, Mr. Vladimir Sovljanski, Fall 2021.
4. Generating Realistic Low Voltage Distribution Networks using Representative Geographical and Socio-economic Information for Switzerland, Bachelor Project, Mr. Kristoffer Berglund, KTH, Spring 2021.
5. Detection of MV and HV poles using Convolutional Neural Network, Bachelor Project, Mr. Louis Drame, EPFL, Spring 2021.
6. Modeling of a PEM Electrolyzer for Model Predictive Control, Bachelor Project, Keske Cem, EPFL, Spring 2021.
7. Solar Irradiance Forecast using Sky-Camera Images, Ms. Maissara Beliazi, Mr. Ahmed Achiche, Bachelor Project, EPFL, Spring 2021.
8. Solar Irradiance Forecast using Time-series Forecasting, Mr. Aziz Ben, Bachelor Project, EPFL, Spring 2021.
9. Generating Realistic Power Distribution Network for Switzerland, Master Semester Project, EPFL, Fall 2020.

10. Data-driven Estimation of Voltage Sensitivity Coefficients in Power Distribution Grids, Master Thesis Project, Mr. Robin Henry, The University of Edinburgh, Fall 2020.
11. State Estimation of Power Grids: Analysis of Available Methods and Effects of Parameter Inaccuracies, Master Thesis Project, Mr. Bruno Gabriele, University of Genova, Spring 2019.
12. Performance Comparison of Different Distributed Algorithms for Grid Aware Predictive Control, Master Semester Project, Mr. Vladimir Sovljanski, EPFL, Fall 2018.

## SERVICE TO THE PROFESSION

I act on a regular basis as a reviewer for among the most important international journals (IEEE PES Transactions on Power Systems, IEEE Transactions on Smart Grids, IEEE PES Transactions on Sustainable Energy, IEEE Transactions on Circuits and Systems, Elsevier Sustainable Energy, Grids and Networks Journal, Elsevier Electric Power Systems Research, Elsevier Sustainable Development, and major international conferences (PSCC, IEEE ISGT, IEEE Powertech, SEST) of the power systems community

## REFEREES

Prof. Mario Paolone  
Distributed Electrical Systems Lab,  
EPFL, Switzerland  
[mario.paolone@epfl.ch](mailto:mario.paolone@epfl.ch)  
☎ +41 21 693 26 62

Prof. Fabrizio Sossan  
Institute of Sustainable Energy,  
HES-SO, Switzerland  
[fabrizio.sossan@hevs.ch](mailto:fabrizio.sossan@hevs.ch)  
☎ +41 58 606 97 96

Dr. Rachid Cherkaoui  
Power System Group,  
EPFL, Switzerland  
[rachid.cherkaoui@epfl.ch](mailto:rachid.cherkaoui@epfl.ch)  
☎ +41 21 693 20 58

Lausanne, 7 Dec 2022

Rahul K. Gupta